Title
A Quantitative Seismic Behavior Assessment of Buried Structures

Author
Zhang, Wenyang

Publication Date
2019

Peer reviewed|Thesis/dissertation

UNIVERSITY OF CALIFORNIA

Los Angeles

A Quantitative Seismic Behavior Assessment of Buried Structures

A dissertation submitted in partial satisfaction

of the requirements for the degree

Doctor of Philosophy in Civil and Environmental Engineering

by

Wenyang Zhang

2019

ABSTRACT OF THE DISSERTATION

A Quantitative Seismic Behavior Assessment of Buried Structures

by

Wenyang Zhang
Doctor of Philosophy in Civil and Environmental Engineering
University of California, Los Angeles, 2019
Professor Ertugrul Taciroglu, Chair

This dissertation is focused on quantitatively investigating the nonlinear seismic behavior assessment of underground structures, by performing high-fidelity SSI analyses. Specifically, several computer codes are developed for forward simulation of wave propagation in both two- (plane-strain) and three-dimensional semi-infinite heterogeneous solid media. (*i*) a multi-axial bounding surface plasticity model is implemented, calibrated and validated through centrifuge test data, to consider the soil nonlinearities (*ii*) the domain reduction method (DRM) is implemented for both 2D and 3D domains, homogeneous and heterogeneous media, vertical and inclined incident SV waves, to consistently prescribe the input motions in a truncated domain and (*iii*) perfectly matched layer (PML) is implemented for both 2D and 3D domains, to absorb the outgoing waves super efficiently.

By using the aforementioned numerical tools, multiple studies on seismic behavior assessment of underground structures are performed.

1. Development of validated methods for soil-structure analysis of buried structures. State-of-the-art versions of these simplified methods of seismic analysis for buried/embedded structures were most recently articulated in the "NCHRP 611" report, and comparisons of their predictions to experimental data are made in the present study in order to establish the validity (or lack thereof) of this method. Experiments comprises centrifuge

tests on two specimens—one relatively- stiff rectangular and one relatively-flexible circular culvert—embedded in dense dry sand. Comparisons of experimental data are also made with predictions from a calibrated two-dimensional (plane-strain) finite element (FE) model. Predictions made using this FE model are superior and exhibits acceptable errors.

2. Parametric studies of buried circular structures and a proposed improvement of the NCHRP 611 method. The NCHRP 611 method has been widely adopted as a guideline in the analysis design of buried/embedded structures due to its computational simplicity and broadly accepted accuracy for simple soil-structure configurations. However, the method is not without shortcomings. In particular, the NCHRP method is not sensitive to the inherently broadband frequency content of seismic input excitations, soil heterogeneities, and potential kinematic interaction effects. The present study seeks to quantitatively assess the brackets of the validity of the NCHRP 611 method—specifically, for soil-structure analyses of buried circular structures, and offers an improvement that is simple to implement. This is achieved through parametric studies using detailed nonlinear finite element simulations involving a broad range of ground motions, and soil and structural properties. The simulations are carried out with a model that has been validated in a prior centrifuge testing program on embedded structures. A refined version of the NCHRP 611 method, which uses maximum shear strains obtained through one-dimensional site response analyses, is shown to produce fairly accurate results for nearly all of the different cases considered in the parametric studies.

3. Fragility-based seismic performance assessment of buried structures. Fragility-based seismic performance assessment and design procedures are being refined and adopted for many civil structures. With recent advances in computational capabilities as well as broad improvements in ground motion characterization and inelastic modeling of structural and geotechnical systems, large-scale direct models for underground structures—e.g., tunnels, water reservoirs, etc. —can now be devised with relative ease and de-

ployed in engineering practice. In this study, a fragility-based seismic performance assessment of a large buried circular culvert is presented. Existing documents/codes are used to define the performance criteria and develop fragility functions through a Probabilistic Seismic Demand Analysis (PSDA) procedure. The analyses incorporate nonlinear behavior of soils and structural components, various soil layer profiles and account for uncertainties in the expected ground motions.

The dissertation of Wenyang Zhang is approved.

Yousef Bozorgnia

Scott Joseph Brandenberg

Elnaz Esmaeilzadeh Seylabi

Ertugrul Taciroglu, Committee Chair

University of California, Los Angeles

2019

To my loving family . . .

who always supports me to chase my dream

TABLE OF CONTENTS

LIST OF FIGURES

LIST OF TABLES

ACKNOWLEDGMENTS

I would like to express my sincere gratitude to my advisor, Professor Ertugrul Taciroglu, for his guidance, encouragement, and ingenuity. This dissertation would not have been possible without his steadfast support. I would like to thank Professors Yousef Bozorgnia, Scott J. Brandenberg, and Elnaz Esmaeilzadeh Seylabi for serving on my dissertation committee, and for their insightful comments. Special thanks to Professor Elnaz Esmaeilzadeh Seylabi for her countless assistance during my entire Ph.D. study.

VITA

2014	B.S. in Civil Engineering, Tongji University, Shanghai, China.
2015	M.S. in Civil Engineering, University of California, Los Angeles (UCLA), Los Angeles, California.
2015–present	Ph.D. candidate in Civil Engineering, University of California, Los Angeles (UCLA), Los Angeles, California.

PUBLICATIONS

W. Zhang, E. Esmaeilzadeh Seylabi and E. Taciroglu, (2019). A quantitative assessment of the NCHRP 611 method for soil-structure interaction analysis of buried circular structures & a proposed improvement. *Computers and Geotechnics*, 113, 103103.

W. Zhang, E. Esmaeilzadeh Seylabi and E. Taciroglu, (2019). An ABAQUS toolbox for soil-structure interaction analysis. *Computers and Geotechnics*, 114, 103143.

Y. Xie, Q. Zheng, C. S. W. Yang, W. Zhang, R. DesRoches, J. E. Padgett and E. Taciroglu, (2019). Probabilistic models of abutment backfills for regional seismic assessment of highway bridges in California. *Engineering Structures*, 180, 452-467.

W. Zhang, E. Esmaeilzadeh Seylabi and E. Taciroglu, (2017). Validation of a three-dimensional constitutive model for nonlinear site response and soil-structure interaction analyses using centrifuge test data. *International Journal for Numerical and Analytical Methods in Geomechanics*, 41(18), 1828-1847.

CHAPTER 1

Introduction

1.1 What is soil-structure-interaction (SSI)?

Almost all civil structures have foundation/support elements that either rest on, or are embedded in, soil. Because of complexities in modeling the mechanical behavior of soils, and the high degree of uncertainty and variability in their properties, it is not uncommon among structural engineers to completely ignore their response and effects on the structure, and to simply assume that the base of the structure is rigid. This simplistic approach—wherein the soil-structure-interaction (SSI) effects are unaccounted for—might yield acceptable designs for certain cases (e.g., lightweight structures on rock or stiff soils), but can also bear perilous consequences under extreme loading events such as earthquakes [5].

Different types of agents—e.g., rotating machinery, earthquakes, traffic, etc.—excite a structure. Depending on the nature of the loading, the ensuing structural vibrations result in time-harmonic or time-varying tractions at the soil-structure interface. These tractions will cause further deformations within the structure due to the soil's flexibility, which may reach significant levels under certain combinations of soil's and structure's properties (e.g., a massive structure resting on soft soil) [6]. On the positive side, the surrounding/supporting soil transmits energy away from the structure in the form of outgoing elastic waves. The amount of this radiated energy depends, to a large extent, on the soil profile and properties [5].

1.1.1 Kinematic versus inertial SSI

Soil-structure interaction (SSI) effects generally have two fundamental mechanisms—namely, kinematic (KI) and inertial (II) interactions. Differences in motion between the free-field soil and the foundation system in the absence of excess or deficient mass between the two that are due to their stiffness contrast are collectively referred as kinematic interaction (KI) effects. Inertial interaction (II) effects are, therefore, complementary, and are concerned with the soil reactions that develop to resist inertial forces associated with accelerations of the foundation-structure system relative to the soil.

More specifically, kinematic interaction generally results from (*i*) base-slab averaging, (*ii*) deconvolution/embedment effects, and (*iii*) wave scattering effects. The base-slab averaging effects result from wave fields which have an angle of incidence relative to the vertical, or which are incoherent in time and space, so that the motion of a rigid surface foundation differs from the free-field motion [7]. Such effects can reduce the base-slab translation, the but introduce the torsion and rocking, and tend to become more significant with increasing frequency [8]. The presence of embedded foundations can reduce the variation of ground motion with depth, and hence such so-called embedment effects make the ground motion amplitude decreases with depth [9, 10, 11]. The wave scattering effects are due to the scattering of seismic waves off of corners and asperities of the foundation.

As for inertial interaction, the inertia developed in the structure due to its own vibrations gives rise to base shear and moment, which in turn cause displacements of the foundation relative to the free-field motion. The impedance function, which represents the dynamic stiffness and damping characteristics of foundation-soil interaction, is used to relates the forces (e.g. base shear and moment) at the base of the structure to the displacements and rotations of the foundation relative to the free-field. The components of the impedance function are complex-valued and frequency dependent. A number of analytical and semi-analytical impedance functions are developed, many of which are summarized in [12].

1.1.2 Surface structures versus underground structures

The SSI effects are different for surface and underground structures. The kinematic component is generally considered to be more significant for underground structures due to their modest mass and their confinement by soil. The focus of underground seismic design, therefore, is on the free-field deformation of the ground and its interaction with the structure [13]. However, for the surface structures and superstructures, owing to their enormous mass and significant height, the SSI effects are dominated by inertial interaction effects. In this sense, an accurate impedance function is crucial for modeling the SSI effects of surface structures.

1.1.3 Is neglecting SSI effects always beneficial?

Analysis and design guidelines on SSI had first been developed in the U.S. by the Applied Technology Council [14]. In these provisions, the effects of SSI were accounted for by increasing the fundamental-mode period of the fixed-base structure and by modifying the system damping ratio, to take the effects of soil flexibility and energy radiation into account, respectively. These recommendations were barely used in practice, since it was assumed that the nominal seismic demands specified in code provisions would already led to safe designs. However, later studies would show that ignoring the effects of SSI is not always a safe route, and would indicate the need for more comprehensive studies (see, for example, [6]).

1.2 How to model SSI effects?

1.2.1 Simplified approaches

In engineering practice, common approaches (e.g., NIST approach[15] and ASCE 7-10[16]) for superstructures that take the effects of SSI into account are typically based on modifying the dynamic properties of the fixed-base structure by attaching representative soil springs and dashpots at the base of the structure or giving a direct reduction for base shear force, and modifying the input motion or modifying the shapes of the superstructures. However,

reliability of these simple models is still questionable [17]. The main drawback of these methods is their inability to include frequency-dependency of the soil impedance functions. This oversimplification, though acceptable for time-harmonic analysis, may not be reasonable for design of structures against time-varying non-stationary loads such as seismic excitations. This is especially true for problems that variation of soil impedance functions is appreciable in range of frequencies where frequency content of the input ground motion is high, as well.

As for underground structures, current seismic design practices—articulated in, for example, the NCHRP Report 611 [18]—are based on the procedures proposed by [19] for circular and rectangular buried structures. The method is derived based on the assumptions that (*i*) the entire system is linear elastic (*ii*) the structure is embedded in a full-space homogeneous soil media (*iii*) uniform shear stress is statically applied at infinity and (*iv*) the soil-structure interface is either full-slip or no-slip. Then the analytical solutions are devised based on linear elasticity theory and Airy's function to compute the seismic bending moments and hoop forces in circular structures. And for rectangular structures, on the other hand, are based on static frame analysis.

1.2.2 Approaches based on reduced order models (substructure method)

Apparently, it is not possible to discretize the semi-infinite soil domain with a finite number of elements; and thus, it is necessary to truncate it by introducing appropriate boundary conditions. For an exact representation of the omitted domain—dubbed the *far-field*—, the introduced fictitious boundaries on the computational domain (the *near-field*) must have the ability to transmit the energy of the outgoing and incoming waves perfectly[1].

In problems where the source of excitation is inside the near-field, all waves impinging upon the fictitious boundaries are outgoing; and the inserted boundary condition must absorb the energy of these outgoing waves through the, so-called, absorbing-boundary-conditions (ABCs). On the other hand, for problems where the source of excitation outside the near-

[1]In this text, the terms 'outgoing' and 'incoming' refer to wave-fields within the near-field.

field, the forged boundary conditions must not only absorb the energy of the outgoing waves but also be transparent to all incoming waves. The latter device is usually referred to as an open-boundary-condition (OBC). The modified direct modeling method is described in Fig. 1.1. The undamped regular domain (Ω_0) is truncated by PMLs, which serve as the ABCs.

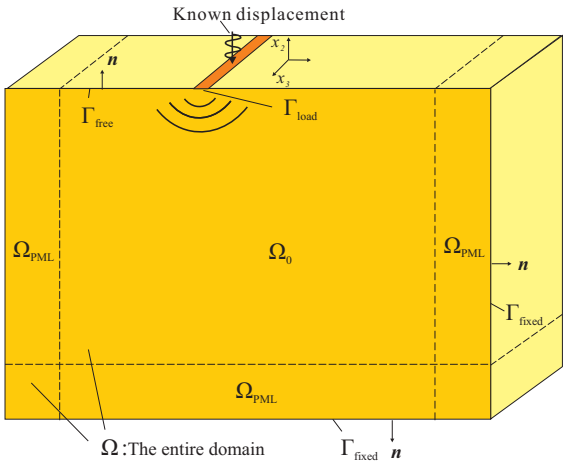

Figure 1.1: The problem geometry and boundary conditions.

The first ABC was introduced by [20]. Though exact for waves with normal incidence, the Lysmer and Kuhlemeyer (LK) ABC cannot absorb inclined incident waves totally, which results in trapping of energy inside the near-field. Since then, different ABCs had been formulated with the aim of improving the effectiveness in absorbing the radiation energy. Some methods had also aimed to extending the application of ABCs to problems where the excitation source is in the far-field (e.g., seismic excitations).

Although domain truncation together with insertion of an appropriate boundary condition reduces the order of the original problem, it is still computationally expensive and is rarely used in engineering practice. Therefore, it is desirable to entirely avoid the discretization of the soil domain by defining the near-field boundaries at the soil-foundation interface. This approach, which is known as the *substructure method*, is described in Fig. 1.2 and 1.3.

For problems where the foundation of the structure is fairly rigid, the substructure method reduces the order of the model significantly by restricting the degrees-of-freedom

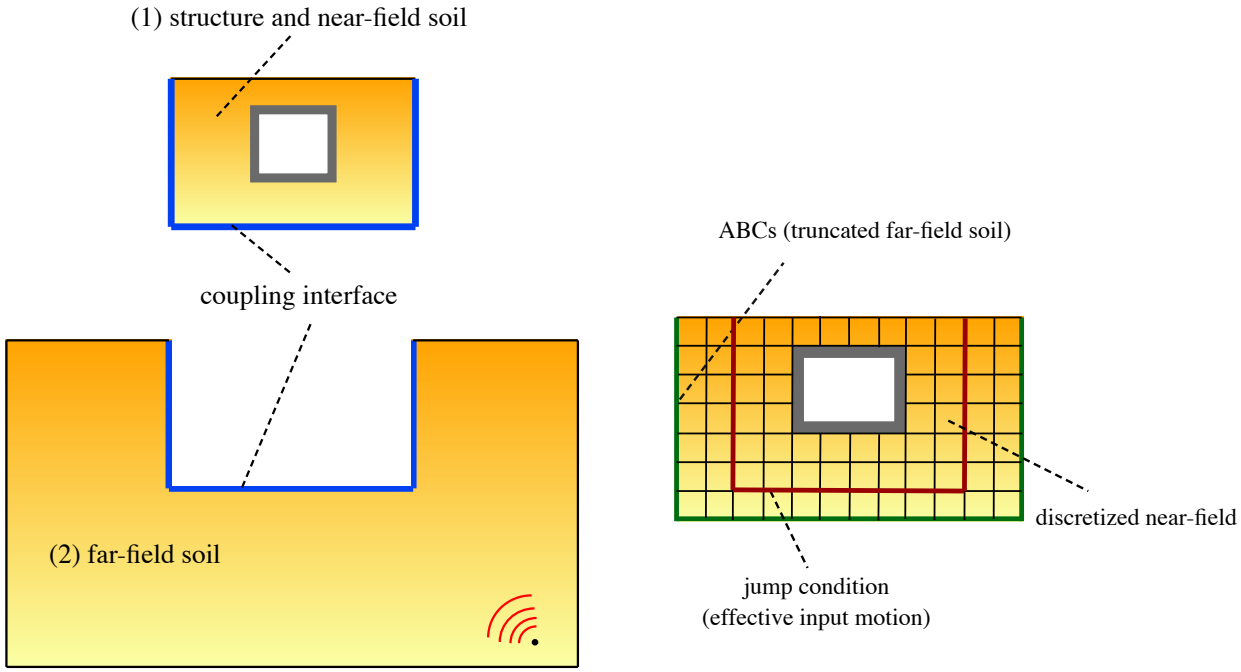

(a) decoupled components (b) coupled structure-near-field-ABC system

Figure 1.2: Sub-structuring view of direct SFSI analysis

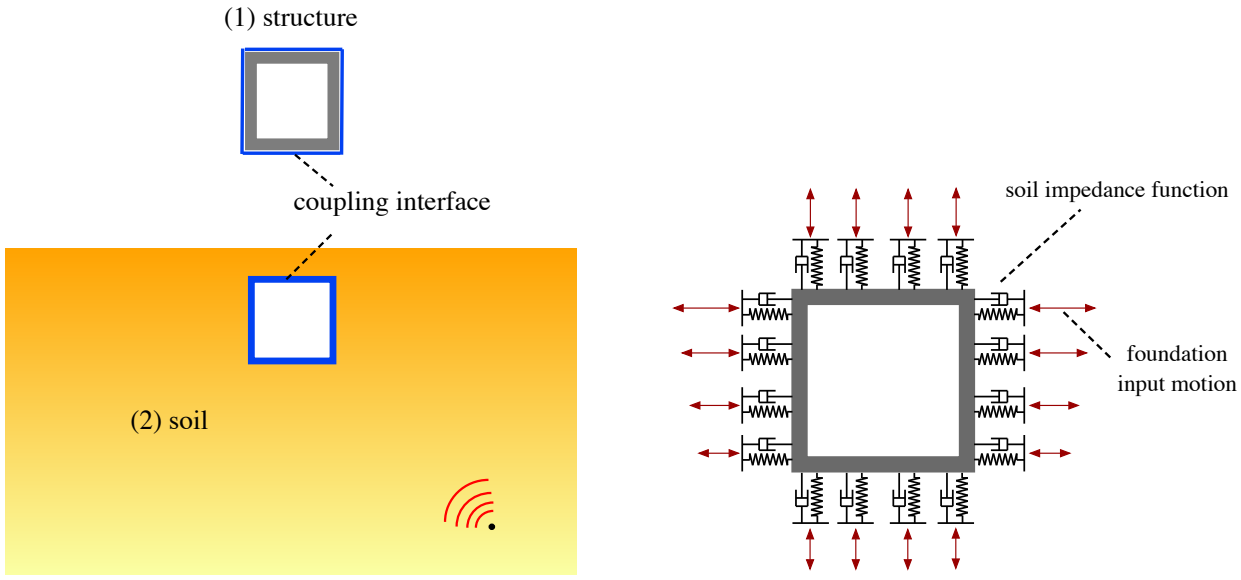

(a) decoupled components (b) coupled structure-soil-impedance system

Figure 1.3: Sub-structuring view of substructure SFSI analysis

(DOFs) of the soil domain to those of the foundation[2]. However, it requires defining an appropriate Dirichlet-to-Neumann (DtN) map at the soil-foundation interface, which relates the interacting force and displacement components. Moreover, in cases where the source of excitation is within the soil medium—e.g., seismic excitations—the input motion at the soil-foundation interface—a.k.a. the foundation input motion, or FIM—may be different from the so-called free-field motion. This is mainly because of the so-called "base-slab averaging" effects, and requires the free-field motion to somehow be transformed into an approximation of the (true) foundation input motion [21]. Starting as early as 1960s, a fairly large number of studies focused on deriving appropriate DtN-maps in the frequency domain [22]. These DtN-maps are better known as "soil impedance functions," which are frequency-dependent and complex-valued functions that represents the stiffness and radiation damping at the soil-foundation interface.

For linear SSI analysis it is convenient to solve the problem in the frequency domain, using the soil impedance functions and the modified input motion, together with dynamic characteristic of the structure. While the use of impedance functions in linear SSI analyses are quite straightforward, they cannot be used—at least, directly—in nonlinear SSI analysis, even for cases where *only* the structural components are behaving nonlinearly. This is because it is not possible to solve nonlinear problems in the frequency domain. Therefore, soil impedance functions must be transformed into the time domain, where we can approximate each impedance function as a ratio of two complex polynomials that could subsequently be incorporated into the system's equations of motion as a recursive discrete-time digital filter.

The use of inverse Fourier transform techniques results in integro-differential equations, which in turn leads to exact representation of impedance functions in time. However, it is typically more appealing to deal with differential equations in time. This is mainly because these equations can be solved using standard numerical schemes, such as the standard finite element or finite difference methods. In some cases, it is possible to represent SSI effects by

[2]These are typically the rigid body modes of the foundation—e.g. the lateral, vertical, and rocking DOFs of the foundation for two-dimensional problems.

appropriate arrangements of discrete elements—viz., masses, dashpots, and springs [23]. A third alternative is to approximate the original impedance function with another approximate transfer function, using the concept of rational approximations [24]. The resulting DtN-map has the advantage of being represented in time as a differential or difference equations, and in simple cases being represented as discrete mechanical models [25, 26, 27, 28, 29].

1.2.3 Continuum approaches (direct method)

One classical continuum approach to take the effects of SSI into account is to use the finite element method (FEM) to model a portion of the supporting/surrounding soil media along with the structure. This approach is known as the *direct modeling* [5, 30] method. Figure 1.4 displays schematically the direct modeling of a semi-infinite domain problem in the context of soil-structure-interaction.

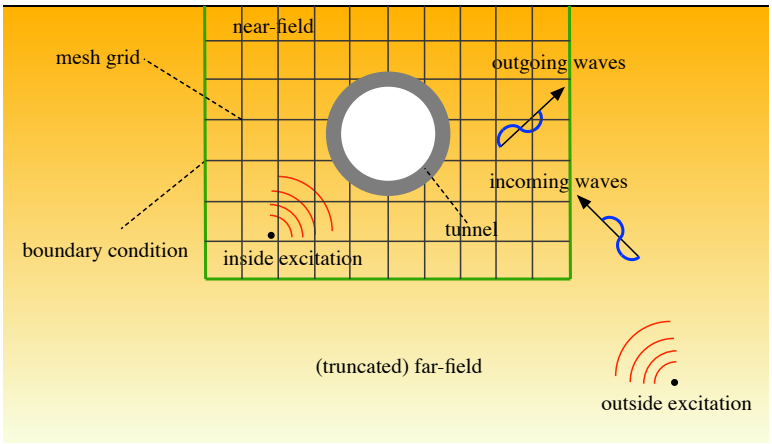

Figure 1.4: Schematic direct modeling of soil-structure interaction problem

Direct modeling of SSI problems usually suffer from defining inappropriate absorb boundary conditions and input ground motions [31, 32, 33]. In order to increase the modeling accuracy, a large extent of the soil domain has to be discretized, and this is usually fatal because of the high level of computational effort required [34]. On the other hand, to date, impedance functions and foundation input motions are only forged for simple foundation shapes and soil profiles, which limits their usefulness in substructure modeling of SSI problems. Moreover, in almost all studies to date, it is assumed that the foundation behaves

rigidly, and a only few studies have addressed the effects of foundation flexibility (see, for example, [35, 36, 37, 38, 39]). Furthermore, despite the appealing characteristics of the substructuring approach, the path extend it to problems featuring near-field irregularities and/or nonlinearities is not very clear. In addition, even for cases where only the structural components behave nonlinearly, time domain representations of elastic soil impedance functions—which may be in scalar or matrix form—is not a straightforward task, and may suffer from numerical instability issues [24, 40].

1.3 Methods for SSI analysis of buried structures

Seismic response of underground structures is a complex soil-structure interaction (SSI) problem. Limit equilibrium methods [41] are not appropriate for the seismic design of buried structures because their formulation does not reflect the SSI processes that are responsible for the formation of interface pressures. As such, a number of researchers [19] proposed pseudo-static deformation-based approaches to take the effects of SSI into account for the seismic design of underground structures, followed by [42] and [13]. In the said approaches, analytical elasticity-based formulations are provided to compute the seismic bending moments and hoop forces in circular structures. Methods proposed for computing internal seismic forces for rectangular structures, on the other hand, are based on static frame analysis.

More recently, [43] presented a finite element approach to obtain the seismic responses of buried culverts and cut-and-cover tunnels, by specifying quasi-static displacement profiles at the soil boundaries. These profiles taken as the products of free-field ground strains and the height of the modeled soil domain. As a result, the frequency content of the ground motion—which, in turn, controls the wavelength—is indirectly represented in these methods through their impact on the shear strain. It should be noted that pseudo-static methods described in [19] and [13] are very similar to the implementation in [43], so these are conceptually similar methods.

Limitations of the aforementioned methods are manifold: (1) They do not directly ac-

count for the broadband frequency content of seismic input excitations, as it is now well understood that seismic earth pressures vary with excitation wavelength [44]; (2) By conditioning the analyses on shear strain, their results are impacted by the challenges and limitations of 1D ground response assumption [45]; (3) The shear strain field is taken as uniform over the height of the buried structure, which may not be a valid assumption depending on the frequency of the seismic excitation, size of the underground structure, heterogeneity of the soil profile, and the mode of free-field wave. Finally, (4) these methods do not consider the relative inertia that can develop between the buried structure and the soil (that is, negative inertia that is caused by the culvert's empty space).

1.4 Research Objectives

The studies of seismic response assessment of buried structures, as well as the effects of soil-structure interaction on buried structures have been trending research topics in last few decades. Direct modeling of SSI problems usually suffer from defining inappropriate ABCs, input ground motions and constitutive models [46, 47, 48]. On the other hand, to date, impedance functions and FIMs have been devised only for simple foundation shapes and soil profiles, which limits their usefulness in substructure modeling of SSI problems. The objective of this work, therefore, is to devise and combine the validated nonlinear soil model and advanced reduced order tools for SSI problems, and hence to comprehensively study the seismic response behavior of underground structures, and finally provide recommendations to improve the validity and accuracy of design methods used in engineering practice.

1.5 Organization of this document

The remainder of this document is organized as follows:

Chapter 2 provides a more detailed overview of the state-of-the-art nonlinear soil models, and the model adopted in this study, and corresponding calibration and validation of that model by using centrifuge test data.

Chapter 3 presents the formulations, verification studies and applications of the implemented reduced order modeling tools—i.e., domain reduction method (DRM) and perfectly matched layer (PML)—for time domain SSI analysis.

Chapter 4 compares the experimental findings with the design method described in NCHRP Report 611 and the calibrated numerical models, in order to develop validated methods for SSI analysis of buried structures.

Chapter 5 contains parametric studies of buried circular structures using detailed nonlinear finite element simulations involving a broad range of ground motions, and soil and structural properties.And it seeks to quantitatively assess the brackets of the validity of the NCHRP 611 method, and offers an improvement that is simple to implement.

Chapter 6 describes the fragility-based seismic performance assessment of buried circular structures. Fragility curves are developed through a Probabilistic Seismic Demand Analysis (PSDA) procedure, from hundreds of nonlinear time history analyses, by using validated nonlinear soil and structural models, and DRM and PML.

Chapter 7 concludes this document by providing a roadmap for the conducted research ahead.

CHAPTER 2

Modeling the soil nonlinearity

Studies of seismic site response analysis have been continuously probed over the last half century and have revealed and demonstrated the importance of accurately modeling the soil behavior under seismic motions. Also, studies of soil behavior have indicated that soil behavior is highly nonlinear and hysteretic even under very small strains.

In the late 1960's, [49] published a pioneering paper proposing an equivalent linear model where using a linear spring and a dashpot to represent the function of shear modulus and damping, respectively, which is considered as the cornerstone of technique of modern seismic site response analysis. Then, [50] proposed a computer program, SHAKE and utilized frequency domain to conduct the response analysis. During a very long time the frequency domain methods are more popular because they are easy to be implemented, their computational cost is pretty low, and because of their robustness and flexibility.

The most widely used frequency domain method to analyze the soil behavior is the equivalent linear method, which is proposed by [51] that relates the ratio of effective shear strain to maximum shear strain (R_γ) with the earthquake magnitude (M) is common used in Eq. (2.1).

$$R_\gamma = \frac{M-1}{10} \tag{2.1}$$

To finally determine the maximum level of strain in each layer of the soil, this equivalent linear method needs to be implemented iteratively. The first step is to make an initial guess for soil stiffness and damping properties for each layer, then perform a shear wave propagation analysis. Hence the values of strain obtained, while corresponding stiffness and

damping properties need to be updated based on the strain by multiplying the maximum strain at each layer by R_γ. The procedure will be done iteratively until maximum strain for all layers converge for two consecutive iterations. An example of the equivalent linear iterative procedure is presented in Fig. 2.1.

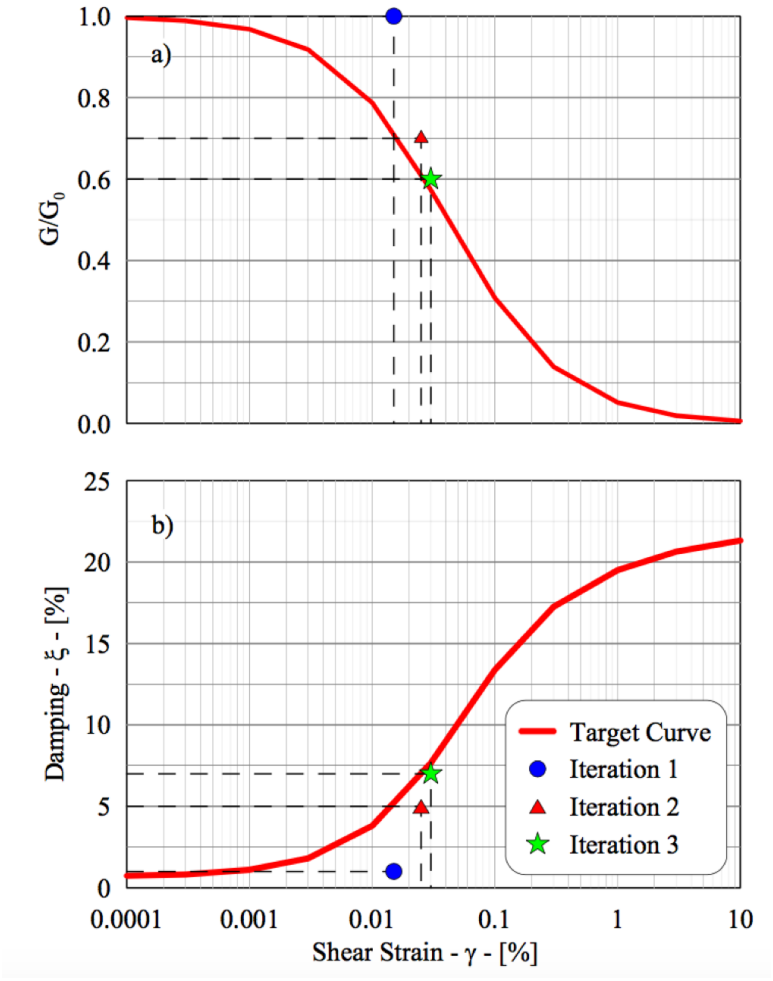

Figure 2.1: Equivalent Linear iterative procedure a) Modulus reduction curve, b) Damping curve

Some researchers observed that for sites with soft soil or sites under strong seismic motions, the equivalent linear method doesn't show enough accuracy when compared with recorded data. [52] and [53] extended the stiffness and damping properties with frequency dependency. [54] conducted a series of site response analysis with modified equivalent linear method to observe and characterize the effect of the rate-dependent soil behavior. Conclusion

has been drawn that the rate-dependence on soil behavior is inconspicuous.

2.1 State-of-the-art in nonlinear soil models for SSI

Even at very small strains, soil nonlinearities appear. Thus incorporating the soil nonlinear behavior is very important for SSI problems. To numerically simulate the soil nonlinearities, modeling soil behavior under cyclic/dynamic loading becomes crucial in most geotechnical earthquake engineering problems, especially for site response analysis and SSI problems. In last decades, a broad range of simplified and advanced, one-dimensional and three-dimensional soil constitutive models have been developed and applied in SSI problems. Due to the complexity of the soil behavior, such as nonlinearity, irreversibility, anisotropy, rate-sensitivity, path-dependence, pore water pressure generation, dilation, etc. An advanced soil model that can capture as many soil characteristics as possible is preferred.

2.1.1 Models for one-dimensional site response analyses

In last a few decades, 1-D nonlinear soil models are widely used in 1-D site response analyses and SSI problems because of its simplicity of computer implementation and durable accuracy. [55] proposed a plastic soil model that includes both drained and undrained, anisotropic, path-dependent stress-strain properties of saturated soils. [56] proposed a constitutive model for nonlinear 1-D cyclic soil behavior applied to seismic analysis of layered deposits. [57] devised an one dimensional nonlinear soil model for ground response analysis that can perfectly fit both shear modulus reduction and damping ratio curves.

The most widely used 1-D nonlinear soil model for current studies is a hyperbolic model, the modified Kondner-Zelasko (MKZ) model ([58]). The hyperbolic model can be described by using two sets of equations; the first equation - known as the backbone - decribes the stress-strain relationship for load; the second equation defines the stress-strain relationship for unloading-reloading conditions. Eq. (2.2) and Eq. (2.3)

$$\tau = \frac{\gamma \cdot G_0}{1 + \beta(\frac{\gamma}{\gamma_r})^s} \tag{2.2}$$

$$\tau = \frac{2 \cdot G_0 \cdot (\frac{\gamma - \gamma_{rev}}{2})}{1 + \beta(\frac{\gamma - \gamma_{rev}}{2 \cdot \gamma_r})^s} + \tau_{rev} \tag{2.3}$$

Where γ is the given shear strain, γ_r is the reference shear strain, β is a dimensionless factor, G_0 is the maximum shear modulus, and s is a dimensionless exponent.

Later [59] demonstrated that the confining pressure is also one of the impact factors. The greater confining pressure results a less shear modulus reduction (G/G_{max} and a smaller strain damping ratio. Based on this idea, [60] proposed a new model introducing a parameter - damping reduction factor - to accurately mimic the soil behavior. Eq. (2.4) presents the function of the damping reduction factor.

$$F(\gamma_m) = p_1 - p_2\Big(1 - \frac{G_{\gamma_m}}{G_0}\Big)^{p_3} \tag{2.4}$$

Where p_1, p_2, p_3 are non-dimensional parameters selected to obtain the best possible fit with the target damping curve. By introducing the parameter, [60] proposed a modified model based on the MKZ model, which is proved to be able to fit both shear modulus reduction and damping curves very well. The following equations, Eq. (2.5) and Eq. (2.6) describe the modified loading/backbone curve and unloading/reloading curve, respectively.

$$\tau = \frac{\gamma \cdot G_0}{1 + \beta(\frac{\gamma}{\gamma_r})^s} \tag{2.5}$$

$$\tau = F(\gamma_m) \cdot \left[\frac{2 \cdot G_0 \cdot (\frac{\gamma - \gamma_{rev}}{2})}{1 + \beta(\frac{\gamma - \gamma_{rev}}{2 \cdot \gamma_r})^s} - \frac{G_0 \cdot (\gamma - \gamma_{rev})}{1 + \beta(\frac{\gamma_m}{\gamma_r})^s}\right] + \frac{G_0 \cdot (\gamma - \gamma_{rev})}{1 + \beta(\frac{\gamma_m}{\gamma_r})^s} + \tau_{rev} \tag{2.6}$$

One-dimensional constitutive models still have some drawbacks that may lead to huge inaccuracy when doing multi-dimensional site response analyses or SSI problems. The main disadvantage of 1-D models is the disability to reproduce a sound coupled multi-axial behav-

ior when external loadings are multi-axial instead of one-dimensional, which is more than general in real world.

2.1.2 Models for continuum (3-D) analyses

Referring to the observations of 1-D nonlinear soil models, it's necessary to develop a multi-dimensional (3-D) nonlinear material model. In past decades, lots of researchers made great contributions to it. [61] proposed a simple plastic model that can be applied to frictional cohesionless soils. [62] developed a hypoplastic model that can handle very complex loading conditions. [63] showed a multiaxial plastic model vanished the elastic region, where plasticity can emerge even under low strains. [64] proposed a two-surface plasticity (yielding and bounding) model that can reproduce the sands behavior under either undrained or drained loading conditions. [65] came up a multi-surface plasticity model with a non-associative flow rule that can incorporate the dilative response phase of soils.

An example of advanced nonlinear soil models is the multi-surface constitutive model devised by Elgamal and co-workers [66][1]—a.k.a., the pressure-dependent multi-yield (PDMY) model—, which is frequently used in direct simulation of SSI problems within the research community. The main advantage of this model is that its many hierarchical yield surfaces enable it to approximate soil behavior within a broad range of strain regimes including post-liquefaction, but this is also a disadvantage in that the large number of requisite model parameters renders the calibration process formidable [67].

2.2 The Borja-Amies nonlinear soil model

A model with a simpler scaffold is that by Borja and Amies [63], which was later extended by Chao and Borja [68]. This is also a multi-surface model, but it has only a bounding surface—which can translate in stress-space through the extension proposed in [68]—in addition to a vanishing elastic region. Incidentally, it needs just a few parameters for calibration. The

[1]This model is, in fact, an extension of that devised by Prévost in 1985 [61].

validity of this model was previously examined by utilizing the downhole array motions recorded at Lotung, Taiwan through one-dimensional nonlinear site response analyses [69]. Due to its mathematical/thermodynamical consistency and relative simplicity, this model by Borja and co-workers holds great promise in capturing the multi-axial behavior of soil deposits in general wave propagation problems. While soil behavior in one-dimensional settings—especially for vertically propagating horizontally-polarized shear waves—have been well understood, and numerous models have been devised and validated (see, for example, [70]), models that can capture soil behavior in more general settings are needed to extend the present capabilities in SSI analyses beyond this simplest configuration (for example, to consider inclined waves from a distant source, surface waves, waves emanating from a buried scatterer, waves propagating in non-horizontally layered media, etc.).

In this chapter[71], we explore the capabilities of Borja and co-workers' model [63, 68, 72]. in capturing the dynamic responses measured during a centrifuge test, wherein multi-axial stress conditions were generated due to the presence of an embedded scatterer. These tests were conducted by Hushmand et al. [73] at the University of Colorado Boulder to investigate the seismic performance of relatively stiff structures buried in dry sand.

In what follows, we first derive the consistent tangent operator of Borja's model for the multi-axial case, and implement it as a user-defined material subroutine (UMAT) in ABAQUS [74]. For verification, we make comparisons of one-dimensional (1D) wave propagation analysis results with those obtained using with DEEPSOIL [75], which is a site-response analysis software that features well-accepted 1D model(s) of the hysteretic behavior of well-confined soils under low-to-moderate (shear) strains, (see, for example, [58]). Next, we explore the capability of this soil model in predicting responses measured during the tests by Hushmand et al. [73]. In this, we also make comparisons with numerical results obtained by Deng et al. [76] and Esmaeilzadeh Seylabi et al. [77], who used the PDMY [66] and equivalent linear soil models, respectively.

2.2.1 Formulation

It is well known that soil nonlinearity comes into effect even at very small strain levels [78] and that omission of such nonlinearities may result in significant errors in free-field (and thus, foundation input) motions in SSI analyses [70]. In the present study, we implement and validate a multi-axial viscoplastic soil model with a vanishing elastic region and coupled fully nonlinear behavior [72]. This constitutive model is a minor extension of the model proposed by Borja and Amies [63]—in that, it features a material-point-level stiffness-proportional viscous damping. A summary formulation of this model, which include its fourth-order consistent tangent material tensor, are presented next.

The total stress tensor $\boldsymbol{\sigma}$ of the model consists of two major—namely, the inviscid ($\boldsymbol{\sigma}^{\mathbf{inv}}$) and the viscous ($\boldsymbol{\sigma}^{\mathbf{vis}}$)—parts, as given by

$$\boldsymbol{\sigma} = \boldsymbol{\sigma}^{\mathbf{inv}} + \boldsymbol{\sigma}^{\mathbf{vis}} \tag{2.7}$$

where

$$\begin{aligned} \boldsymbol{\sigma}^{\mathbf{inv}} &= \boldsymbol{C}^{\mathbf{e}} : (\boldsymbol{\epsilon} - \boldsymbol{\epsilon}^{\mathbf{p}}), \\ \boldsymbol{\sigma}^{\mathbf{vis}} &= \boldsymbol{D} : \dot{\boldsymbol{\epsilon}}, \end{aligned} \tag{2.8}$$

and $\boldsymbol{C}^{\mathbf{e}}$ and $\boldsymbol{D}$ are elastic stiffness and viscous damping tensors, respectively; $\boldsymbol{\epsilon}$ is the total strain tensor; $\boldsymbol{\epsilon}^{\mathbf{p}}$ is the plastic strain tensor, and $\dot{\boldsymbol{\epsilon}}$ is the total strain rate. In this study, a linear stiffness-proportional damping is adopted [72], which can be devised by defining $\boldsymbol{D}$ as

$$\boldsymbol{D} = \frac{2\xi_0}{\omega_0}\boldsymbol{C}^{\mathbf{e}} \tag{2.9}$$

where ω_0 is the frequency at which the small strain damping ratio is equal to ξ_0; and the term ω_0 can be calibrated to match the dominant frequency of the input motion.

To achieve an optimal rate of convergence for Newton's method, the consistent tangent moduli are required [79]. For their model, Borja et al. [80] derived this fourth-order tensor

as,

$$\boldsymbol{C}_{\mathbf{ep}}^{\mathbf{inv}} = \frac{d\boldsymbol{\sigma}_{n+1}^{\mathbf{inv}}}{d\boldsymbol{\epsilon}_{n+1}} = K\mathbf{1}\otimes\mathbf{1} + \psi\mathbf{I}_{\mathbf{dev}} + \frac{\partial\psi}{\partial\boldsymbol{\epsilon}_{n+1}}\otimes\Delta\boldsymbol{\epsilon}' \tag{2.10}$$

where $\mathbf{I}_{\mathbf{dev}} = \mathbf{I} - \frac{1}{3}\mathbf{1}\otimes\mathbf{1}$, is the deviatoric identity tensor and K is the bulk modulus. The parameter ψ is defined through the equation $\Delta\boldsymbol{\sigma}' = \psi\,\Delta\boldsymbol{\epsilon}'$, where $\Delta\boldsymbol{\sigma}'$ and $\Delta\boldsymbol{\epsilon}'$ denote the deviatoric stress and strain increments, respectively. Further details of derivation are omitted here for brevity, and may be found in [63, 72, 80].

As seen, the third term on the right-hand side of Eq. (2.10) renders $\boldsymbol{C}_{\mathrm{ep}}^{\mathbf{inv}}$ non-symmetric in general. However, as demonstrated by Borja and Wu [80], the symmetric part of this consistent tangent stiffness tensor is often efficient enough to produce accurate solutions at superlinear convergence rates. Incidentally, a symmetric tangent also facilitates significant savings in memory requirements as well as in flops for solving the system-level linear equations.

After incorporating the viscous stress and by using the forward-difference method to approximate the total strain rate, we can derive from Eqs. (2.8) and (2.9)

$$\boldsymbol{\sigma}_{n+1}^{\mathbf{vis}} = \boldsymbol{C}_{\mathbf{ep}}^{\mathbf{vis}} : \mathrm{d}\boldsymbol{\epsilon}_{n+1} = \frac{2\xi_0}{\omega_0}\boldsymbol{C}^{\mathbf{e}} : \dot{\boldsymbol{\epsilon}}_{n+1} = \frac{1}{\mathrm{dt}}\frac{2\xi_0}{\omega_0}\boldsymbol{C}^{\mathbf{e}} : \mathrm{d}\boldsymbol{\epsilon}_{n+1} \tag{2.11}$$

which yields,

$$\boldsymbol{C}_{\mathbf{ep}}^{\mathbf{vis}} = \frac{1}{\mathrm{d}t}\frac{2\xi_0}{\omega_0}\boldsymbol{C}^{\mathbf{e}} \tag{2.12}$$

By only retaining the symmetric part of the consistent tangent of Borja's model, we obtain the total consistent tangent stiffness moduli as,

$$\boldsymbol{C}_{\mathbf{ep}} = \boldsymbol{C}_{\mathbf{ep,symm}}^{\mathbf{inv}} + \boldsymbol{C}_{\mathbf{ep}}^{\mathbf{vis}} = K\mathbf{1}\otimes\mathbf{1} + \psi\mathbf{I}_{\mathbf{dev}} + \frac{1}{\mathrm{d}t}\frac{2\xi_0}{\omega_0}\boldsymbol{C}^{\mathbf{e}} \tag{2.13}$$

where $\mathrm{d}t$ is the time increment chosen for the approximation of $\dot{\boldsymbol{\epsilon}}_{n+1}$.

2.2.2 Model calibration

For nonlinear soil models, the computational cost and mathematical difficulties associated with the calibration of the model parameters often critically affect their application in practical engineering problems. This is especially true for models featuring a large set of phenomenological parameters, which, in turn, require a large set of case-specific experimental data for calibration.

The present soil model has only a few parameters, yet it can effectively reproduce the key soil behavior attributes such as stiffness degradation and damping curves over a wide range of strains. As shown in [72], the main equation to calibrate the soil parameters is,

$$\frac{G}{G_{\max}} = 1 - \frac{3}{2\gamma_0}\int_0^{2\tau_0}\left[h\left(\frac{R/\sqrt{2}+\tau_0-\tau}{\tau}\right)^m + H_0\right]^{-1} d\tau \tag{2.14}$$

where $G = \tau_0/\gamma_0$ is the secant shear stiffness, and R is the radius of the bounding surface. Parameters h, m and H_0 control the intensity of the hardening. Given this equation, as will be demonstrated subsequently in detail, it is possible to use a nonlinear solution method—here, Broyden's [81]—and an appropriate initial guess, to calibrate the model parameters h and m from two points on the $G/G_{\max}$ curve. Alternatively, a nonlinear least-squares regression can be used to determine the optimal values for h, m and H_0, if more than two points are selected. Matlab [82] scripts for both cases are provided in the Appendix for the readers' convenience. Moreover, to facilitate broad use, we implemented all variants of the model—namely, plastic, viscoplastic, with symmetric or non-symmetric tangent, plane-strain, axisymmetric, and three-dimensional—in the commonly used commercial finite element analysis software ABAQUS [74], through its user-defined material (UMAT) subroutine interface.

2.2.3 Model verification

Here, the basic model is verified, first by examining its output and parameter-sensitivities under numerical simple shear tests, and next by comparing its output for a site-response

analysis with that from DEEPSOIL [75], which is a tool specifically designed for (and limited to) one-dimensional shear wave propagation.

2.2.4 A simple shear test

Strain-controlled numerical shear tests are carried out with and without the viscous part. For each test, a sinusoidal loading with the frequency of $\omega_0 = 1$ rad/s is applied. Fig. 2.2a displays the resulting hysteresis loops for different values of ξ_0 and maximum shear strain $\gamma_{\max} = 10\%$. Figs. 2.2b and 2.2c display the resulting normalized shear modulus degradation and damping curves for $\gamma_{\max}$ ranging from $10^{-4}\%$ to 10%. As seen, depending on the value of ξ_0, adding more viscous damping results in smoother stress-strain curves and more energy dissipation per loading cycle. On the other hand, viscous damping does not appear to affect, as expected, the effective secant shear stiffness for this test.

In order to explore the rate of convergence for the symmetric and non-symmetric (i.e., full) consistent tangent stiffness moduli, a simple shear test with sinusoidal loading on a unit cube is carried out. Table 2.1 displays the normalized maximum residual forces obtained using both moduli, and with and without considering the viscous part, using the Newton-Raphson method. As these results indicate, although the non-symmetric moduli has a higher rate of convergence, the symmetric one still converges successfully, and its rate of convergence is acceptable. Moreover, the use of viscous part improves the rate of convergence, possibly because the stress-strain curves are becoming smoother with increased damping.

Table 2.1: Normalized maximum residual force for simple shear test.

	Plastic only		Viscoplastic	
Iteration	non-symmetric	symmetric	non-symmetric	symmetric
1	1	1	1	1
2	0.039990	0.113682	0.038129	0.111368
3	0.002032	0.030282	0.001851	0.028722
4	0.000304	0.011871	0.000255	0.010915
5	0.000088	0.005332	0.000072	0.004784

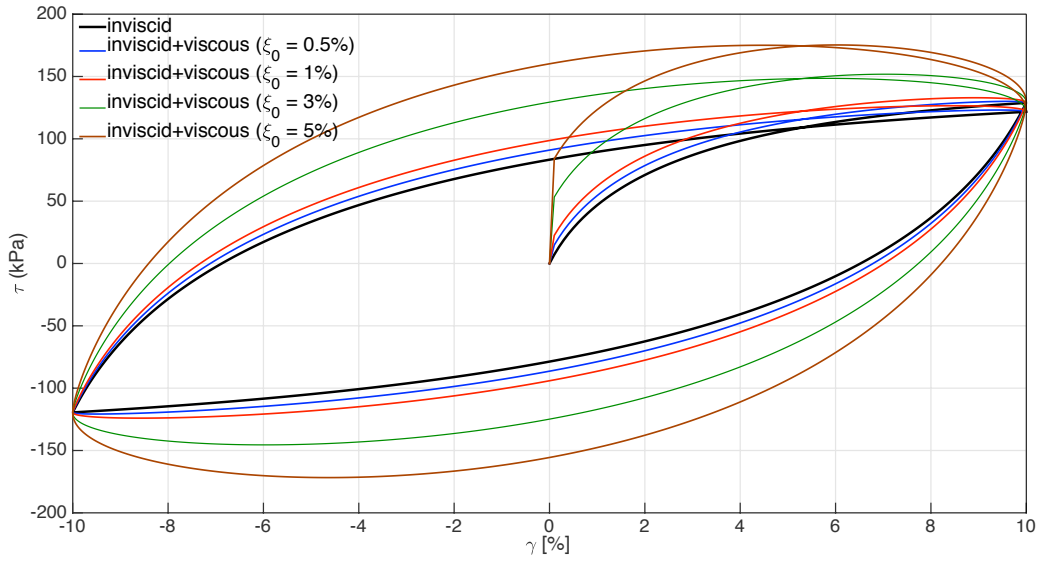

(a)

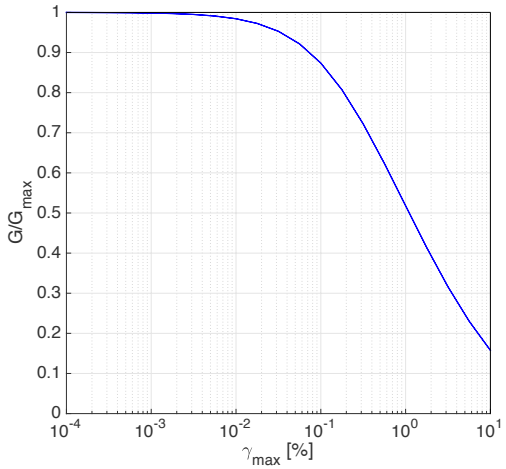

(b)

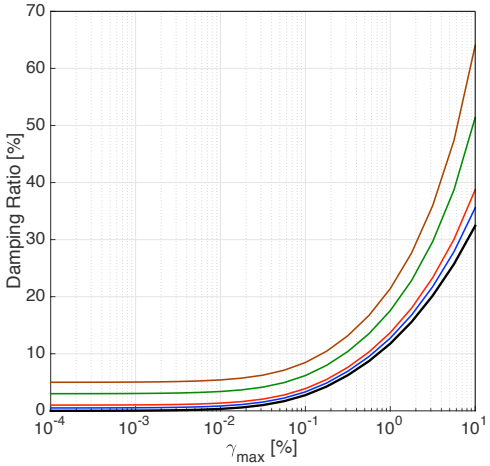

(c)

Figure 2.2: (a) Hysteresis loops, (b) normalized shear modulus degradation and (c) damping ratio curves for $G_{\max} = 20$ MPa, $\nu = 0.3$, $h = G_{\max}$, $m = 1$, $R = 200$ kPa, $H_0 = 0$, $\omega_0 = 1$ rad/s, and $\xi_0 = [0\ 0.005\ 0.01\ 0.03\ 0.05]$.

2.2.4.1 Model verification through one-dimensional nonlinear site response analyses

One-dimensional nonlinear site response analyses are conducted using the implemented nonlinear soil model and the results are compared with those obtained from DEEPSOIL [75], which is a well-known computer code for site response analysis that features linear, equivalent linear, and validated nonlinear soil models. Reasonable—and otherwise unremarkable—soil and model parameters are chosen for the simulations: the height of the soil column is 28.9 m, $G_{\max} = 8$ MPa, $h = G_{\max}$, $m = 0.5$, $R = 50$ kPa, $\omega_0 = 4\pi$ rad/s, $\xi_0 = 1\%$, and $H_0 = 0$.

Fig. 2.3 displays the acceleration time-series and the 5%-damped spectral accelerations obtained at the surface of the soil column, which was subjected to a Ricker wavelet [83] with a central frequency that is equal to the natural frequency of the homogeneous soil layer considered. Fig. 2.4 displays the results obtained for the same soil column when it is

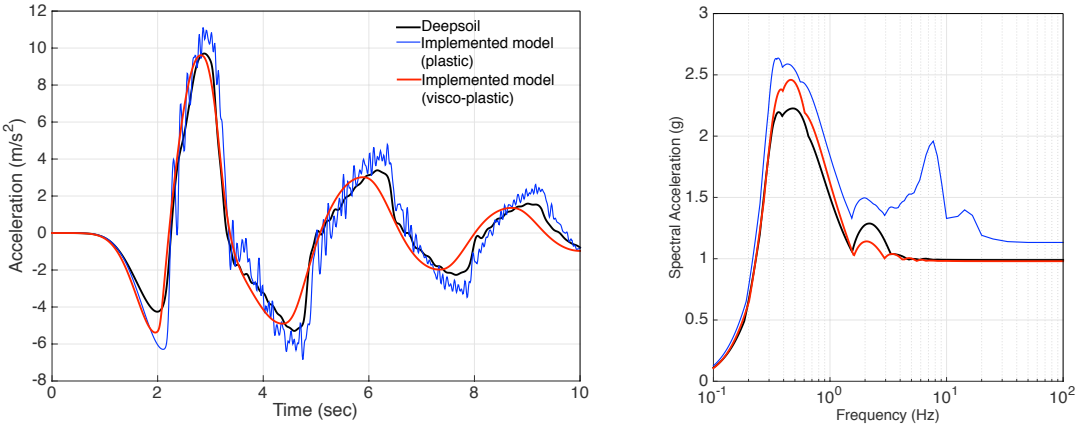

(a) Acceleration history (b) Spectral acceleration

Figure 2.3: 1D site response analysis (a) Acceleration history and (b) 5%-damped spectral acceleration subjected to the Ricker wavelet input.

subjected to an earthquake motion. As seen for both cases, the results of the implemented soil model are in very good agreement with those obtained using DEEPSOIL, especially after adding the viscous damping term.

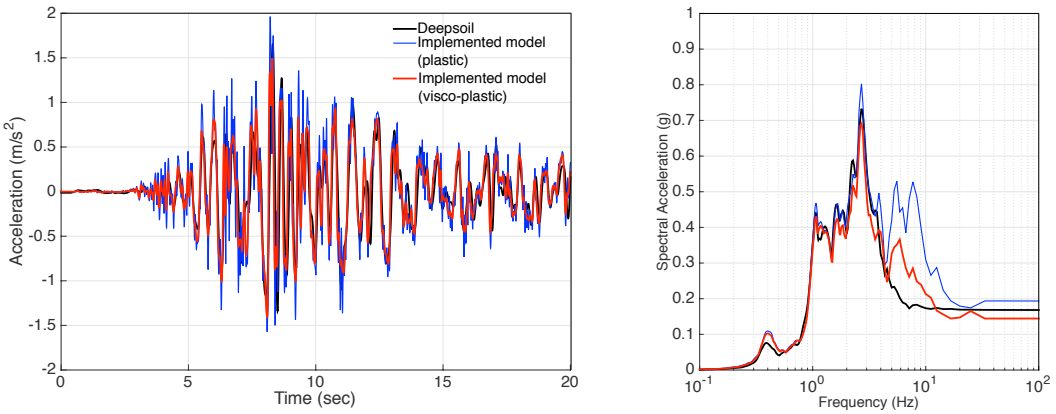

(a) Acceleration history (b) Spectral acceleration

Figure 2.4: 1D site response analysis (a) Acceleration history and (b) 5%-damped spectral acceleration subjected to the earthquake input.

2.2.5 Model validation: Nonlinear SSI analyses of centrifuge experiments on buried structures

Hushmand et al. [73] conducted a series of centrifuge experiments at the University of Colorado Boulder to investigate the seismic performance of relatively stiff structures buried in dry sand. Three different box-shaped specimens were designed to represent the characteristics of prototype reinforced concrete reservoir structures with varying stiffnesses. Aspect ratios and dimensions of these structures, as well as their stiff roofs restrained excessive rotational movements and produced significant seismic pressures (and bending strains) on the walls. Three distinct ground motions were applied to each structure.

Fig. 2.5 shows the centrifuge test layout and instrumentation. The dimensions and properties of the model structures used for the experiments are provided in Table 2.2. The material properties of the steel structures were chosen as follows: density, $\rho = 7870$ kg/m^3, Young's modulus, $E = 200$ GPa and Poisson's ratio, $\nu = 0.29$. The 5%-damped spectral accelerations and Arias intensity time-histories as recorded in the centrifuge test on the flexible structure are shown in Fig. 2.6.

Deng et al. [76] explored the capability of the so-called PDMY model, which is a pressure-dependent multi-yield-surface plasticity model, in predicting the response of the specimen

structures and the far-field soil. The PDMY model has 20 material parameters, great majority of which are not directly calibrated, but have judiciously chosen "assumed" values. Using the same test data, Esmaeilzadeh Seylabi et al. [77] explored the range of applicability of calibrated equivalent linear soil models in capturing the response of the tested structures. Here, we investigate the capability of the implemented nonlinear soil model in predicting the response of the tested structures, and also make comparisons to results obtained with PDMY model by Deng et al. [76] and with equivalent linear models by Esmaeilzadeh Seylabi et al. [77].

Two-dimensional meshes are used for discretizing tests on the flexible and stiff specimens, and each mesh comprised 18 soil layers with a uniform element size of 0.25 m to capture the soil heterogeneity. It should be noted that the element size is selected small enough to resolve wave propagation in the frequency range of interest. In order to set up the initial stress condition appropriately, a static analysis under gravity loading is performed prior to each dynamic analysis. During the static analyses, horizontal degrees of freedom (DOFs) at the left and right vertical edges of the domain are fixed, and the vertical DOFs are left free. For the dynamic analyses, the horizontal DOFs at the said edges are slaved to each other at every elevation—per the boundary condition imposed by the centrifuge's container—and the vertical DOFs are considered free.

Table 2.2: Dimensions and properties of model structures in prototype scale.

	Thickness			Fundamental frequency
Structure	Base (m)	Roof (m)	Walls (m)	(Hz)
Flexible	0.5	0.28	0.28	1.9
Baseline	0.69	0.37	0.56	3.9
Stiff	1.46	1.12	1.13	9.1

2.2.5.1 Soil model calibration

In the centrifuge experiments, dry Nevada sand was used, and it had the following material properties: $\nu = 0.3$, $G_s = 2.65$, $e_{\min} = 0.56$, $e_{\max} = 0.84$, $D_{50} = 0.13$ mm, and $C_{\mathrm{u}} = 1.67$. The sand was pluviated inside the flexible shear beam container of the centrifuge such that

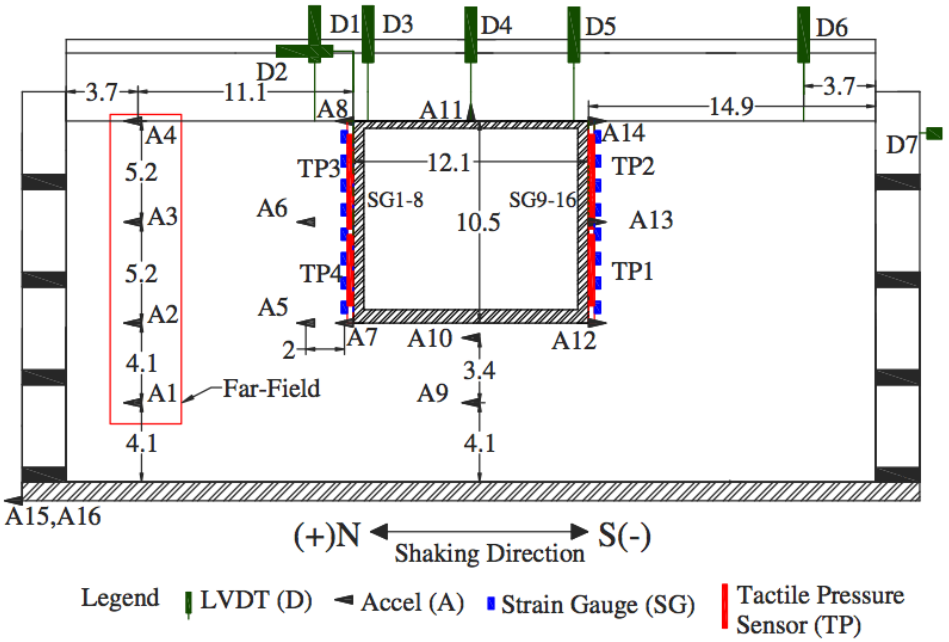

Figure 2.5: Layout and instrumentation of centrifuge experiments in prototype scale.

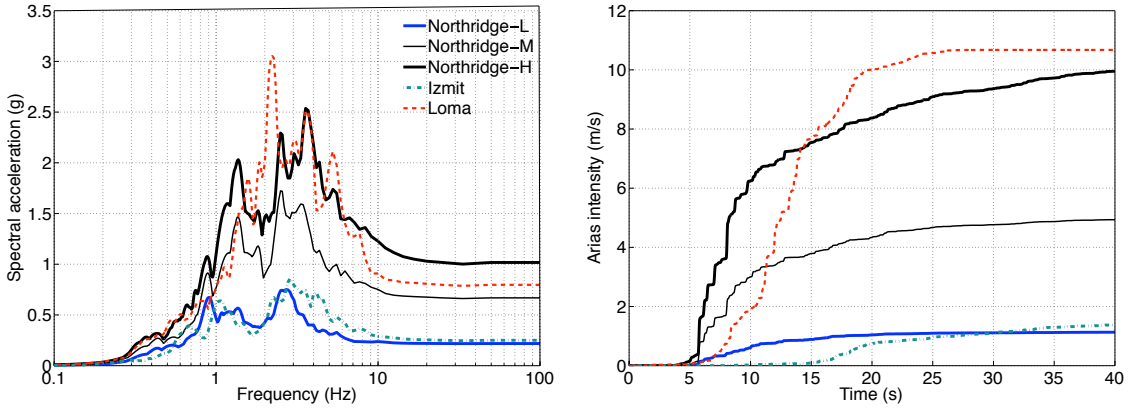

(a) %5-damped spectral acceleration

(b) Arias intensity time history

Figure 2.6: (a) 5%-damped spectral accelerations and (b) Arias intensity time histories of the container base motions recorded for the test on flexible structure.

an approximately uniform soil layer with a dry unit weight of $\rho = 1590$ kg/m^3, or a relative density (D_r) of approximately 60%, could be achieved. The small-strain shear wave velocity profile of the soil deposit is predicted using the equation proposed by Bardet et al. [84],

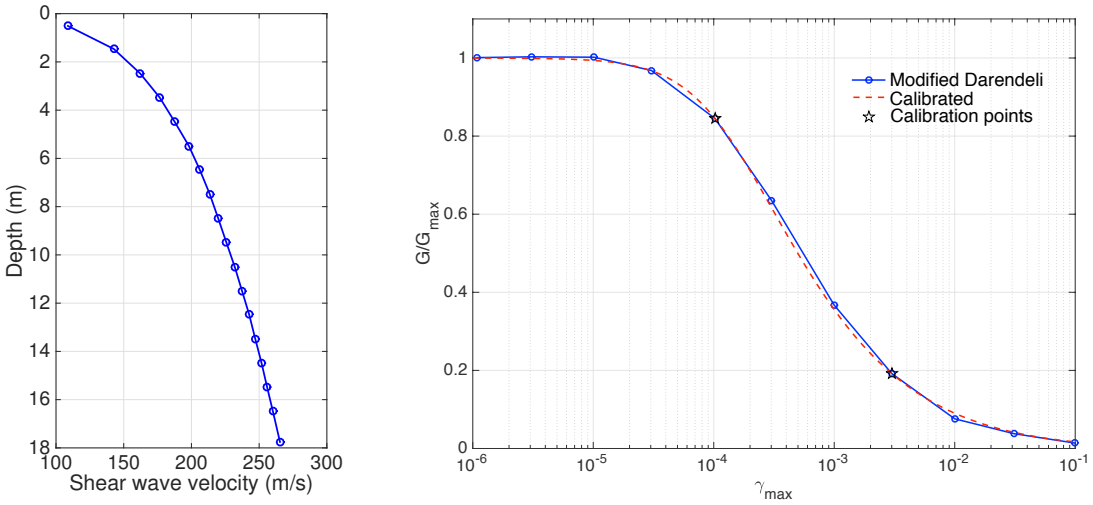

(a) Shear wave velocity (b) Stiffness degradation

Figure 2.7: (a) Shear wave velocity and (b) Stiffness degradation curves.

$$G_{\max} = A\frac{(a-e)^2}{1+e}p^n\,, \tag{2.15}$$

where $A = 8.811$, $a = 1.935$ and $n = 0.5$ are the three constants determined for the Nevada Sand [85]. The parameters e and p are, respectively, the void ratio and the mean pressure expressed in kPa. Fig. 2.7a displays the resulting maximum shear wave velocity profile.

It can be shown that the model by Borja et al. [68] implies the following relationship between normalized shear modulus, the shear strain, and other material parameters:

$$\frac{G}{G_{\max}} + \frac{3}{2\gamma}\int_0^{2G_i\gamma}\left[h\left(\frac{R/\sqrt{2}+G\gamma-\tau}{\tau}\right)^m + H_0\right]^{-1}\mathrm{d}\tau - 1 = 0. \tag{2.16}$$

The secant stiffness tends to be zero when the amplitude of shear strain is large, which yields

$H_0 = 0$. The radius of the bounding surface can also be simply computed as,

$$R = \sqrt{2}\tau_{\max} \approx \sqrt{2}G\big|_{\gamma_{\max=5\%}} \gamma_{\max=5\%} \approx 0.003\ G_{\max}\,. \tag{2.17}$$

As such, the material parameter calibration procedure involves the estimation/calibration of two parameters only—namely, h and m in Eq. (4.31).

Here, we use the shear modulus degradation curves proposed by Darendeli [59], and pick two representative points on that curve for (γ, $G/G_{\max}$) as (0.003, 0.192) and (1.023E-4, 0.845). Plugging these choices in Eq. (4.31) yields two nonlinear equations in parameters h and m. Using Broyden's method [86] eliminates the need to compute an analytical Jacobian for iterative solution procedure to obtain h and m. Using initial guesses of $h_0 = 0.1\ G_{\max}$ and $m_0 = 1.0$, yields the materials parameter as $h = 0.1363\ G_{\max}$ and $m = 1.5477$, with a resulting L_2 residual norm of 1×10^{-16}.

It is also possible to obtain the optimal h, m and H_0 values when more than two experimental data points from the (γ, $G/G_{\max}$) curve are provided. As this would then produce an over-determined system, nonlinear least-squares procedures are needed to obtain the optimal material parameter values. One such procedure for the present model is implemented in Matlab, and this code along with an example dataset are provided in the Appendix for the readers' convenience.

2.2.5.2 Numerical analyses

Two types of nonlinear SSI analyses are conducted with the implemented nonlinear model. These are either purely plastic or plastic with 3% viscous damping, which are henceforth referred to as NL and NLV models respectively. For each soil model, four cases that cover a range of stiffness and ground motion intensities are considered. These are, specifically, "flexible" and "stiff" buried structures that were subjected to the "Northridge-L" and "Northridge-H" motions (henceforth referred to as AL and AH). The experiments on the flexible and stiff structures are similarly named as T-Flexible and T-Stiff, respectively.

To examine the performance of the implemented nonlinear soil model, we present the measured and predicted responses for the centrifuge experiments in terms of accelerations, specimen racking displacements, bending strain and lateral earth pressure along the specimen's walls, as well as soil surface settlement. Also, back-calculated stress-strain relationships and the associated effective stiffness in all four tests are presented.

As mentioned above, numerical results are compared with not only the experimental data but also with the numerical results from Deng et al. [76] and Esmaeilzadeh Seylabi et al. [77], who respectively used the PDMY and equivalent linear soil models (referred to as EL below). It is important to note that in their analyses, Deng et al. used three sets of material parameters that were calibrated from three different $G/G_{\max}$ curves to achieve better agreement in a variety of tests. Similarly, Esmaeilzadeh Seylabi et al. used an optimization based method to calibrate the shear wave velocity profile and the Rayleigh damping model of a soil column using the available far-field acceleration data for *each* test. In the present study, we only use *one* set of material parameters, which are calibrated from a *single* $G/G_{\max}$ curve as described in the previous section.

Acceleration: Fig. 2.8 displays the 5%-damped spectral accelerations at different locations for all of the studied test cases. Under the relatively low-amplitude input motion Northridge-L, the equivalent linear (EL) model yields satisfying results at all locations at lower frequencies. However, a better agreement is achieved with experimental data at higher frequencies using the implemented nonlinear soil model. This observation reveals the nonlinear model's advantages over the equivalent linear model, which experiences high damping at higher frequencies. Under the high-amplitude input motion Northridge-H, where the soil nonlinearity is more prominent, the EL model *always overestimates* the spectral accelerations, even at low frequencies. For the nonlinear model, on the other hand, predictions match the measurements well at deeper locations (this trend is generally true, in fact, for all models, because the input motions at the bottom of the container are known and prescribed in all of the numerical simulations). However, as we get closer to the soil surface, discrepancies increase and the nonlinear models (NL, NLV) underestimate the responses.

Fig. 2.9 displays the Arias intensity time-series at the far-field (see Fig. 2.5). As seen in Figs. 2.8 and 2.9, the NLV performs better than NL. The presently used stiffness-proportional viscous damping in the NLV model increases linearly with frequency, and thus, it appears possible to improve the NLV's agreement with measurements even further, especially at higher frequencies, by using a more sophisticated viscous part—a task deferred to a future study.

Fig. 2.10 displays the time-frequency distributions of the signal energy density [87] for acceleration time-series of T-Flexible-AH test (for which we expect significant nonlinear behavior) at locations A4 and A14 (cf. Fig. 2.5). As seen, both the NLV and EL models are generally capable of capturing the general patterns of experimental data, and as expected, the NLV model outperforms EL model at higher frequencies. On the other hand, the time-frequency distributions resulting from the NL model have spurious energy content at higher frequencies, which are non-existent in the experimental data, especially towards the end of the signal. This ascertains the discrepancies observed in the 5% damped spectral acceleration and Arias Intensity results presented for the NL model in Figs. 2.8 and 2.9, respectively.

Bending strains and lateral earth pressures: bending strains and lateral earth pressures along the walls of buried structures are two of the most important response/demand measures used in the design of such structures. As shown in Fig. 2.5, there were eight strain gauges installed outside of each wall in the centrifuge tests (SG1-8 and SG9-16). Figs. 2.11 and 2.12 compare, respectively, the bending strains obtained numerically and measured experimentally at the location of SG8 and the spatial variation of the maximum bending strains along the north wall. Strains predicted by NLV and EL are generally in very good agreement with experimental data for all the tests, which are both superior in this respect strains predicted by Deng et al. [76] using the PDMY model[2].

Static and total lateral earth pressures were experimentally measured on the walls of buried structures using tactile pressure sensors that were statically and dynamically cali-

[2]In their study, Deng et al. [76] did not present the Fourier amplitude spectra of their results for the PDMY model. These calculations are made here using their reported time series results. Also noted here is that a low-pass Butterworth filter is used to reduce the noise in strain data measured for the stiff structure.

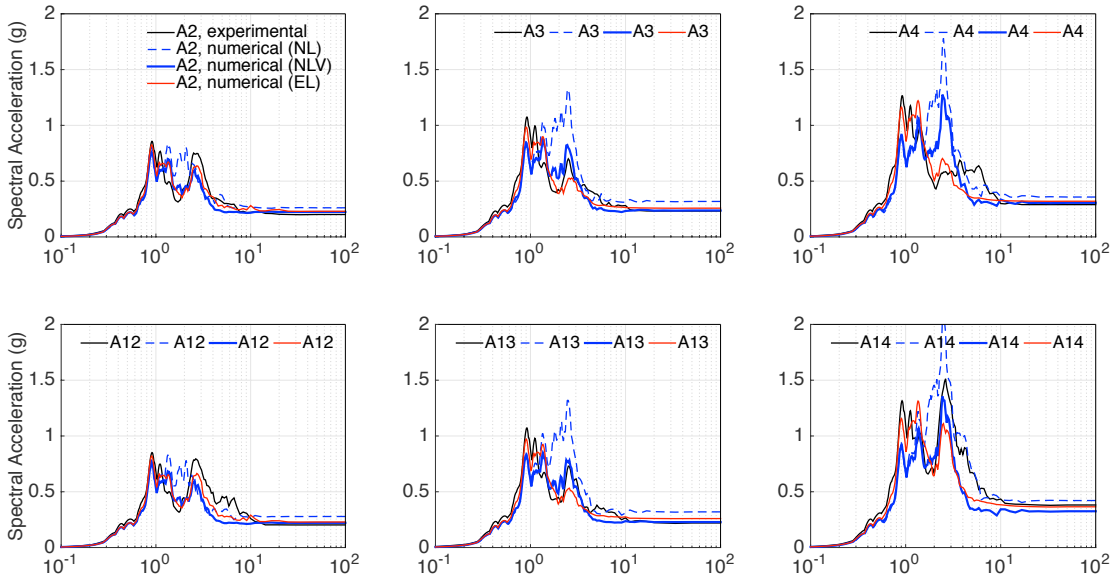

(a) T-Flexible-AL

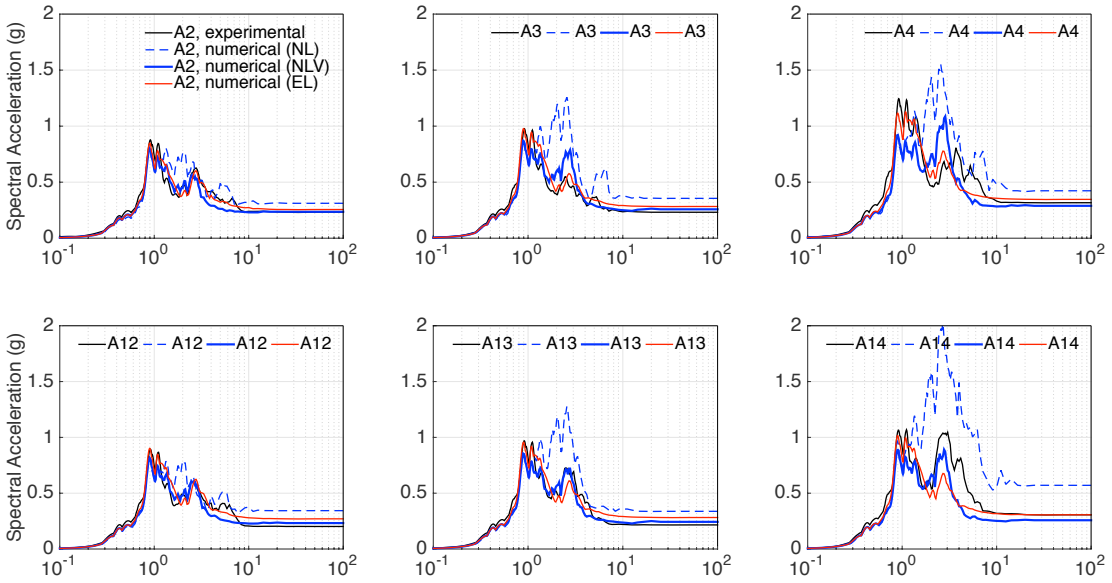

(b) T-Stiff-AL

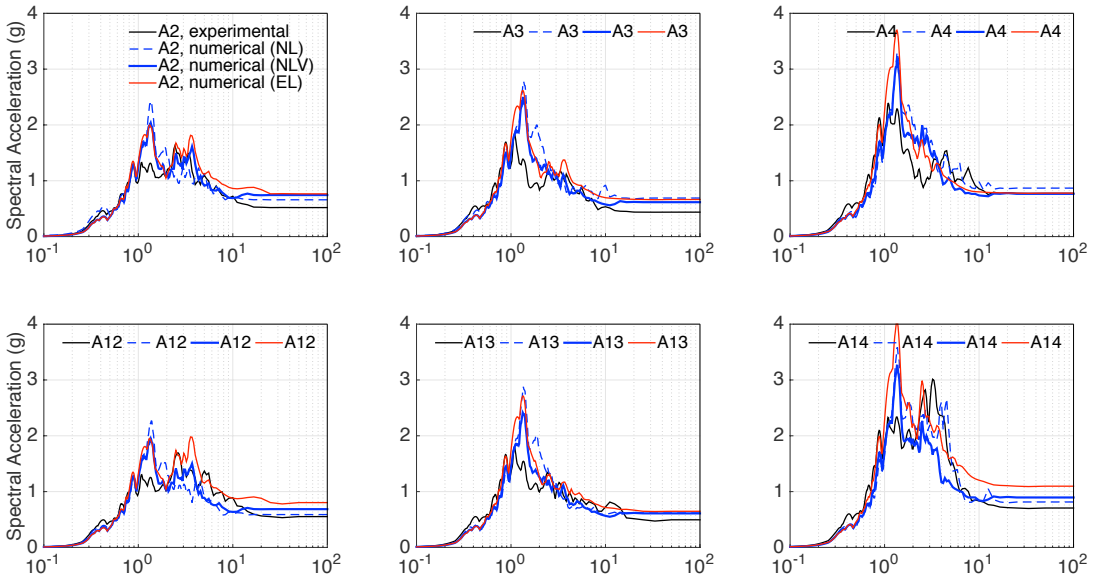

(c) T-Flexible-AH

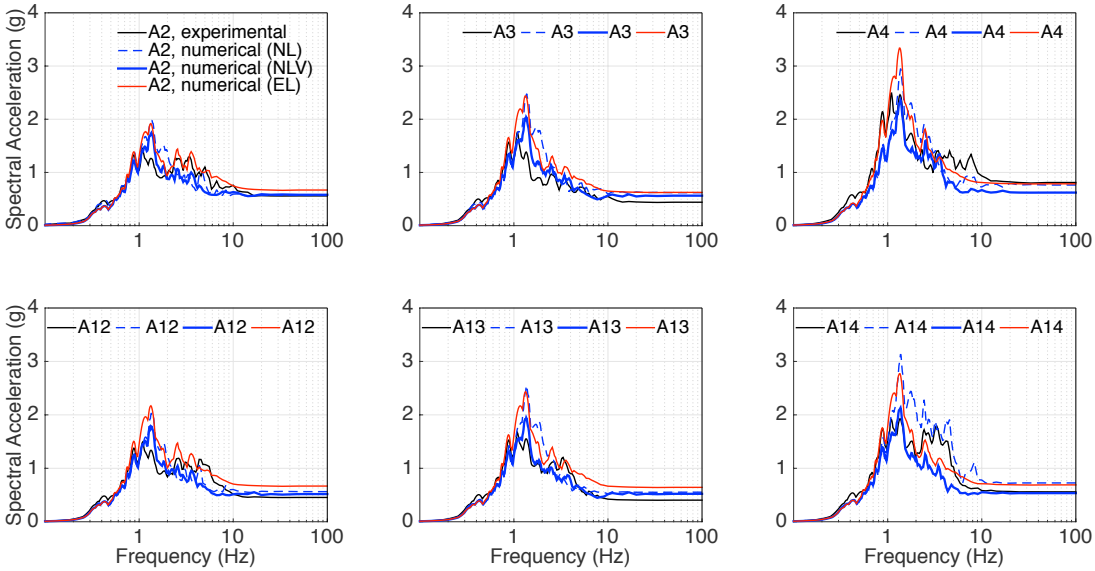

(d) T-Stiff-AH

Figure 2.8: 5% damped spectral acceleration at far-field (A2, A3, A4) and on structure (A12, A13, A14) for T-Flexible-AL, Stiff-AL, Flexible-AH, and Stiff-AH obtained numerically and experimentally.

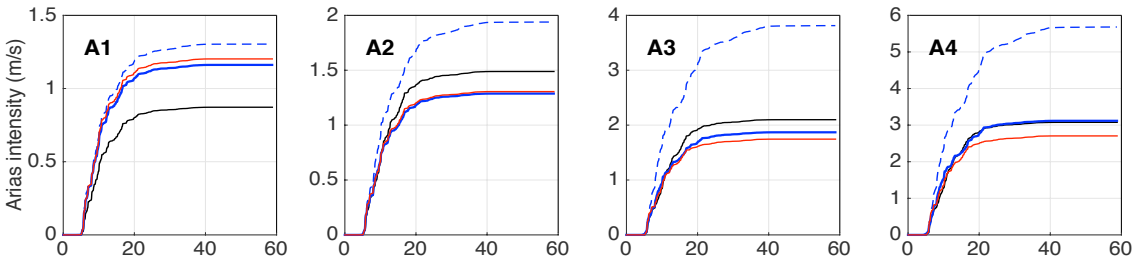

(a) T-Flexible-AL

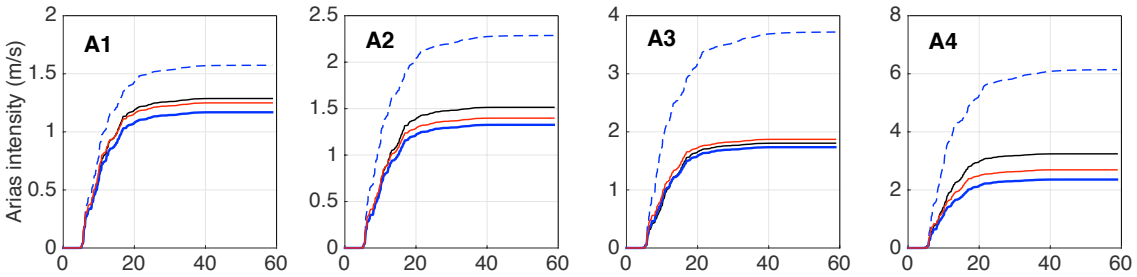

(b) T-Stiff-AL

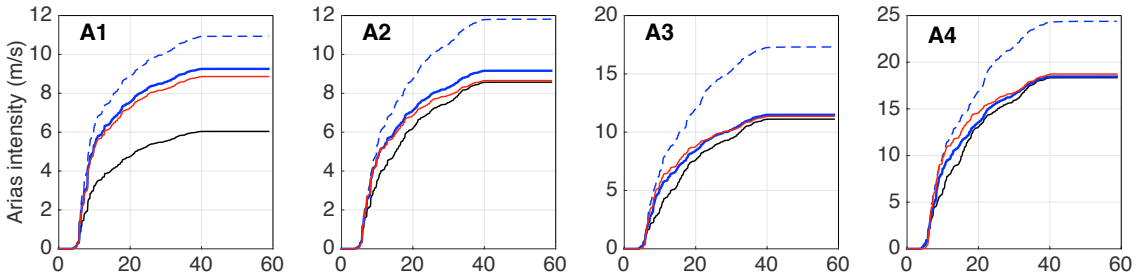

(c) T-Flexible-AH

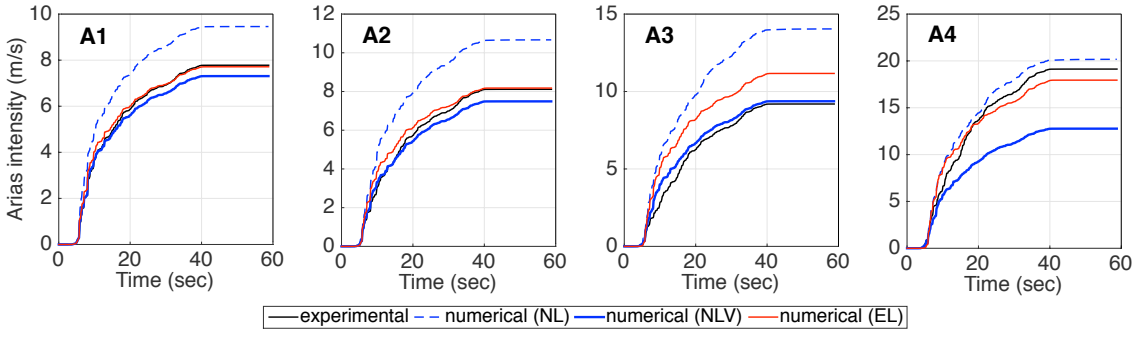

(d) T-Stiff-AH

Figure 2.9: Arias intensity at far-field (A1, A2, A3, A4) for T-Flexible-AL, Stiff-AL, Flexible-AH, and Stiff-AH obtained numerically and experimentally.

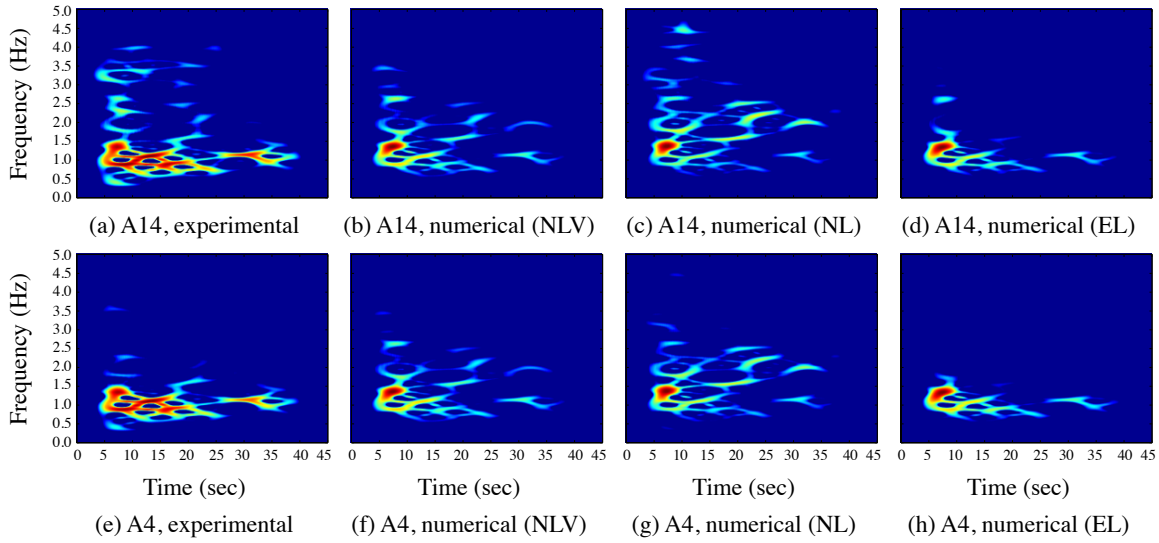

Figure 2.10: Time-frequency distribution of the energy density of acceleration time series for T-Flexible AH test using experimental and numerical data.

brated as detailed by Gillis et al. [88]. Data was averaged over each row of sensels to reduce scatter [73]. In nonlinear numerical simulations, frictional contact elements are used to consider the potential effects of the soil-structure interface sliding on the distribution of the lateral earth pressure on the structures. The friction coefficient of the interface is computed using,

$$\tan\left(\phi_{\text{interface}}\right) = 0.7 \tan\left(\phi_{\text{soil}}\right) \approx 0.33\,. \tag{2.18}$$

which agrees with typical values used in engineering practice [89], and was also used by Deng et al. [76]. Fig. 2.13 displays the distribution of the maximum dynamic (i.e., total minus static) and total lateral earth pressures along the north walls of the specimens. As seen, the NLV and contact models are successful in capturing the experimentally measured lateral earth pressures[3], especially for the stiff specimen and strong input motions for which the EL model has a poor performance. The NLV model also outperforms the PDMY model used by Deng et al. [76], who only reported results for low-intensity (Northridge-L) base motions.

Racking: the racking deformations—i.e., the relative displacement between the roof and

[3]In general, earth pressures in dynamic centrifuge experiments are difficult to measure reliably due the sensor limitations. Therefore, a higher degree of uncertainty should be expected in "measured" earth pressures than, for example, direct strain measurements.

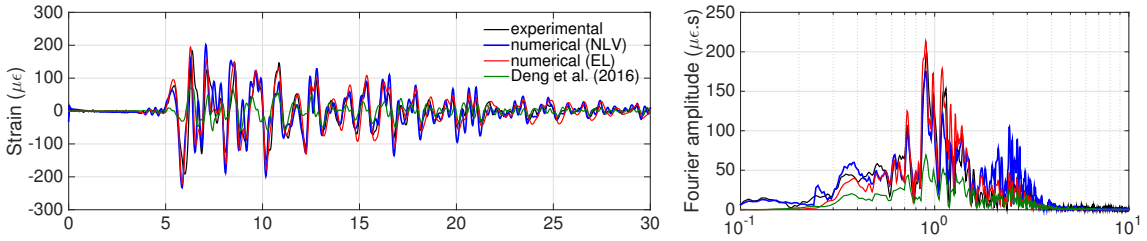

(a) T-Flexible-AL

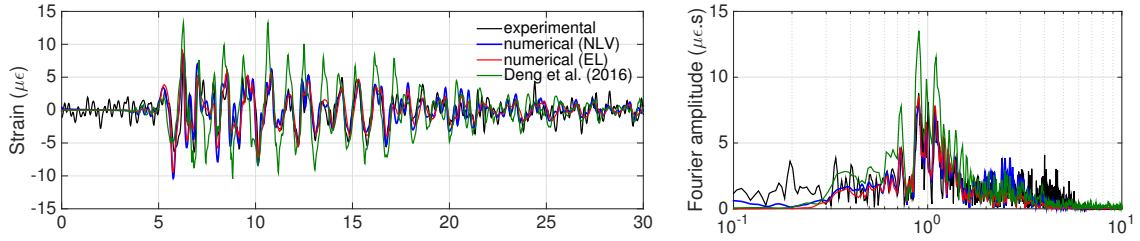

(b) T-Stiff-AL

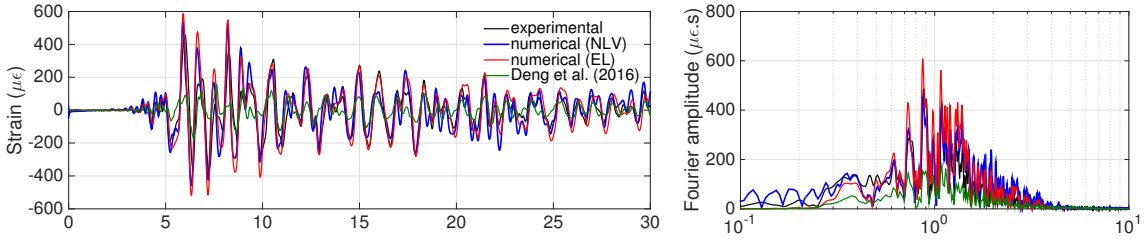

(c) T-Flexible-AH

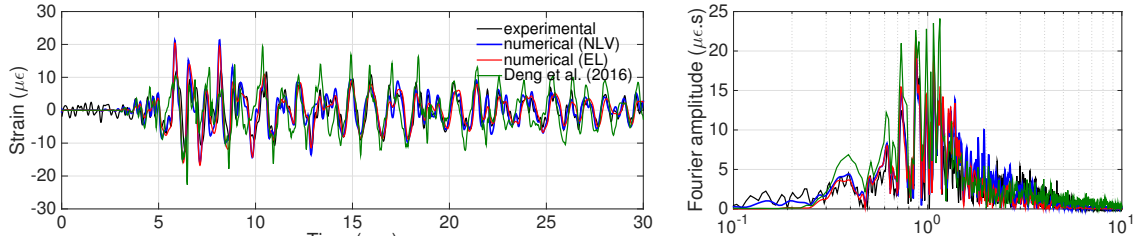

(d) T-Stiff-AH

Figure 2.11: Dynamic bending strains and their corresponding Fourier amplitude spectra of the sensor SG8 at the bottom of the north wall obtained numerically and experimentally.

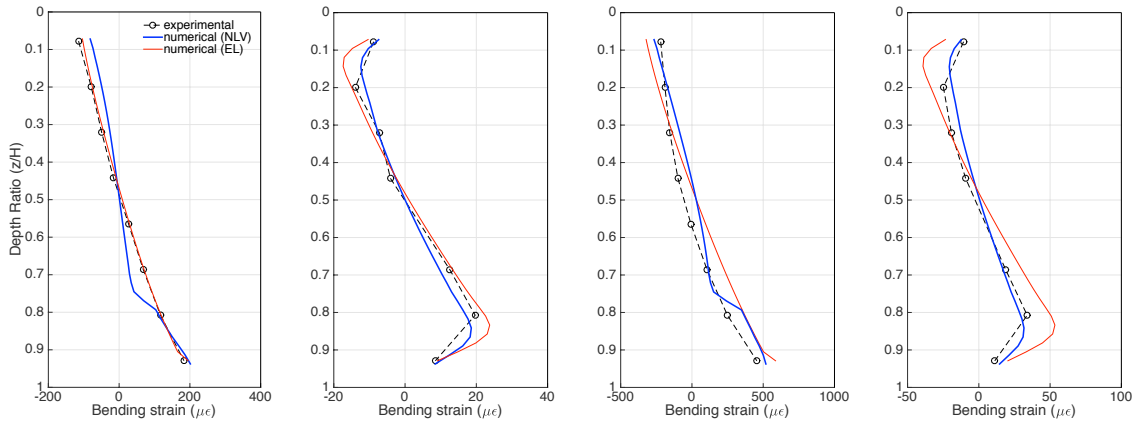

(a) T-Flexible-AL (b) T-Stiff-AL (c) T-Flexible-AH (d) T-Stiff-AH

Figure 2.12: The distribution of maximum bending strains along the north wall for T-Flexible-AL, Stiff-AL, Flexible-AH, and Stiff-AH obtained numerically and experimentally.

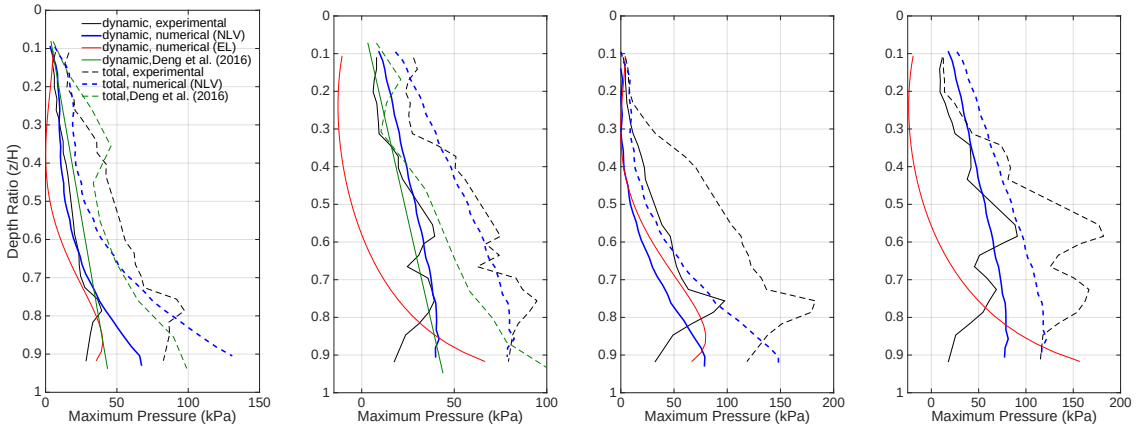

(a) T-Flexible-AL (b) T-Stiff-AL (c) T-Flexible-AH (d) T-Stiff-AH

Figure 2.13: The distribution of the maximum dynamic and total lateral earth pressure profiles for T-Flexible-AL, Stiff-AL, Flexible-AH, and Stiff-AH obtained numerically and experimentally.

base—is another critical parameter in the design procedures for buried structures. Experimental racking deformations are obtained by double-integrating the accelerations at locations A14 and A12, which are then subtracted from each other (i.e., D12 − D14). Fig. 2.14 displays the racking deformations for all the tests. As seen, the numerical and experimental results are in good agreement in all the tests, and NLV displays significantly better performance than PDMY under high-amplitude base motions.

Stress-strain curves and secant stiffness values: in order to visualize the level of nonlinearity/hysteresis that the NLV model exhibited under the earthquake excitations used in the tests, shear stress-strain curves at the representative locations, A1, A2, A3 and A4, are plotted for all of the base motions. The components of stress and strain are computed at the centers of the finite elements representing the far-field soil. As seen in Fig. 2.15, the NLV model exhibited a high degree of hysteretic behavior and the model also experienced permanent deformations.

Additionally, the maximum and "effective" shear strains measured in the far-field soil are used to compute the secant and effective shear stiffnesses using Fig. 2.7b. It is assumed that effective shear strain is equal to 65% of the maximum shear strain [90]. Fig. 2.16 displays the resulting secant and effective shear wave velocity profiles as well as those used in the equivalent linear (EL) model simulations conducted by Esmaeilzadeh Seylabi et al. [77]. As seen, for T-Flexible-AL and T-Stiff-AL, the shear wave velocities profile used in the EL model a lower than those that the NLV model yields. This is mainly because the associated Rayleigh damping used for the EL model is higher than those assumed for NLV. For the high-amplitude motion cases T-Flexible-AH and T-Stiff-AH, significant soil nonlinearities are induced, the the EL and NLV profiles become closer to each other.

Surface settlements: during the tests, surface settlements are measured by 7 linear variable differential transducers (LVDTs), as shown in Fig. 2.5. Here, the experimental and numerical surface settlements at locations D3 and D6 are compared, which represent the settlements experienced by the specimen structures and the far-field, respectively. As seen in Fig. 2.17, in most cases, the NLV model can capture the settlement at the specimen

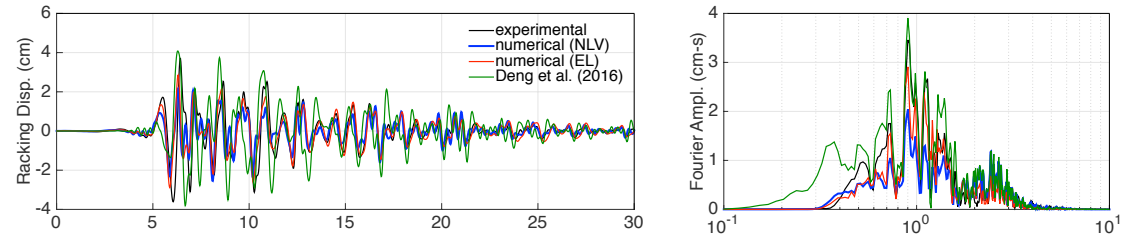

(a) T-Flexible-AL

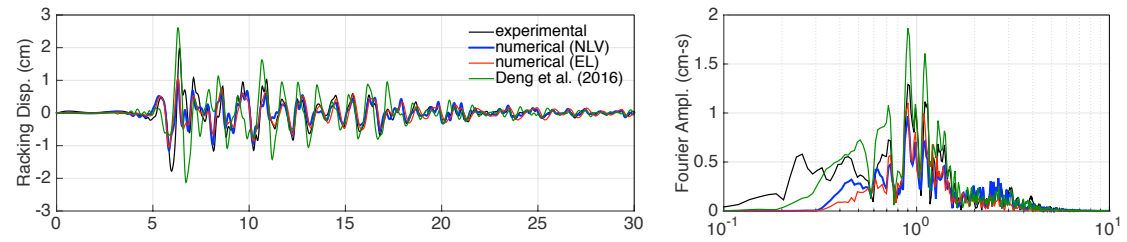

(b) T-Stiff-AL

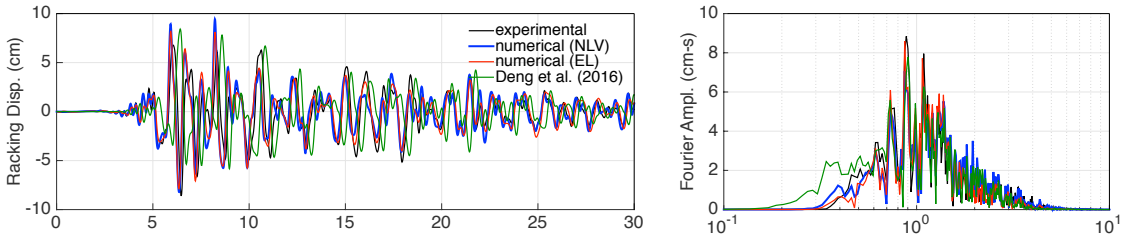

(c) T-Flexible-AH

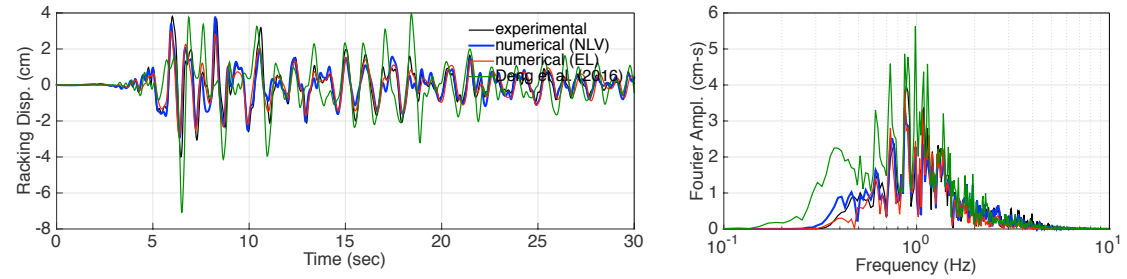

(d) T-Stiff-AH

Figure 2.14: Racking profiles for T-Flexible-AL, Stiff-AL, Flexible-AH, and Stiff-AH obtained numerically and experimentally.

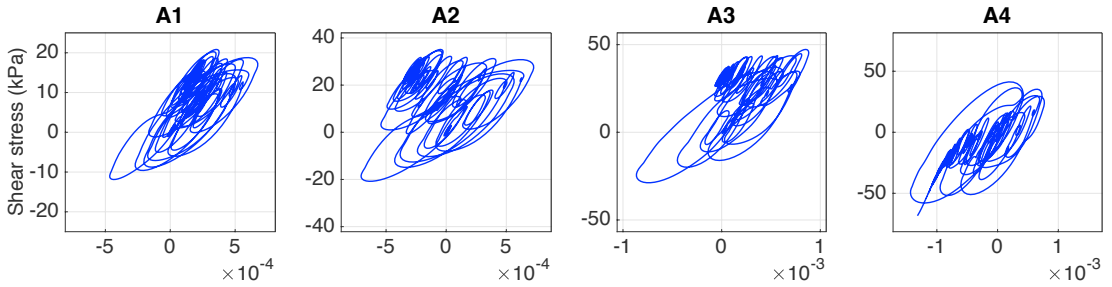

(a) T-Flexible-AL

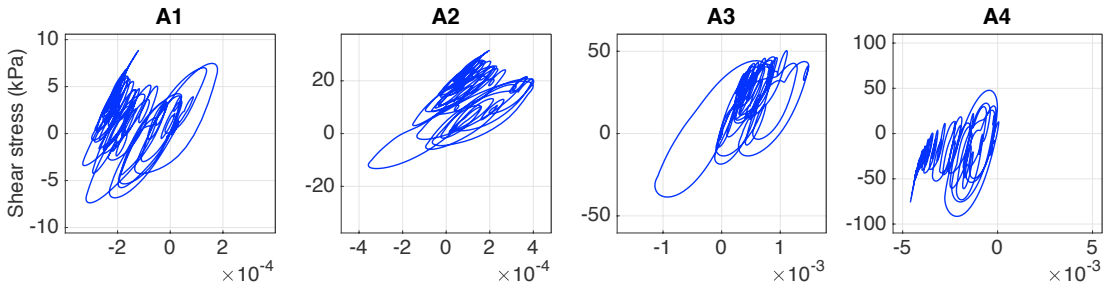

(b) T-Stiff-AL

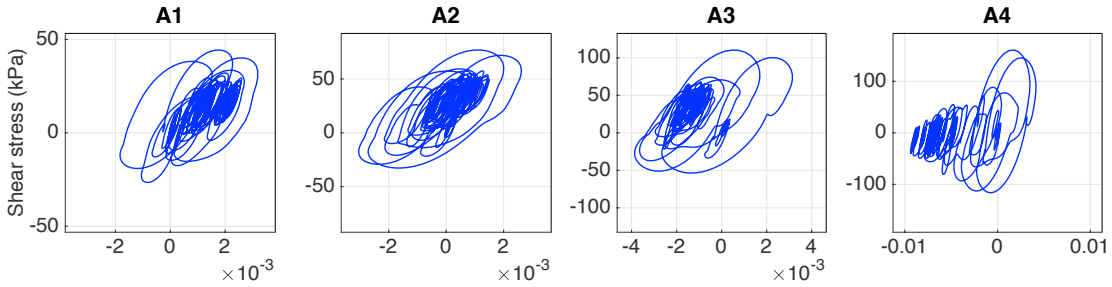

(c) T-Flexible-AH

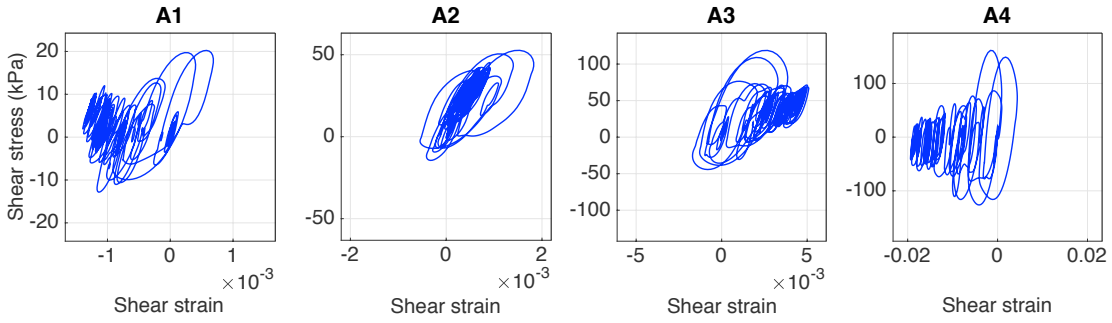

(d) T-Stiff-AH

Figure 2.15: Numerically predicted stress-strain curves for T-Flexible-AL, Stiff-AL, Flexible-AH, and Stiff-AH.

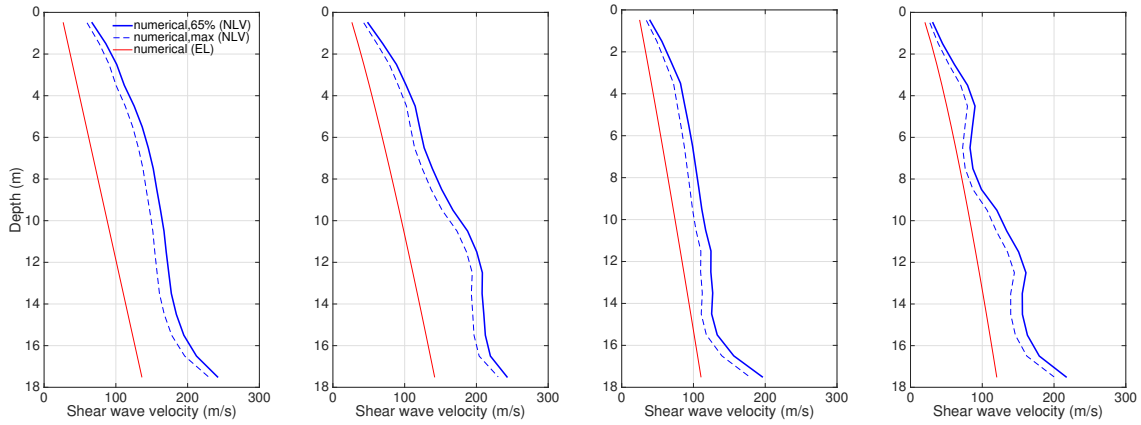

(a) T-Flexible-AL (b) T-Stiff-AL (c) T-Flexible-AH (d) T-Stiff-AH

Figure 2.16: Comparisons of shear wave velocity profiles for T-Flexible-AL, Stiff-AL, Flexible-AH, and Stiff-AH obtained from nonlinear and equivalent linear method.

location very well. Discrepancies that exist, especially for the low-amplitude tests, may be due to the soil densification that occured during these tests, which were conducted before the high-amplitude motion tests for each structure. In their study, Deng et al. [76] only presented results for surface settlements obtained for the baseline structure, and the agreement achieved there with PDMY is generally inferior to NVL.

Error analyses of numerical simulation results: in order to explore the capability of nonlinear and equivalent linear soil models in predicting different response parameters investigated in this study, we compute the residual for each response parameter, as in [85]:

$$\text{Residual } X = \log\left(\frac{X_{\text{measured}}}{X_{\text{predicted}}}\right) \tag{2.19}$$

where X refers to a given response parameter of interest. Fig. 2.18 shows the range of residuals and variances for each analysis type and response parameter—namely, PGA profiles for the far-field and the structural walls, surface response spectra, surface far-field Arias intensity, racking displacement, bending strain and pressure profiles of structural walls, and the amplitude of surface settlement. As these results indicate, the EL model exhibits satisfactory performance, especially for the low-amplitude motions, with residuals ranging from

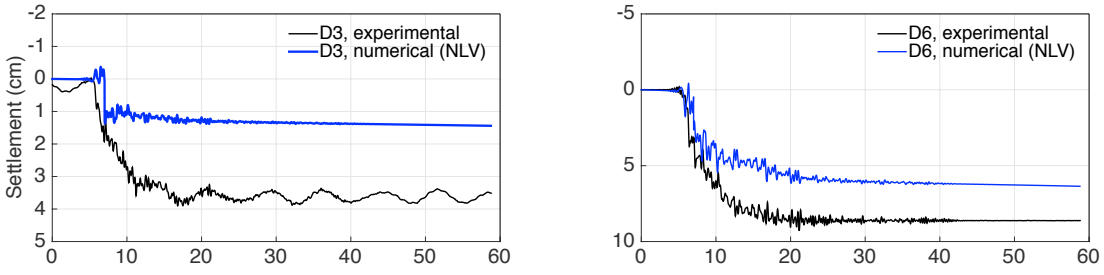

(a) T-Flexible-AL

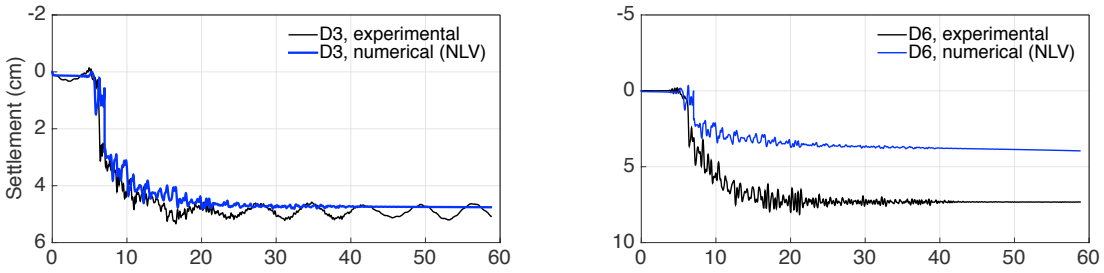

(b) T-Stiff-AL

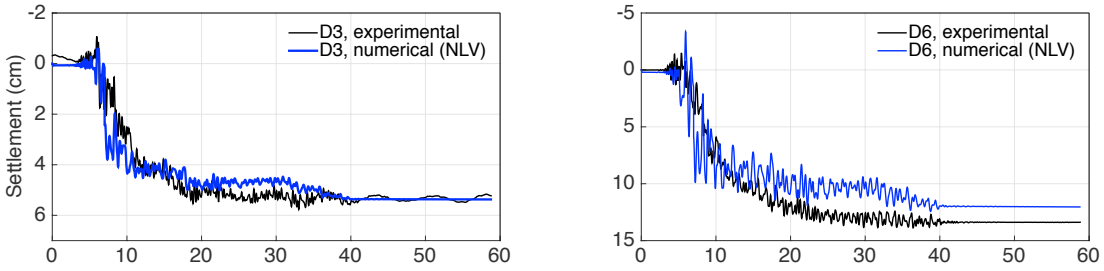

(c) T-Flexible-AH

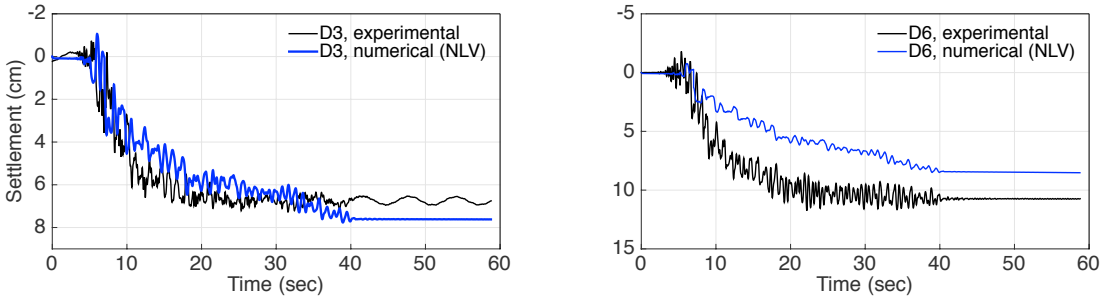

(d) T-Stiff-AH

Figure 2.17: Measured (experimental) and predicted (numerical) surface settlements at the sensor locations LVDT3 (structure) and LVDT6 (free-field).

about −0.22 to 0.31, if we exclude the pressure residuals (as pressure transducers have yet unknown reliability). NLV is superior with residuals ranging from about −0.16 to 0.2, if we exclude the pressure and settlement residuals (as full settlement data is only available for NLV). This performance of NLV is especially impressive, because unlike EL, the NLV model is calibrated from a single material dataset, whereas the EL model was specifically calibrated [77] to match—in a weighted least-squares sense—soil behavior in seperate (low- and high-amplitude input) tests.

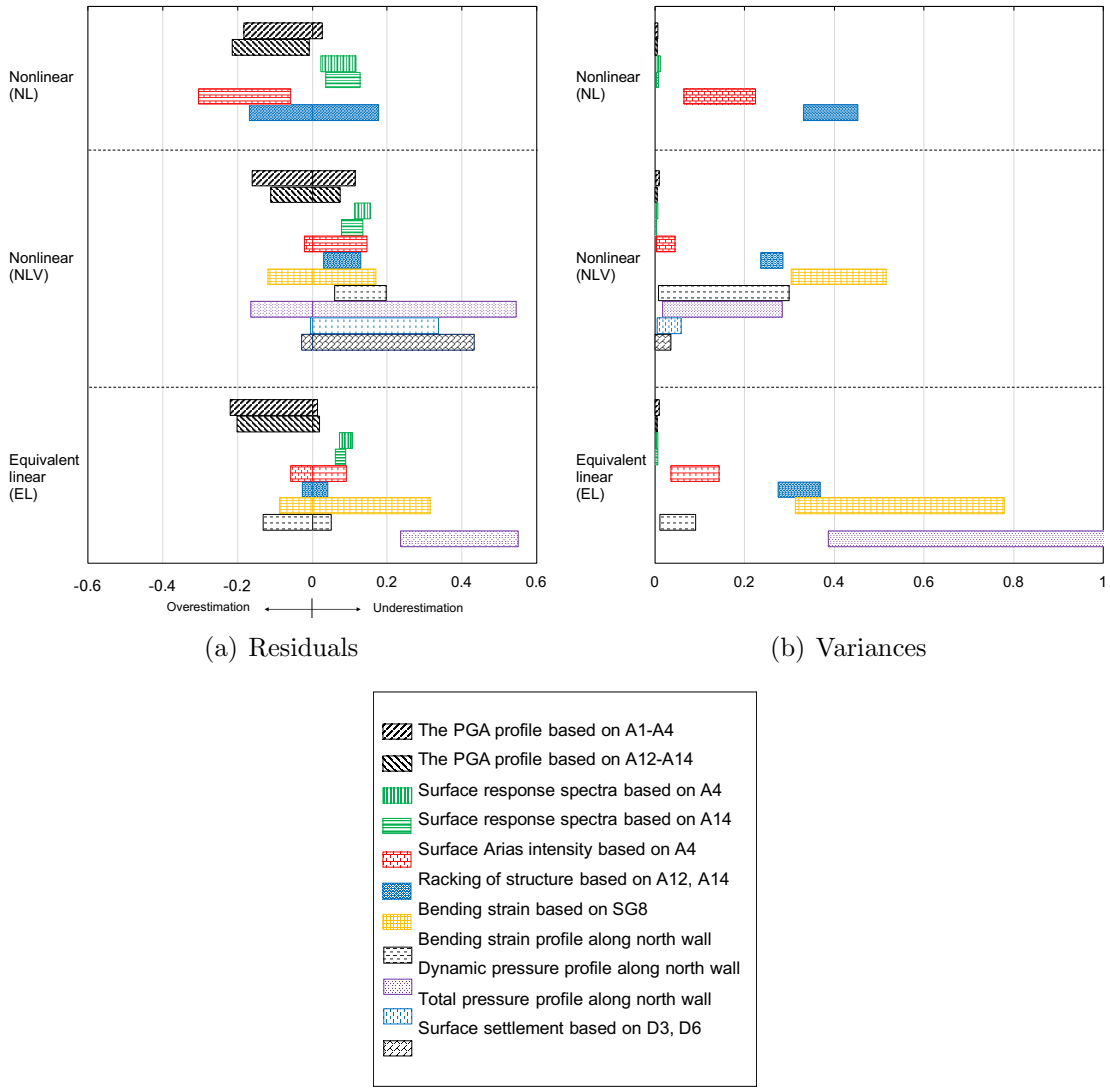

(a) Residuals

(b) Variances

(c) Legends

Figure 2.18: The range of (a) residuals and (b) variances for each analysis type and response parameters.

CHAPTER 3

Reduced order modeling tools for SSI

3.1 Review of the reduced order modeling techniques for SSI problems

All civil structures have foundations and other support elements that either rest on, or are embedded in, soil. Because of complexities in modeling the mechanical behavior of soils, and the high degree of uncertainty and variability in their properties, it is not uncommon among structural engineers to completely ignore their effects on the structural system. This simplistic approach, wherein the soil-structure interaction (SSI) effects are unaccounted for, might yield acceptable designs for certain cases—for example, for lightweight aboveground structures resting on, or stiff underground structures buried in, rock and stiff soils [5]. Nevertheless, the omission of SSI effects can also bear perilous consequences under strong earthquakes—for example, for a massive structure resting on soft soil [6]. For buried structures, although the inertially induced tractions may become negligible, the nominal contrast between the flexibilities of the foundation system and its surrounding soil may significantly affect their responses.

One approach to take the effects of SSI into account is to use the finite element method (FEM) to model a portion of the supporting/surrounding soil media along with the structure. This approach is known as the direct modeling [5, 30] method. Apparently, it is not possible to discretize the semi-infinite soil domain with a finite number of elements; and thus, it is necessary to truncate it by introducing appropriate boundary conditions. For an exact representation of the omitted domain—dubbed the far-field—, the introduced boundaries on

the computational domain (the near-field) must have the ability to transmit the energy of the outgoing and incoming waves perfectly. In problems where the source of excitation is inside the near-field, all waves impinging upon the imposed boundaries are outgoing; and the inserted boundary condition must absorb the energy of these outgoing waves through the so-called, absorbing-boundary-conditions (ABCs).

Lysmer and Kuhlemeyer [20] proposed the first local ABC [1], which could only absorb waves traveling along a prescribed direction. Higdon [93] proposed the m-th order multi-directional boundary condition that can absorb traveling waves with m different angles of incidence perfectly. Although the accuracy of this boundary condition increases by m, its usage in application is limited to $m \leq 2$. This is because it is very complicated to define high-order derivatives in standard numerical schemes, such as the finite element method. Since then, different high-order ABCs have been proposed [94]. Almost all these boundary conditions are limited to scalar problems such as electrodynamics and acoustic problems. Although many infinite domain problems involve vectorial elastic waves, only a few high-order ABCs have been developed for elastodynamics problems thus far [95, 96]. However, all of them suffer from long-time instability [2] issues [97]. Recently, Baffet et al. [97] proposed the first long-time stable high-order local ABC. Thus far, this high-order ABC is only available for the relatively simple case of 2D elastodynamics with a single artificial boundary and two physical boundaries. Extensions to more involved cases, such as problems in SSI analysis, which consist of a single physical boundary and three artificial boundaries, do not yet exist.

The paraxial boundary is also an ABC that is based on the paraxial approximations of the one-way wave equations, and has been developed for both scalar wave [98, 99] and elastic wave equation [100, 101, 102]. However, it was demonstrated that this approximation is very accurate only for high-frequency waves and for waves impinging the boundary with small

[1] ABCs may be classified as nonlocal and local. Nonlocal ABCs are derived by using analytical solutions of waves propagating in the far-field, and involves a boundary integral operator, meaning that all the nodes on the boundary interact with each other. However, local ABCs are represented as a differential operator, so that after discretization, each node on the boundary interacts only with its neighbors, resulting less computational costs [91, 92].

[2] The solution grows exponentially after a sufficiently long amount of time.

incident angles [101].

Besides the high-order ABCs and the paraxial boundary, another class of local ABCs is perfectly matched layers (PMLs), which were originally introduced by Berenger [103] for absorbing electromagnetic waves, and extended to elastodynamic problems by Basu and Chopra [104], but using a rather complicated time integration scheme [105] to compute the internal forces. In short, a PML is an absorbing layer adjacent to the finite computational domain–i.e., near-field–with two main properties [96]:

- It results in no reflections at the truncated near-field boundary (i.e., "perfect matches" it) for all non-zero-frequency impinging waves, irrespective of their angles of incidence.
- It attenuates the wave energy within itself.

Due to the applicability for heterogeneous media [106], PMLs have become more popular than high-order ABCs in dealing with infinite domain problems. Kucukcoban and Kallivokas [106] proposed a mixed finite element implementation of the displacement-stress unsplit-field formulation in 2D elastic heterogeneous media, with superior stability and efficacy. Later they derived the symmetric formulation of this approach [107] and also extended it to 3D elastic heterogeneous media [108].

However, considering the relatively complex formulations of the PMLs, few of them have been implemented to commercial finite element packages for broader use, which eventually limits the considerable advantages of combining the PMLs with other advanced tools, e.g., contact elements, nonlinear constitutive models, etc. Plaxis [109] and FLAC [110] —two commonly used commercial software in geotechnical engineering area—are equipped with viscous and free-field ABCs. Obviously, those two ABCs are not capable of efficiently absorbing the outgoing waves when the incident angle is neither 0 nor 90 degree. Basu [111] implemented an elastic PML in LS-DYNA [112], but it is only available in 3D media and with explicit integration scheme. Poul and Zerva [113] implemented a viscoelastic PML in ABAQUS [114] based on the work of Zheng and Huang [115]. However, it is 2D plane-strain only, and the recursive convolution technique used in the evaluation of internal forces incurs

more computational efforts.

In this work, we employ the symmetric hybrid PML formulation proposed by Kucukcoban and Kallivokas, and Fathi et al. [107, 108], by writing a user-defined element (aka UEL) subroutine with Hilber-Hughes-Taylor implicit time integration scheme (HHT-α method [116]), for simulation of wave propagation in both 2D and 3D heterogeneous half-spaces. This implementation has been verified by comparing our results obtained from PML-truncated domain against an enlarged domain solution with fixed boundaries. Excellent agreement is acquired in different cases in terms of loading conditions, material properties and geometry dimensions.

Besides prescribing proper ABCs, direct modeling of SSI problems also usually suffer from defining inappropriate input ground motions [46, 47]. So far the Domain Reduction Method (DRM) [30, 117] is recognized to be the best approach for modeling a semi-infinite domain under remote excitations. In this study, we first implement the DRM by computing the effective nodal forces based on the formulations derived in [117], and then thoroughly verify it by comparing the DRM-generated free-field responses with either analytical solutions (if exist) or results computed from 1D site response analysis. Moreover, for both homogeneous and heterogeneous soil layers, vertical and inclined incident SV waves, 2D and 3D domains, we achieve excellent accuracy.

In the end, by using the powerful coupled DRM-PML system, 1) we compute the impedance functions for different problems and then compare our results with analytical or semi-analytical solutions. Given the facts that impedance functions are indispensable for substructure method, but they have been devised only for specific conditions, we can use DRM-PML system to compute them regardless of foundation shapes and soil profiles, with extremely low computational cost and desirable accuracy. 2) A buried rectangular structure in 2D domain is modeled to study the effects of the angle of incidence. Inclined SV waves with different angles of incidence are applied, and the resulting horizontal and vertical accelerations, maximum axial forces and bending moments, and maximum deformations of the structures are plotted. For more details regarding this work, please refer to [118].

3.2 Perfectly-Matched-Layer (PML)

To render the semi-infinite extent of soils, we will truncate it by using a robust wave absorbing boundary, Perfectly-Matched-Layer (PML). The PML can eliminate reflections at the truncated near-field boundary for all non-zero-frequency impinging waves, irrespective of their angles of incidence. And the wave energy will be attenuated rapidly within its zones.

3.2.1 Implementation

In this study we implement both 2D and 3D PMLs developed by Kucukcoban and Kallivokas [106] and Fathi et al. [119], respectively, that can be used for wave propagation related simulation in an arbitrarily heterogeneous media. The PML is treated via an unsplit-field, but mixed-field, symmetric displacement-stress formulation, which then can be directly coupled to a standard displacement-only formulation for the interior domain, resulting to a relatively computationally efficient hybrid scheme.

In order to implement this PML-type element in ABAQUS, we write a user-defined element (UEL) subroutine in Fortran90. Adding the convenient features of the solver in ABAQUS, we do not need to be concerned regarding the assembling process of the matrices, even though this mixed PML element consists of displacement and stress components. The principal component required for constructing a PML is the complex stretching function. And the idea is to "stretch" the originally physical coordinates to the virtually infinite coordinates. The complex stretching function we employ in this study is defined as,

$$\lambda_i(x_i, \omega) = \alpha(x_i) + \frac{1}{j\omega}\beta(x_i) \tag{3.1}$$

where α and β are the scaling functions that stretch the coordinate variable x, and the attenuation function that enforces the amplitude decay of outgoing waves, respectively, which

are given in terms of polynomials, as

$$\alpha_i(x_i) = 1 + \alpha_0 \left[\frac{(x_i - x_i^0) n_i}{L_{\mathrm{PML},i}} \right]^m, \; x_i^0 \leq x_i \leq x_i^t \tag{3.2a}$$

$$\beta_i(x_i) = \beta_0 \left[\frac{(x_i - x_i^0) n_i}{L_{\mathrm{PML},i}} \right]^m, \qquad x_i^0 \leq x_i \leq x_i^t \tag{3.2b}$$

where $i = x,\ y$ and z, and α_0 and β_0 are two user-chosen parameters that control the amplitude decay, n_i is component of the outward unit normal at the interface in i direction, and m represents the polynomial degree. And here we use the suggested expressions [106] for them, as shown in Eq. 3.3. x_i^0 and x_i^t denote the coordinates of the inner and outer PML boundaries. $L_{\mathrm{PML},i}$ is the thickness of the PML boundary in i direction.

$$\alpha_0 = \frac{(m+1)b}{2L_{\mathrm{PML},i}} \log\left(\frac{1}{R}\right) \tag{3.3a}$$

$$\beta_0 = \frac{(m+1)c_p}{2L_{\mathrm{PML},i}} \log\left(\frac{1}{R}\right) \tag{3.3b}$$

where c_p is the P-wave velocity, R is a user-tunable reflection coefficient and b is a characteristic length of the domain. In the following study we always set $m = 2, R = 10^{-10}$ and $b =$ ten times the average element size. Also, please be advised that the outer PML boundary should always be fixed (in terms of the displacement field), and for heterogeneous soils, constant β_0 is required for different soil layers. See Fig. 3.1 for an illustration of those parameters in the 2D PML domain.

Based on the definition of the complex stretching functions, we can derive the corresponding semi-discrete forms and submatrices for PMLs in 2D and 3D domains [119], which are included in the Appendix A.

In ABAQUS, the Hilber-Hughes-Taylor (HHT-α method) implicit time integration scheme is the default approach for solving both linear and nonlinear problems. And in the UEL sub-

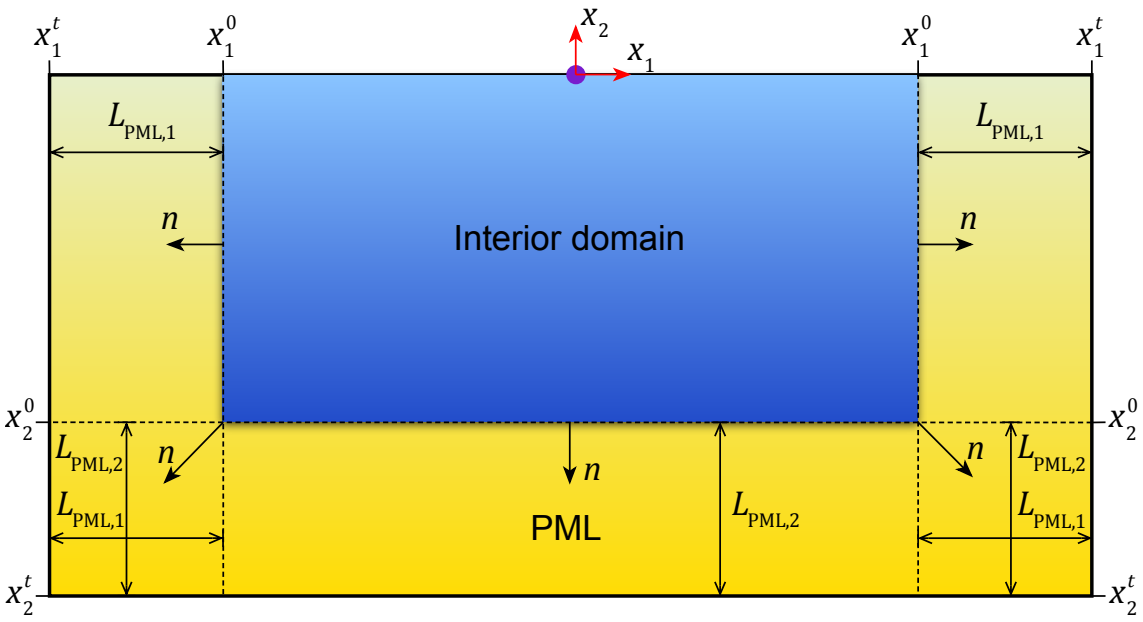

Figure 3.1: Illustration of a 2D PML domain attached to the interior domain.

routine, the effective stiffness matrix (AMATRX, $\mathbf{K}_{\text{eff}}$) and the residual vector (RHS, $\mathbf{F}_{\text{R}}$), which have the relationship in incremental form, as shown in Eq. 3.4, need to be computed and updated in every step.

$$\mathbf{K}_{\text{eff}}\Delta\mathbf{u} = \mathbf{F}_{\text{R}} \tag{3.4}$$

where $\mathbf{K}_{\text{eff}}$ and $\mathbf{F}_{\text{R}}$ can be derived, as

For 2D domain,

$$\mathbf{K}_{\text{eff}} = \frac{1}{\beta\Delta t^2}\mathbf{M}_{\text{PML}} + \frac{1+\alpha}{\beta\Delta t}\mathbf{C}_{\text{PML}} + (1+\alpha)\mathbf{K}_{\text{PML}} \tag{3.5a}$$

$$\begin{aligned}\mathbf{F}_{\text{R}} = &-\mathbf{M}_{\text{PML}}\ddot{\mathbf{u}}^{t+\Delta t} + (1+\alpha)(\mathbf{F}_{\text{ext}}^{t+\Delta t} - \mathbf{K}_{\text{PML}}\mathbf{u}^{t+\Delta t} - \mathbf{C}_{\text{PML}}\dot{\mathbf{u}}^{t+\Delta t}) - \\ &\alpha(\mathbf{F}_{\text{ext}}^{t} - \mathbf{K}_{\text{PML}}\mathbf{u}^{t} - \mathbf{C}_{\text{PML}}\dot{\mathbf{u}}^{t})\end{aligned} \tag{3.5b}$$

For 3D domain,

$$\mathbf{K}_{\text{eff}} = \frac{1}{\beta\Delta t^2}\mathbf{M}_{\text{PML}} + \frac{1+\alpha}{\beta\Delta t}\mathbf{C}_{\text{PML}} + (1+\alpha)\mathbf{K}_{\text{PML}} + \frac{\eta\Delta t}{\beta}\mathbf{G}_{\text{PML}} \tag{3.6a}$$

$$\begin{aligned}\mathbf{F}_{\text{R}} = &-\mathbf{M}_{\text{PML}}\ddot{\mathbf{u}}^{t+\Delta t} + (1+\alpha)(\mathbf{F}_{\text{ext}}^{t+\Delta t} - \mathbf{G}_{\text{PML}}\bar{\mathbf{u}}^{t+\Delta t} - \mathbf{K}_{\text{PML}}\mathbf{u}^{t+\Delta t} - \mathbf{C}_{\text{PML}}\dot{\mathbf{u}}^{t+\Delta t}) - \\ &\alpha(\mathbf{F}_{\text{ext}}^{t} - \mathbf{G}_{\text{PML}}\bar{\mathbf{u}}^{t} - \mathbf{K}_{\text{PML}}\mathbf{u}^{t} - \mathbf{C}_{\text{PML}}\dot{\mathbf{u}}^{t})\end{aligned} \tag{3.6b}$$

where α, β and γ are time increment parameters for HHT-α method that have the conditions as,

$$-1/3 \leq \alpha \leq 0,\ \beta = (1+\alpha)^2/4,\ \gamma = 1/2 + \alpha \tag{3.7}$$

The default value is $\alpha = -1/20$.

From Eq. A.4 we can deduce that the governing equation for PML in 3D domain is a third-order ODE, however the solver in the ABAQUS is designed for second-order ODE. Therefore here we need to store the variable $\bar{\mathbf{u}}^{\Delta t}$ (see Eq. A.4(b)) into SVARS (state variables in UEL). By using the extended Newmark-beta method [119], $\bar{\mathbf{u}}^{t+\Delta t}$ can be expressed as,

$$\bar{\mathbf{u}}^{t+\Delta t} = \bar{\mathbf{u}}^{t} + \Delta t\mathbf{u}^{t} + \frac{\Delta t^2}{2}\dot{\mathbf{u}}^{t} + \Big(\frac{1}{6} - \eta\Big)\Delta t^3\ddot{\mathbf{u}}^{t} + \eta\Delta t^3\mathbf{u}^{t+\Delta t} \tag{3.8}$$

where $\eta = 1/12$ is a parameter chosen to be consistent with the average-acceleration scheme.

3.2.2 Verification

In this section, we comprehensively verify the accuracy and stability of the implemented PML, and compare its performance with other ABCs (i.e., Lysmer and Kuhlemeyer [20] and ABAQUS built-in infinite element), in both 2D and 3D domains, homogeneous and heterogeneous soil layers, under concentrated and distributed loads. Lysmer and Kuhlemeyer [20] ABC simply places dashpots on the outside boundary. The infinite elements in ABAQUS, per descriptions in the manual [114], provide "quiet" boundaries to the finite element model through the effect of a damping matrix and a suppressed stiffness matrix. And it does not

provide perfect transmission of energy out of the mesh except in the case of plane body waves impinging orthogonally on the boundary in an isotropic medium.

3.2.2.1 2D semi-infinite rod

A 2D semi-infinite rod (see Fig. 3.2(a)) with uniform cross-section and homogeneous material properties (i.e., $V_s = 200$ m/s, $\nu = 0.3$, $\rho = 2000$ kg/m^3), excited by a horizontal load using the function defined in Eq. 3.18 with an amplitude of 100 kN, a central frequency of 5 Hz and a total period of $t = 1.0$ sec, is analyzed by attaching i) PML elements (see Fig. 3.2(b)), ii) infinite elements (CINPE4) and placing iii) dashpots on the right end (i.e., $x = 30$ m) in horizontal direction with coefficient $c_x = \rho V_p/2$. The rod has a thickness of 1 m, and here we use the 4-node plane-strain element (CPE4) with a size of 1 m by 1m for the regular domain. The same element size applies to the PML boundary. Besides, the vertical DOF is fixed and hence only the horizontal DOF is free. To investigate the performance of the PML and other ABCs, we create an enlarged domain with a total size of 1 m $\times$ 400 m, element size of 1 m $\times$ 1 m and fixed boundaries on the outer surface, where the domain is large enough to avoid the reflected waves enter the regular domain, to be the reference solutions.

Fig. 3.3 shows the comparisons of horizontal displacements for two selected points obtained by using different ABCs, i.e., PML, dashpots and infinite element, against the enlarged domain solutions. All three ABCs show excellent agreement, which is because both Lysmer and Kuhlemeyer [20] and ABAQUS infinite plane-strain element (CINPE4) are designed for 1D wave propagation analysis.

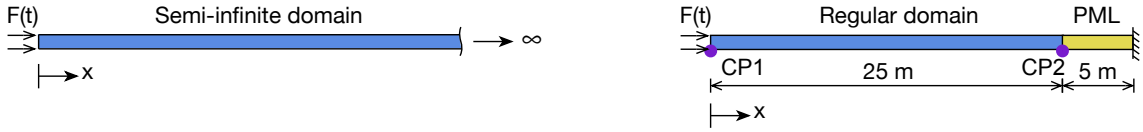

(a) Original problem (b) PML-truncated domain

Figure 3.2: Configuration of (a) the original 2D semi-infinite rod problem and (b) the PML-truncated domain.

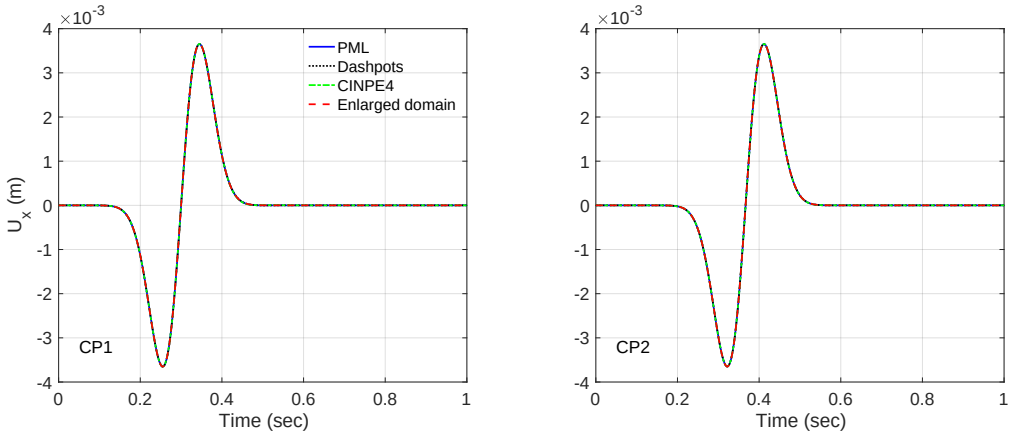

Figure 3.3: Comparisons of horizontal displacements for two selected points.

3.2.2.2 2D three-layered half-space

A 2D three-layered half-space case (see Fig. 3.4(a)) with material properties summarized in Table. 3.1, excited by a vertical point load using the function defined in Eq. 3.18 with an amplitude of 100 kN, a central frequency of 5 Hz and a total period of $t = 2.0$ sec, is analyzed by attaching i) PML elements (see Fig. 3.4(b)), ii) infinite elements (simply replacing PML by CINPE4) and placing iii) dashpots on both bottom ($y = -110$ m) and side boundaries ($x = \pm 110$ m) with coefficients defined in Eq. 3.9. Similarly, here we use the 4-node plane-strain element (CPE4) with a size of 1 m by 1m for the interior domain. The same element size applies to the PML boundary. Again, an enlarged domain with a total size of 750 m $\times$ 1500 m, element size of 1 m $\times$ 1 m and fixed boundaries on the outer surface is constructed to be used for the reference solutions.

Table 3.1: Material properties of the three-layered soil deposits.

	Shear wave velocity V_s (m/s)	Poisson's Ratio	Density (kg/m^3)
Layer 1	200	0.3	2000
Layer 2	300	0.3	2000
Layer 3	400	0.3	2000

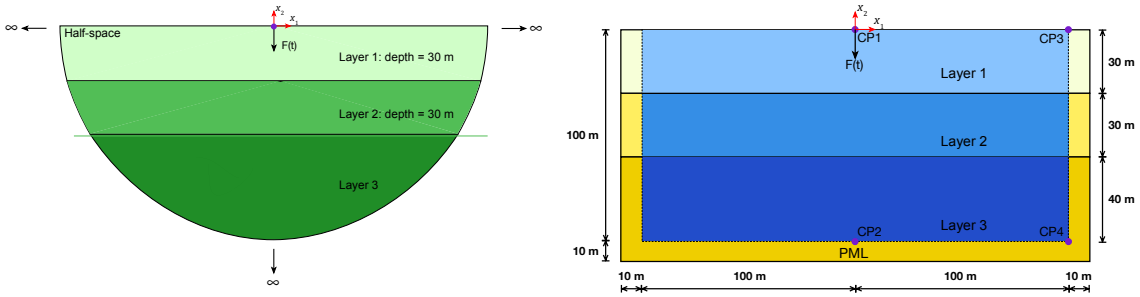

(a) Original problem (b) PML-truncated domain

Figure 3.4: Configuration of (a) the original 2D three-layered half-space problem and (b) the PML-truncated domain.

$$\text{For the bottom boundary } \rightarrow \begin{cases} c_x = \rho \cdot V_s \cdot A_b \\ c_y = \rho \cdot V_p \cdot A_b \end{cases} \tag{3.9a}$$

$$\text{For the side boundaries } \rightarrow \begin{cases} c_x = \rho \cdot V_p \cdot A_s \\ c_y = \rho \cdot V_s \cdot A_s \end{cases} \tag{3.9b}$$

where ρ is the density of the soil; A_b and A_s are the areas of the bottom and side soil elements that correspond to the dashpots used.

Fig. 3.5 shows the comparisons of vertical displacements for CP1 and CP2, both horizontal and vertical displacements for CP3 and CP4, obtained by using different ABCs, i.e., PML, dashpots and infinite element, against the enlarged domain solutions. As seen, the PML boundary behaves perfectly for all selected points, regardless of horizontal and vertical displacements. However, for dashpots and infinite elements, errors appear after the reflected waves enter the interior domain, which is because the outgoing waves are not perfectly absorbed. And due to the fact that these ABCs are sensitive to the angle of incidence, the discrepancies become more apparent for the corner point (i.e., CP4). Besides, the contour plots for the total displacement field at different times (i.e., $t = 0.4,\ 0.6,\ 0.8,\ 1.0,\ 1.5$ sec) obtained by using PML boundary, are presented in Fig. 3.6, which on the other hand, proves that the PML boundary absorbs all the outgoing waves.

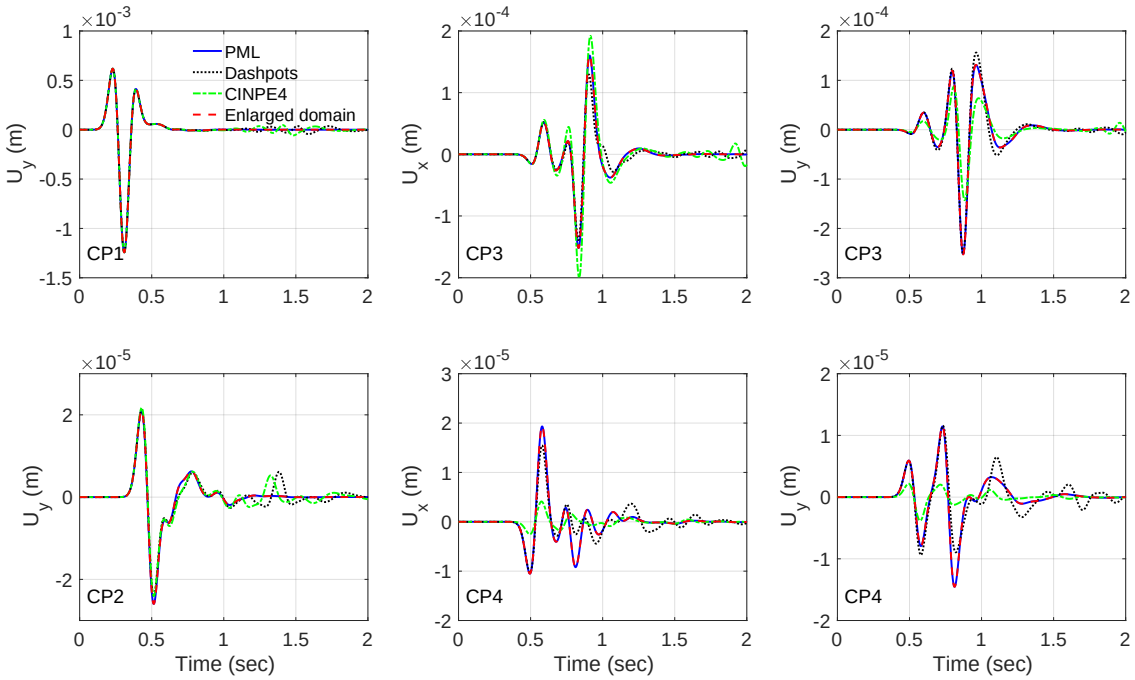

Figure 3.5: Comparisons of horizontal and vertical displacements for four selected points.

3.2.2.3 3D semi-infinite rod

A 3D semi-infinite long rod (see Fig. 3.7(a)) with uniform cross-section of 1 m $\times$ 1 m and homogeneous material properties (i.e., $V_s = 200$ m/s, $\nu = 0.3$, $\rho = 2000$ kg/m^3), excited by a longitudinal load using the function defined in Eq. 3.18 with an amplitude of 100 kN, a central frequency of 5 Hz and a total period of $t = 1.0$ sec, is analyzed by attaching i) PML elements (see Fig. 3.7(b)), ii) 3D infinite elements (CIN3D8) and placing iii) dashpots on the right end (i.e., $x = 30$ m) in x direction with coefficient $c_x = \rho V_s/2$. 8-node tri-linear element (C3D8) with a size of 1 m $\times$ 1 m $\times$ 1 m is used for the regular domain. The same element size applies to the PML boundary. Besides, the DOFs in y- and z-axis are fixed and hence only the x-DOF is free. Still, an enlarged domain with a total size of 1 m $\times$ 1 m $\times$ 400 m, element size of 1 m $\times$ 1 m $\times$ 1 m and fixed boundaries on the outer surface, is used for obtaining the reference solutions.

Fig. 3.8 shows the comparisons of x displacements for two selected points obtained by using different ABCs. The same, all three ABCs show perfect agreement for such 3D in

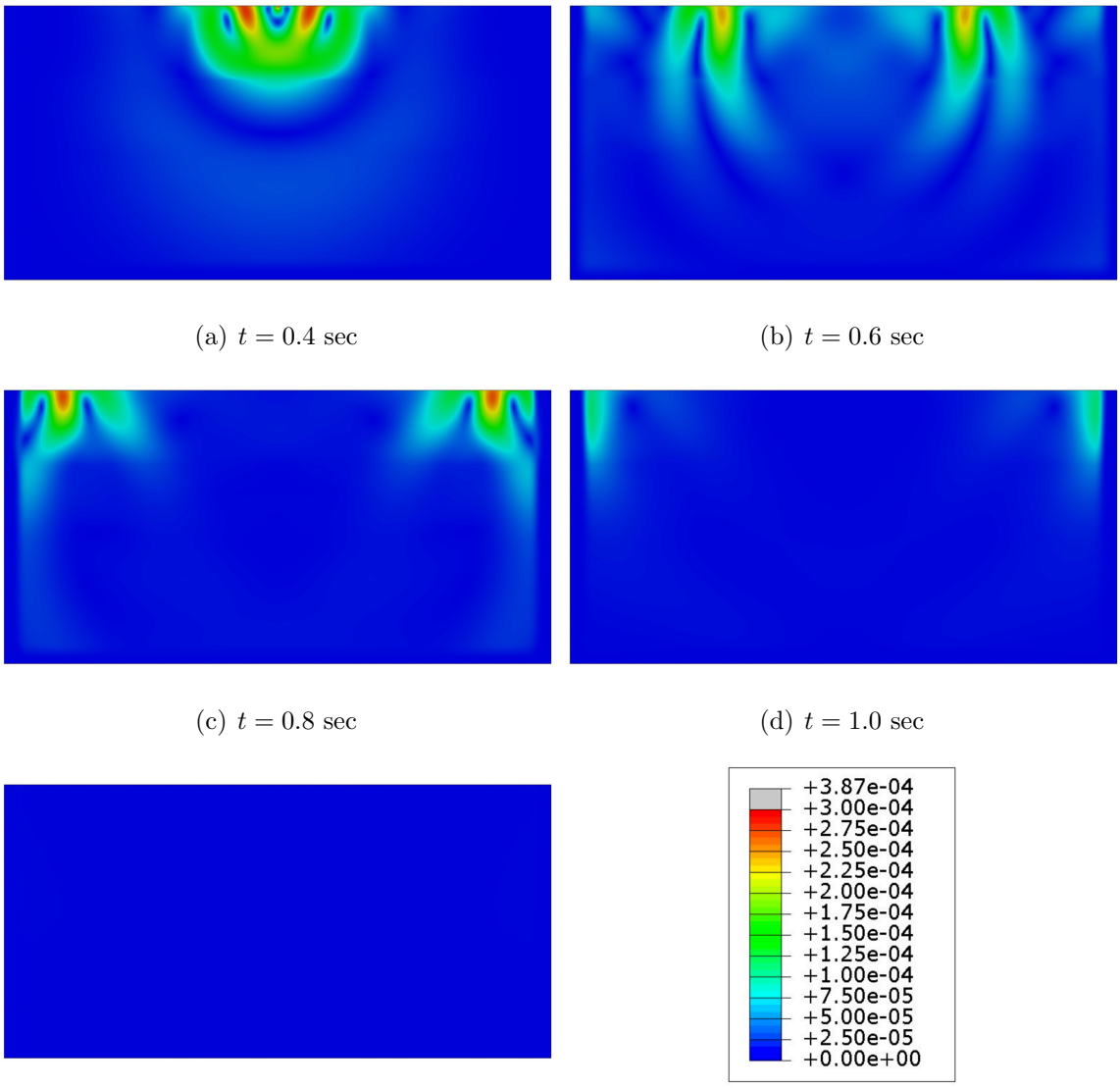

(a) $t = 0.4$ sec

(b) $t = 0.6$ sec

(c) $t = 0.8$ sec

(d) $t = 1.0$ sec

(e) $t = 1.5$ sec

(f) Colorbar

Figure 3.6: Contour plots of the total displacement field at different times obtained by using the PML boundary.

space, but in 1D alignment problem,.

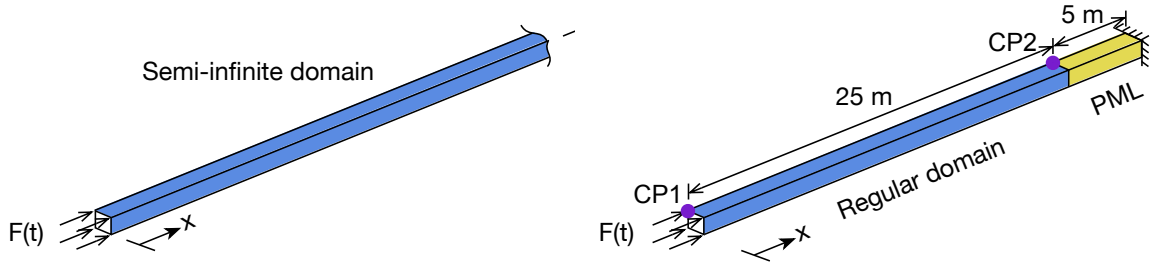

(a) Original problem (b) PML-truncated domain

Figure 3.7: Configuration of (a) the original 3D semi-infinite rod problem and (b) the PML-truncated domain.

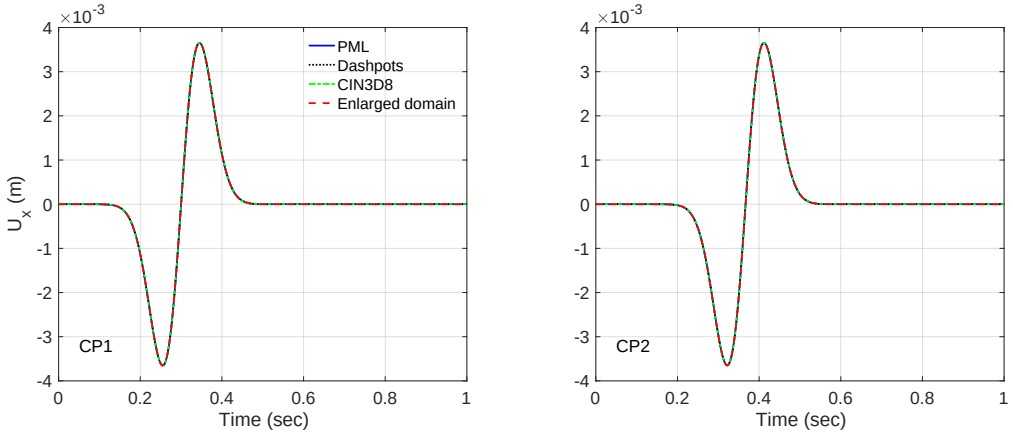

Figure 3.8: Comparisons of x displacements for two selected points.

3.2.2.4 3D homogeneous half-space

A 3D homogeneous half-space model (see Fig. 3.9) with material properties as $V_s = 1$ m/s, $\nu = 0.25$ and $\rho = 1$ kg/m^3, is subjected to a uniformly distributed vertical pressure on the grey area. The function of the applied pressure is defined in [105] with parameters as $t_d = 10$ sec, $\omega_f = 3$ rad/s. The resulting time history and Fourier amplitude plots are shown in Fig. 3.10. This problem is also analyzed by attaching i) PML elements, ii) 3D infinite elements (CIN3D8) and placing iii) dashpots on the outer surface with coefficients defined in Eq. 3.9. 8-node tri-linear element (C3D8) with a size of 0.1 m $\times$ 0.1 m $\times$ 0.1 m is used for the interior domain and $\Delta\ t = 0.05$ sec is used for the time step. The same element

size applies to the PML boundary. Further, in order to investigate the performance of the PML and other ABCs, an enlarged domain with more than 10 million elements are required for such problem [111]. Due to the limitation of the maximum number of elements that the software imposes, it is however impossible to be done in ABAQUS. Therefore here we adopt the reference solutions from [108].

Fig. 3.11 shows the computed vertical displacements for the center and corner points on the grey surface. Still, the PML displays obviously superb behavior compared with dashpots and infinite elements. This example demonstrates that the PML can shrink the computational domain as close to the loading area as possible, and maintains the same excellent performance.

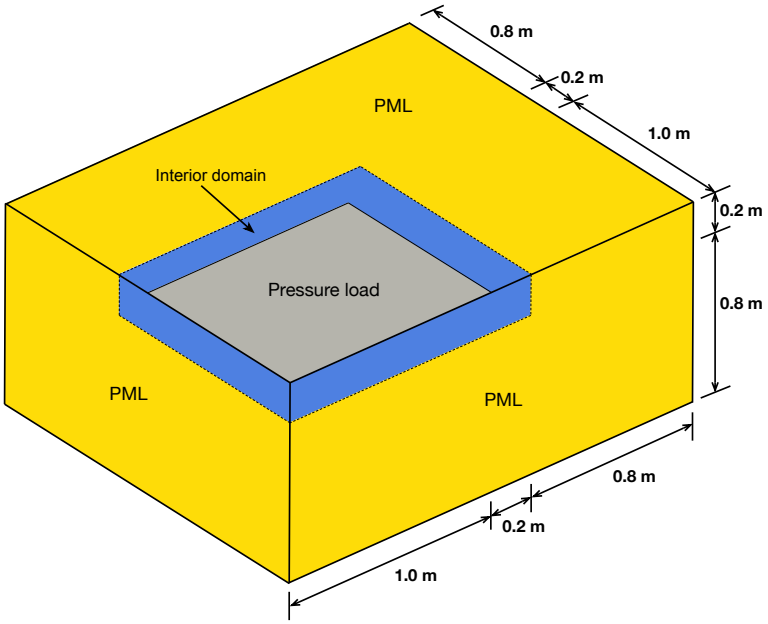

Figure 3.9: Quarter model of a PML-truncated 3D homogeneous half-space model.

3.2.2.5 3D three-layered half-space

A 3D three-layered half-space case (see Fig. 3.12) with material properties summarized in Table. 3.1, excited by a vertical point load using the function defined in Eq. 3.18 with an amplitude of 100 kN, a central frequency of 5 Hz a total simulation time of $t = 10.0$ sec and $\Delta t = 0.001$ sec, is analyzed by using PML boundary. 8-node tri-linear element (C3D8) with

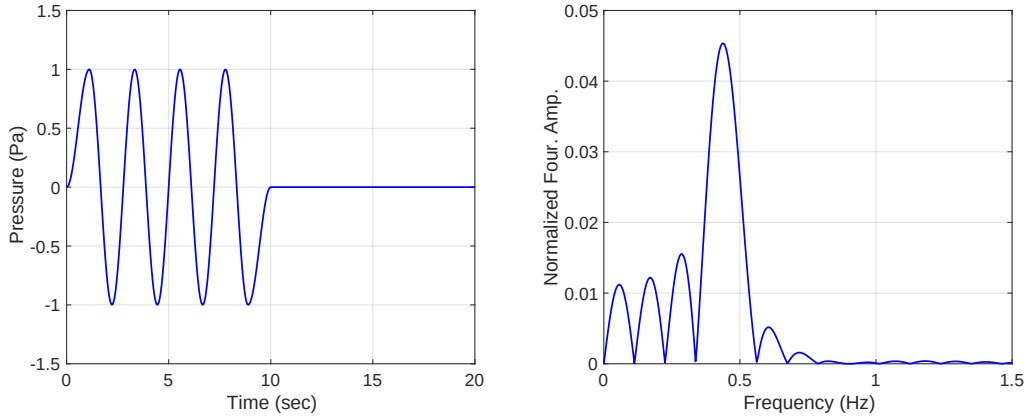

Figure 3.10: Time history and its Fourier amplitude plots for the applied surface pressure.

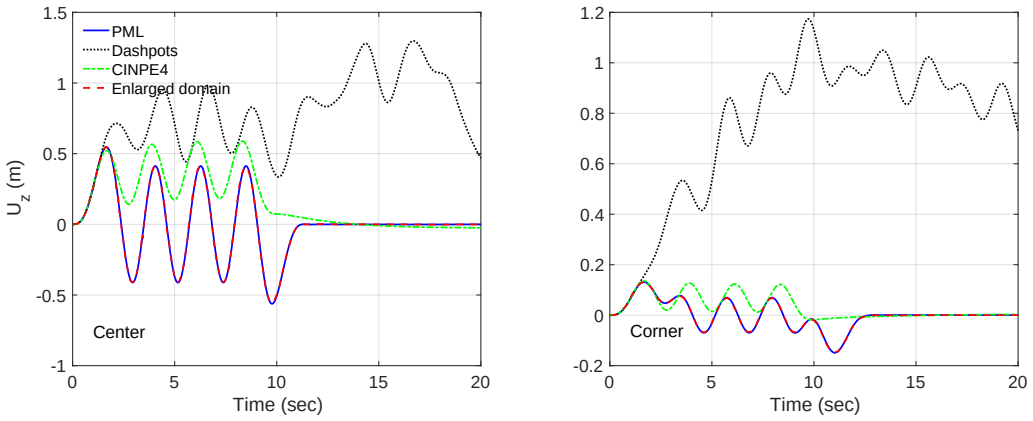

Figure 3.11: Comparisons of z displacements for center and corner points.

a size of 1 m $\times$ 1 m $\times$ 1 m is used for the interior domain and the same element size for the PML elements.

Because for such a problem there are no reference solutions in literature and we are unable to conduct an enlarged domain analysis in ABAQUS, we utilize this model to examine the long-time stability of the implemented PML. As we know, some other PML formulations may suffer long-time instability issue [120]. This simulation has a total of $T/\Delta t = 10/0.001 = 10000$ steps, which is considered adequate to examine the stability of the model. The time histories of displacements of six selected points are shown in Fig. 3.13. The locations of CP1, CP2, CP3 and CP4 are indicated in Fig. 3.12. CP5 and CP6 have the coordinates as $(25, 25, 0)$ and $(25, 25, -25)$, respectively. And the contour plots of the total displacement field at different times are also presented in Fig. 3.14. It can be observed that the whole model becomes silent after around $t = 0.7$ sec, and there is no visible reflection at the interface of the interior domain and the PML boundary.

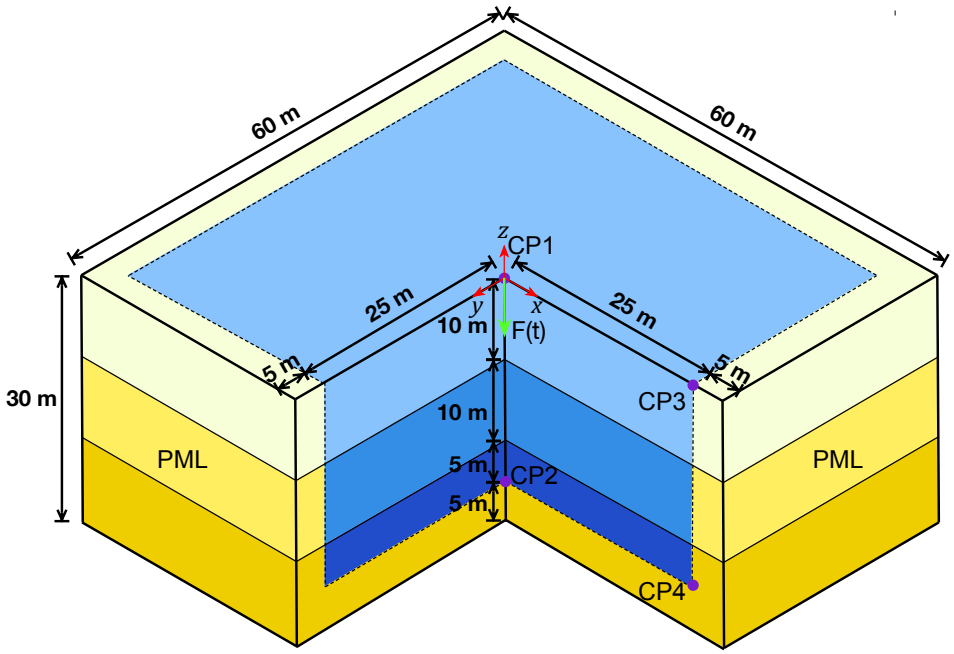

Figure 3.12: Configuration of the PML-truncated 3D three-layered half-space model.

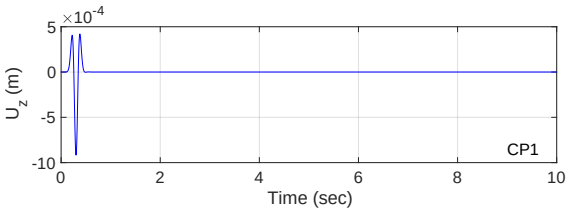

(a) U_z at CP1

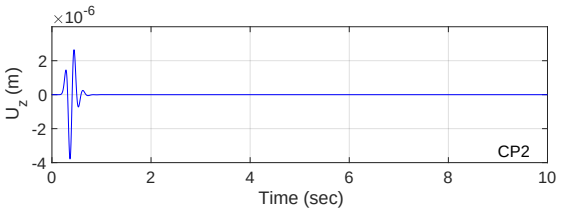

(b) U_z at CP2

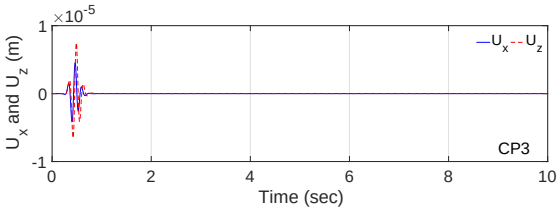

(c) U_x and U_z at CP3

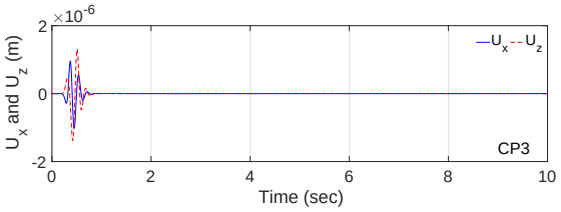

(d) U_x and U_z at CP4

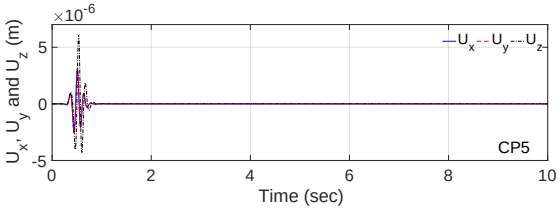

(e) U_x, U_y and U_z at CP5

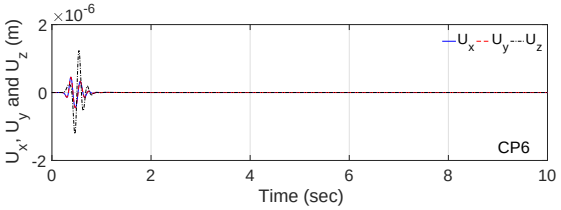

(f) U_x, U_y and U_z at CP6

Figure 3.13: Time histories of displacements of six selected points.

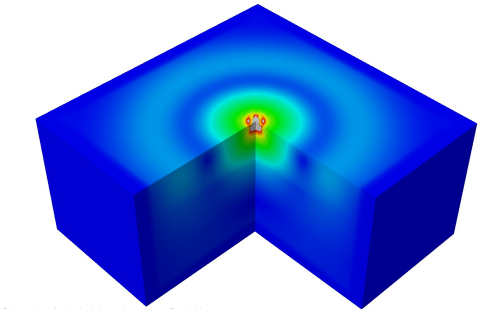

(a) $t = 0.4$ sec

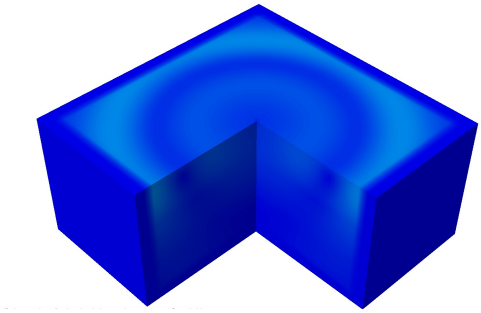

(b) $t = 0.5$ sec

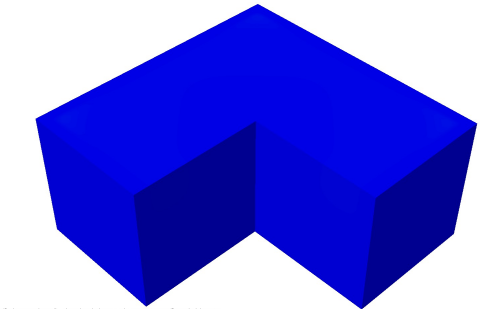

(c) $t = 0.7$ sec

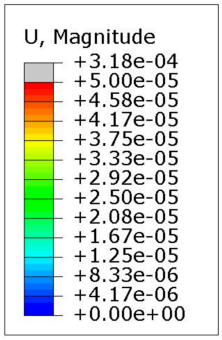

(d) Colorbar

Figure 3.14: Contour plots of the total displacement field at different times.

3.3 Domain Reduction Method (DRM)

DRM is a two-step finite element procedure proposed by Bielak et al. [117] for modeling the seismic responses of heterogeneous subdomains. The most appealing advantage of DRM is that it enables the conversion of the half-space problem to an equivalent one in which the effects of incoming waves due to remote excitations are translated into equivalent nodal forces that are applied inside a domain that is truncated by ABCs.

3.3.1 Implementation

In DRM, the equivalent nodal force vector is computed using Eq. 5.3 per [117] and applied to the nodes located at a single layer of elements that form the boundary between the ABCs and the near-field domain as shown in Fig. 3.15(a),

$$\mathbf{P}^{eff} = \begin{bmatrix} \mathbf{P}_i^{eff} \\ \mathbf{P}_b^{eff} \\ \mathbf{P}_e^{eff} \end{bmatrix} = \begin{bmatrix} \mathbf{0} \\ -\mathbf{M}_{be}^{\Omega+}\ddot{\mathbf{u}}_e^0 - \mathbf{C}_{be}^{\Omega+}\dot{\mathbf{u}}_e^0 - \mathbf{K}_{be}^{\Omega+}\mathbf{u}_e^0 \\ +\mathbf{M}_{eb}^{\Omega+}\ddot{\mathbf{u}}_b^0 + \mathbf{C}_{eb}^{\Omega+}\dot{\mathbf{u}}_b^0 + \mathbf{K}_{eb}^{\Omega+}\mathbf{u}_b^0 \end{bmatrix} \tag{3.10}$$

where the subscripts $_i$, $_b$ and $_e$ refer to the nodes inside the domain of interest, along the inside and outside boundary of the one layer of elements, respectively. The terms $\mathbf{u}^0$ and $\mathbf{P}^{eff}$ respectively denote the free-field displacements and forces along nodes of the one layer of elements. $\mathbf{M}^{\Omega+}$, $\mathbf{C}^{\Omega+}$ and $\mathbf{K}^{\Omega+}$ are the mass, damping and stiffness matrices assembled for only the single layer of elements that form the interface between the exterior and interior domains. In this study, we 1) use analytical solutions (if exist) or perform 1D site response analysis to obtain the free-field response, 2) extract the nodes' coordinates and meshes' connectivity information from ABAQUS input file, 3) use the information and the computed free-field response in step 1) to compute the $\mathbf{M}^{\Omega+}$, $\mathbf{C}^{\Omega+}$, $\mathbf{K}^{\Omega+}$ matrices, and $\mathbf{P}^{eff}$ vector, 4) insert the computed $\mathbf{P}^{eff}$ vectors, that are considered as concentrated force time-history functions for all DRM nodes, into the ABAQUS input file. A routine has been developed in MATLAB [82] to perform the aforementioned tasks.

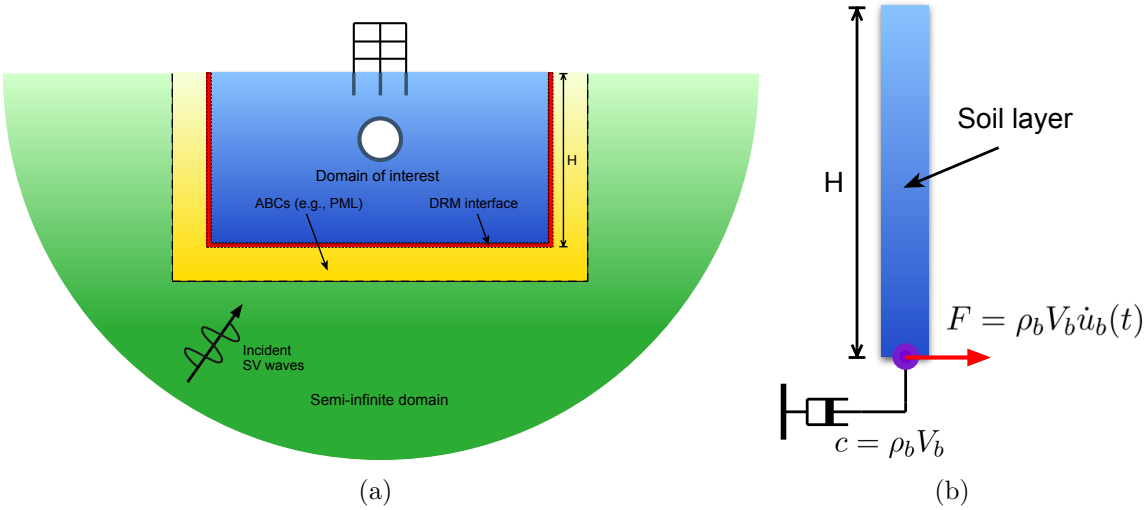

Figure 3.15: (a) Configuration of modeling semi-infinite domain by using DRM and ABCs, and (b) equivalent 1D site response analysis model for evaluation of free-field response for DRM interface.

As for the inclined incident SV waves, it is extremely difficult to calculate free-field response by conducting 1D site response analysis and analytical solutions are only available for the homogeneous half-space case in time domain. Here we adopt the time domain analytical solutions for the inclined SV-wave propagation in a homogeneous flat half-plane derived by [121]. The displacement field solution is given in Eq. 3.11

$$\begin{aligned}\begin{bmatrix} u_{x'}(x',z) \\ u_z(x',z) \end{bmatrix} = {} & U_s^i \begin{bmatrix} +\cos\theta_s \\ +\sin\theta_s \end{bmatrix} f\Big(-\frac{x'}{c_s}\sin\theta_s + \frac{z}{c_s}\cos\theta_s + t\Big) + \\ & U_s^r \begin{bmatrix} -\cos\theta_s \\ +\sin\theta_s \end{bmatrix} f\Big(-\frac{x'}{c_s}\sin\theta_s - \frac{z}{c_s}\cos\theta_s + t\Big) + \\ & U_p^r \begin{bmatrix} +\sin\theta_p \\ +\cos\theta_p \end{bmatrix} f\Big(-\frac{x'}{c_p}\sin\theta_p - \frac{z}{c_p}\cos\theta_p + t\Big)\end{aligned} \tag{3.11}$$

where $u_{x'}$ and u_z are the displacement fields in horizontal and vertical directions, respectively. Fig. 3.16 shows the schematic propagation of the inclined incident SV wave in a flat homogeneous half-space in 2D and 3D domains. Eq. 3.11 is originally derived for plane-wave,

but it can be easily converted to 3D formulation, by using the knowledge of transformation of coordinate system (see Eq. 3.12 for details). U_s^i (usually defined as 1), U_s^r and U_p^r are the amplitudes for the incident SV wave, reflected SV wave and reflected P wave fronts, respectively, which are defined as,

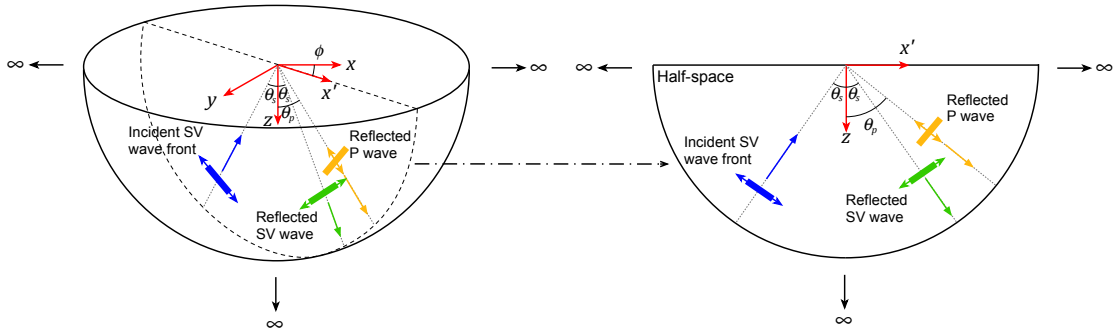

Figure 3.16: Schematic propagation of the inclined incident SV wave in a flat homogeneous half-space in 2D and 3D domains.

$$\mathbf{u} = \begin{bmatrix} u_x \\ u_y \\ u_z \end{bmatrix} = \mathbf{\Phi}^T \mathbf{u}' = \begin{bmatrix} \cos\phi & \sin\phi & 0 \\ -\sin\phi & \cos\phi & 0 \\ 0 & 0 & 1 \end{bmatrix}^T \begin{bmatrix} u_{x'} \\ u_{y'} = 0 \\ u_z \end{bmatrix} \tag{3.12}$$

$$U_s^i = A_s^i k_s,\ U_s^r = A_s^r k_s,\ U_p^r = A_p^r k_p \tag{3.13}$$

where A_s^r and A_p^r have relationships with A_s^i as,

$$A_s^r = \frac{\sin(2\theta_s)\sin(2\theta_p) - k^2\cos^2(2\theta_s)}{\sin(2\theta_s)\sin(2\theta_p) + k^2\cos^2(2\theta_s)} A_s^i \tag{3.14a}$$

$$A_p^r = \frac{-2k^2\sin(2\theta_s)\cos(2\theta_s)}{\sin(2\theta_s)\sin(2\theta_p) + k^2\cos^2(2\theta_s)} A_s^i \tag{3.14b}$$

and $k = c_p/c_s$, and c_s and c_p are the shear and compressional wave velocities. k_p and k_s in

Eq. 3.13 are shear and compressional wavenumbers, which are defined as,

$$k_s = \frac{\omega}{c_s},\ k_p = \frac{\omega}{c_p} \tag{3.15}$$

where ω is the natural frequency of the soil. By combining Eq. 3.13-3.15, we have

$$U_s^r = \frac{\sin(2\theta_s)\sin(2\theta_p) - k^2\cos^2(2\theta_s)}{\sin(2\theta_s)\sin(2\theta_p) + k^2\cos^2(2\theta_s)} U_s^i \tag{3.16a}$$

$$U_p^r = \frac{-2k^2\sin(2\theta_s)\cos(2\theta_s)}{\sin(2\theta_s)\sin(2\theta_p) + k^2\cos^2(2\theta_s)} \frac{C_s}{C_p} U_s^i \tag{3.16b}$$

Besides, θ_s is the angle of SV incidence, which is also equivalent to the angle of reflected SV-wave, and θ_p is the angle of reflected P-wave that can be obtained based on Snell's law:

$$\theta_p = \arcsin\left(\frac{c_p}{c_s}\sin\theta_s\right) \tag{3.17}$$

Function $f = f(t)$ in Eq. 3.11 is any time-dependent function that determines the temporal variation of the incident wave.

3.3.2 Verification

In the present study, the DRM method is implemented in ABAQUS [114], and the accuracy of this implementation is verified by comparing the numerical results obtained from DRM and analytical solutions (for homogeneous cases, vertical and inclined incident SV waves) and single-soil-column simulations (for heterogeneous cases, vertically propagated SV waves). In these verification problems, a single soil column that has an identical height and material properties as the full DRM model (see Fig. 3.15(b)) is used in 1D wave propagation analyses to obtain free-field ground responses. Where ρ_b and V_b are the density and the shear wave velocity of the elastic bedrock, respectively; $u_b(t) = 2u_I(0,t)$ and u_I is the incident wave function.

For all the verification problems, we use Ricker pulse defined in Eq. 3.18, with the selected parameters as $A_{\text{Ricker}} = 1e^{-4}$ m, $f_{\text{Ricker}} = 5$ Hz and $t_0 = 0.3$ sec, as the incident wave function. And a total step equals to 1 sec with $\Delta t = 0.001$ sec is used. Corresponding displacement, velocity and acceleration time histories and Fourier amplitude are shown in Fig. 3.17. Besides, A Northridge earthquake motion with duration equals to 28.6 sec and $\Delta t = 0.005$ sec, is adopted for the case **DRM-2D-Hetero-Ver** (see Table.3.2 for definition) to verify the accuracy of the DRM when earthquake motion is applied. Its displacement time histories and Fourier amplitude are shown in Fig. 3.18.

$$u(\tau) = A_{\text{Ricker}}\Big[1 - (2\pi f_{\text{Ricker}}\tau)^2\Big]e^{(-\pi f_{\text{Ricker}}\tau)^2},\ \tau = t - t_0 \tag{3.18}$$

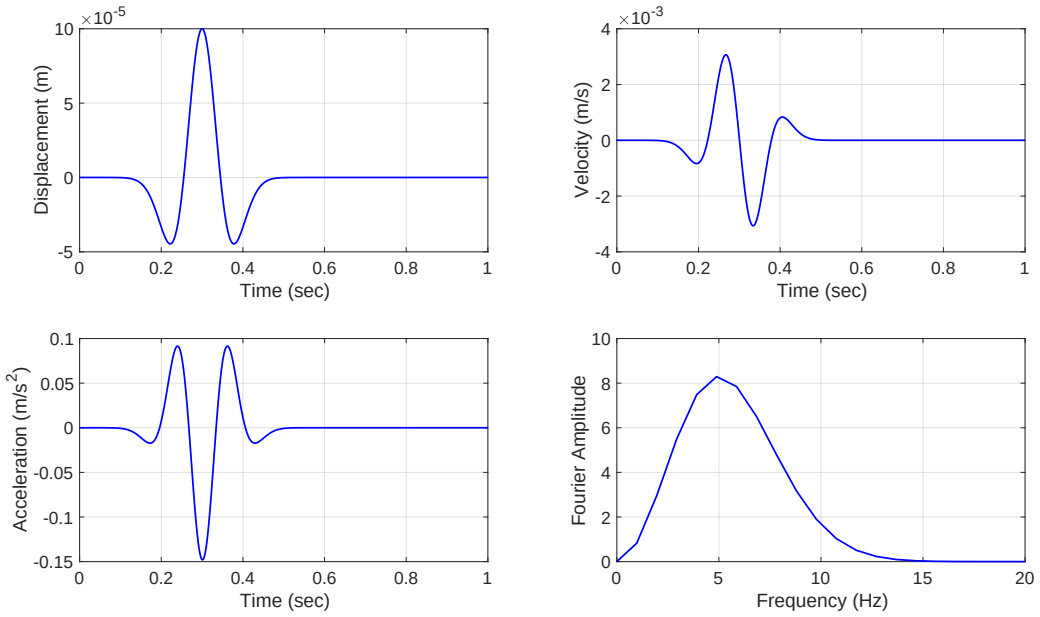

Figure 3.17: Displacement, velocity, acceleration and Fourier amplitude plots for the applied Ricker pulse.

In the numerical simulations, we verify DRM in a total of 5 different cases. 3 for 2D and 2 for 3D domains, with 1) inclined incident SV waves in homogeneous media and 2) vertically propagated SV wave in heterogeneous media (one Ricker pulse and one earthquake motion). For all 5 cases, uniform density $\rho = 2000$ kg/m^3 and Poisson's ratio $\nu = 0.3$ are selected. And for homogeneous cases, the shear wave velocity $V_s^{\text{homo}} = 200$ m/s is used. For

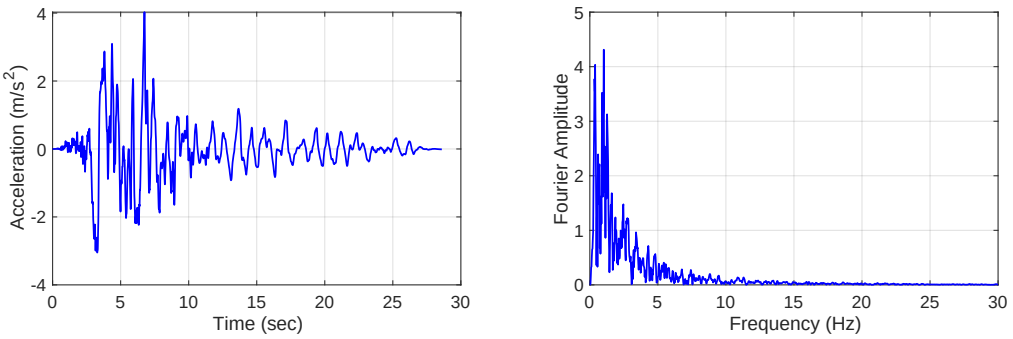

Figure 3.18: Acceleration and Fourier amplitude plots for the applied earthquake motion.

heterogeneous cases, we adopt a continuous function as $V_s^{\text{hetero}} = V_H\left[b + (1-b)\frac{z}{H}\right]^n$, where $b = (V_0/V_H)^{1/n}$, $V_0 = 200$ m/s, $V_H = 400$ m/s, $n = 0.5$, $H = 25$ m, z is the downward vertical coordinate measured from the soil surface; and V_0 and V_H are shear wave velocities at $z = 0$ and $z = H$, respectively. All the necessary information for DRM verification problems is summarized in Table. 3.2 for a more transparent view. In the full DRM models (see Fig. 3.19), with a uniform element size of 1 m, 98 4-node quadrilateral plane strain elements (CPE4) and 7204 8-node linear isoparametric elements (C3D8) are used for the single layer of elements for 2D and 3D models, respectively, and a thickness of 5 m PML are attached to the interior domains to absorb the noises coming from numerical imprecision.

Figs. 3.20-3.24 displays the displacement results for the three selected points (see Fig.3.19) obtained using DRM, analytical solutions and the single soil column modeled as shown in Fig. 3.15(b). As seen, the DRM yields a near-perfect match compared to both analytical solutions and the single-soil-column results, for both homogeneous and heterogeneous soil media, vertical and inclined incident SV waves, and in 2D and 3D domains.

3.4 Applications

After the successful implementation and verification of both DRM and PML in ABAQUS, in this section, we present some applications that can be conducted by using the PML or coupled DRM-PML system, e.g., computing the impedance functions and investigating the effects of angle of incidence.

Table 3.2: Five verification problems of the DRM implementation.

Dimension	Label	Definition	V_s	Angle of incidence
2D	**DRM-2D-Homo-Inc**	Homogeneous soil layer with inclined incident SV wave in 2D domain.	200 m/s	25°
	DRM-2D-Hetero-Ver (i. Ricker pulse, ii. earthquake motion)	Heterogeneous soil layer.	$V_s = V_H\left[b + (1-b)\frac{z}{H}\right]^n$, where $b = (V_0/V_H)^{1/n}$, $V_0 =$ 200 m/s, $V_H =$ 400 m/s, $n = 0.5$, $H =$ 25 m.	0°
3D	**DRM-3D-Homo-Inc**	Homogeneous soil layer with inclined incident SV wave in 3D domain.	200 m/s	$\theta_s = 25°$ and $\phi = 45°$
	DRM-3D-Hetero-Ver	Heterogeneous soil layer with vertical incident SV wave in 3D domain.	$V_s = V_H\left[b + (1-b)\frac{z}{H}\right]^n$, where $b = (V_0/V_H)^{1/n}$, $V_0 =$ 200 m/s, $V_H =$ 400 m/s, $n = 0.5$, $H =$ 25 m.	0°

Note: for all 5 cases, the same density $\rho = 2000$ kg/m^3 and Poisson's ratio $\nu = 0.3$ are selected. The Ricker pulse defined in Eq. 3.18, with $A_{\text{Ricker}} = 1e^{-4}$ m, $f_{\text{Ricker}} = 5$ Hz and $t_0 = 0.3$ sec, is used for the incident wave function.

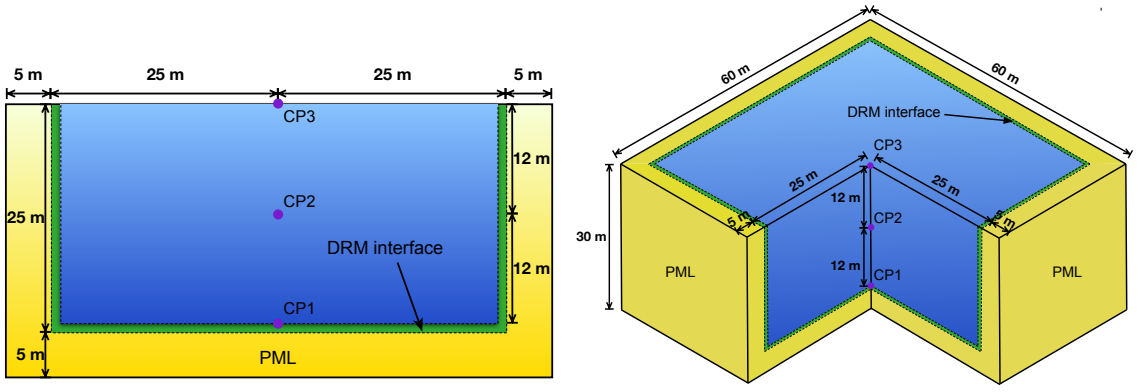

(a) (b)

Figure 3.19: Numerical models constructed for DRM verification problems in (a) 2D, and (b) 3D domains.

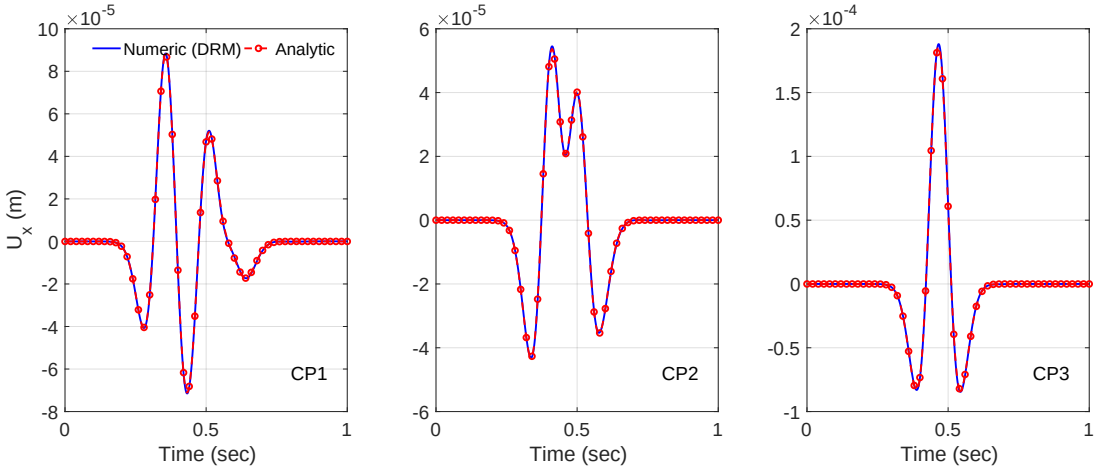

(a) Horizontal displacement

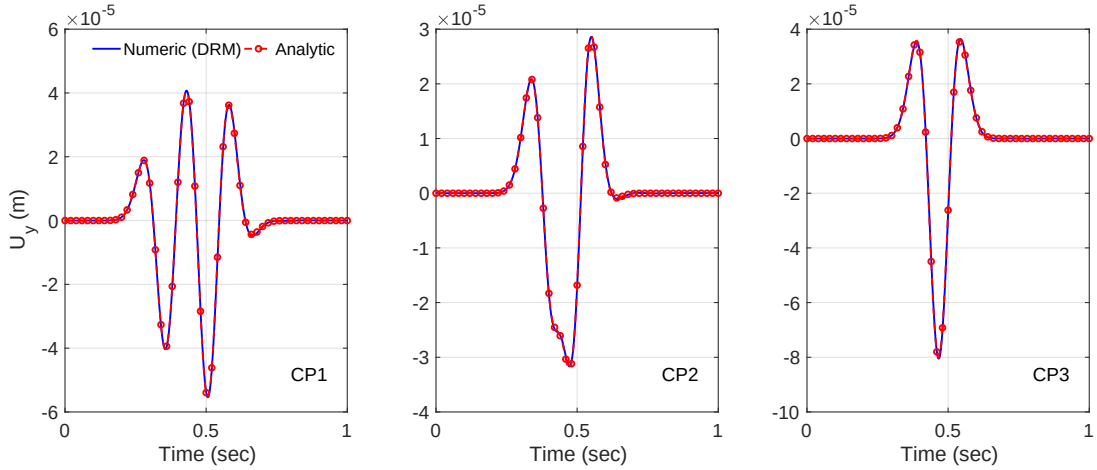

(b) Vertical displacement

Figure 3.20: Comparisons of horizontal and vertical displacement results for the case **DRM-2D-Homo-Inc**.

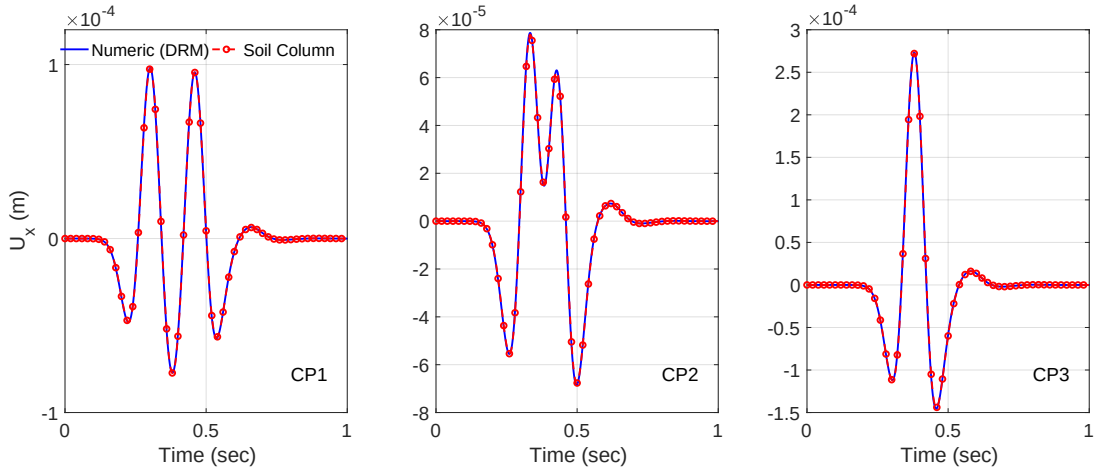

Figure 3.21: Comparisons of horizontal displacement results for the case **DRM-2D-Hetero-Ver** (Ricker Pulse).

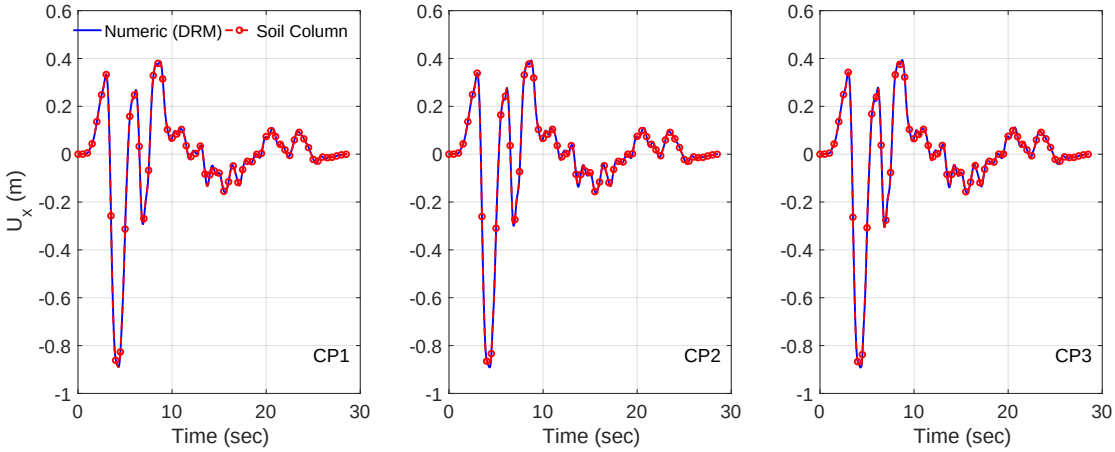

Figure 3.22: Comparisons of horizontal displacement results for the case **DRM-2D-Hetero-Ver** (earthquake motion).

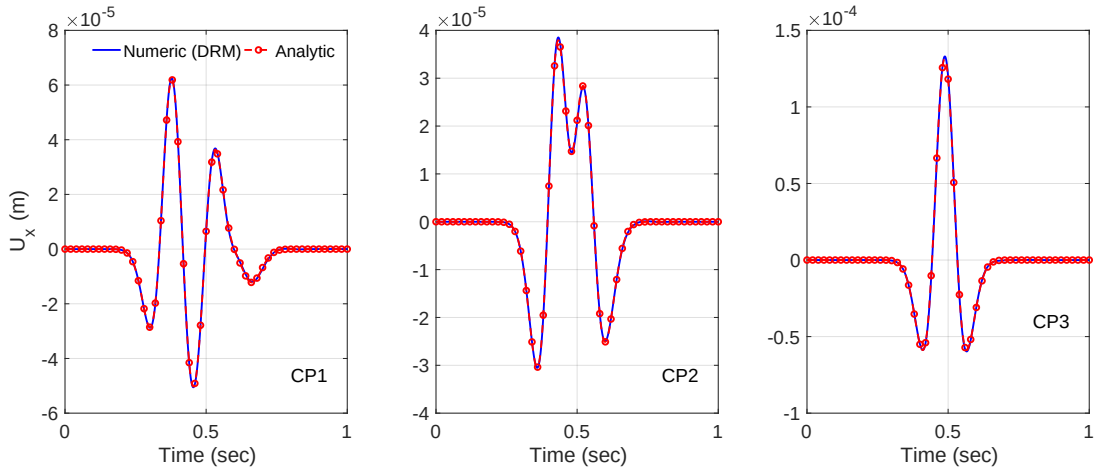

(a) U_x

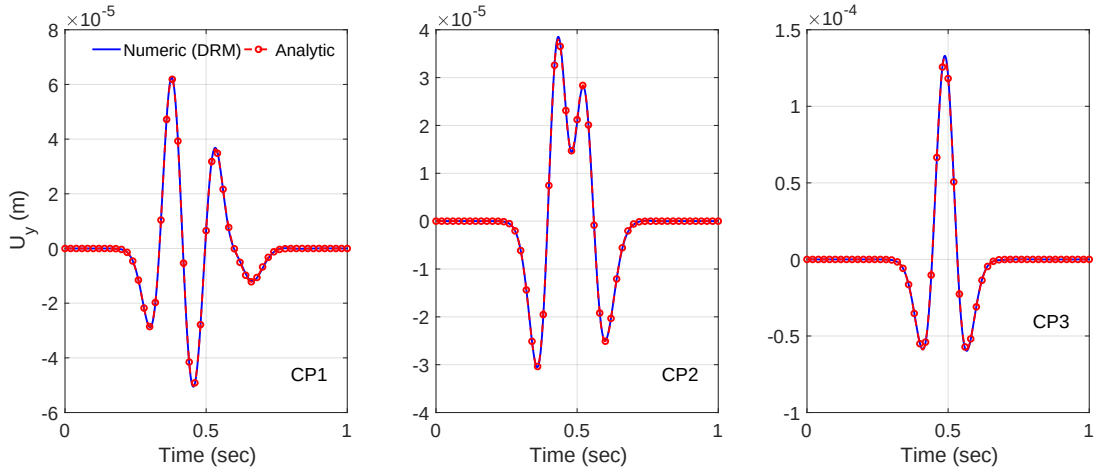

(b) U_y

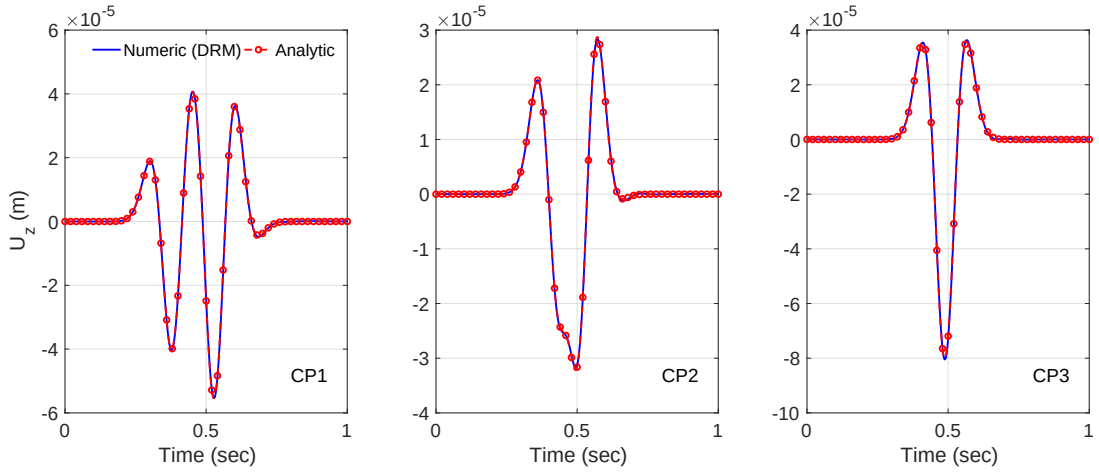

(c) U_z

Figure 3.23: Comparisons of U_x, U_y and U_z for the case **DRM-3D-Homo-Inc**.

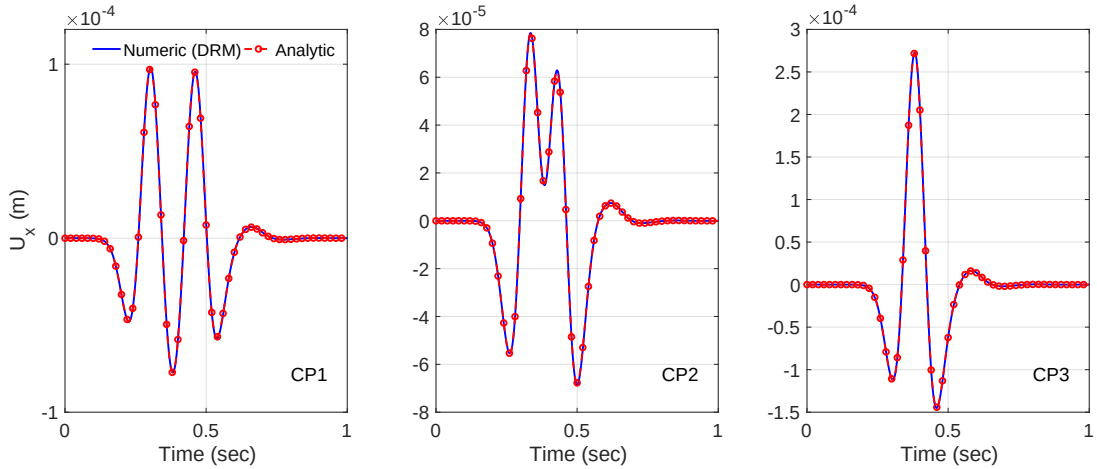

Figure 3.24: Comparisons of U_x for the case **DRM-3D-Hetero-Ver**.

3.4.1 Impedance functions

It is well known that the substructure method is a computationally efficient alternative where a reduced-order model for the near-field is utilized [5, 122, 123]. However, the impedance function of the near-field soil-foundation system is the ingredient of the substructure method. The impedance function represents the complex-valued frequency-dependent stiffness matrix, where its real part corresponds to the stiffness and mass inertia effect of the soil and the imaginary part accounts for radiation damping.

In this section, we follow the procedures mentioned by Seylabi et al. [83] to extract the impedance functions with time-domain analysis in ABAQUS for four different problems. And in the subsequent analyses, we always apply the Ricker pulse (see Eq. 3.18) with parameters as $A_{\text{Ricker}} = 1e^{-4}$ m, $f_{\text{Ricker}} = 10$ Hz to be the input displacements. A total simulation time $T = 0.5$ sec and stepsize $\Delta t = 0.001$ sec are used. For 2D problems, we use 4-node quadrilateral plane-strain element (CPE4) with element size of 0.5 m $\times$ 0.5 m for the interior domain, and for 3D problems, we adopt 8-node tri-linear solid element (C3D8) with element size of 0.5 m $\times$ 0.5 m $\times$ 0.5 m. The PML elements always keep the same element size as the regular elements.

3.4.1.1 2D rigid strip surface foundation

The compliance function (i.e., inverse matrix of the impedance function) of the rigid strip foundation shown in Fig. 3.25(a), resting on the surface of an elastic homogeneous half-space, with material properties as $E = 1$ GPa, $\nu = 0.25$ and $\rho = 2000$ kg/m^3, is computed. The reference analytical solution to this problem is provided by Luco and Westmann [124]. As shown in Fig. 3.26, the numerically-evaluated compliance functions show an excellent

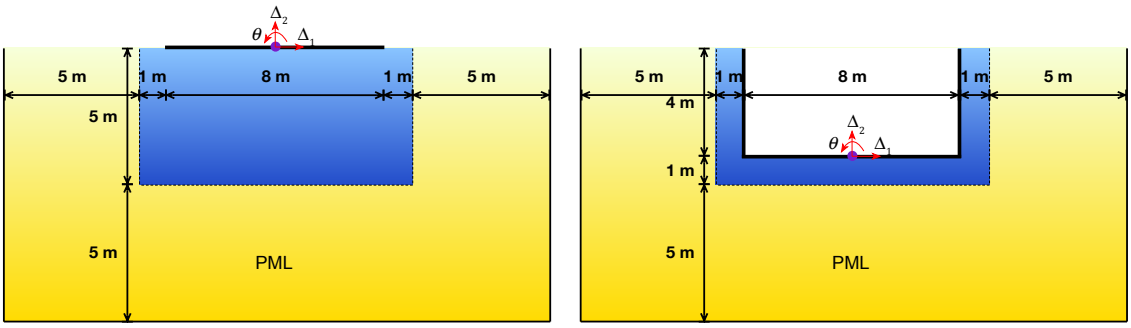

(a) Original problem (b) PML-truncated domain

Figure 3.25: Configuration of (a) the 2D rigid strip surface foundation problem and (b) the 2D embedded rigid foundation problem.

agreement with the reference solutions for both diagonal terms (i.e., C_{HH}, C_{VV}, and C_{MM}) and the coupled term (i.e., C_{HM}/C_{MH}). B denotes the half-width of the foundation.

3.4.1.2 2D embedded rigid foundation

The impedance function of a rigid foundation embedded in a homogenous soil shown in Fig. 3.25(b), with identical material properties as the previous case, is computed. The reference solution to this problem is due to Wang and Rajapakse [125], obtained by using the indirect boundary integral equation method. Fig. 3.27 shows the numerically-computed impedance functions versus the reference solution, which again are in good agreements.

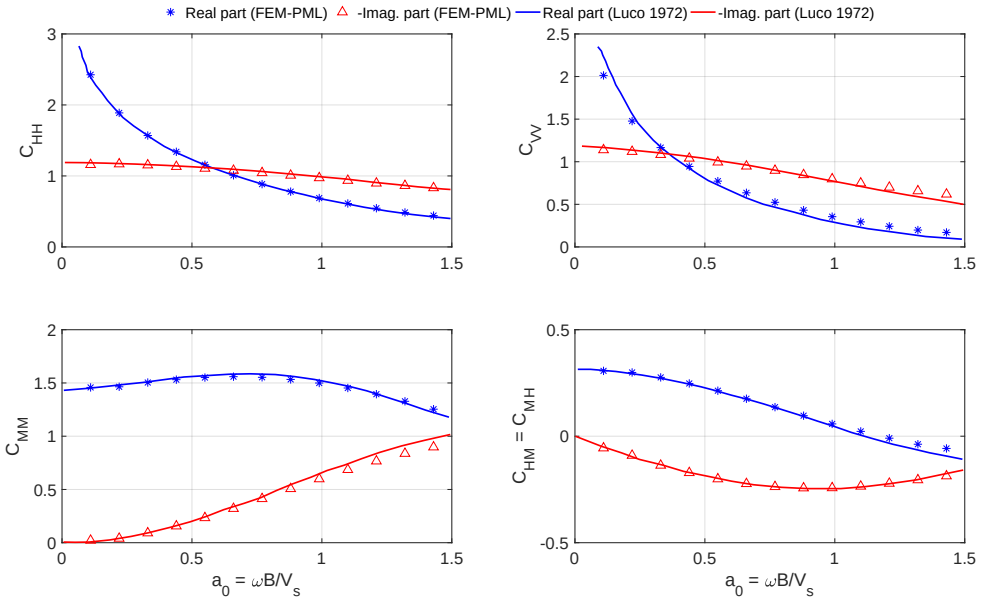

Figure 3.26: Compliance function of a rigid strip surface foundation computed using FEM-PML versus analytical solution.

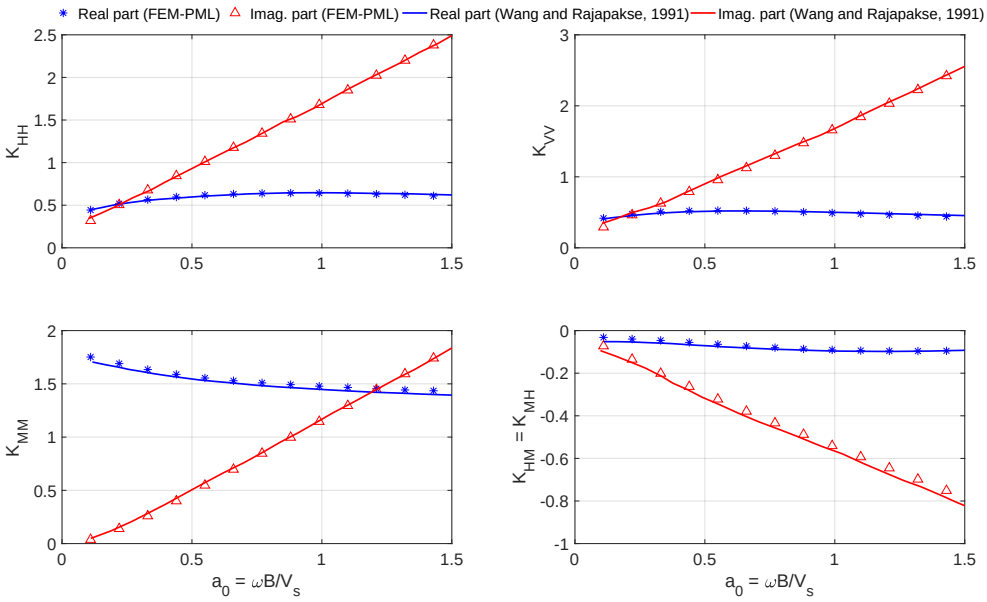

Figure 3.27: Compliance function of an embedded rigid foundation computed using FEM-PML versus reference solution.

3.4.1.3 3D rigid circular plate surface foundation in homogeneous media

The compliance function of the rigid circular plate foundation shown in Fig. 3.28, resting on the surface of an elastic homogeneous half-space, with material properties as $E = 1$ GPa, $\nu = 1/3$ and $\rho = 2000$ kg/m^3, is computed. The reference analytical solution to this problem is proposed by Luco and Westmann [126]. As shown in Fig. 3.28, by using the implemented

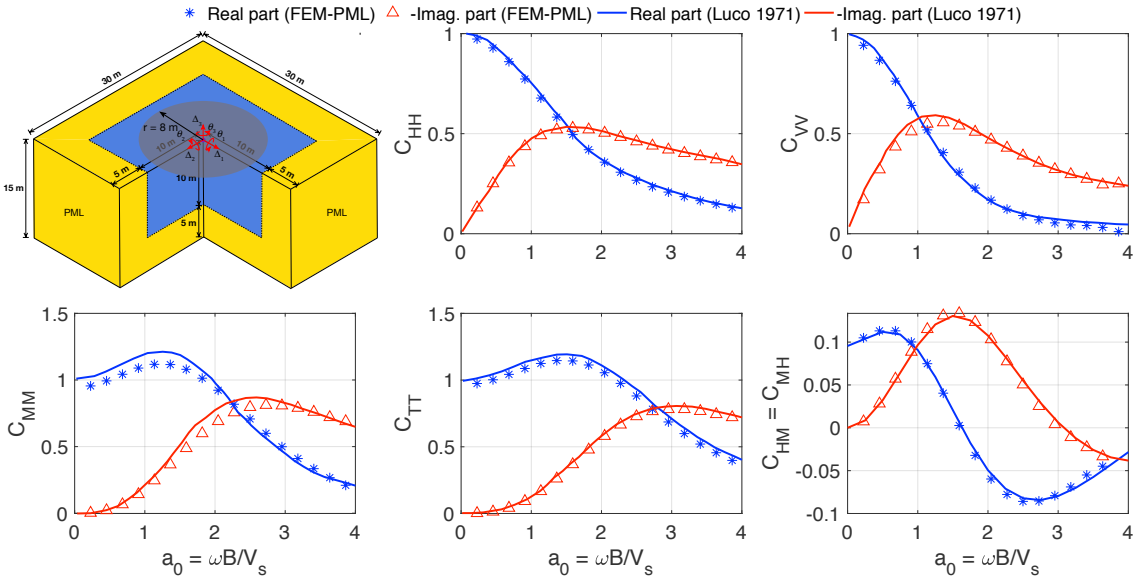

Figure 3.28: Compliance function of a rigid circular plate surface foundation in homogeneous media computed using FEM-PML versus reference solution.

3D PML boundary, the numerically-calculated compliance functions match the analytical solutions very well, for all horizontal, vertical, rocking and torsional results. Here $B = 8$ m represents the radius of the rigid plate.

3.4.1.4 3D rigid circular plate surface foundation in two-layered half-space media

To test the performance of the FEM-PML method in layered media, we also compute the impedance function of a 3D rigid circular plate on the surface of a two-layered half-space shown in Fig. 3.29. The material properties of two soil layers are included in Table. 3.4. The analytical solution due to Luco[127] only provides the horizontal, vertical and rocking

terms (i.e., K_{HH}, K_{VV} and K_{MM}). For the torsional term (K_{TT}), we compare our result with a semi-analytical solution proposed by Lin et al.[128]. And for the coupled term ($K_{HM} = K_{MH}$), we just include our result because no analytical/semi-analytical solution has been found in the literature. In all cases, FEM-PML method could reproduce the reference solutions with high accuracy.

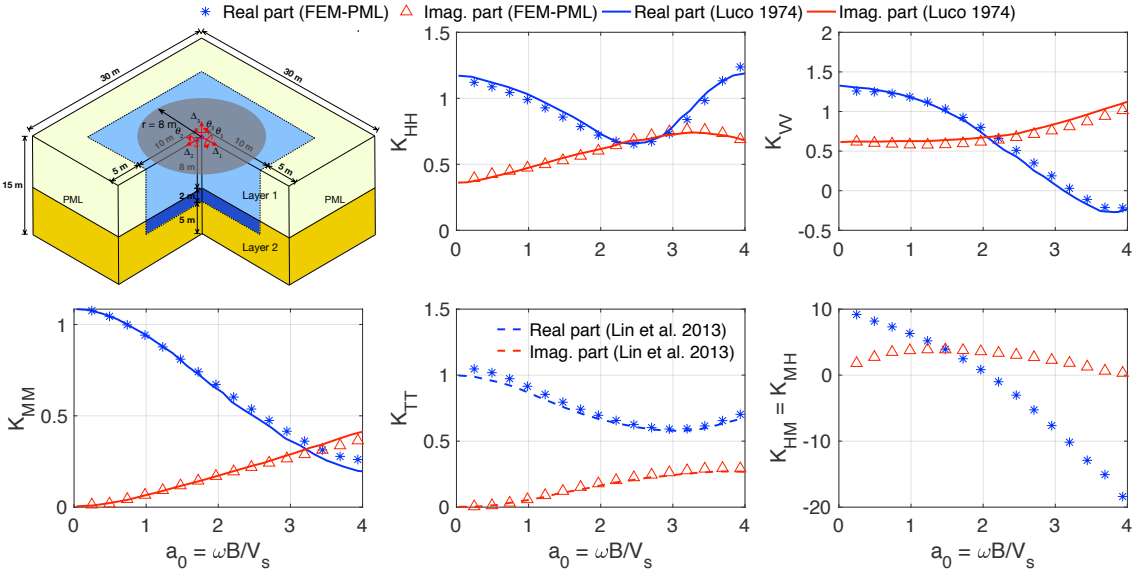

Figure 3.29: Compliance function of a rigid circular plate surface foundation in two-layered half-space media computed using FEM-PML versus reference solution.

3.4.2 Effects of the angle of incidence

As been reported in [129, 130], the angle of incidence can significantly affect the response of the buried structures, especially for vertical ones. In this section, we analyze a 2D rectangular tunnel in homogeneous media excited by SV waves with different angles of incidence. The numerical model is shown in Fig. 3.30. Here we use the DRM interface to prescribe the input motion, and the PML to truncate the domain and absorb the scattering waves. Eq. 3.18 with the selected parameters as $A_{\text{Ricker}} = 1e^{-4}$ m, $f_{\text{Ricker}} = 2$ Hz and $t_0 = 0.8$ sec, is used as the incident wave function. A total simulation time is $T = 3$ sec and time stepsize is $\Delta t = 0.005$ sec. 4-node quadrilateral plane strain elements (CPE4) with element size of 1 m $\times$ 1 m are used for the soil in the interior domain. 2-node beam elements (B21) with element size of

0.5 m and thickness 1 m are used for the rectangular structure. No-slip interface condition is used for the soil-structure interface. Material properties for the homogeneous soil and the rectangular structure are summarized in Table. 3.3. The effects of the distance between the DRM interface and the buried structure need to be further investigated [131].

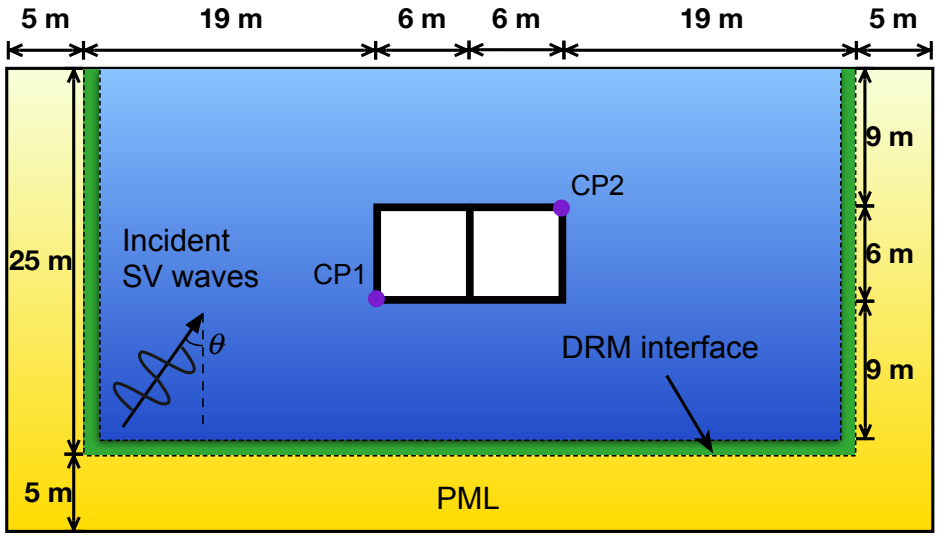

Figure 3.30: Plan view of the buried rectangular tunnel for studying the effects of angle of incidence.

Table 3.3: Material properties of homogeneous soil and the rectangular structure.

	Young's modulus (MPa)	Poisson's Ratio	Density (kg/m^3)
Soil	208	0.3	2000
Structure	32000	0.2	2500

Table 3.4: Material properties of the two-layered soil deposits.

	Shear wave velocity V_s (m/s)	Poisson's Ratio	Density (kg/m^3)
Layer 1	400	1/3	1700
Layer 2	500	1/3	2000

First, we compare the accelerations for two corner points on the structure (i.e., bottom left and top right). As we can see in Fig. 3.31, for this specific case, by increasing the angle of incidence, both maximum values of horizontal and vertical accelerations increases and the amplification factors can reach 2.57 and 6.52, respectively. Then the racking displacements

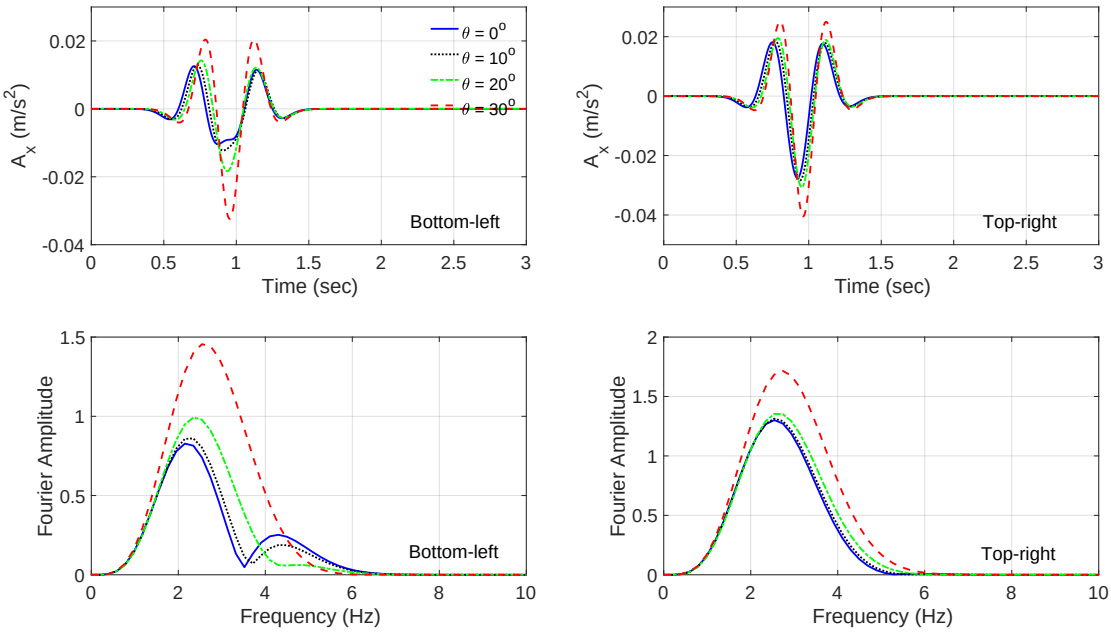

(a) Horizontal acceleration

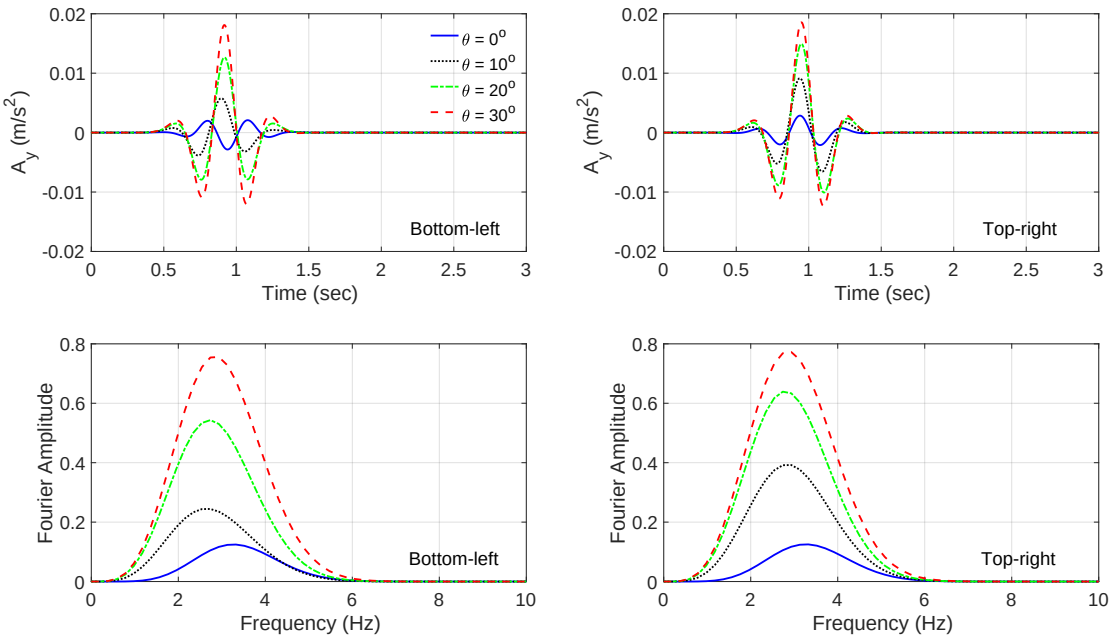

(b) Vertical acceleration

Figure 3.31: Time histories and the Fourier amplitudes of the horizontal and vertical accelerations.

for different columns and its Fourier spectrums are computed and shown in Fig. 3.32. As seen, the racking displacements actually decrease when the angle of incidence increases, for all left, middle and right columns.

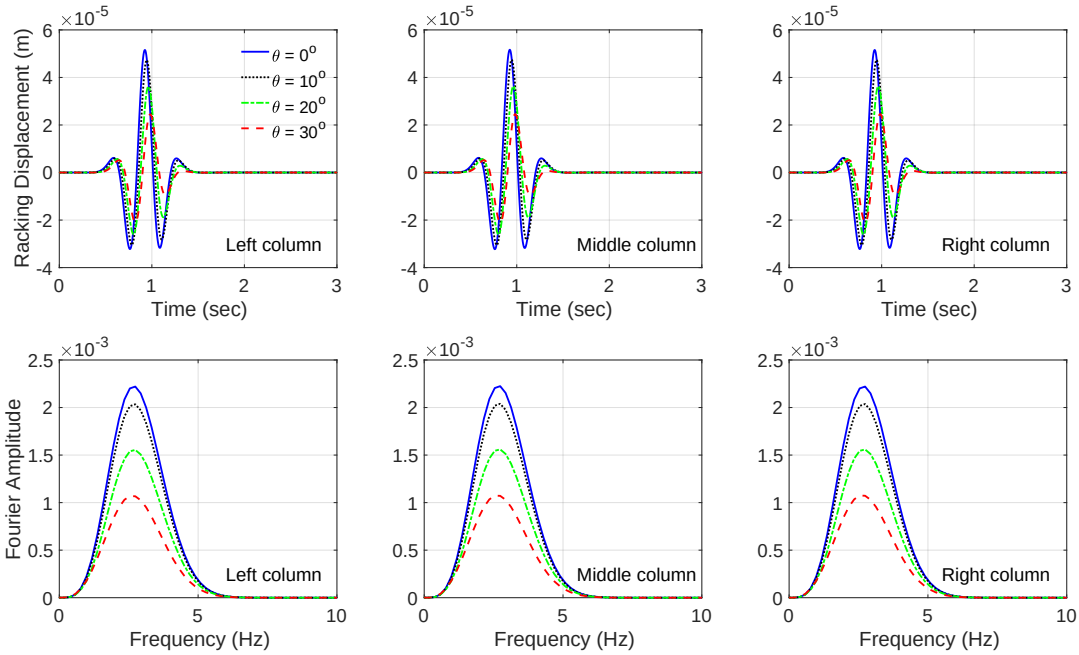

Figure 3.32: Time histories and the Fourier amplitudes of the racking displacements.

Finally, we explore the effects of the angles of incidence on the axial force, bending moment, as well as the deformation mode. Figs. 3.33(a) and (b) show the profiles of the maximum axial force and bending moment, respectively. As seen, with the increasing angles of incidence, the axial force increases, while the bending moment decreases. And Fig. 3.34 shows the deformation plot when the maximum bending moment happens, for different angles of incidence. More bending deformation is observed for small angles, and more rotation is noticed for larger angles. It should be noted that in all figures the resulting deformations are magnified 30000 times.

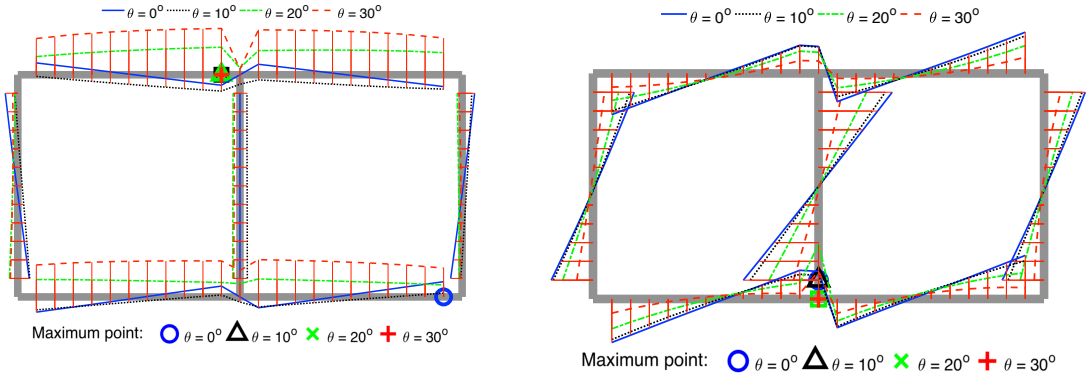

(a) Axial force (b) Bending moment

Figure 3.33: Profiles of the maximum (a) axial force and (b) bending moment.

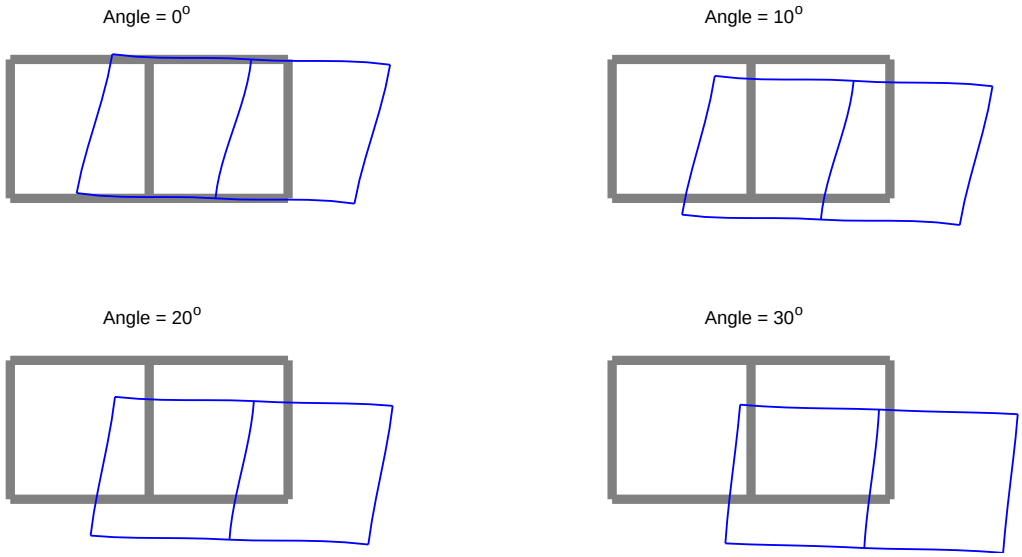

Figure 3.34: Maximum deformation plot for different angles of incidence.

CHAPTER 4

Development of validated methods for soil-structure analysis of buried structures

Seismic response of underground structures is a complex soil-structure interaction (SSI) problem in which two fundamental mechanisms are at play. Differences in motion between the free-field soil and the buried structure in the absence of excess or deficient mass between the two that are due to their stiffness contrast are collectively referred as Kinematic Interaction (KI) effects. Inertial Interaction (II) effects are, therefore, complementary, and are concerned with the soil reactions that develop to resist inertial forces associated with accelerations of the foundation-structure system relative to the soil. The kinematic component is generally considered to be more significant for buried structures due to their modest mass and their confinement by soil.

Current seismic design practices—articulated in, for example, the NCHRP Report 611 [18]—are based on the procedures proposed by [19] for circular and rectangular buried structures. During the last few years, a number of experimental [132, 133, 134, 135, 136, 137, 138], numerical [139, 140, 135, 141, 142] and analytical [143, 144, 145] studies have been conducted to explore the accuracy of the aforementioned simplified procedures. A non-exhaustive list of previously performed experimental studies on buried structures in dry sand is provided in Table 4.1.

We have undertaken here a centrifuge modeling program that is designed to extend the previous test results by (1) applying a wider range of ground motions spanning frequency contents where interaction effects are expected to range from significant to negligible; (2) applying a wider range of shaking amplitudes to investigate variable effects of soil nonlinearity;

and (3) deploying a relatively dense instrument configuration to enable detailed measurements of the culvert section responses as well as near- and far-field soils. The centrifuge tests were performed using the 9m-radius centrifuge at the Center for Geotechnical Modeling (CGM) at UC Davis [146]. Specimens consisted of two representative structures that were selected per Caltrans Standard Plans 2015 A62E and A62F [147], which were embedded in a granular backfill.

The main objectives of this chapter were (1) to compare the experimental findings with the design method described in NCHRP Report 611 [18] in order to establish the validity (or lack thereof) of this method for the specific Caltrans configurations tested; (2) to formulate preliminary recommendations for Caltrans practice; and (3) to identify future research needs in this area, as needed.

Table 4.1: A list of previous experimental studies on buried structures in dry sand.

References	Structure				Input motion			Soil
	Type	Dimensions (m)	Material (model)	Material (prototype)	Type	PGA (g)	Frequency (Hz)	relative density
[132, 133]	S	5×0.061 5×0.155	A	A	H	$0.08 - 0.32$	$0.8 - 1.2$	45%
	C	5×0.088	A	A	E	$0.22 - 0.62$	$1 - 3$	
[134, 135]	C	6×0.06	A	CR	H	$0.05 - 0.15$	$0.37 - 0.75$	40%, 75%
[136]	S	5×0.13	A	CR	H, SS	$0.02 - 0.24$	$0.6 - 1.2$	90%
[137]	S	2×0.06	A	A	H	$0.25 - 0.4$	$2 - 3.5$	70%
[138]	S	4.57×0.27 4.57×0.53	A	CR	E	$0.11 - 0.33$	$0.46 - 1.45$	50%, 90%

In the second column, S and C stand for Square and Circle, respectively.
In the third column, dimensions are in width×thickness for square sections and in diameter×thickness for circular sections.
In the fourth and fifth columns, A and CR stand for aluminum and concrete, respectively.
In the sixth column, H, E, and SS stand for Harmonic, Earthquake and Sine Sweep motions, respectively.

4.1 Centrifuge modeling

4.1.1 Centrifuge modeling and scaling laws

Scaling laws are used in centrifuge modeling so that the stress field at any point within the model is similar to what is expected in the prototype. As shown in Figure 4.1, if we scale down the size of the prototype by N, and increase the centrifugal acceleration by the same amount, the stress field in the model and the prototype—e.g., γH in Figure 4.1—will be similar. In other words, by using the aforementioned scaling law, we can capture the actual nonlinear and pressure-dependent behavior of the soil with the scaled model. Scaling laws

for different parameters relevant to this research are listed in Table 4.2. It should be noted that in this project $N = 21$.

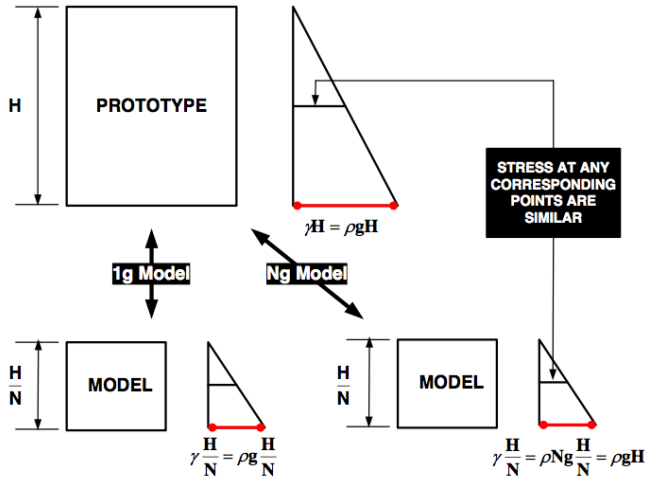

Figure 4.1: Scaling law for the stress field [1].

Table 4.2: Scaling laws [4].

Parameter	Model/Prototype
Length	$1/N$
Area	$1/N^2$
Volume	$1/N^3$
Mass	$1/N^3$
Stress	1
Strain	1
Force	$1/N^2$
Moment	$1/N^3$
Time (dynamic)	$1/N$
Frequency	N
Displacement	$1/N$
Velocity	1
Acceleration	N

4.1.2 UC Davis centrifuge and model container

We used the NEES@UCDavis Flexible Shear Beam Container 2 (FSB2), which has a number of aluminum shear rings as well as rubber shear layers to replicate free-field shear conditions in the soil deposit when no structure is present. The length, width, and height of this

container are shown in Figure 4.2. After model construction and instrumentation, the filled container was mounted on the centrifuge arm to be spun. An illustrative example of a mounted model is shown in Figure 4.3.

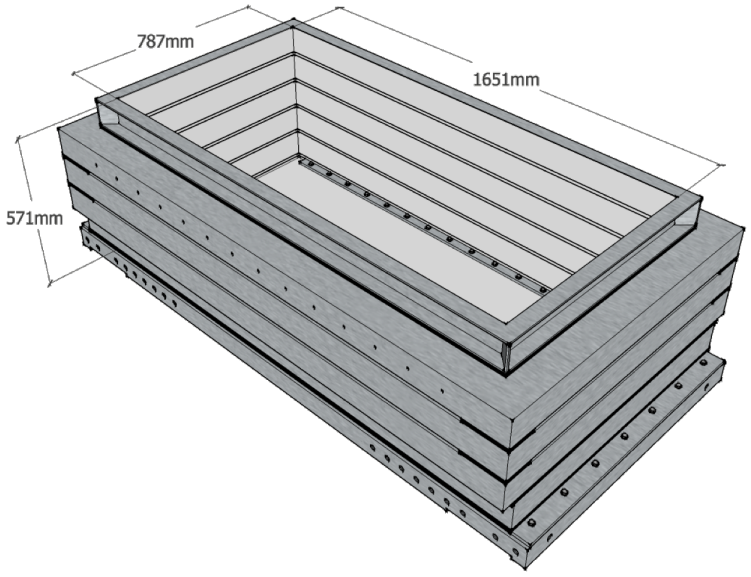

Figure 4.2: Geometry of the flexible shear beam container (FSB2).

4.1.3 Soil properties

4.1.3.1 Mechanical properties of the Ottawa sand

Ottawa sand, which is a pure quartz sand composed of naturally rounded grains, was used in the centrifuge experiments. Representative mechanical properties of the Ottawa sand are summarized in Table 4.3.

Table 4.3: Mechanical properties of the Ottawa sand (CGM, personal comunication).

Soil paeameter	Value
Specific gravity, G_s	2.673
Mean grain size, D_{50}	≈ 0.2 mm
Coefficient of uniformity, C_u	1.73
Coefficient of gradation, C_c	1.08

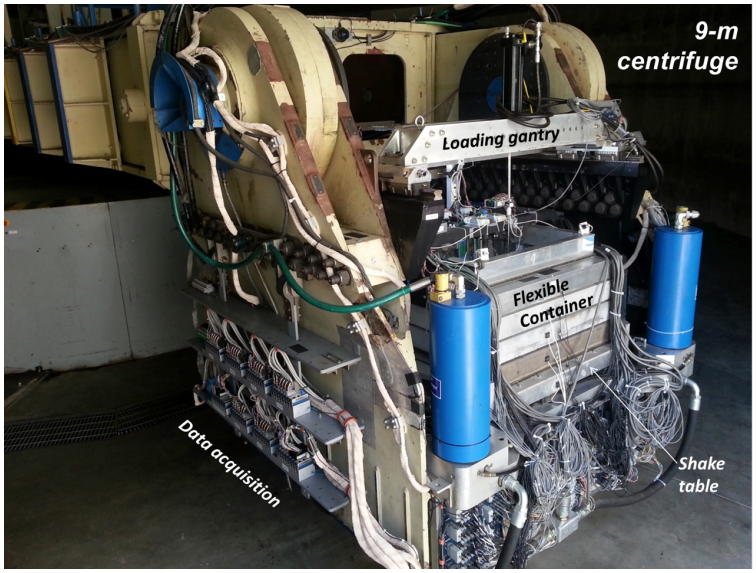

Figure 4.3: Configuration of the instrumented container mounted on the 9 m centrifuge arm.

4.1.3.2 Shear wave velocity

Shear wave velocity measurements were obtained by bender elements [148] at four positions in the soil profile; near the bottom of the container, below the circular pipe, below the rectangular culvert and close to the surface of the container. Figure 4.4 shows the array next to the box structure. Center-to-center distance between bender elements is about 10 cm. In all these arrays, three bender elements are used, which act as piezoelectric transducers, one being the source and the other two being the receivers of the signal. The measurements are taken at 20g (during spinning). A high voltage step wave motion is imposed on the source bender element, which causes the element to rapidly bend inducing a horizontally propagating shear wave with vertical particle motion. The wave travels through the soil and deforms the receivers, resulting in a recorded voltage signal. Shear wave velocity can then be estimated by measuring the time it takes for the waves to travel between receivers. Details of bender element signal processing is provided in [149].

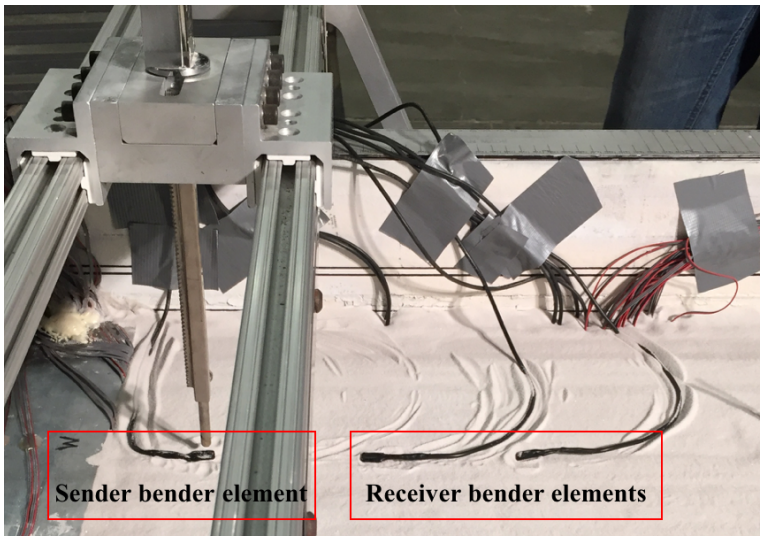

Figure 4.4: One array of the bender elements used for measuring shear wave velocity.

4.1.4 Culvert structures

4.1.4.1 Mechanical properties of the culvert structures

The Caltrans Standard Plans [147] present common configurations for culvert structures used in California. These culverts are composed of corrugated steel pipe or reinforced concrete box structures. The model structures, embedment depths, and soil properties utilized in the centrifuge models were selected to be consistent with these commonly used culvert structures.

Pipe structure: the model specimen is a uniform seamless aluminum pipe with a thickness of 0.16 cm (0.065 in) and inside diameter of 12.37 cm (4.87 in). It is made from Aluminum 6061-T6 with $E = 68.95$ GPa (10^7 psi), $\gamma = 26.48$ kN/m^3 (0.0975 lb/in^3), and $\nu = 0.33$ (all based on manufacturer specifications rather than measurements). These dimensions were selected to match the static flexural stiffness of a representative prototype corrugated steel pipe structure (cf. Caltrans Standard Plans).

Box structure: the model specimen is a box tube with inside dimensions of 18.4cm×10.8cm (7.25in×4.25in) and uniform thickness of 0.95 cm (0.375 in). It is also made of Aluminum 6061-T6. These dimensions are selected to match the flexural stiffness of a representative reinforced concrete culvert structure (cf. Caltrans Standard Plans).

4.1.5 Model construction and instrumentation configurations

Figure 4.5 displays an elevation view of the centrifuge model.

Sensors were placed in six stages at different elevations in the model, including 59 accelerometers, 43 of which were installed in soil or on the container and the rest inside the specimens. A frame is mounted on top of the container to secure LPs in order to measure soil surface settlements and to capture vertical displacements of the specimens. Another frame is used to attach LPs to the container wall and to measure the associated lateral displacements (see Figure 4.5). All sensors used in the model were connected to a data acquisition system as shown in Figure 4.3. We used thin aluminum sheets to close the two ends of each specimen in order to avoid intrusion of sand inside the specimens. The configurations and labels of the sensors installed on the pipe and box structures are provided in Figure 4.6. The IDs used for labeling the sensors, along with their positions and configurations, are provided in Table. 2.3 of [149].

A total of 25 shaking events were applied at approximately $N = 21g$ centrifugal acceleration. Shaking was applied transverse to the culverts' long axes in the north-south direction. The sequence of the type of motions used to shake the model, including step-, earthquake-, and sinusoidal-functions are provided in Table 4.4.

Three earthquake ground motions are used in this study, which are obtained from the PEER ground motion database. The characteristics of these motions—i.e., target earthquake motions—are provided in Table 4.5. Figure 4.7 shows the 5%-damped spectral accelerations and the Arias intensity time series of the target earthquake motions.

Since the shake table on the centrifuge cannot perfectly reproduce a target motion, some signal modification needs to applied. This is typically achieved by first computing a command motion in which the high frequency content is increased relative to the target motion. This accounts for a loss of high-frequency content due to the mechanics of the shake table feedback control system. The achieved motion is then compared to the target motion, and the command motion is adjusted. Through an iterative process, the achieved base motions

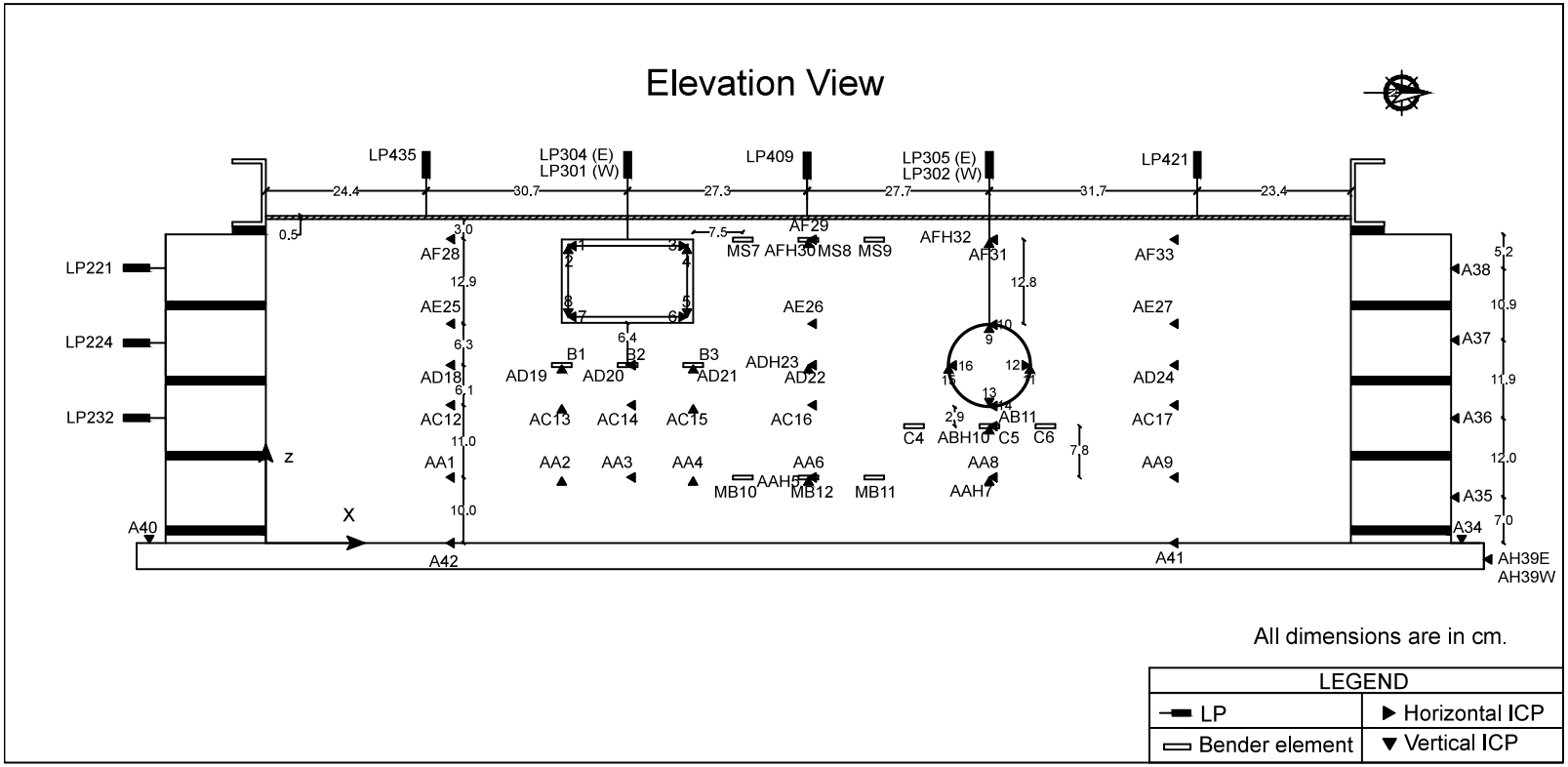

Figure 4.5: Elevation view of the centrifuge model.

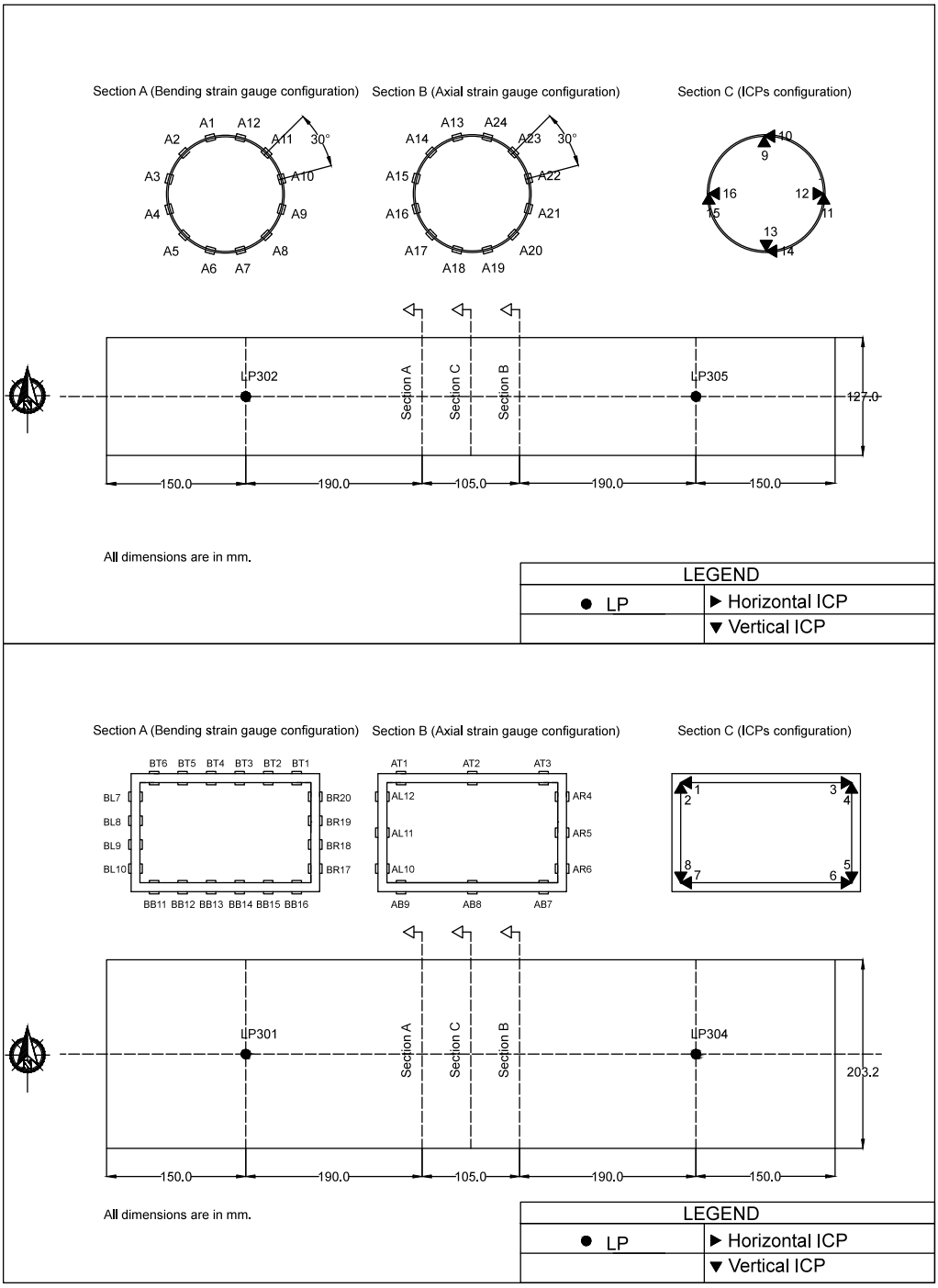

Figure 4.6: Layout of the instrumentation for the rectangular and circular structure.

in the present tests were similar to, but not perfectly equivalent with, the target motions. For this reason, we suggest always using the measured base motions when interpreting the test data. The 5%-damped spectral accelerations and the Arias intensities of the measured base motions for the earthquakes (i.e., motions #03 to #11) are shown in Figure 4.8.

Sine-sweep motions were also used to shake the model the prototype frequencies of up to 25 Hz. As mentioned before, it was expected that soil-structure interaction effects would be more significant at higher frequencies. Two types—namely, constant acceleration and constant-velocity—target motions were used. It was found that constant velocity motions provided command inputs with richer high-frequency energy content.

The model was also excited with stepped-sine signals with discrete frequencies of 1.25, 1.85, 2.5, 3.75, 5, 7.5, 10, 17.5, and 25 Hz. At each iteration, the amplitudes of the stepped-sine functions at different frequencies were updated so that the amplitude of measured accelerations at the soil surface (as recorded by sensor AFH30) were nearly the same at all discrete frequencies considered. It should be noted that ideally a sine sweep function could be used for this purpose. However, calibration of the command input using sine sweep functions was not straightforward. This is why stepped sine functions were applied. Shaking the models with motions with the same surface acceleration amplitude permits observation of the frequency-dependence of the structural response.

Table 4.4: The sequence of the input motions used for shaking the model.

Event #	Command input type	Amp. factor applied to target motion	Command input file name	Measured data file name
1	Step function	0.6	01-Step.txt	01_011420161421131428l446.5rpm
2	Step function	1.5	02-Step.txt	02_011420161421131446234 6.6rpm
3	Earthquake MUL279	0.1	03-RSN953_NORTHR_MUL279.shk	03_011420161421131511324 6.3rpm
4	Earthquake SMT090	0.1	04-RSN1077_NORTHR_STM090.shk	04_011420161421131532054 6.3rpm
5	Earthquake HEC000	0.33	05-HEC000.shk	05_011420161421131544334 6.2rpm
6	Earthquake MUL279	0.5	03-RSN953_NORTHR_MUL279.shk	06_011420161421131550454 6.2rpm
7	Earthquake SMT090	0.5	04-RSN1077_NORTHR_STM090.shk	07_011420161421131555564 6.3rpm
8	Earthquake HEC000	1	05-HEC000.shk	08_011420161421131559254 6.3rpm
9	Earthquake MUL279	1	03-RSN953_NORTHR_MUL279.shk	09_011420161421131603534 6.3rpm
10	Earthquake SMT090	1	04-RSN1077_NORTHR_STM090.shk	10_011420161421131628594 6.5rpm
11	Earthquake HEC000	3	05-HEC000.shk	11_011420161421131632534 6.5rpm
12	Sine sweep 1 (constant acceleration)	1	12-input_command.txt	12_011420161421131645284 6.4rpm
13	Sine sweep 1 (constant acceleration)	3	13-input_command.txt	13_011420161421131649494 6.4rpm
14	Sine sweep 2 (constant acceleration)	1	14-sw-25to500-0.3g-iter00	14_011520160942021137524 6.6rpm
15	Sine sweep 3	0.5	15-sw-25to500-0.1g-iter01	15_011520160942021200184 6.5rpm
16	Sine sweep 3	0.1	16-sw-25to500-0.1g-iter01	16_011520160942021218424 6.2rpm
17	Stepped sine 1 (iteration 0)	1	17-sine-0.1g-iter00	17_011520160942021253124 6.4rpm
18	Stepped sine 2 (iteration 1)	1	18-sine-0.1g-iter01	18_011520160942021345314 6.3rpm
19	Stepped sine 3 (iteration 2)	1	19-sine-0.1g-iter02	19_011520160942021358094 6.3rpm
20	Stepped sine 4 (iteration 3)	1	20-sine-0.1g-iter03	20_011520160942021437014 6.4rpm
21	Stepped sine 5 (iteration 4)	3	21-sine-0.1g-iter04	21_011520160942021454514 6.4rpm
22	Stepped sine 6 (iteration 5)	3	22-sine-0.1g-iter05	22_011520160942021514554 6.4rpm
23	Stepped sine 7 (iteration 6)	5	23-sine-0.1g-iter06	23_011520160942021523194 6.5rpm
24	Sine sweep 4 (constant velocity)	0.5	24-ExponentialSineSweep.shk	24_011520160942021531434 6.3rpm
25	Sine sweep 4 (constant velocity)	0.75	25-ExponentialSineSweep.shk	25_011520160942021541184 6.3rpm

Table 4.5: Characteristics of the earthquake ground motions used in this study.

Earthquake	Year	Station	Component	Magnitude	R_{jb} (km)	V_{s30} (m/s)
Northridge	1994	Beverly Hills	MUL279	6.69	9.44	355.81
Northridge	1994	Santa Monica City Hall	STM090	6.69	17.28	336.20
Hector Mine	1999	Hector	HEC000	7.13	10.35	726.00

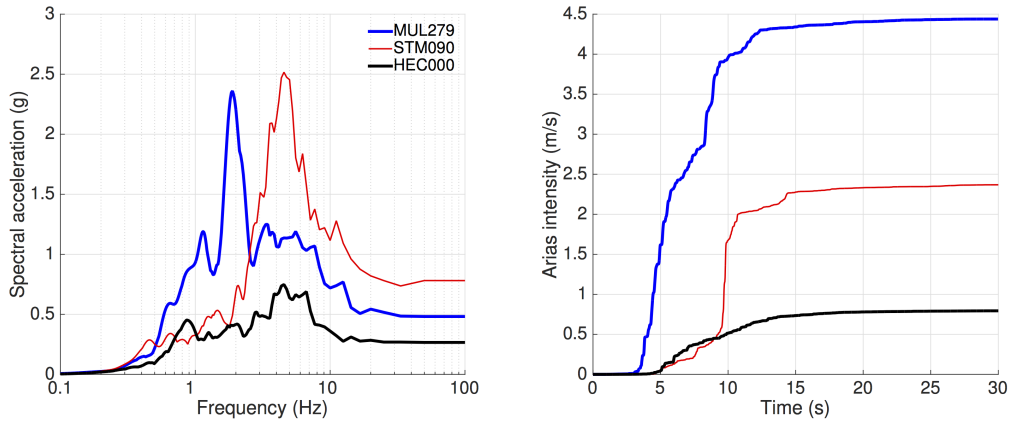

Figure 4.7: 5%-damped spectral acceleration and Arias intensity time series of the earthquake motions used in this study.

4.2 The NCHRP 611 approach

The current AASHTO LRFD Bridge Design Specifications do not cover the seismic response of buried structures; and only the recent National Cooperative Highway Research Program (NCHRP) Report 611—titled "Seismic Analysis and Design of Retaining Walls, Buried Structures, Slopes, and Embankments"—offers various recommendations on the topic. As culvert structures in transportation applications generally have a limited length, their potential failure modes are due to their transverse deformations under transient ground shaking—namely, ovaling and racking of circular and rectangular culverts, respectively [18]—, which are illustrated in Figure 4.9.

4.2.1 Ovaling of a circular culvert

It is widely accepted that plane strain models provide reasonable approximations to the failure modes of circular culverts, as their most critical mode is the ovaling deformation mode [140]. Transient ovaling effects in circular culverts can be quantified by the change in their diameters, which can then be used to obtain reasonable estimates of the peak seismically induced internal forces. For flexible culverts, buckling is the most critical failure mode, which

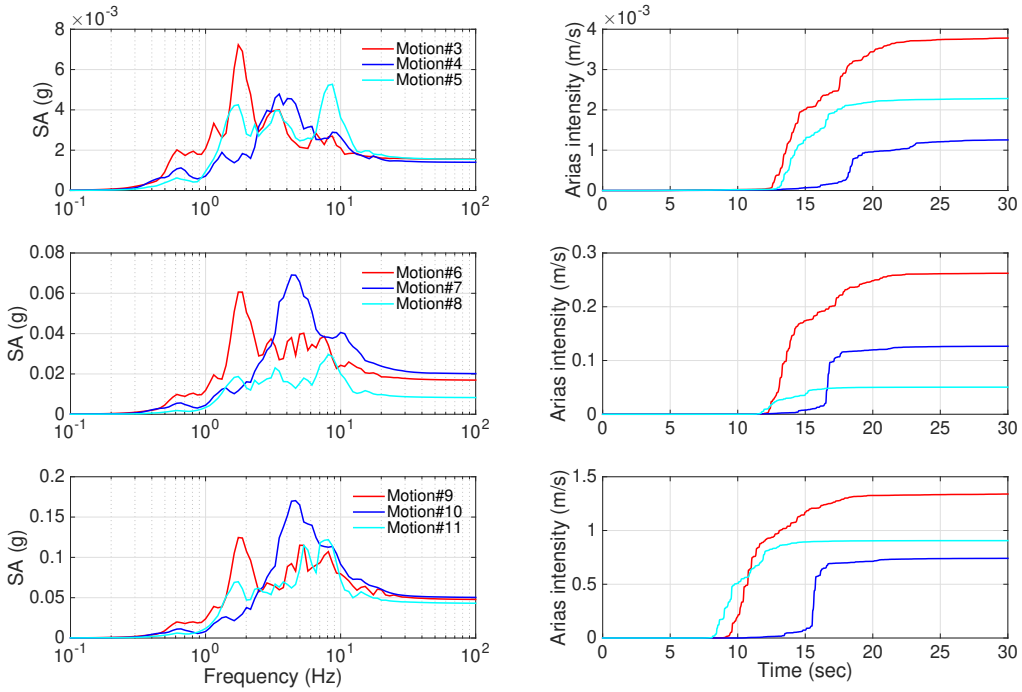

Figure 4.8: 5%-damped spectral acceleration and Arias intensity time series of the measured base motions for shake events #03 to #11.

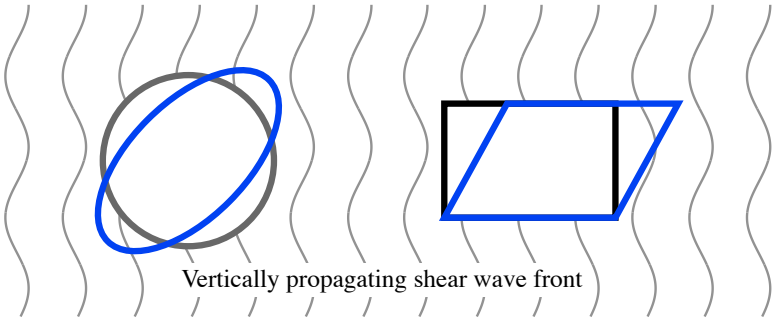

Figure 4.9: Ovaling and racking deformation of the circular and rectangular cross sections.

is governed by the thrust force. For rigid culverts, on the other hand, the lining deformation, bending, thrust, and the resulting strains are all important parameters to evaluate [18].

Currently, four analytical closed-form solutions are available [150, 151, 144, 145], which are all based on the assumption that, under seismic loading, the tunnel lining acts as an elastic beam subject to a uniform shear strain field of amplitude $\gamma_{\max}$, wherein the inertial soil-lining interaction effects are ignored. As enumerated by [140], the dynamic interaction can become important when (i) the dimensions of the tunnel cross-section is comparable to the wavelengths of the seismic loading, (ii) the tunnel is relatively shallow, and (iii) the structure is significantly stiffer than the surrounding soil.

The methodology provided in NCHRP Report 611 [18] is based on the solution provided by [150]. An engineer needs to execute the following steps to determine the seismic demands due to ovaling of the circular culvert:

1. *Estimate the free-field ground strains (γ_{max}) at the top and bottom elevations of the culvert structure*: For highway culverts with burial depths less than 50 ft, γ_{max} may be estimated using the equation below:

$$\gamma_{max} = \frac{\tau_{max}}{G_m}, \quad \tau_{max} = (\text{PGA}/g)\sigma_v R_d \tag{4.1}$$

where G_m is the effective-strain-compatible shear modulus of the surrounding soil, PGA is the peak ground acceleration, σ_v is the overburden pressure at the depth corresponding to the invert of the culvert, and R_d is a depth-dependent stress reduction factor given by

$$R_d = \begin{cases} 1 - 0.00233z & z < 30\text{ft} \\ 1.174 - 0.00814z & 30\text{ft} \leq z \leq 75\text{ft} \end{cases} \tag{4.2}$$

and z is the depth to the midpoint of the culvert. One may also estimate γ_{max} by performing free-field site response analysis.

2. *Calculate of the flexibility and compressibility ratios*: Compressibility ($C^{\bigcirc}$) and flexibility ($F^{\bigcirc}$) ratios are used to determine the relative stiffness of the culvert lining with respect to the surrounding ground [150], and can be computed as:

$$F^{\bigcirc} = \frac{E_m(1-\nu_1^2)R^3}{6E_1I_1(1+\nu_m)} \tag{4.3}$$

$$C^{\bigcirc} = \frac{E_m(1-\nu_1^2)R}{E_1A_1(1+\nu_m)(1-2\nu_m)} \tag{4.4}$$

where E_m is the strain-compatible elastic modulus, and ν_m is the Poisson's ratio of the surrounding soil. The terms R, E_1, ν_1, A_1, t and I_1 respectively denote nominal radius, elastic modulus, Poisson's ratio, cross-sectional area, thickness, and moment of inertia of the culvert lining. For $F^{\bigcirc} < 1$, the lining is considered to be stiffer than the surrounding soil while for $F^{\bigcirc} > 1$, it is expected that the lining deforms more than the free-field.

3. *Estimate the lining deformation and seismic demands*: For estimation of the lining diameter change (ΔD_{EQ}) and the resulting moment (M), it is recommended to consider a full-slip interface assumption, which allows normal stresses without normal separation and tangential forces. On the other hand, for estimation of the resulting thrust (T), a no-slip interface assumption is recommended. Therefore,

$$\Delta D_{\mathrm{EQ}} = \pm\frac{1}{3}k_1F^{\bigcirc}\gamma_{\max}D \tag{4.5}$$

$$M^{\bigcirc} = -\frac{1}{6}k_1\frac{E_m}{1+\nu_m}R^2\gamma_{\max}\cos 2(\theta+\frac{\pi}{4}) \quad \text{(full-slip)} \tag{4.6}$$

$$T^{\bigcirc} = -k_2\frac{E_m}{2(1+\nu_m)}R\gamma_{\max}\cos 2(\theta+\frac{\pi}{4}) \quad \text{(no-slip)} \tag{4.7}$$

where

$$k_1 = 12\frac{1-\nu_m}{2F^{\bigcirc}+5-6\nu_m}\,, \tag{4.8}$$

$$k_2 = 1+\frac{F^{\bigcirc}(1-2\nu_m)(1-C^{\bigcirc})-0.5(1-2\nu_m)^2C^{\bigcirc}+2}{F^{\bigcirc}[(3-2\nu_m)+(1-2\nu_m)C^{\bigcirc}]+C^{\bigcirc}[2.5-8\nu_m+6\nu_m^2]+6-8\nu_m}\,. \tag{4.9}$$

4.2.2 Racking of a rectangular culvert

Contrary to circular culverts, no closed form solution is available for quantifying the racking deformations in rectangular culverts. The procedure provided in NCHRP Report 611 is based on the pseudo-static method proposed by [150], which again does not take inertial interaction effects into account. The following steps are recommended therein to estimate the seismic demands due to racking of a rectangular culvert.

1. *Estimate of the free-field ground strains* (γ_{max}) *at the elevation of the culvert structure*: γ_{max} can be computed following the procedure provided for circular culverts in §4.2.1.

2. *Estimate the differential free-field relative displacement* ($\Delta_{\text{freefield}}$) *at the corresponding top and bottom elevations of the rectangular structure*. That is:

$$\Delta_{\text{freefield}} = H\gamma_{max} \tag{4.10}$$

   where H is the height of the structure. As seen in Equation (4.10), it is assumed that the racking is due to a uniform shear strain field. This assumption is the same as that used for ovaling of circular culverts.

3. *Calculate the racking stiffness* (K_s) *of the structure*: This value can be computed through a simple structural frame analysis by applying a unit horizontal force at the roof of the structure, while its base is restrained as shown in Figure 4.10 and reading the resulting lateral displacement Δ. That is,

$$K_s = \frac{1}{\Delta}. \tag{4.11}$$

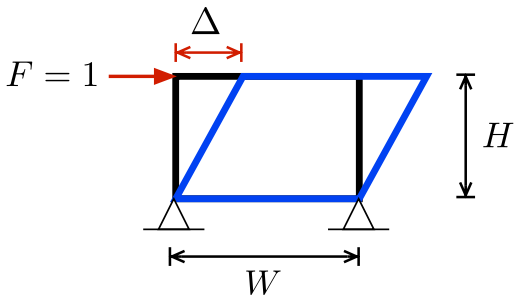

Figure 4.10: Racking stiffness of the rectangular culvert.

4. *Calculate the flexibility ratio*: The flexibility ratio $F^{\square}$ is the measure of the relative stiffness of the structure to the surrounding soil and can be estimated as follows.

$$F^{\square} = \frac{G_m}{K_s}\frac{W}{H} \tag{4.12}$$

where W is the width of the culvert structure as shown in Figure 4.10.

5. *Estimate the racking ratio*: The racking ratio $R^{\square}$ determines the ratio of the actual racking deformation of the structure with respect to the free-field racking deformation of the surrounding soil and can be defined as:

$$R^{\square} = \frac{2F^{\square}}{1 + F^{\square}}\,. \tag{4.13}$$

6. *Estimate the racking deformation of the structure*: Using the racking ratio and the free-field relative displacements, the racking deformation Δ_s can be computed as follows:

$$\Delta_s = R^{\square}\Delta_{\text{freefield}}\,. \tag{4.14}$$

7. *Determine the seismic demands*: Internal forces and the resulting strains can be computed by imposing the racking deformation at the roof of the structure as shown in Figure 4.11, and by performing a structural frame analysis.

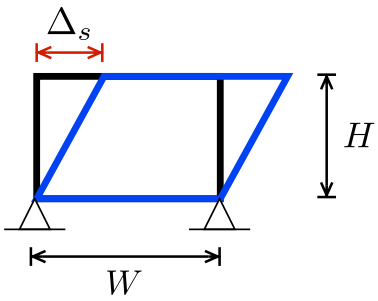

Figure 4.11: Imposition of the racking displacement to determine the resulting internal forces and moments from structural frame analysis.

4.3 Comparison of centrifuge results with NCHRP 611 method

In this section, comparisons of seismic demands obtained from centrifuge test data with those calculated using the NCHRP 611 method (see section 4.2) are presented.

4.3.1 NCHRP 611 method

In order to compute seismic demands using the NCHRP 611 methodology, we first need to estimate the free field maximum strain γ_{max} in the soil deposit as well as the corresponding effective compatible shear modulus G_m. Then, the seismic demands can be computed following the steps outlined in section 4.2.

4.3.1.1 Estimation of G_m at the elevation of the culvert structures

In chapter 3 of [149], we provided details of a signal processing procedure for obtaining shear wave velocities at different elevations of the soil deposit inside the container using bender element sensors. [3] also used a Bayesian approach to infer the shear wave velocity profile using data measured by the far-field accelerometer array {AA1,AC12,AD18,AE25,AF28} during low-amplitude earthquake motions (i.e., motions #3, #4, and #5) with maximum input acceleration of $\sim 0.015g$. The resulting estimated shear wave velocity profile was given

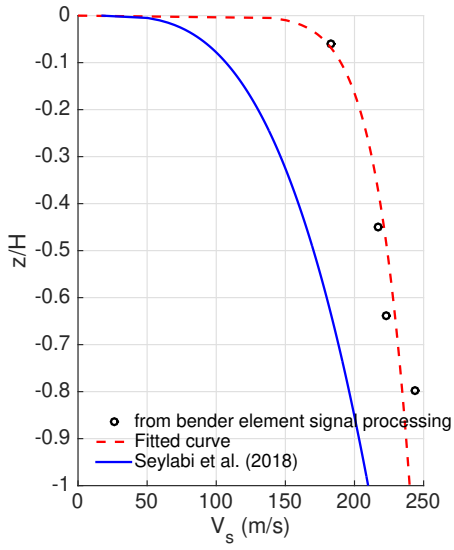

Figure 4.12: Shear wave velocity profile obtained from post-processing of the bender element signals and from a Bayesian estimation method.

as,

$$V_s \text{ (m/s)} = 16.905 + 192.976 \left(\frac{z}{H}\right)^{0.331} , \tag{4.15}$$

which is shown in Figure 4.12 along with the curve fitted through the data points obtained from bender element signal processing. As it will be shown in section 4.4, using this new shear wave velocity profile will result in acceleration responses that are highly correlated with experimentally recorded ones. Therefore, in the subsequent analyses, we will use Equation (4.15) for computing the shear wave velocity associated with small soil strains. Then, one may also compute the maximum shear modulus G_{max} as follows:

$$G_{max} = \rho V_s^2 \tag{4.16}$$

where ρ is the density of the soil deposit, which is equal to 1733 kg/m^3 for the present case.

The maximum shear modulus may be an appropriate representation of G_m for only low-amplitude motions for which the soil nonlinearity is negligible and the shear strains are very

small (i.e., $\sim 10^{-5}$). Therefore, we also need to use a representative modulus reduction curve along with the computed G_{max} to estimate the effective strain compatible shear modulus G_m at elevations of the tested culvert structures. Based on available soil properties for the Ottawa sand, one may use the empirical equations given by [2] to estimate the modulus reduction curve. That is,

$$\frac{G}{G_{max}} = \frac{1}{1 + (\gamma/\gamma_r)^a} \tag{4.17}$$

where

$$\gamma_r = 0.12 C_u^{-0.6} \left(\frac{\sigma'_m}{p_a}\right)^{0.5 C_u^{-0.15}}, \qquad a = 0.86 + 0.1 \log\left(\frac{\sigma'_m}{p_a}\right) \tag{4.18}$$

and C_u is the coefficient of uniformity, which, for Ottawa sand, is equal to 1.73. In order to decrease the uncertainties emanating from the use of empirical equations, [3] used an approach to estimate the modulus reduction curve from far-field acceleration data, which was similar to what was used for inferring the shear wave velocities from the same data. A multi-axial cyclic plasticity model by [72] was used to model the nonlinear/inelastic behavior of the soil deposit. The mean value of the estimated soil model parameters are as follows [1].

$$h = \left[0.107 + 0.474 \left(\frac{z}{H}\right)^{4.581}\right] G_{\max},\ m = 1.579,\ R = 0.0028\ G_{\max},\ H_0 = 0\,, \tag{4.19}$$

Figure 4.13 displays the resulting modulus reduction curves from both approaches at the elevations of the rectangular and circular structures. Finally, with using the estimated G/G_{max} curves and the G_{max} profile, we can compute the effective-strain-compatible shear modulus G_m for a given maximum shear strain in each event.

[1] Details of the nonlinear soil model and definitions of its parameters are provided later in section 4.4. It should also be noted here that our prior studies on centrifuge experiments involving structures embedded in dry sands have demonstrated that this soil model exhibits very good performance in predicting the main features of soil and embedded structure responses under broadband/seismic excitations [71].

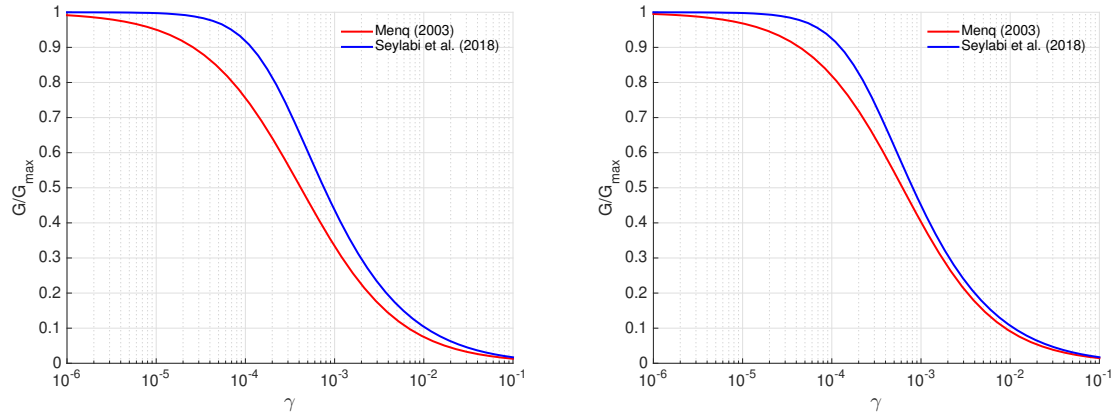

(a) At the elevation of the rectangular culvert, $z/H = 0.19$

(b) At the elevation of the circular culvert, $z/H = 0.46$

Figure 4.13: Shear modulus reduction curves obtained from the empirical equations by [2] and from the Bayesian estimation [3] at the elevations of the rectangular and circular culvert structures.

4.3.1.2 Estimation of γ_{max} at the elevation of the culvert structures

For shallow structures one may use the procedure provided in section 4.2 to estimate γ_{max}. However, in order to use that procedure, we need to know the effective compatible shear modulus G_m, which itself is a function of γ_{max}. Therefore, in order to use the NCHRP 611 method, we need to obtain it iteratively as follows:

1. To start the procedure (iteration $i = 0$), we need to have initial guesses for the maximum shear strains at the elevation of the rectangular and circular culverts. In order to compute the maximum strain at the elevation of the rectangular culvert, i.e. $\gamma^{\square}_{max,0}$, we use the acceleration measurements at AF28 and AE25, which correspond to the elevations at the roof and invert levels of the culvert. The displacement responses at these elevations can be computed by double integration of the acceleration time-series. Then, the relative free-field displacement history $\Delta u^{\square}_{\text{free-field}}$ can be computed as follows.

$$\Delta u^{\square}_{\text{free-field}}(t) = u^{\text{AF28}}(t) - u^{\text{AE25}}(t)\,. \tag{4.20}$$

Since NCHRP 611 considers the purely uniform shear in estimation of the seismic de-

mands, $\gamma^{\square}_{max,0}$ can be computed dividing the maximum relative free-field displacement, i.e. $\Delta^{\square}_{\text{free-field}}$, by the height of the culvert structure H. That is,

$$\gamma^{\square}_{max,0} = \frac{\Delta^{\square}_{\text{free-field}}}{H} \,. \tag{4.21}$$

For the circular culvert, we use the acceleration measurements at AE27 and AC17 to determine the relative free-field displacement at the elevation of the structure. That is,

$$\Delta u^{\bigcirc}_{\text{free-field}}(t) = u^{\text{AE27}}(t) - u^{\text{AC17}}(t) \,. \tag{4.22}$$

Again, the maximum strain at the elevation of the circular culvert can be computed by dividing the maximum relative free-field displacement $\Delta^{\bigcirc}_{\text{free-field}}$ by the height (diameter) of the structure D. Therefore,

$$\gamma^{\bigcirc}_{max,0} = \frac{\Delta^{\bigcirc}_{\text{free-field}}}{D} \,. \tag{4.23}$$

2. For iteration i, we can predict G_m for the rectangular and circular culverts using $\gamma_{max,i-1}$ and Figure 4.13. Then, we can correct the maximum shear strain $\gamma_{max,i}$ using Equation 4.1.

3. We need to repeat step 2 until $|\gamma_{max,i} - \gamma_{max,i-1}| <= \text{TOL}$ for the predefined tolerance TOL.

Figures 4.14, 4.15 and 4.16 show the iterative procedure for base shakings #3, #6, and #9, respectively. The resulting maximum shear strains are also tabulated in Table 4.6. As shown, in all cases the use of the iterative procedure results in higher maximum shear strains compared to those obtained from dividing the relative free field displacements at elevations of the rectangular and circular structures by the height of the structure.

As mentioned before, NCHRP 611 also suggests using 1D site response analysis to com-

pute the maximum shear strain. In order to investigate the accuracy of NCHRP 611 equations against this refined procedure, we performed 1D wave propagation analysis, using the multiaxial cyclic plasticity model. The resulting maximum strain profiles for all nine input motions are shown in Figure 4.17 and the strain values at elevations of the culverts are provided in Table 4.6 (i.e., $\gamma^{\square}_{max,1D}$ and $\gamma^{\bigcirc}_{max,1D}$). As shown, the shear profile is not constant with depth (especially for medium and high amplitude motions) and its curvature is a function of soil behavior and input motion characteristics. Moreover, the values of maximum strain obtained from 1D wave propagation analysis are considerably smaller than those obtained from the iterative procedure and are close to those obtained from the experimental data (i.e., our initial guesses for the iterative procedure). The effect of this difference will be studied in the subsequent sections.

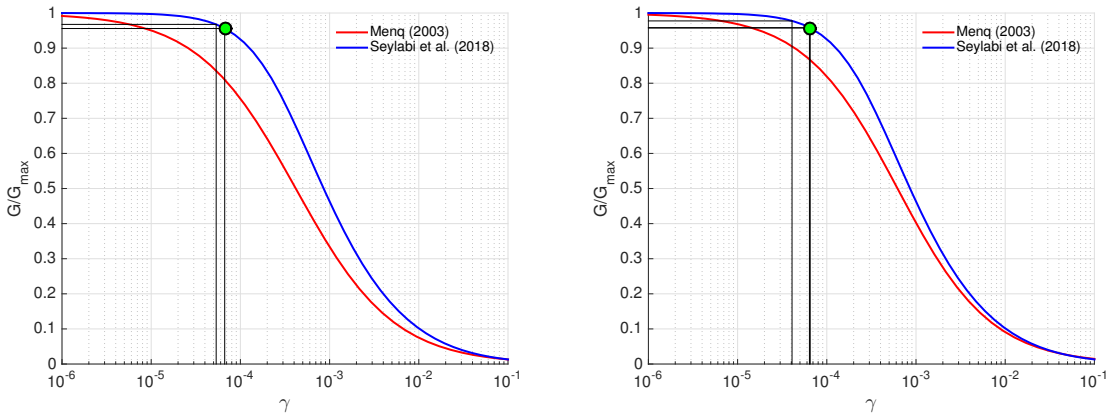

(a) At the elevation of the rectangular structure (b) At the elevation of the circular structure

Figure 4.14: Iterations for computing γ_{max} at the elevation of the rectangular and circular structures when subjected to the base shaking #3.

4.3.1.3 Seismic strains of the rectangular culvert

As mentioned in section 4.2, for determination of the flexibility ratio, we need to compute the racking stiffness K_s. To this end, we modeled the rectangular structure in ANSYS and analyzed it under the unit horizontal force. This resulted in $K_s = 26882$ kN/m. We consider

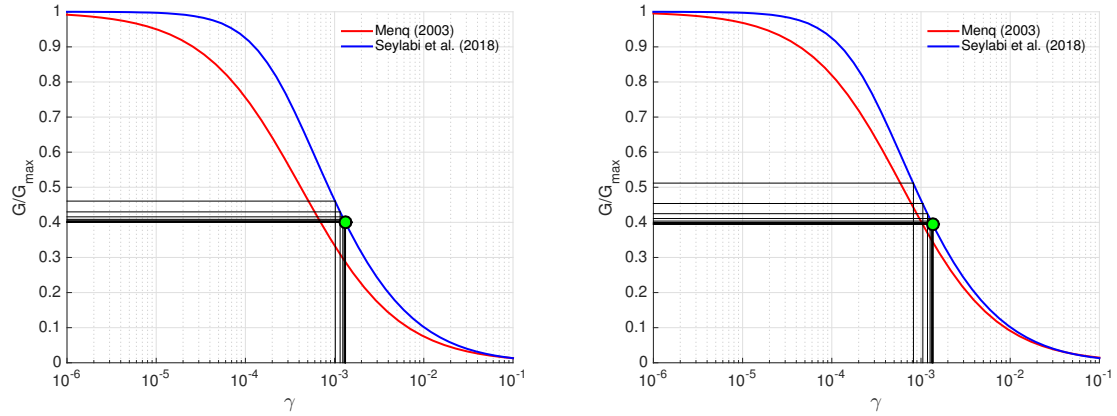

(a) At the elevation of the rectangular structure (b) At the elevation of the circular structure

Figure 4.15: Iterations for computing γ_{max} at the elevation of the rectangular and circular structures when subjected to the base shaking #6.

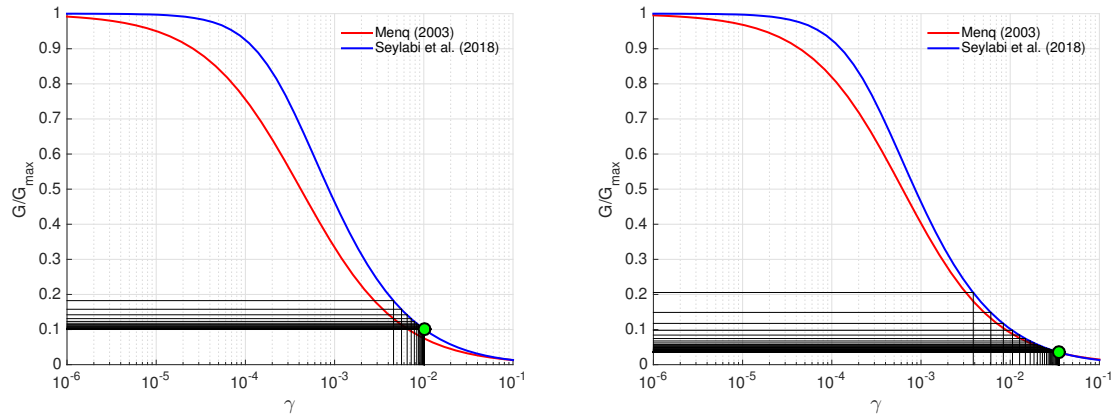

(a) At the elevation of the rectangular structure (b) At the elevation of the circular structure

Figure 4.16: Iterations for computing γ_{max} at the elevation of the rectangular and circular structures when subjected to the base shaking #9.

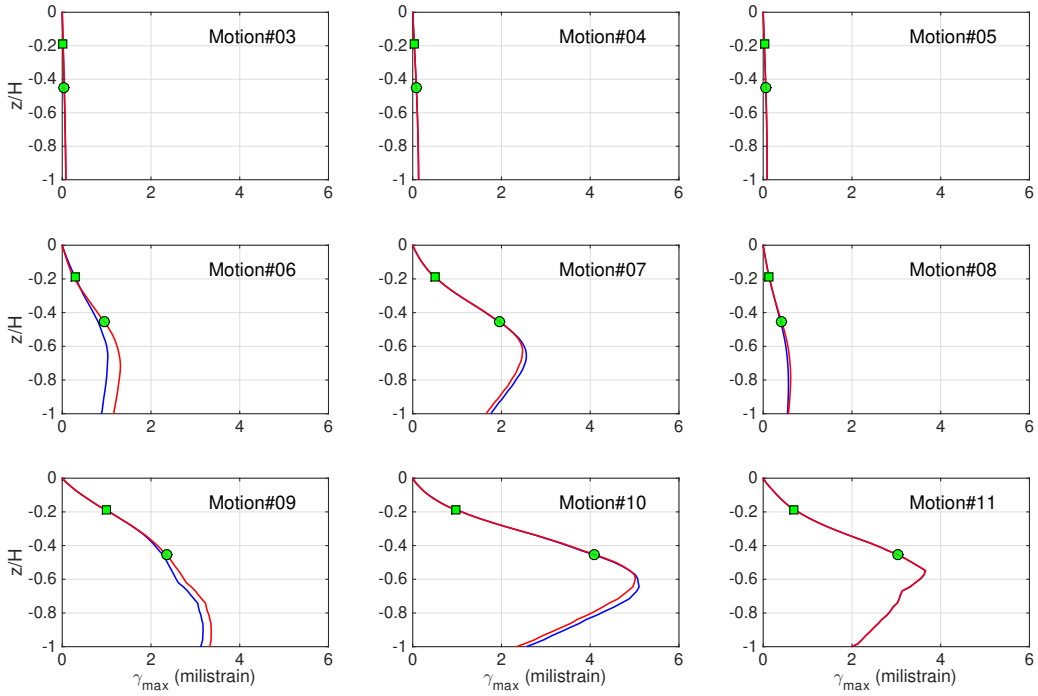

Figure 4.17: Maximum shear strain profile obtained from 1D wave propagation analyses.

Table 4.6: The computed maximum free field shear strains at the elevation of the rectangular and circular structures.

Motion #	$\gamma^{\square}_{max,0}$ (milistrain)	$\gamma^{\square}_{max}$ (milistrain)	$\gamma^{\square}_{max,1D}$ (milistrain)	$\gamma^{\bigcirc}_{max,0}$ (milistrain)	$\gamma^{\bigcirc}_{max}$ (milistrain)	$\gamma^{\bigcirc}_{max,1D}$ (milistrain)
3	0.054	0.067	0.020	0.041	0.066	0.046
4	0.092	0.127	0.036	0.075	0.124	0.082
5	0.061	0.086	0.025	0.043	0.080	0.059
6	1.019	1.495	0.298	0.823	1.504	0.943
7	1.235	1.882	0.497	1.082	2.477	1.950
8	0.381	0.612	0.138	0.313	0.815	0.412
9	4.580	9.108	0.993	3.855	18.181	2.355
10	3.553	16.993	0.983	2.508	7.022	4.088
11	2.156	8.280	0.702	1.702	7.660	3.039

W and H to be equal to 4.3 m and 2.7 m, respectively, in prototype scale. After computing the flexibility and racking ratios, we can compute the resulting racking displacement and impose it on top of the structure to obtain internal forces and moments from a simple frame analysis. We performed this analysis in ANSYS.

4.3.1.4 Seismic strains of the circular culvert

As mentioned in section 4.2, we first need to determine the flexibility and compressibility ratios to determine the internal forces in the circular culvert (see Equations 4.3 and 4.4). After obtaining G_m, one can compute the effective-strain-compatible Young's modulus of the surrounding soil using the following equation

$$E_m = 2G_m(1 + \nu_m) \tag{4.24}$$

where ν_m is the Poisson's ratio of the soil and is equal to 0.3 for the present case. I_1 and A_1 are the moment of inertia and area of the cross-section, and are equal to $1/12t_1^3$ and t_1, respectively, for the unit length of the circular culvert with the thickness of t_1. After the determination of $F^{\bigcirc}$ and $C^{\bigcirc}$, we can calculate the internal forces and the resulting strains for each test. In-plane bending strain ($\epsilon_b^{\bigcirc}$) and in-plane axial (hoop) strain ($\epsilon_h^{\bigcirc}$) are related to the internal bending ($M^{\bigcirc}$) and thrust ($T^{\bigcirc}$) as follows:

$$\epsilon_b^{\bigcirc} = \frac{M^{\bigcirc} t_1}{2E_1 I_1}, \quad \epsilon_h^{\bigcirc} = \frac{T^{\bigcirc}}{A_1}\,. \tag{4.25}$$

4.3.2 Static and dynamic increments of measured strains

As mentioned in section 4.1.1, we use the full bridge arrangement to measure the in-plane bending and in-plane axial strains at different points along the edges of the structures. Prior to interpretation and comparisons, the strain data need to be processed, the procedural details of which are provided in chapter 5 of [149].

In the following sections, we provide the strain results for both the static offset at the

beginning of each base shaking and the corresponding dynamic increment. It should be noted that for the rectangular structure, the results for only the bending strains are provided. This is mainly because the recorded in-plane axial strains were too small, even for the large amplitude motions.

4.3.3 Comparison of the in-plane bending strains for the rectangular culvert

In order to compare the experimental bending strain data against those computed using the NCHRP 611 method, we need to obtain the maximum bending strain profiles. To this end, we use the processed strain data from each event to determine the maximum bending strain among all recorded bending strains on the rectangular structure as well as the time it occurs. Then, we read the value of bending strains at *all* locations at the time that the maximum bending strain has occurred. Figure 4.19 displays the bending strain comparisons for each base shaking. In each sub-figure, the maximum dynamic increment (red bars) along with those obtained from the NCHRP 611 method (blue bars) are shown. It should be noted that different scaling factors are used among different events. Therefore, these figures provide only a qualitative understanding of differences between the experimental data and the NCHRP 611 analysis results.

In order to compare the actual bending strain values, we compute the maximum bending strain for each event. Table 4.7 summarizes the values of the important parameters including the flexibility and racking ratios, and the maximum bending strains. We observe that:

- The application sequence of base shakings had negligible effects on the maximum value of the static strain offset. However, the static offset profile has slightly changed (specifically, along the invert and bottom sides of the culvert walls).

- Since the box structure remained elastic, $F^{\square}$ is proportional to G_m. Therefore, as the surrounding soil becomes softer, the flexibility ratio—and therefore the racking ratio—decreases.

- In all cases, the NCHRP 611 method overestimates the maximum bending strain.

- The experimental bending strain profiles along the walls, roof, and invert vary almost linearly, and conform to the bending strain profile obtained from static frame analysis.

In order to have a closer look at how the maximum bending strain is related to different parameters of interest (PoIs), we plot each PoI against the maximum bending strains obtained from the centrifuge data directly, and the NCHRP method. This is shown in Figure 4.18. Although the range of $\epsilon_b^{\text{Centrifuge}}$ is different from the range of $\epsilon_b^{\text{NCHRP}}$, visually they both follow similar trends, especially with respect to γ_{max} and R.

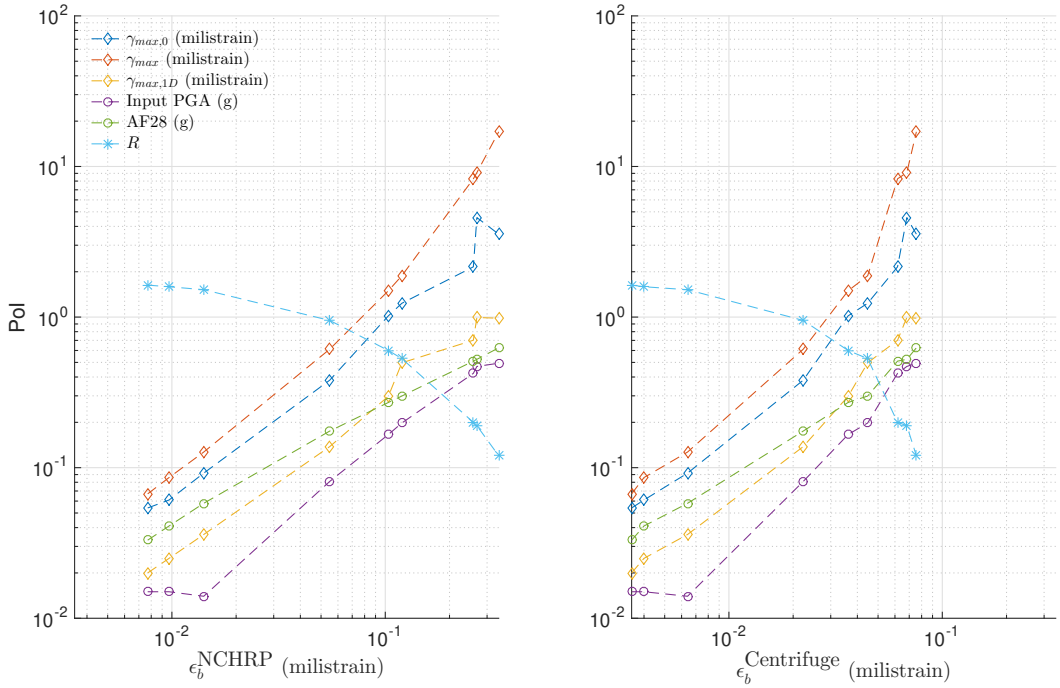

Figure 4.18: Variation of different PoIs with maximum bending strain of the rectangular structure.

Table 4.7: Comparison of the maximum bending strains of the rectangular structure.

Motion #	Input (g)	AF28 (g)	G_m/G_{max}	V_s (m/s)	$\gamma^{\square}_{max}$ (milistrain)	$F^{\square}$	$R^{\square}$	$\epsilon^{\square}_b$ (milistrain) NCHRP	$\epsilon^{\square}_b$ (milistrain) Centrifuge, Static	$\epsilon^{\square}_b$ (milistrain) Centrifuge, Dynamic	$e_b^{\text{NCHRP}}/e_b^{\text{Centrifuge}}$
3	0.015	0.033	0.954	125.8	0.07	1.63	1.24	0.0077	0.0337	0.0035	2.17
4	0.014	0.058	0.890	121.6	0.13	1.52	1.21	0.0141	0.0335	0.0064	2.21
5	0.015	0.041	0.934	124.5	0.09	1.59	1.23	0.0097	0.0334	0.0040	2.42
6	0.166	0.271	0.352	76.5	1.50	0.60	0.75	0.1034	0.0334	0.0362	2.86
7	0.198	0.299	0.309	71.6	1.88	0.53	0.69	0.1196	0.0328	0.0447	2.68
8	0.081	0.175	0.555	96.0	0.61	0.95	0.97	0.0549	0.0325	0.0223	2.46
9	0.470	0.524	0.112	43.1	9.11	0.19	0.32	0.2687	0.0324	0.0682	3.94
10	0.494	0.625	0.071	34.4	16.99	0.12	0.22	0.3401	0.0332	0.0756	4.50
11	0.423	0.510	0.120	44.6	8.28	0.20	0.34	0.2587	0.0331	0.0617	4.20

Table 4.8: Comparison of the maximum bending strains of the circular structure.

Motion #	Input (g)	AF33 (g)	G_m/G_{max}	V_s (m/s)	$\gamma^{\bigcirc}_{max}$ (milistrain)	$F^{\bigcirc}$	$\epsilon^{\bigcirc}_b$ (milistrain) NCHRP	$\epsilon^{\bigcirc}_b$ (milistrain) Centrifuge, Static	$\epsilon^{\bigcirc}_b$ (milistrain) Centrifuge, Dynamic	$e_b^{\text{NCHRP}}/e_b^{\text{Centrifuge}}$
3	0.015	0.030	0.958	162.2	0.066	129.0	0.0041	0.1471	0.0024	1.72
4	0.014	0.054	0.905	158.9	0.122	123.7	0.0075	0.1489	0.0046	1.64
5	0.015	0.037	0.945	161.1	0.080	127.2	0.0049	0.1510	0.0026	1.89
6	0.166	0.262	0.362	99.8	1.504	48.8	0.0904	0.1542	0.0700	1.29
7	0.198	0.323	0.271	86.3	2.477	36.5	0.1473	0.2167	0.0824	1.79
8	0.081	0.196	0.500	117.2	0.815	67.3	0.0494	0.2356	0.0249	1.99
9	0.470	0.608	0.070	43.7	18.181	9.4	0.9640	0.2415	0.3604	2.67
10	0.494	0.466	0.138	61.6	7.022	18.6	0.4013	0.3311	0.2521	1.59
11	0.423	0.476	0.129	59.6	7.660	17.4	0.4355	0.3363	0.1528	2.85

Table 4.9: Comparison of the maximum hoop strains of the circular structure.

Motion #	Input (g)	AF33 (g)	G_m/G_{max}	V_s (m/s)	$\gamma^{\bigcirc}_{max}$ (milistrain)	$C^{\bigcirc}$	$\epsilon^{\bigcirc}_h$ (milistrain) NCHRP	$\epsilon^{\bigcirc}_h$ (milistrain) Centrifuge, Static	$\epsilon^{\bigcirc}_h$ (milistrain) Centrifuge, Dynamic	$e_h^{\text{NCHRP}}/e_h^{\text{Centrifuge}}$
3	0.015	0.030	0.958	162.2	0.066	0.1119	0.0019	0.0698	0.0020	0.96
4	0.014	0.054	0.905	158.9	0.122	0.1073	0.0034	0.0700	0.0038	0.90
5	0.015	0.037	0.945	161.1	0.080	0.1103	0.0023	0.0699	0.0024	0.96
6	0.166	0.262	0.362	99.8	1.504	0.0423	0.0167	0.0699	0.0298	0.56
7	0.198	0.323	0.271	86.3	2.477	0.0317	0.0207	0.0779	0.0290	0.72
8	0.081	0.196	0.500	117.2	0.815	0.0584	0.0124	0.0792	0.0112	1.11
9	0.470	0.608	0.070	43.7	18.181	0.0081	0.0404	0.0792	0.0782	0.52
10	0.494	0.466	0.138	61.6	7.022	0.0161	0.0303	0.0823	0.0632	0.48
11	0.423	0.476	0.129	59.6	7.660	0.0151	0.0310	0.0942	0.0443	0.70

4.3.4 Comparison of the in-plane bending strains for the circular culvert

We use the same approach here for the circular culvert as we did for obtaining the bending strain of the rectangular structure. Figure 4.21 displays the static offset and dynamic increment of bending strain data recorded during different base shakings. Again, the bending strain data obtained from the NCHRP 611 method are included in the figures for comparison. As mentioned before, since the scaling factors that are used are not the same, these figures only provide a qualitative means of comparison as well as how the static and dynamic strain profiles vary with different motions. Table 4.8 summarizes the maximum values of the bending strains along with PoIs, and their relationships are illustrated in Figure 4.20. We observe that:

- The static strain offset increases as the model is subjected to more base shakings. This may be partially due to the densification of the soil around of the structure.
- In all cases, the flexibility ratio is greater than 1; and its value decreases as the surrounding soil becomes softer. Therefore, for low-amplitude motions, ovaling should be the dominant mode of deformation of the structure. On the other hand, as $F^{\bigcirc}$ decreases, the relative stiffness of the structure with respect to the surrounding soil increases, which would result in more (dynamic) SSI effects and therefore more complex behavior. The bending strain profiles shown in the figures ascertain this observation.
- In general, the NCHRP method overestimates the bending strains.
- Again, although the range of $\epsilon_b^{\text{NCHRP}}$ and $\epsilon_b^{\text{Centrifuge}}$ differ, they vary similarly with PoIs, especially with $F^{\bigcirc}$ and $\gamma_{max,0}$.

4.3.5 Comparison of the hoop strains for the circular culvert

We obtained the hoop strain profiles following the same procedure as before, which are shown in Figure 4.23. The summary of the PoIs and maximum hoop strain values are provided in Table 4.9 and Figure 4.22. We observe that:

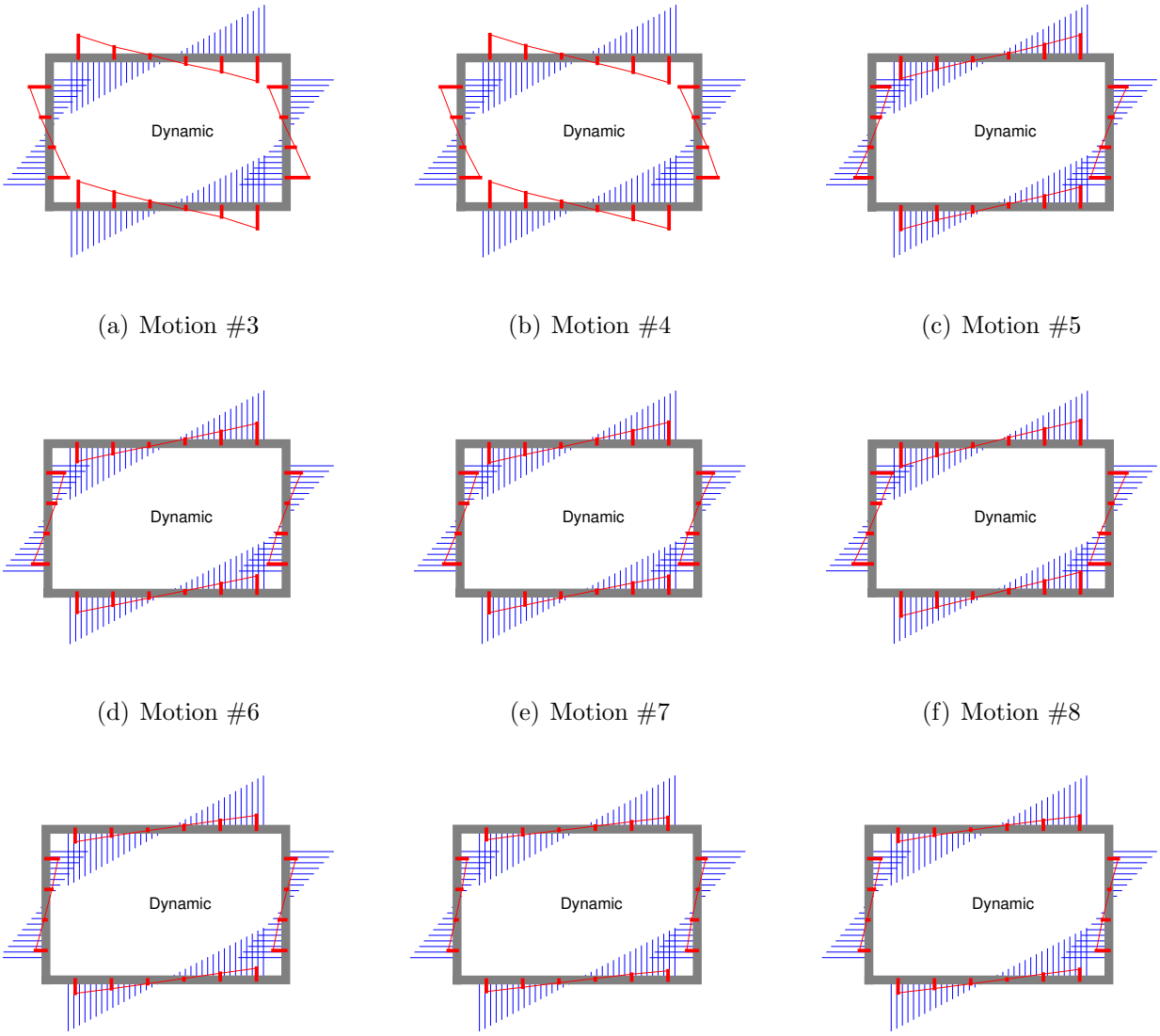

(a) Motion #3 (b) Motion #4 (c) Motion #5

(d) Motion #6 (e) Motion #7 (f) Motion #8

(g) Motion #9 (h) Motion #10 (i) Motion #11

Figure 4.19: Comparison of the experimental in-plane dynamic bending strains in the rectangular culvert with those from the NCHRP 611 method.

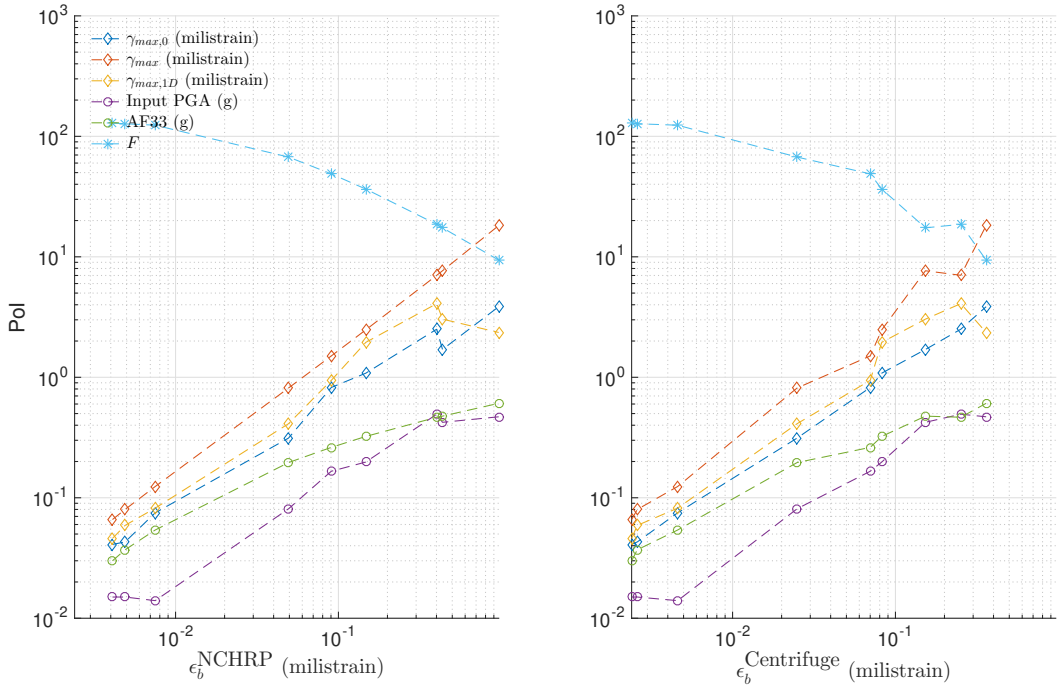

Figure 4.20: PoI correlation with maximum bending strain of the circular structure.

- The static hoop strain offset is less sensitive than the static bending strain to the application sequence of the base shakings.

- The computed compressibility ratios are less than 1 in all cases. Again, as the soil becomes softer, the relative stiffness of the structure with respect to the surrounding soil increases, and therefore, the compressibility ratio decreases. This can lead to more complex hoop strain profiles under higher amplitude base shakings.

- In general, the NCHRP method underestimates the hoop strains. This is while the NCHRP analysis method suggests the use of the full-slip condition in computing the thrust as a conservative approach to take care of amplifications due to dynamic SSI effects. However, we observe that this conservative solution still underestimates the hoop strains in the circular structure.

- The variations of $\epsilon_h^{\text{NCHRP}}$ and $\epsilon_h^{\text{Centrifuge}}$ with PoIs are similar, especially with respect to C.

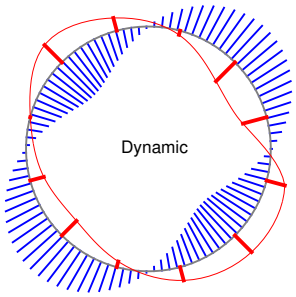

(a) Motion #3

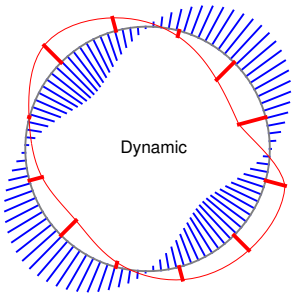

(b) Motion #4

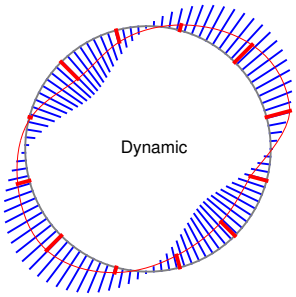

(c) Motion #5

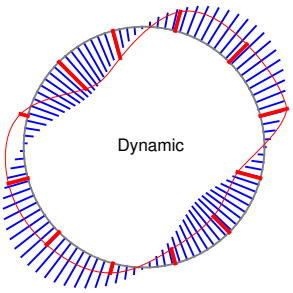

(d) Motion #6

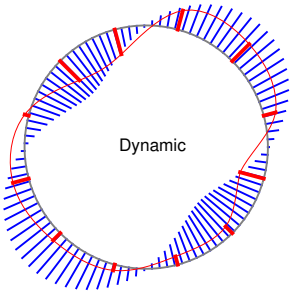

(e) Motion #7

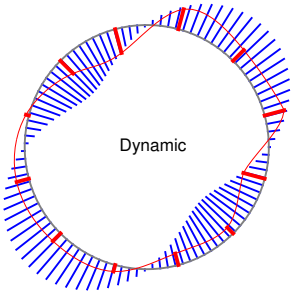

(f) Motion #8

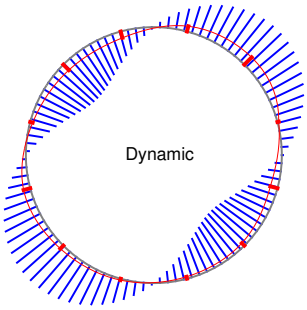

(g) Motion #9

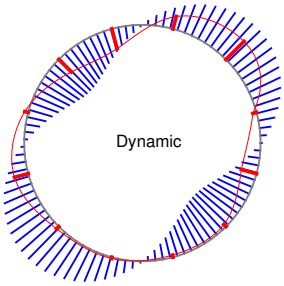

(h) Motion #10

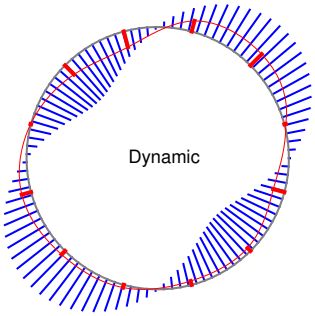

(i) Motion #11

Figure 4.21: Comparison of the experimental in-plane dynamic bending strains in the circular culvert against those from the NCHRP 611 method.

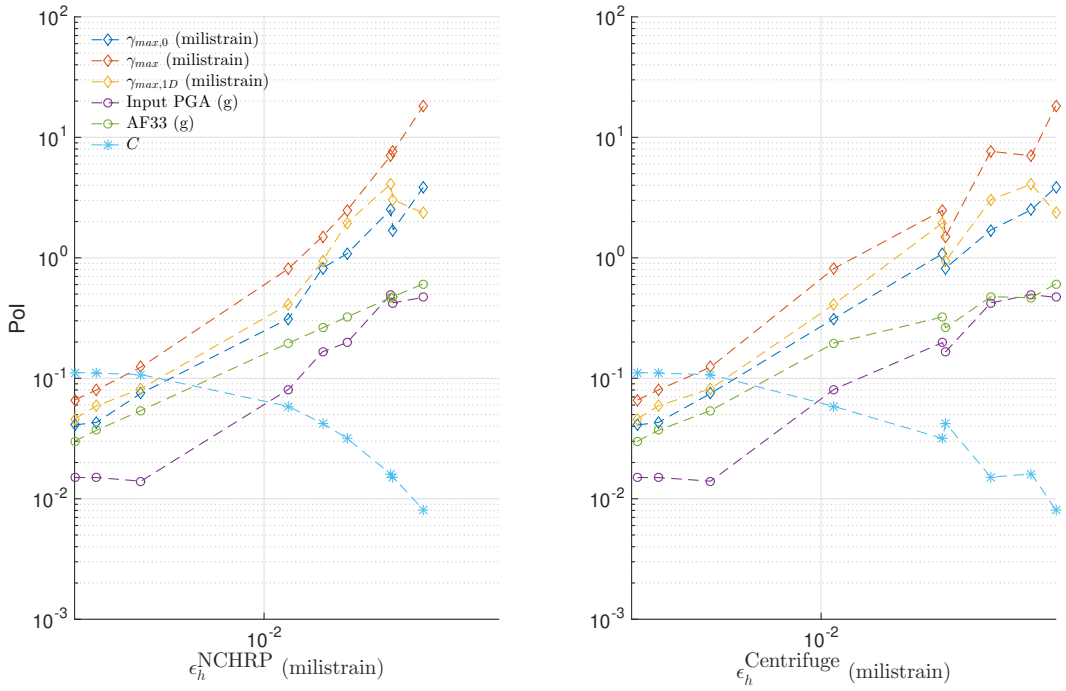

Figure 4.22: PoI correlation with maximum hoop strain of the circular structure.

4.3.6 The racking of the rectangular structure

As shown, the bending strains computed using the NCHRP 611 method have a direct relationship to the racking displacements imposed on the roof of the structure. In order to see how the computed Δ_s differs from the actual racking of the tested structure, we also computed the experimental racking from the recorded accelerations on the structure. That is,

$$\Delta^{\square}_{\text{s,left}} = u_7(t) - u_1(t) \tag{4.26}$$

$$\Delta^{\square}_{\text{s,right}} = u_3(t) - u_6(t) \tag{4.27}$$

where $u_i(t)$ for $i = \{1, 3, 6, 7\}$ are obtained from double integration of the processed acceleration data. Figure 4.24 displays the time series of the resulting racking deformations along the left and right walls of the structure along with the maximum racking deformations that we obtained through the NCHRP 611 method. As shown, the racking displacements along

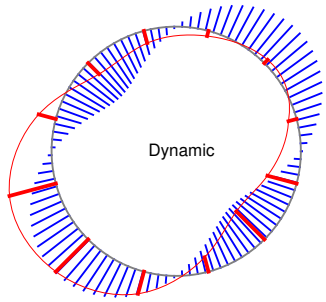

(a) Motion #3

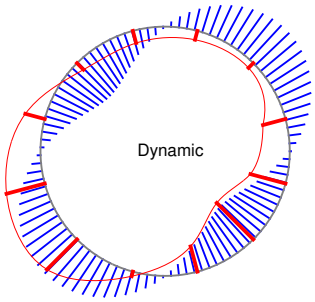

(b) Motion #4

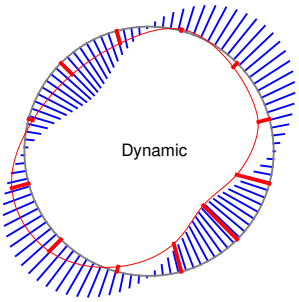

(c) Motion #5

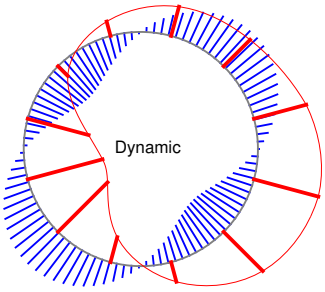

(d) Motion #6

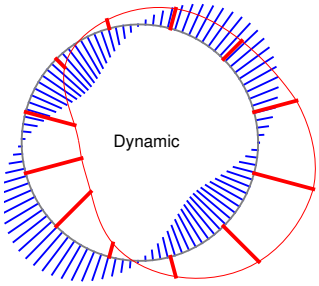

(e) Motion #7

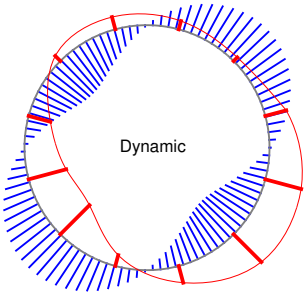

(f) Motion #8

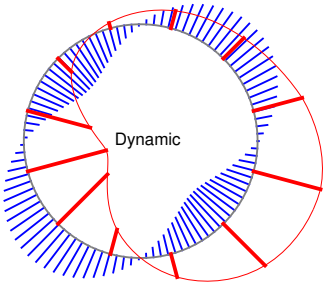

(g) Motion #9

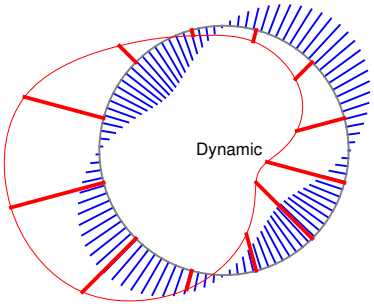

(h) Motion #10

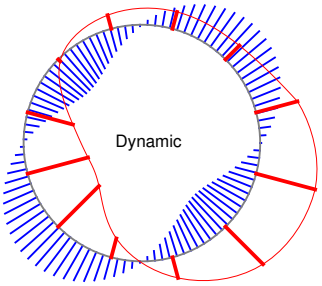

(i) Motion #11

Figure 4.23: Comparison of the experimental dynamic hoop strains in the circular culvert with those from the NCHRP 611 method.

the left and right walls conform to each other and their maximum values are considerably smaller than the NCHRP Δ_s.

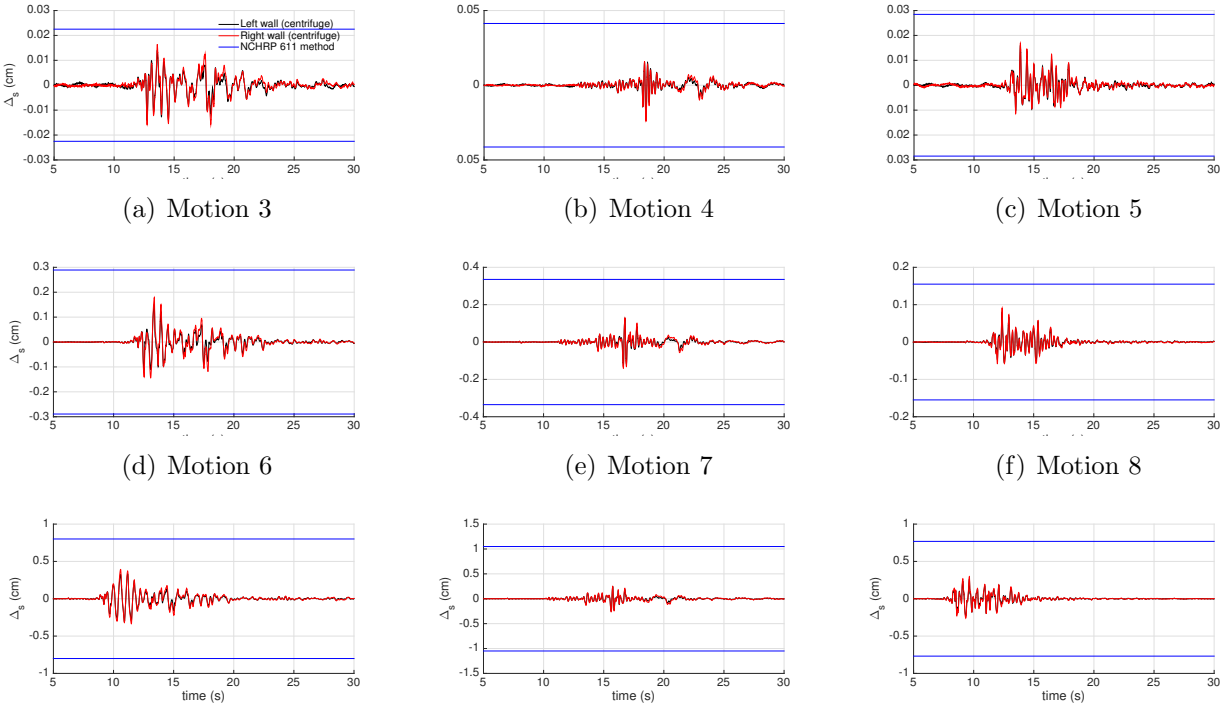

(a) Motion 3 (b) Motion 4 (c) Motion 5

(d) Motion 6 (e) Motion 7 (f) Motion 8

(g) Motion 9 (h) Motion 10 (i) Motion 11

Figure 4.24: Comparison of the rectangular structure racking displacements obtained from recorded accelerations on the structure and from the NCHRP 611 method.

4.3.7 Comparison of the von Mises stresses

In order to quantify the stress level in culvert cross sections, we also computed the von Mises equivalent stress. This stress invariant is a typical metric used in the strength-based design of metal components, and could also be applied to culverts. Using a scalar invariant such as von Mises stress for comparisons of different methods is desirable in that it combines discrepancies in all of the predicted-vs-measured stress/strain components into single measure.

Assuming a plane strain condition[2]:

$$\sigma_{11} = E\epsilon_{11}, \sigma_{22} = 0, \sigma_{33} = \frac{\nu E}{(1+\nu)(1-2\nu)}\epsilon_{11}, \sigma_{12} = \sigma 13 = \sigma 23 = 0\,, \tag{4.28}$$

and therefore,

$$\sigma_{vm} = \sqrt{\sigma_{11}^2 + \sigma_{33}^2 - \sigma_{11}\sigma_{33}}\,. \tag{4.29}$$

Using the above equation and considering $\nu = 1/3$ and $E = 68.95$ GPa for Aluminum, Table 4.10 provides the resulting von Mises stresses σ_{vm} for each motion.

Table 4.10: Comparison of the Von Mises stress in the culvert structures.

Motion #	$\sigma_{vm}^{\bigcirc}$ (MPa) NCHRP (1)	$\sigma_{vm}^{\bigcirc}$ (MPa) NCHRP-1D (2)	$\sigma_{vm}^{\bigcirc}$ (MPa) Centrifuge (3)	$\sigma_{vm}^{\square}$ (MPa) NCHRP (4)	$\sigma_{vm}^{\square}$ (MPa) NCHRP-1D (5)	$\sigma_{vm}^{\square}$ (MPa) Centrifuge (6)	$\sigma_{vm}^{\bigcirc}$ (1/3) (7)	$\sigma_{vm}^{\bigcirc}$ (2/3) (8)	$\sigma_{vm}^{\square}$ (4/6) (9)	$\sigma_{vm}^{\square}$ (5/6) (10)
3	0.4	0.3	0.2	0.5	0.2	0.2	2.0	1.5	2.5	1.0
4	0.7	0.5	0.4	0.9	0.3	0.4	1.8	1.25	2.3	0.75
5	0.4	0.3	0.2	0.6	0.2	0.2	2.0	1.5	3.0	1.0
6	6.6	4.4	4.7	6.7	2.0	2.2	1.4	0.9	3.0	0.9
7	10.4	8.4	5.5	7.8	3.0	2.8	1.9	1.5	2.8	1.1
8	3.8	2.1	1.7	3.6	1.0	1.4	2.2	1.2	2.6	0.7
9	62.4	10.0	22.8	17.4	5.1	4.2	2.7	0.4	4.1	1.2
10	26.8	16.4	16.0	22.1	5.1	4.7	1.7	1.0	4.7	1.1
11	29.0	12.6	10.0	16.8	4.0	3.8	2.9	1.3	4.4	1.1

4.3.8 Effects of using $\gamma_{max,1D}$ for computing bending and hoop strains and racking displacements via the NCHRP 611 method

As shown in the previous sections, using the NCHRP 611 method with the iterative procedure to compute γ_{max} resulted in the over-estimation of bending strains in both rectangular and circular culverts. We repeated the NCHRP 611 procedure using $\gamma_{max,1D}$ as the input. As mentioned before, we computed $\gamma_{max,1D}$ for each case by performing nonlinear 1D wave propagation analyses in ABAQUS using soil model parameters obtained form the Bayesian approach. We will use these parameters for our numerical simulations, as it will be discussed in detail in section 4.4.

[2]It should be noted that in general σ_{22} is not zero and its effects should be considered in computing the von Mises stress.

Figures 4.25, 4.26 and 4.27 provide the dynamic bending strain profiles for the rectangular culvert, dynamic bending strain profiles for the circular culvert, and the dynamic hoop strain profiles for the circular culvert, respectively. Figure 4.28 displays the comparison of the racking displacements in the rectangular culvert. As seen, using the more-refined procedure to compute maximum free field shear strain resulted in bending strain profiles that are closer to those measured in the centrifuge experiments, and tended to underestimate the profiles in many cases. This trend is even worse for the hoop strains. Table 4.11 summarizes the resulting maximum strain ratios compared to those we obtained using the NCHRP 611 iterative procedure. Moreover, as shown in Figure 4.28, the racking displacements have also become in the same order of those computed from the experimental data. This shows the importance of the choice for γ_{max} if/when we want to use the NCHRP 611 method to compute the seismic demands in culvert structures.

Table 4.11: Maximum bending and hoop strain ratio comparisons when we use the NCHRP 611 iterative procedure and the more-refined 1D site response analysis to compute the free shear strain.

Motion	$e_b^{\square}$, using $\gamma_{\max}$	$e_b^{\square}$, using $\gamma_{\max,1D}$	$e_b^{\bigcirc}$, using $\gamma_{\max}$	$e_b^{\bigcirc}$, using $\gamma_{\max,1D}$	$e_h^{\bigcirc}$, using $\gamma_{\max}$	$e_h^{\bigcirc}$, using $\gamma_{\max,1D}$
3	2.17	0.65	1.72	1.19	0.96	0.71
4	2.21	0.65	1.64	1.09	0.90	0.61
5	2.42	0.72	1.89	1.38	0.96	0.71
6	2.86	0.84	1.29	0.82	0.56	0.45
7	2.68	1.04	1.79	1.42	0.72	0.65
8	2.46	0.68	1.99	1.01	1.11	0.75
9	3.94	1.15	2.67	0.39	0.52	0.26
10	4.50	1.03	1.59	0.95	0.48	0.40
11	4.20	0.99	2.85	1.18	0.70	0.51

4.4 Finite element modeling & analysis of the centrifuge tests

In this section, we provide details of direct numerical modeling of the conducted centrifuge experiments and investigate the predictive capabilities of the calibrated finite element model to capture the key response parameters.

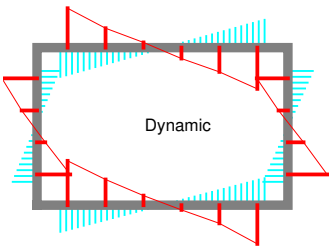

(a) Motion #3

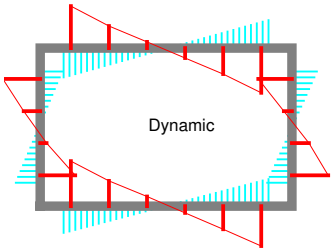

(b) Motion #4

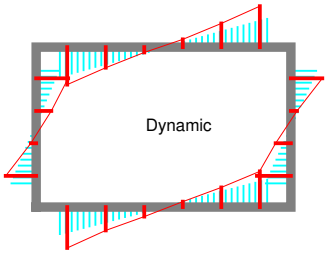

(c) Motion #5

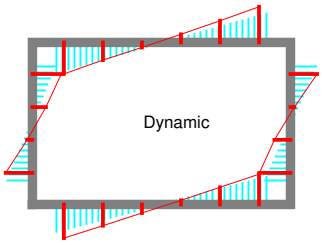

(d) Motion #6

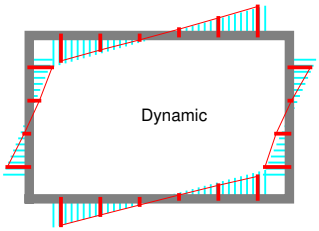

(e) Motion #7

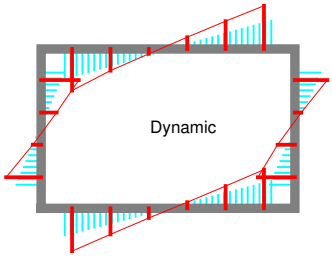

(f) Motion #8

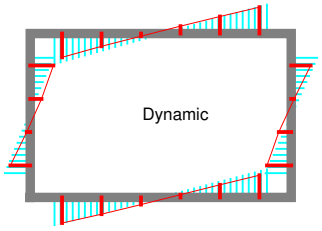

(g) Motion #9

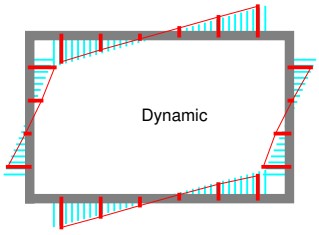

(h) Motion #10

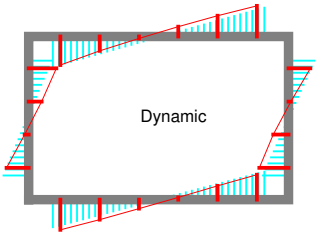

(i) Motion #11

Figure 4.25: Comparison of the experimental in-plane dynamic bending strains in the rectangular culvert against those from the NCHRP 611 method when $\gamma_{max,1D}$ is used as the input maximum free field shear strain.

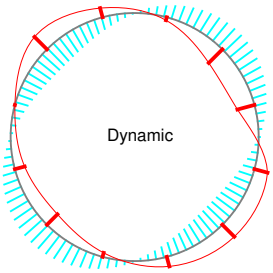

(a) Motion #3

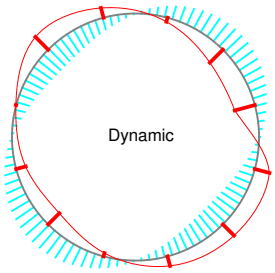

(b) Motion #4

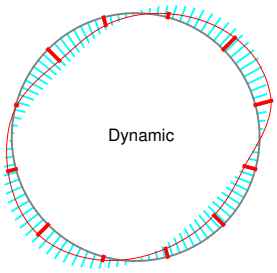

(c) Motion #5

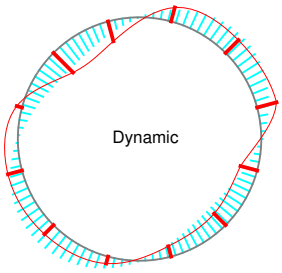

(d) Motion #6

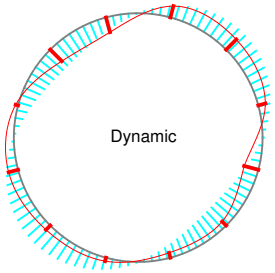

(e) Motion #7

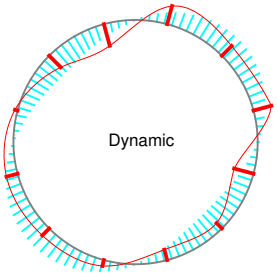

(f) Motion #8

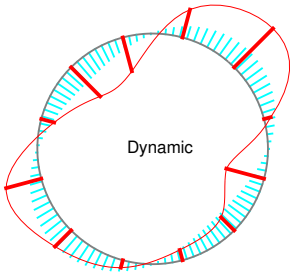

(g) Motion #9

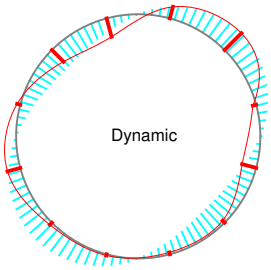

(h) Motion #10

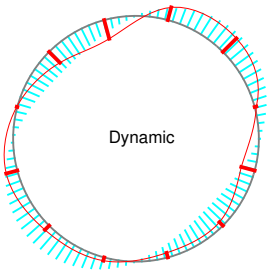

(i) Motion #11

Figure 4.26: Comparison of the experimental in-plane dynamic bending strains in the circular culvert against those from the NCHRP 611 method when $\gamma_{max,1D}$ is used as the input maximum free field shear strain.

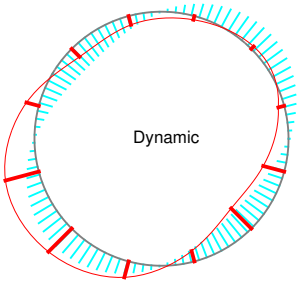

(a) Motion #3

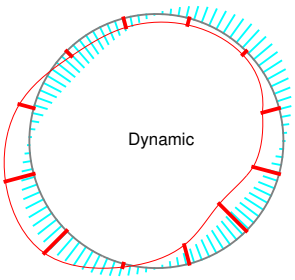

(b) Motion #4

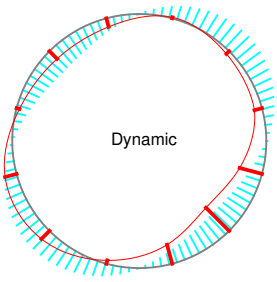

(c) Motion #5

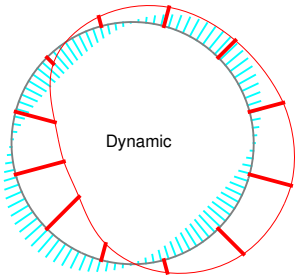

(d) Motion #6

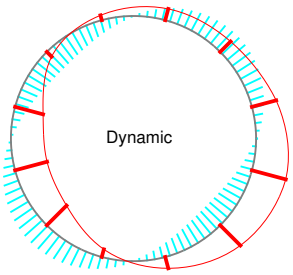

(e) Motion #7

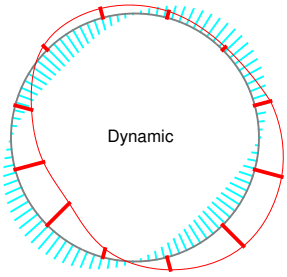

(f) Motion #8

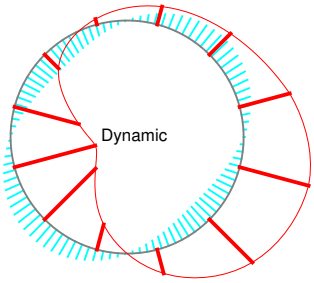

(g) Motion #9

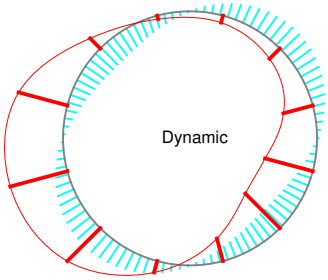

(h) Motion #10

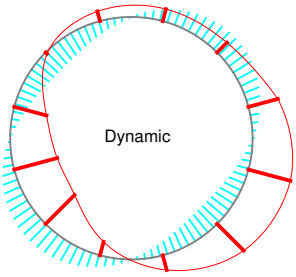

(i) Motion #11

Figure 4.27: Comparison of the experimental dynamic hoop strains in the circular culvert against those from the NCHRP 611 method when $\gamma_{max,1D}$ is used as the input maximum free field shear strain.

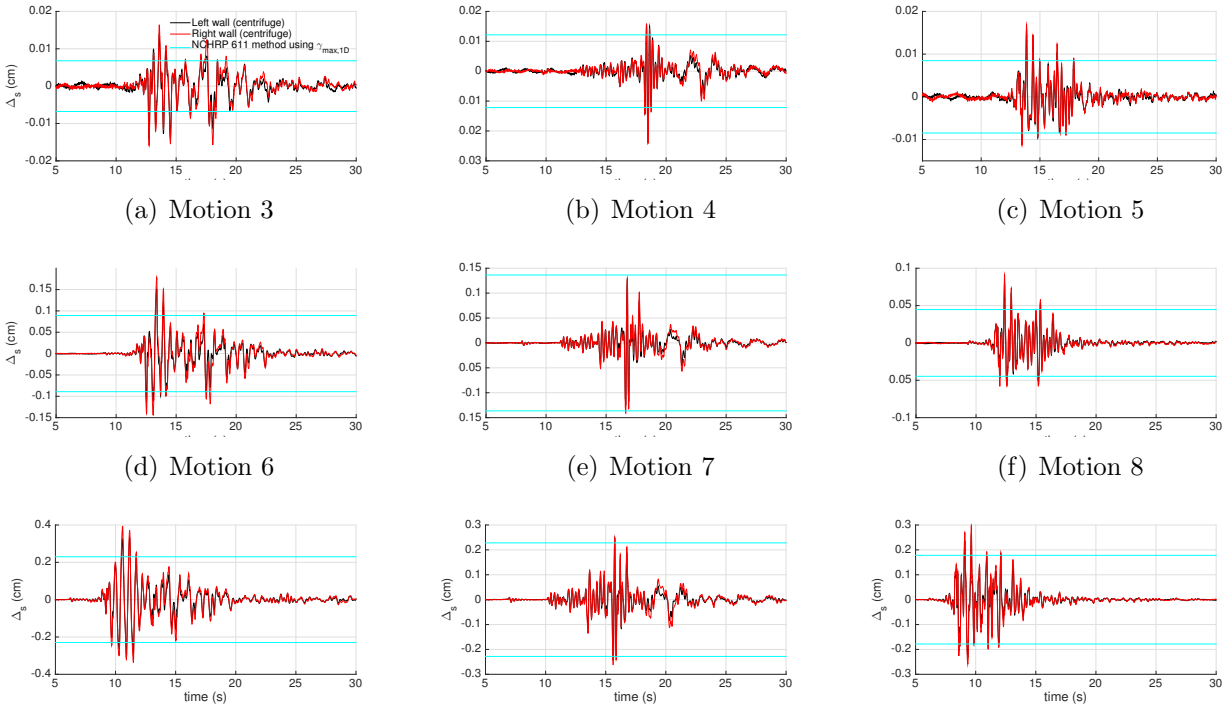

(a) Motion 3 (b) Motion 4 (c) Motion 5

(d) Motion 6 (e) Motion 7 (f) Motion 8

(g) Motion 9 (h) Motion 10 (i) Motion 11

Figure 4.28: Comparison of the rectangular structure racking displacement obtained from recorded accelerations on the structure and from the NCHRP 611 method using $\gamma_{max,1D}$ as the input.

4.4.1 Development of the numerical model

In order to numerically study the dynamic SSI behavior of the centrifuge specimens, a two-dimensional (2D) finite element model was constructed in prototype scale based on the dimensions given in Figure 4.5. In experiments with earthquake excitations (i.e., motions 3 to 11), the scaling factor N ranges from $20.7g$ to $21.1g$. As such, we decided to use the same factor of $N = 21g$ for all numerical simulations in this report. As shown in Figure 4.29, the input motion is applied along the bottom boundary of the model, where the vertical degrees of freedom are fixed. We did not model the container explicitly. Instead, we imposed periodic boundary conditions along horizontal degrees of freedom at the left and right vertical edges of the soil domain while their vertical degrees of freedom are fixed, since a flexible shear beam container is used for the experiments. It should be noted that this configuration is used in the dynamic loading steps of analyses. In order to set up the initial stress conditions appropriately, we also performed a static analyses under gravity loading prior to each dynamic analysis. During the static analyses, we fixed the horizontal degrees of freedom at the left and right vertical edges of the discretized model, while leaving the vertical degrees of freedom free.

We used bilinear plane-strain elements for modeling the soil and the rectangular structure and beam elements for modeling the circular structure. We also used frictional contact elements to model sliding at the soil-structure interface. Following [76] and by considering the soil friction angle of $\phi_{\text{soil}} = 35$ degrees, the friction coefficient of the interface elements is computed as,

$$\tan\left(\phi_{\text{interface}}\right) = 0.7 \tan\left(\phi_{\text{soil}}\right) \approx 0.33\,. \tag{4.30}$$

As the structures were expected to behave linear elastically in all of the experiments, we used linear elastic material models for both culverts using the properties of Aluminum T60-61, which are $\gamma = 26.5$ kN/m^3, $E = 68.9$ GPa and $\nu = 0.33$. On other hand, for capturing the nonlinear soil behavior, which is a relatively dense dry Ottawa sand, we used

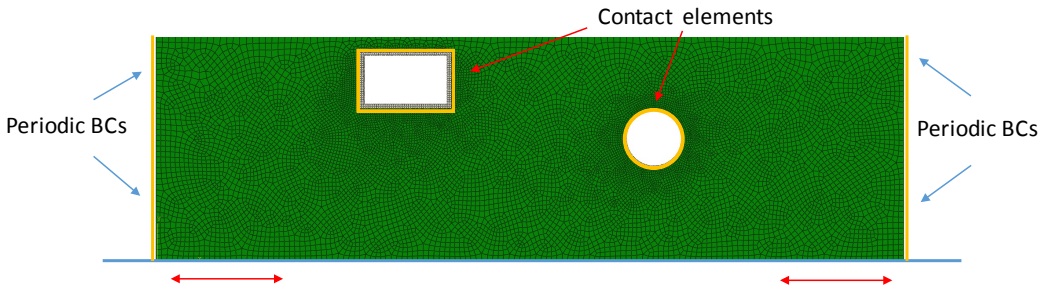

Figure 4.29: Mesh configuration of the finite element model used in numerical analysis.

a multi-axial cyclic plasticity model. Details of this model are provided in chapter 2.

4.4.2 Calibration of the soil parameters from centrifuge data

Borja's model can be defined by small strain shear wave velocity profile, modulus reduction curves, small strain damping, and shear strength of the soil deposit at hand. It can be shown that under the simple shear test condition, the following relationship exists between the normalized shear modulus $G/G_{\max}$ and shear strain γ using Borja's model [68].

$$\frac{G}{G_{\max}} + \frac{3}{2\gamma}\int_0^{2G_i\gamma}\left[h\left(\frac{R/\sqrt{2}+G\gamma-\tau}{\tau}\right)^m + H_0\right]^{-1} \mathrm{d}\tau - 1 = 0. \tag{4.31}$$

Therefore, for the given $G/G_{\max}$ curve, one can obtain the unknown parameters h, m, R and H_0 by solving a series of nonlinear equations or via the least squares method [71]. As mentioned earlier in section 4.3, we used a Bayesian approach to infer the shear wave velocity, $G/G_{\max}$ and the small strain viscous damping coefficient a_1 from free field acceleration measurements. Assuming a power function for the shear wave velocity profile and the hardening parameter h resulted in

$$V_s\ (\mathrm{m/s}) = 16.905 + 192.976\left(\frac{z}{H}\right)^{0.331} \tag{4.32}$$

and

$$h = \left[0.107 + 0.474\left(\frac{z}{H}\right)^{4.581}\right] G_{\max} \tag{4.33}$$

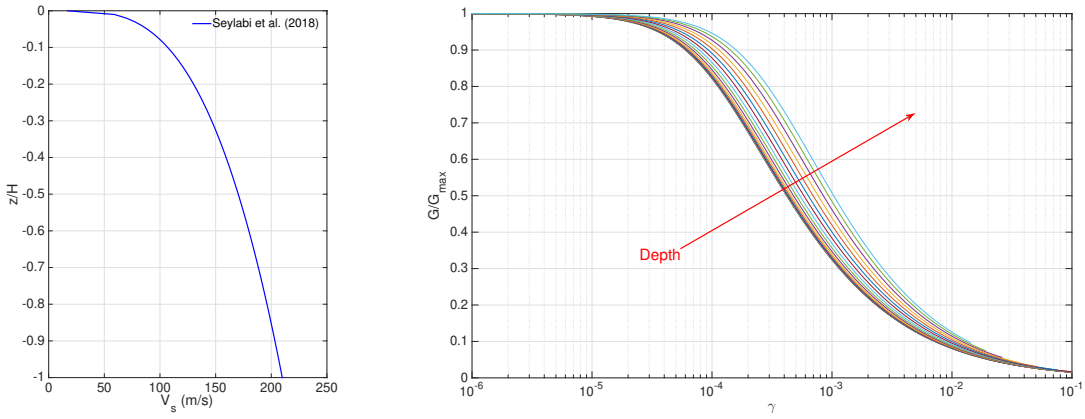

(a) Shear wave velocity profile (b) $G/G_{\max}$ curves for different depth

Figure 4.30: Calibrated shear wave velocity profile and $G/G_{\max}$ curves over the depth.

along with other parameters estimated as

$$m = 1.579,\ R = 0.0028\ G_{\max},\ a_1 = 0.0031\,. \tag{4.34}$$

We also assumed that $H_0 = 0$. Figure 4.30 displays the resulting calibrated shear wave velocity profile and the $G/G_{\max}$ curves for different depths, which are used in various numerical analyses of this report.

4.4.3 Numerical analyses

We used the calibrated soil model in finite element models of the centrifuge tests and performed numerical simulations using the earthquake excitations as input motions. To examine the predictive capabilities of the finite element models, we present the measured and numerically computed accelerations at various locations within the soil and on the specimen structures, the bending strains along the rectangular structure, and the bending and hoop strains along the circular structure in the following subsections.

4.4.3.1 Comparison of horizontal accelerations in soil

Figures 4.31-4.39 display comparisons of horizontal acceleration time-series and Fourier amplitudes for the left/southern acceleration array (i.e., locations AA1, AC12, AD18, AE25 and AF28). Figures 4.40-4.48 display similar data for the middle array (i.e., locations AAH5, AC16, ADH23, AE26 and AFH30). For the reader's convenience, we recall here that the motions 3-5 were low-amplitude, 6-8 were moderate amplitude, and 9-11 were high amplitude excitations (see Figure 4.8). As shown, the finite element models generally capture the time-series and the Fourier amplitude spectra of the measured accelerations for all motion amplitudes. It should be noted that we used only the left array acceleration data from motions #3 and #9 for calibrating the soil constitutive model parameters. Moreover, as shown, ICP AAH5 was only functional during motions 3, 4, and 5.

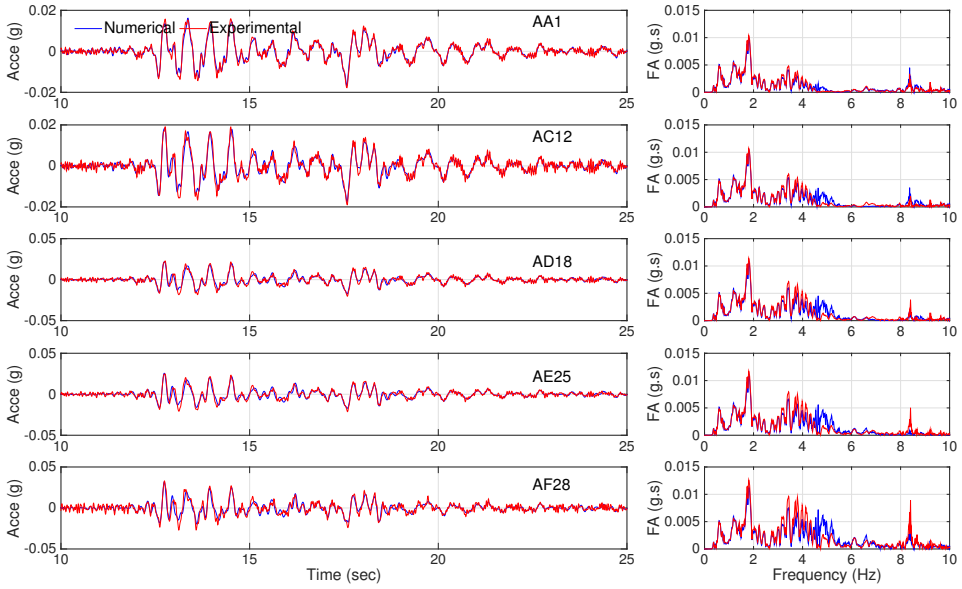

Figure 4.31: Time series and Fourier amplitude spectra of the accelerations recorded at the left array (AA1, AC12, AD18, AE25 and AF28) for motion #3.

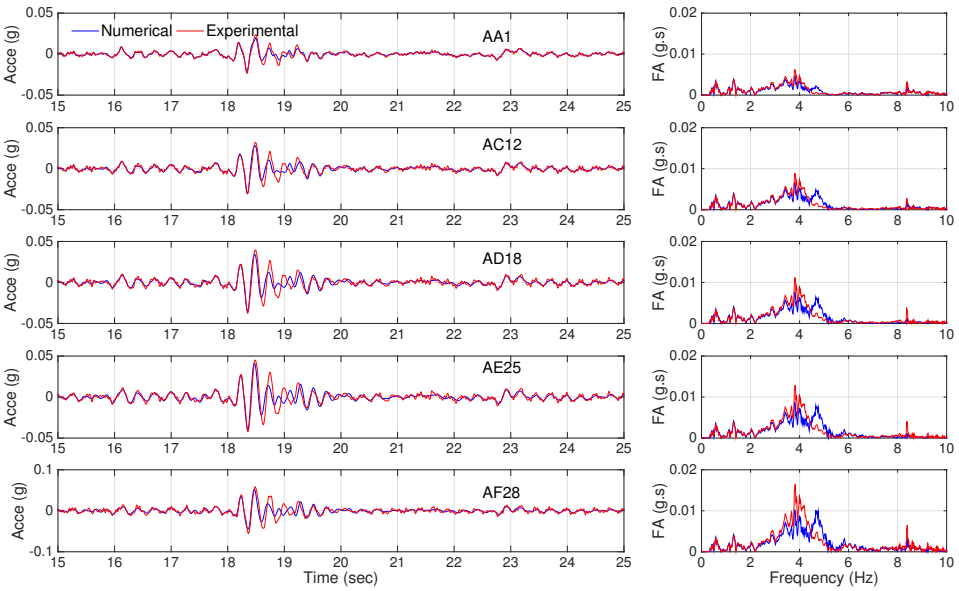

Figure 4.32: Time series and Fourier amplitude spectra of the accelerations recorded at the left array (AA1, AC12, AD18, AE25 and AF28) for motion #4.

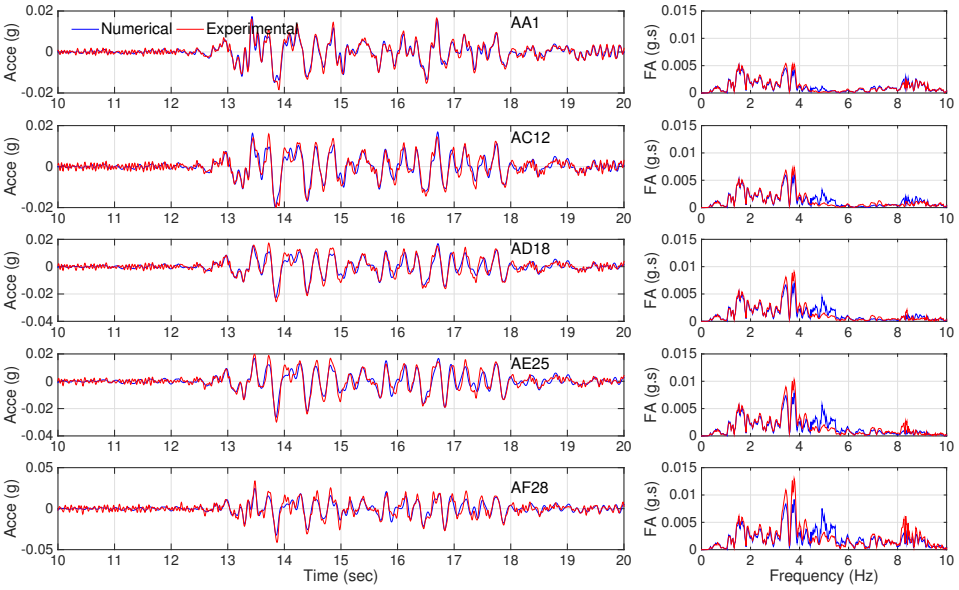

Figure 4.33: Time series and Fourier amplitude spectra of the accelerations recorded at the left array (AA1, AC12, AD18, AE25 and AF28) for motion #5.

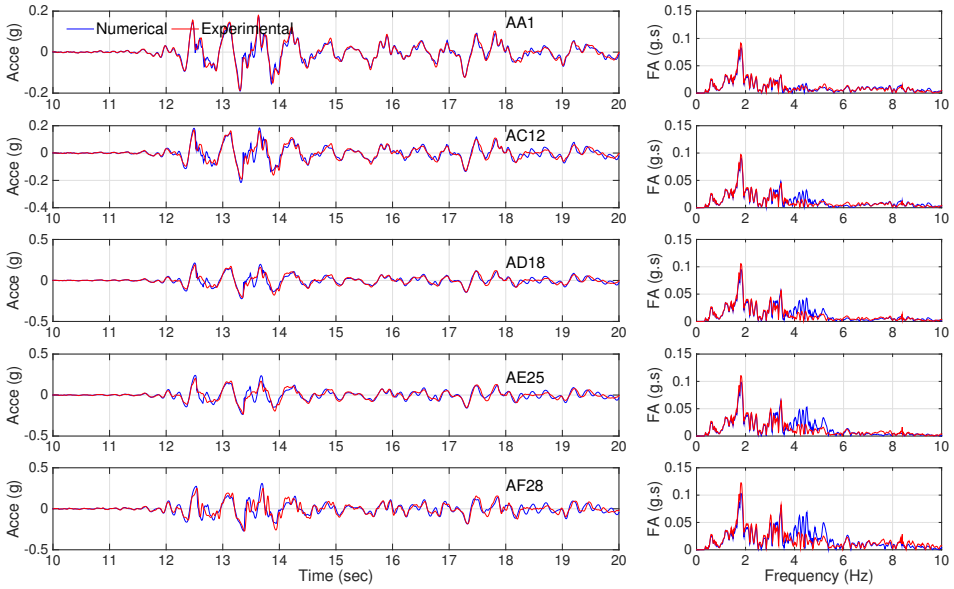

Figure 4.34: Time series and Fourier amplitude spectra of the accelerations recorded at the left array (AA1, AC12, AD18, AE25 and AF28) for motion #6.

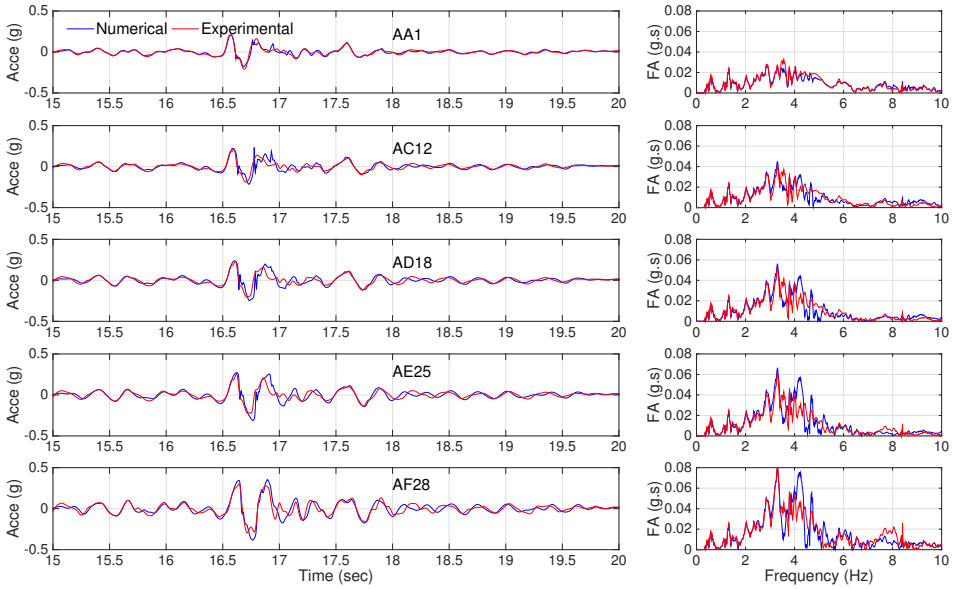

Figure 4.35: Time series and Fourier amplitude spectra of the accelerations recorded at the left array (AA1, AC12, AD18, AE25 and AF28) for motion #7.

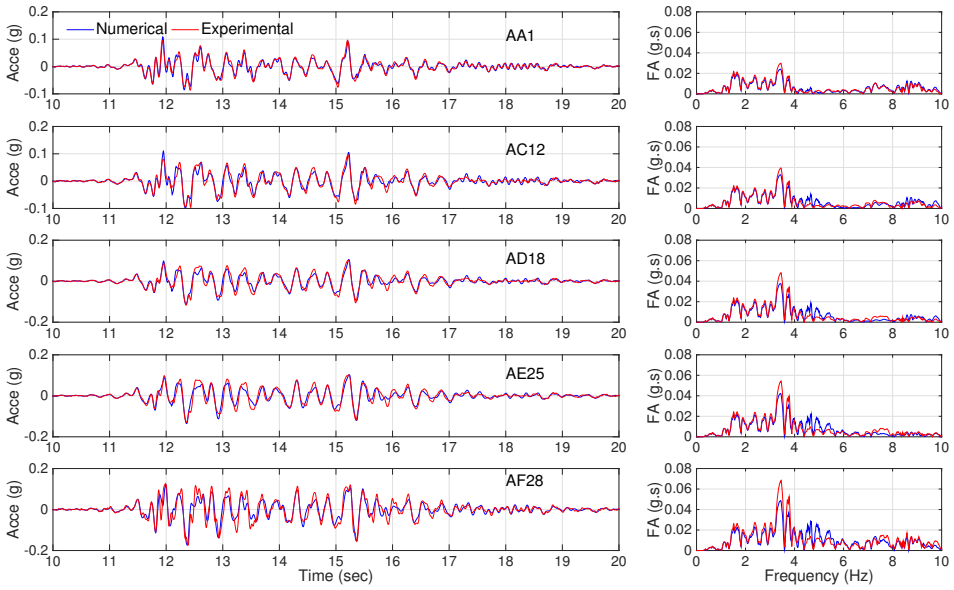

Figure 4.36: Time series and Fourier amplitude spectra of the accelerations recorded at the left array (AA1, AC12, AD18, AE25 and AF28) for motion #8.

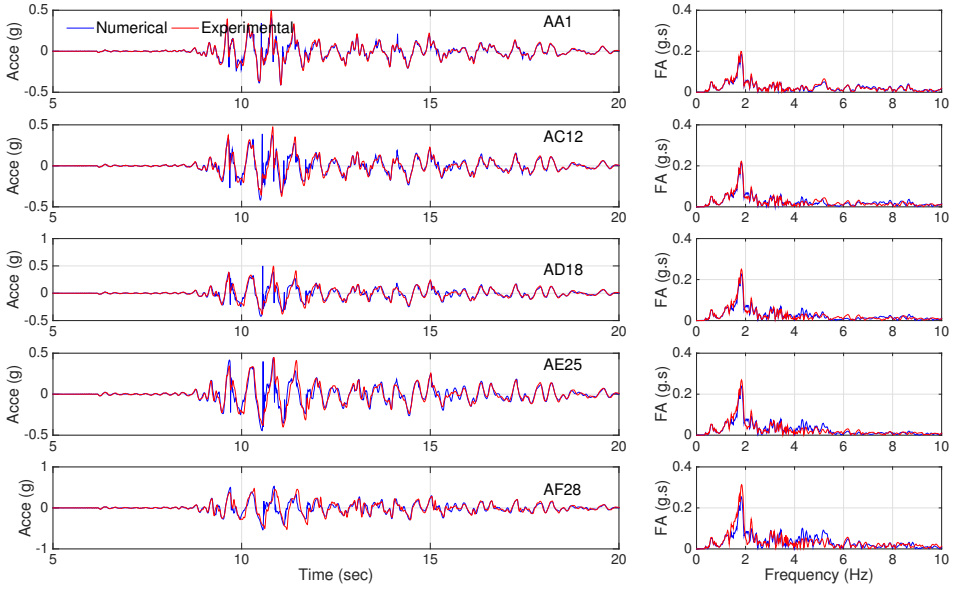

Figure 4.37: Time series and Fourier amplitude spectra of the accelerations recorded at the left array (AA1, AC12, AD18, AE25 and AF28) for motion #9.

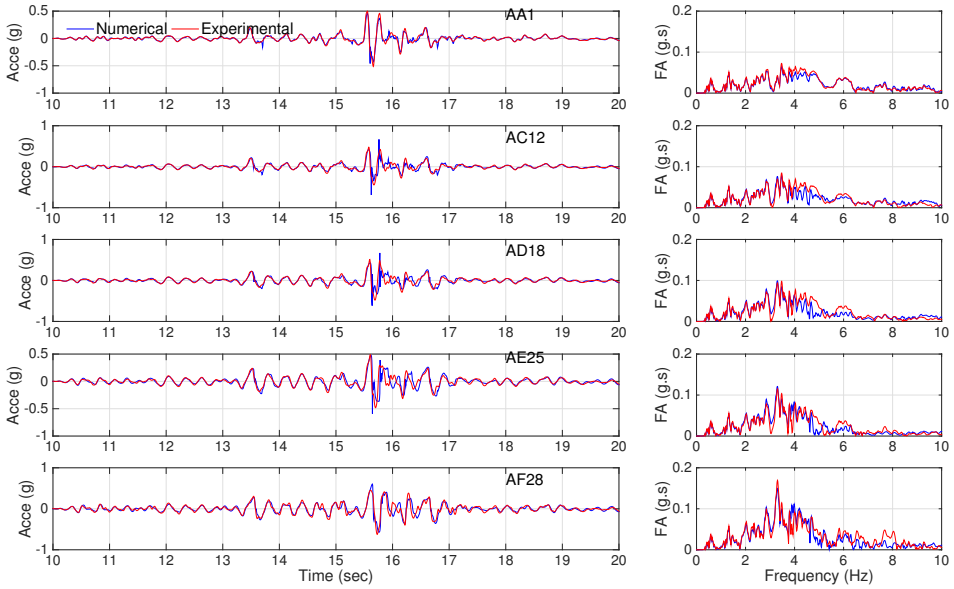

Figure 4.38: Time series and Fourier amplitude spectra of the accelerations recorded at the left array (AA1, AC12, AD18, AE25 and AF28) for motion #10.

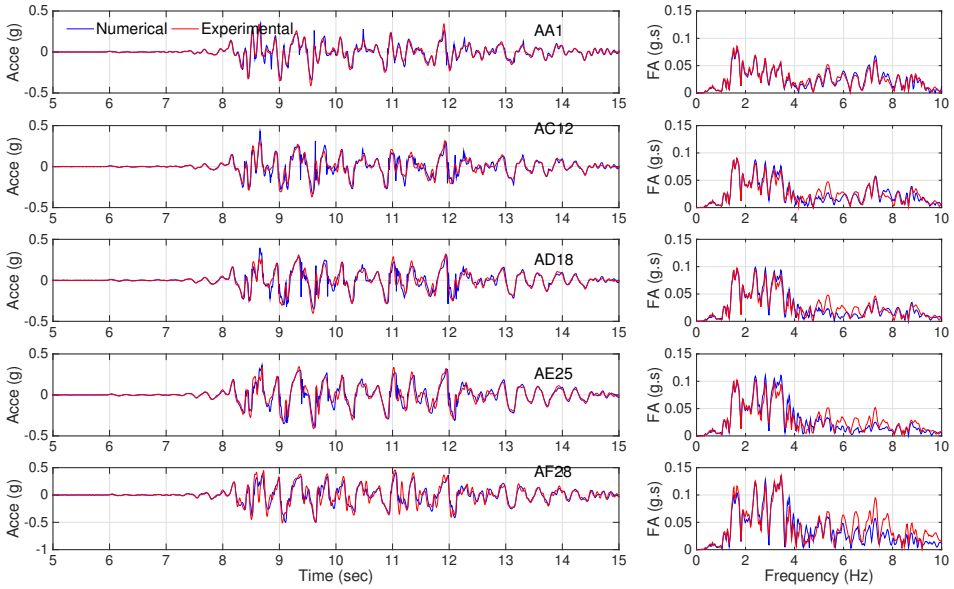

Figure 4.39: Time series and Fourier amplitude spectra of the accelerations recorded at the left array (AA1, AC12, AD18, AE25 and AF28) for motion #11.

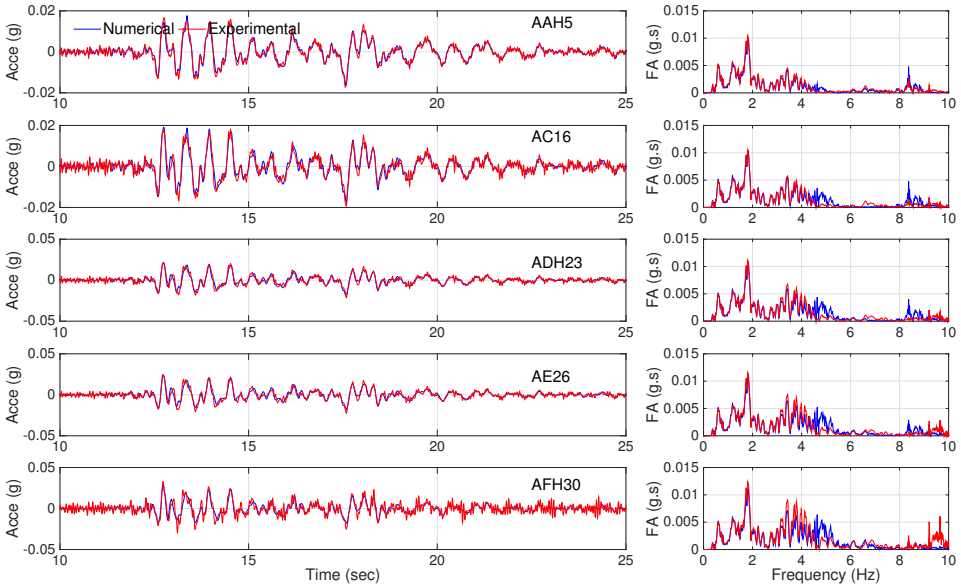

Figure 4.40: Time series and Fourier amplitude spectra of the accelerations recorded at the middle array (AAH5, AC16, ADH23, AE26 and AFH30) for motion #3.

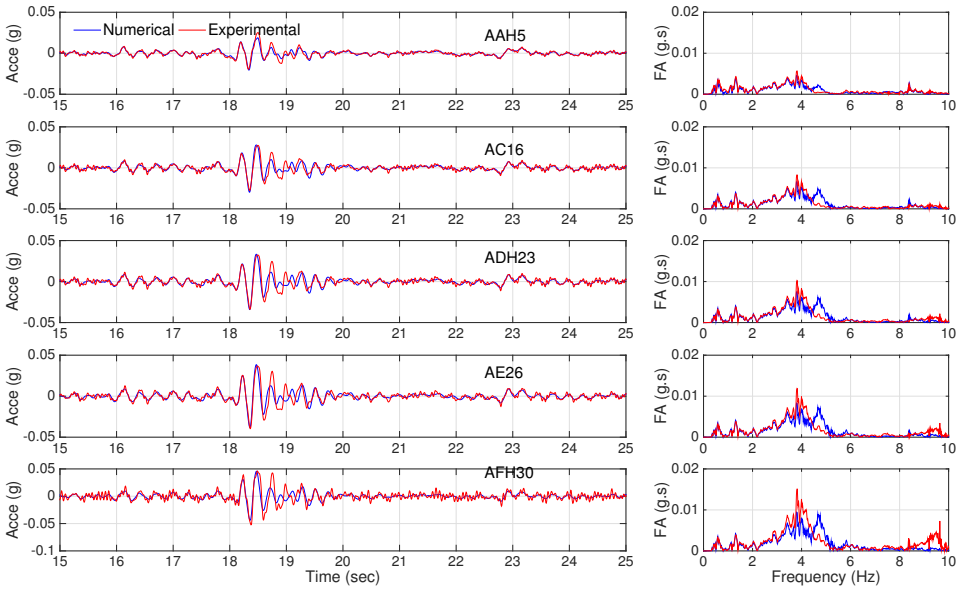

Figure 4.41: Time series and Fourier amplitude spectra of the accelerations recorded at the middle array (AAH5, AC16, ADH23, AE26 and AFH30) for motion #4.

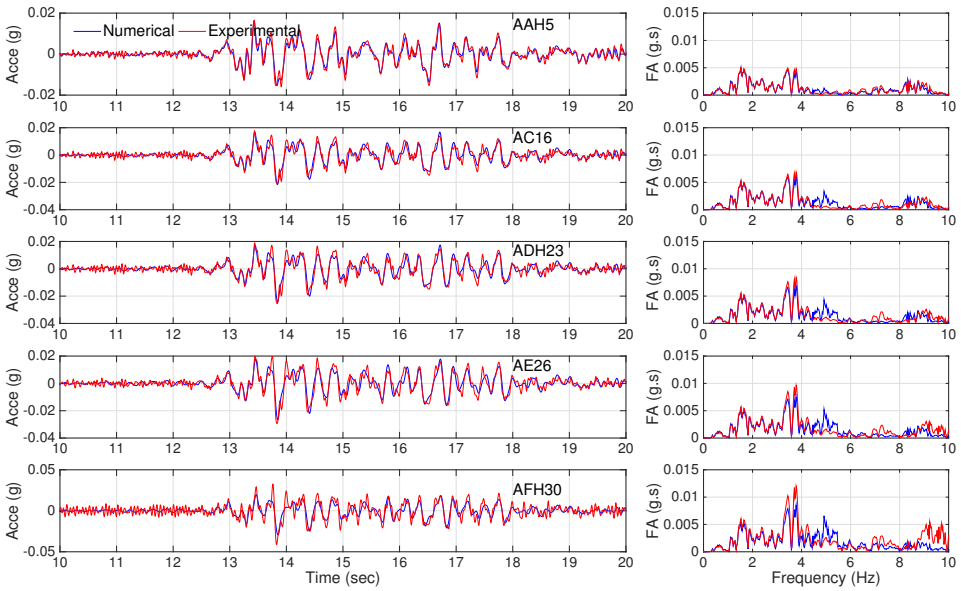

Figure 4.42: Time series and Fourier amplitude spectra of the accelerations recorded at the middle array (AAH5, AC16, ADH23, AE26 and AFH30) for motion #5.

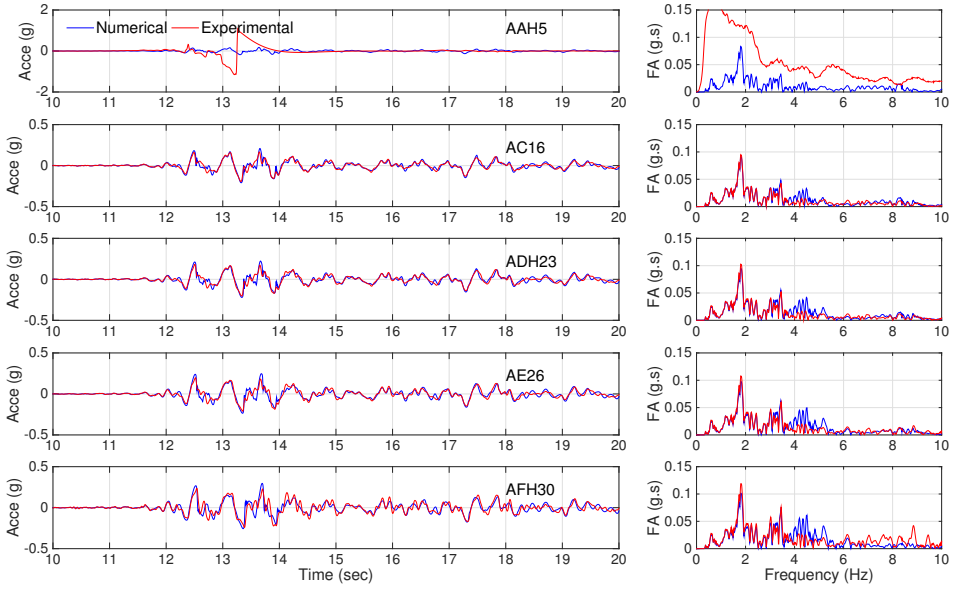

Figure 4.43: Time series and Fourier amplitude spectra of the accelerations recorded at the middle array (AAH5, AC16, ADH23, AE26 and AFH30) for motion #6.

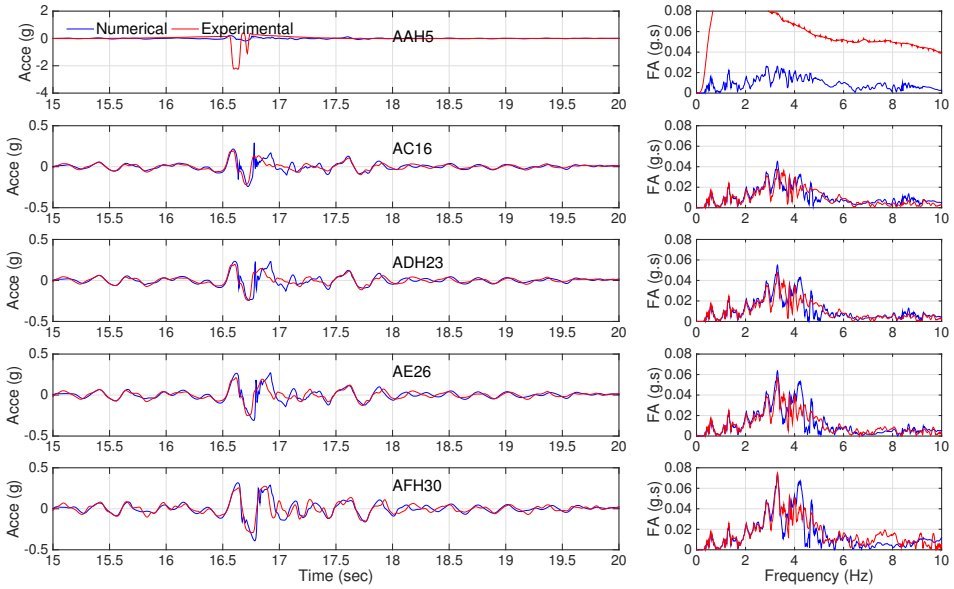

Figure 4.44: Time series and Fourier amplitude spectra of the accelerations recorded at the middle array (AAH5, AC16, ADH23, AE26 and AFH30) for motion #7.

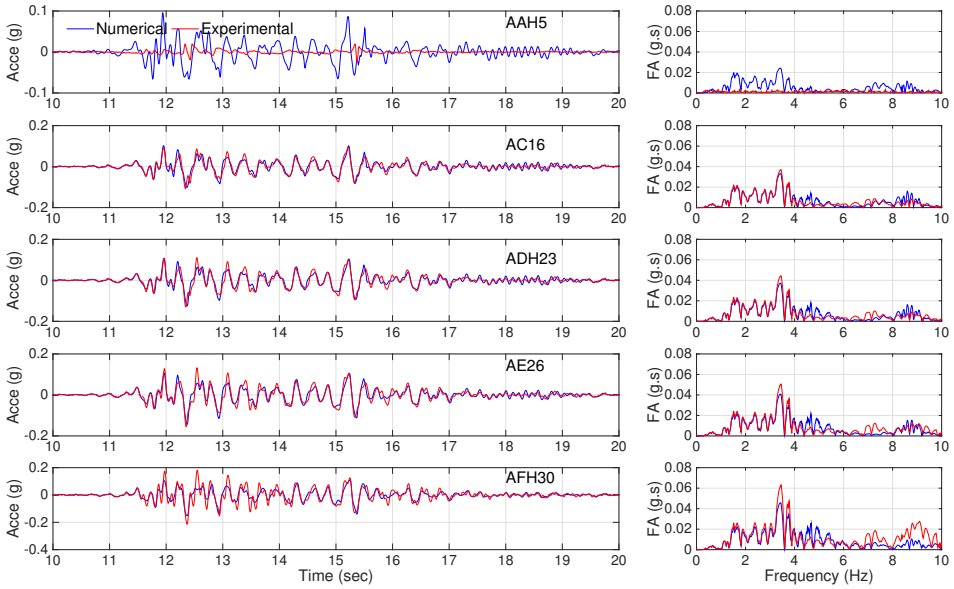

Figure 4.45: Time series and Fourier amplitude spectra of the accelerations recorded at the middle array (AAH5, AC16, ADH23, AE26 and AFH30) for motion #8.

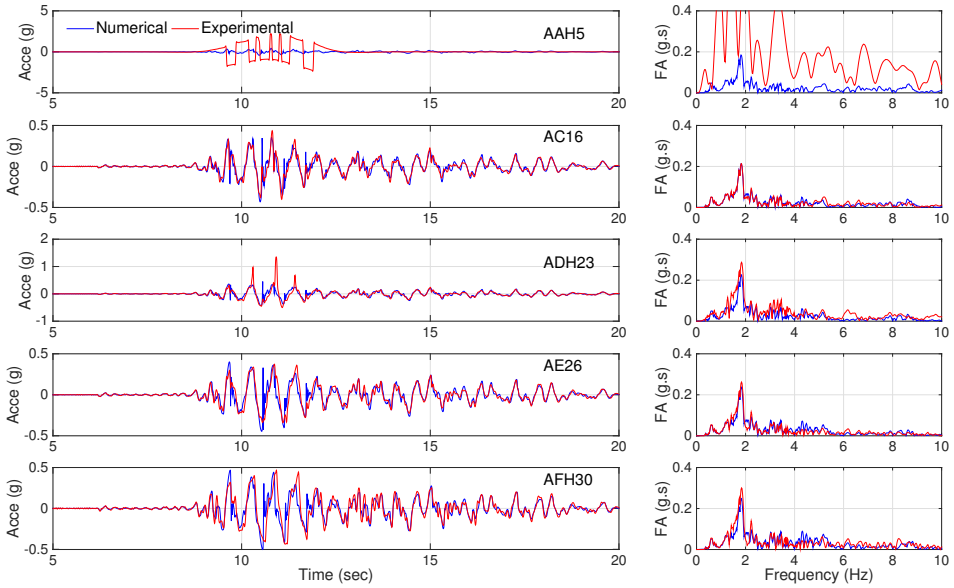

Figure 4.46: Time series and Fourier amplitude spectra of the accelerations recorded at the middle array (AAH5, AC16, ADH23, AE26 and AFH30) for motion #9.

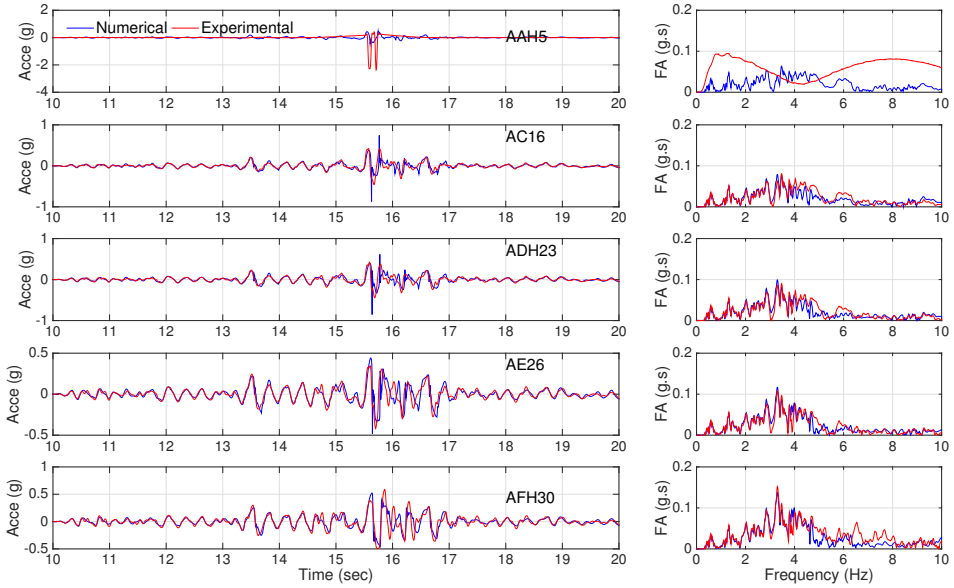

Figure 4.47: Time series and Fourier amplitude spectra of the accelerations recorded at the middle array (AAH5, AC16, ADH23, AE26 and AFH30) for motion #10.

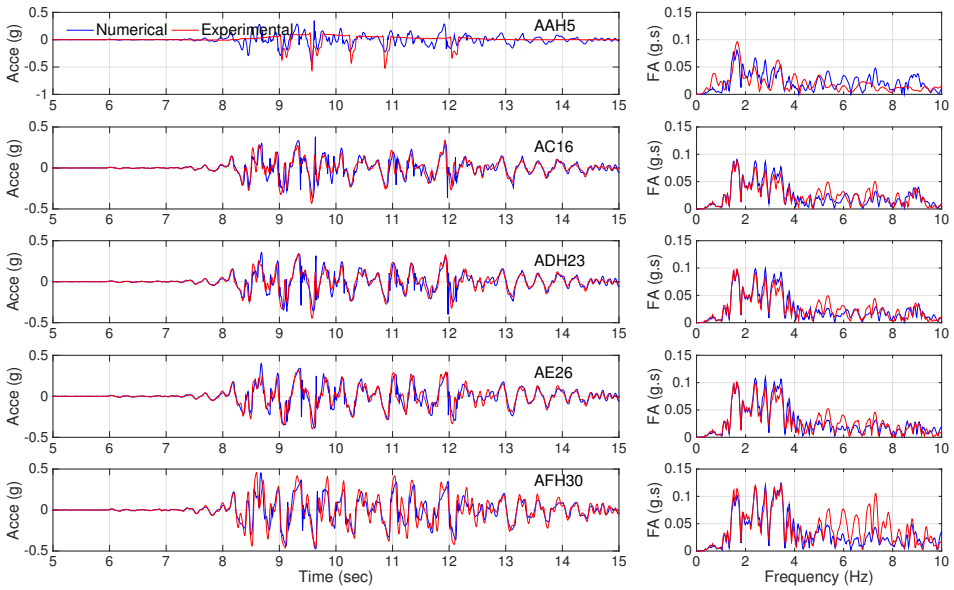

Figure 4.48: Time series and Fourier amplitude spectra of the accelerations recorded at the middle array (AAH5, AC16, ADH23, AE26 and AFH30) for motion #11.

4.4.3.2 Comparison of horizontal accelerations of culvert specimens

Figures 4.49-4.57 display the comparisons for the time series and Fourier amplitude spectra of horizontal accelerations for the rectangular (locations 7 and 1) and circular (locations 16 and 14) culverts. Again, the agreement between the numerical and experimental results for all motions are generally very good.

4.4.3.3 Comparison of in-plane bending strains for rectangular culvert

To compare the maximum bending strain profiles, we used the processed strain data of each event to determine the maximum in-plane bending strains among all the recorded data on the rectangular structure and the time it occurred. Then, we read the value of bending strains at all locations at that particular time. We followed the same procedure to extract the bending strain profile from the numerical simulations. Figures 4.58-4.75 display the comparisons for the time series and Fourier amplitude spectra of the dynamic bending strains for the rectangular culvert, and Figures 4.76-4.84 display the comparisons for both static and dynamic bending strain profiles. Again, as shown, the numerical model was successful in

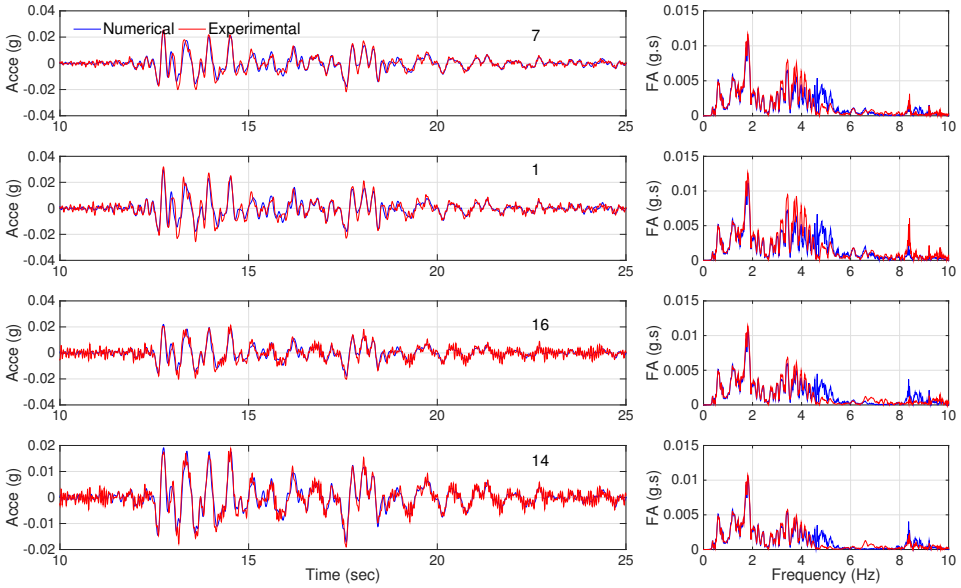

Figure 4.49: Time series and Fourier amplitude spectra of the horizontal accelerations recorded on the specimen structures (7, 1, 16 and 14) for motion #03.

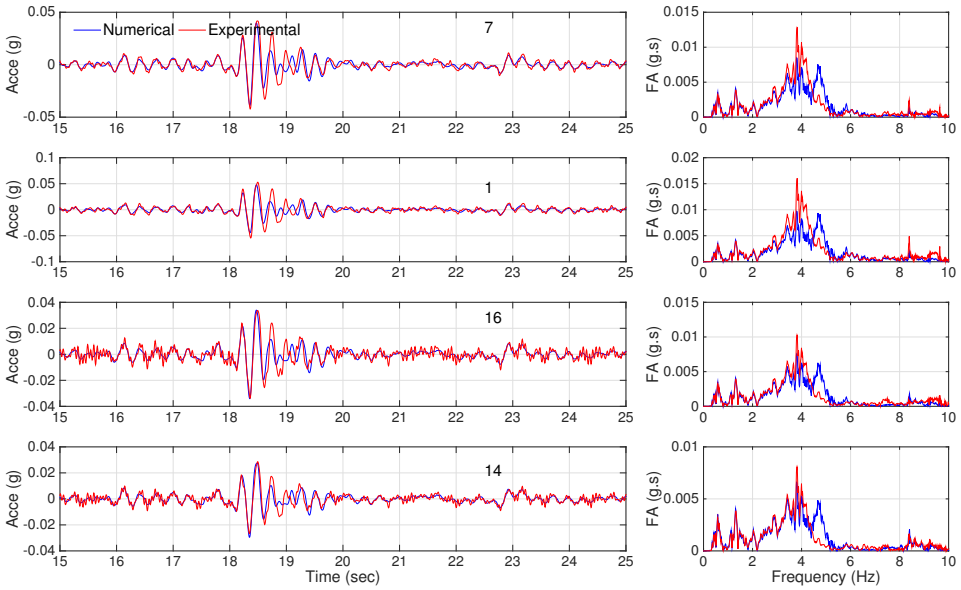

Figure 4.50: Time series and Fourier amplitude spectra of the horizontal accelerations recorded on the specimen structures (7, 1, 16 and 14) for motion #04.

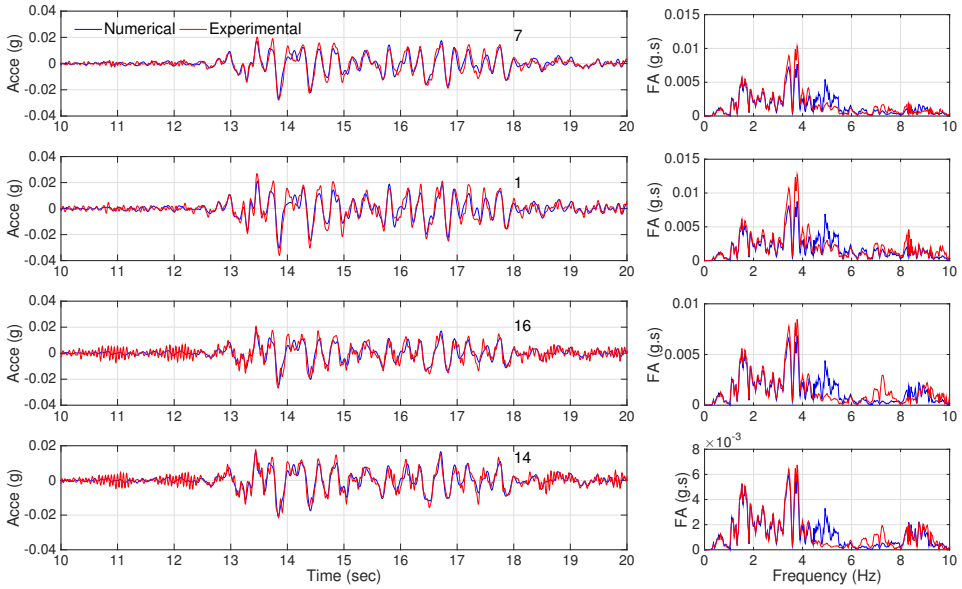

Figure 4.51: Time series and Fourier amplitude spectra of the horizontal accelerations recorded on the specimen structures (7, 1, 16 and 14) for motion #05.

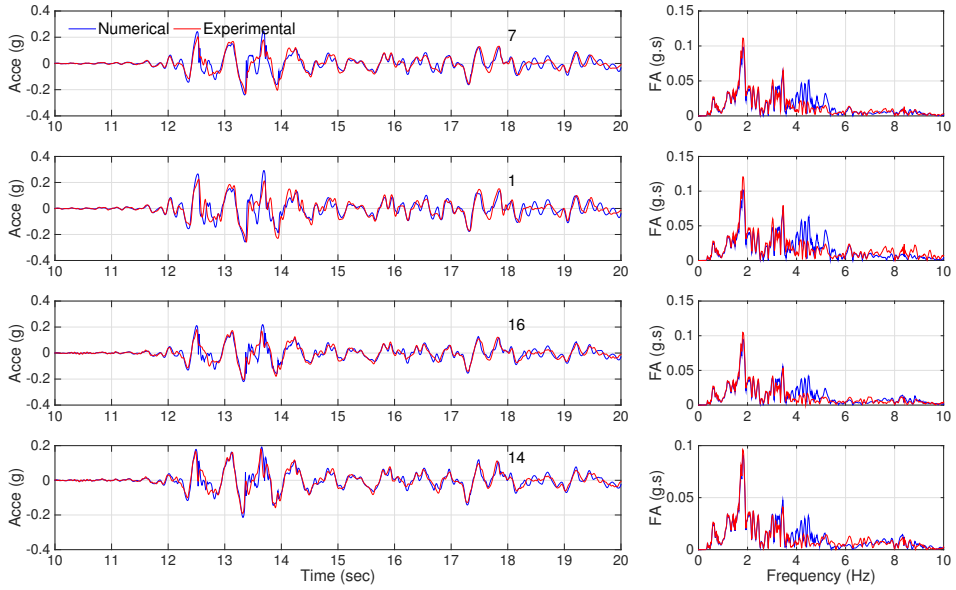

Figure 4.52: Time series and Fourier amplitude spectra of the horizontal accelerations recorded on the specimen structures (7, 1, 16 and 14) for motion #06.

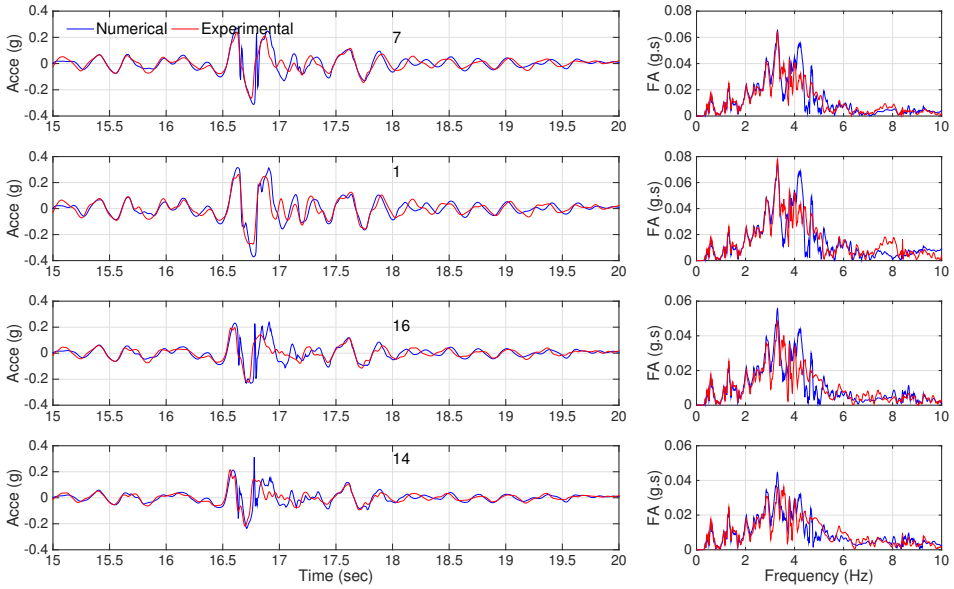

Figure 4.53: Time series and Fourier amplitude spectra of the horizontal accelerations recorded on the specimen structures (7, 1, 16 and 14) for motion #07.

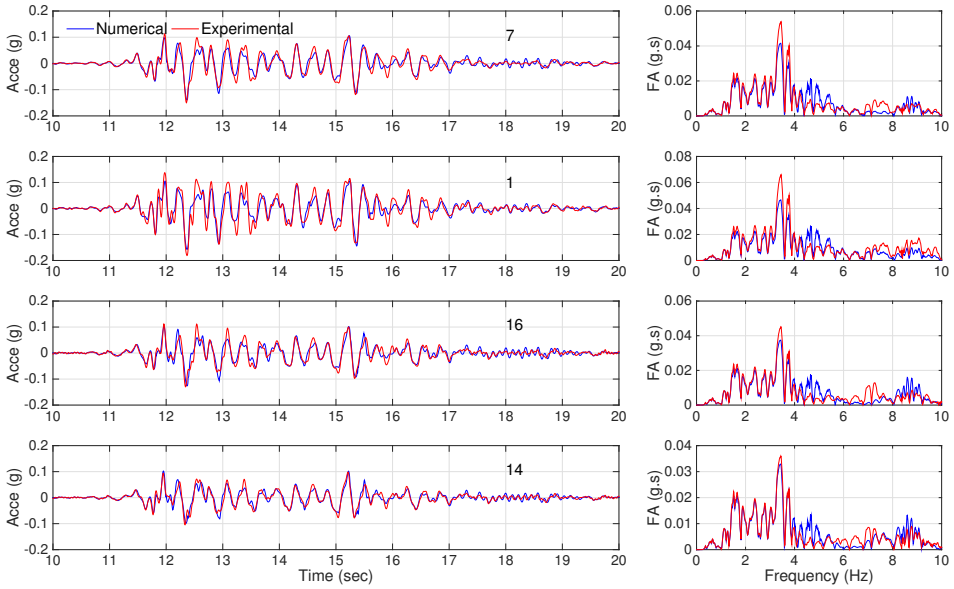

Figure 4.54: Time series and Fourier amplitude spectra of the horizontal accelerations recorded on the specimen structures (7, 1, 16 and 14) for motion #08.

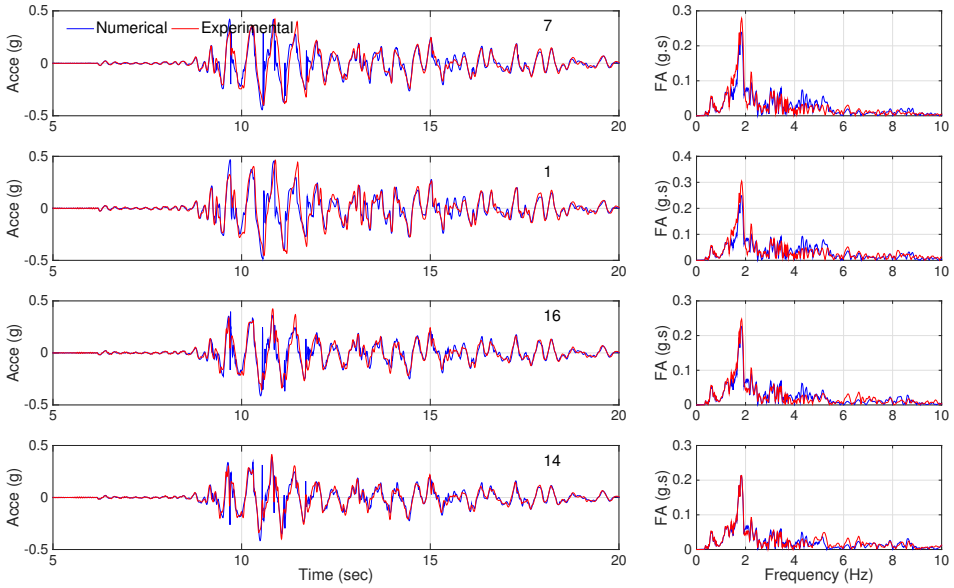

Figure 4.55: Time series and Fourier amplitude spectra of the horizontal accelerations recorded on the specimen structures (7, 1, 16 and 14) for motion #09.

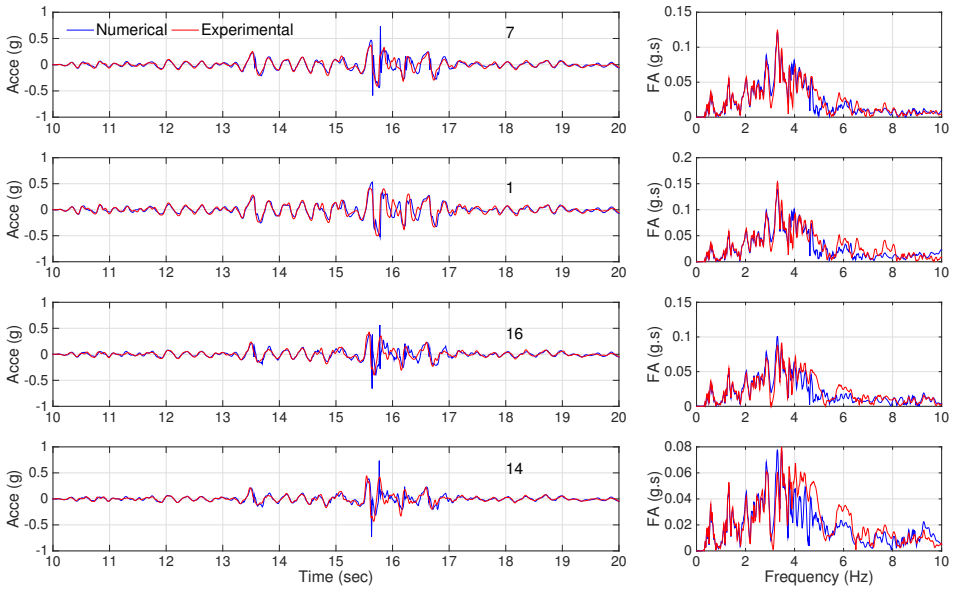

Figure 4.56: Time series and Fourier amplitude spectra of the horizontal accelerations recorded on the specimen structures (7, 1, 16 and 14) for motion #10.

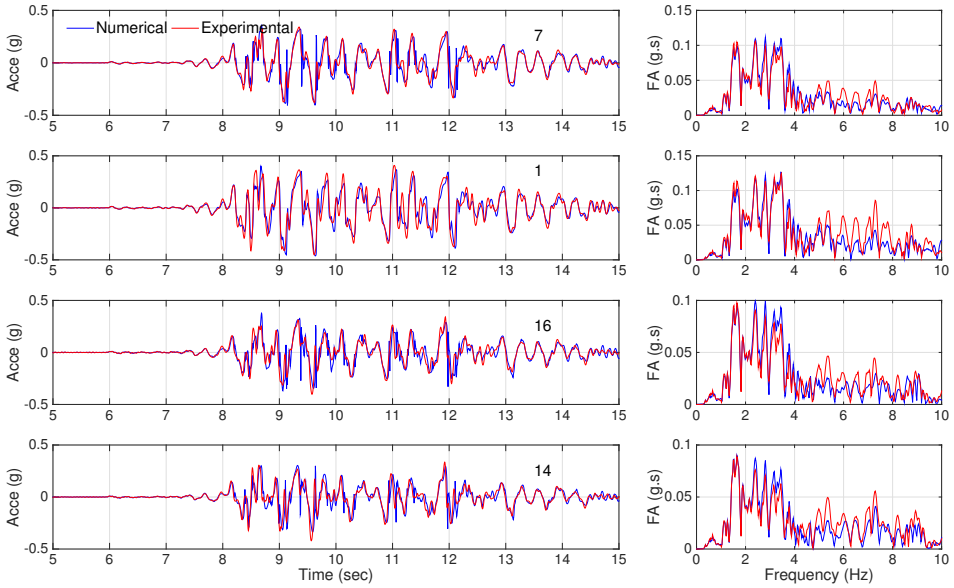

Figure 4.57: Time series and Fourier amplitude spectra of the horizontal accelerations recorded on the specimen structures (7, 1, 16 and 14) for motion #11.

capturing bending strain data for all (low, medium, high amplitude) base shaking events.

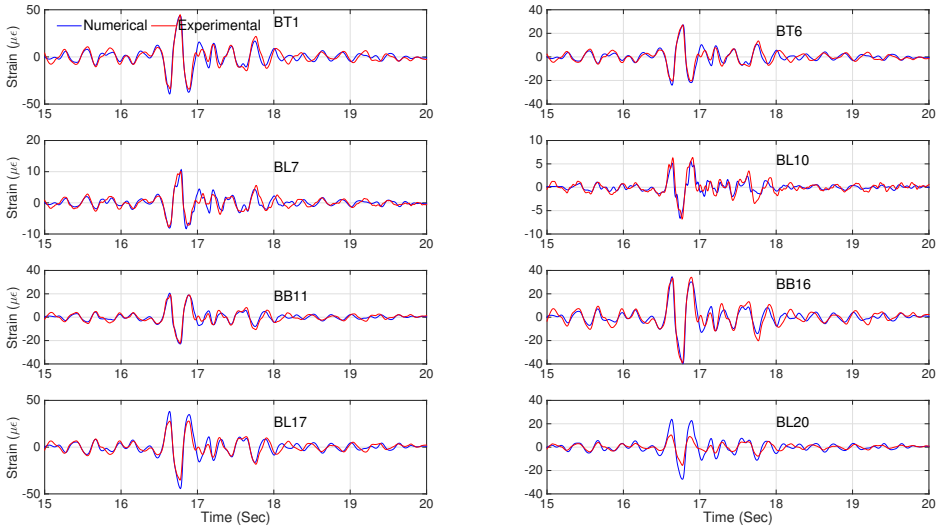

Figure 4.66: Comparison of the time series of the dynamic bending strains of the rectangular structure for motion #07.

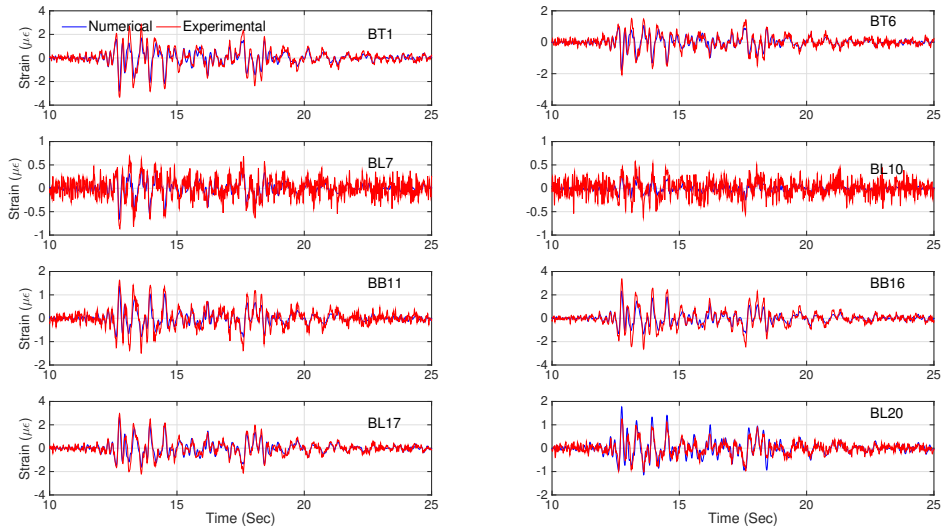

Figure 4.58: Comparison of the time series of the dynamic bending strains of the rectangular structure for motion #03.

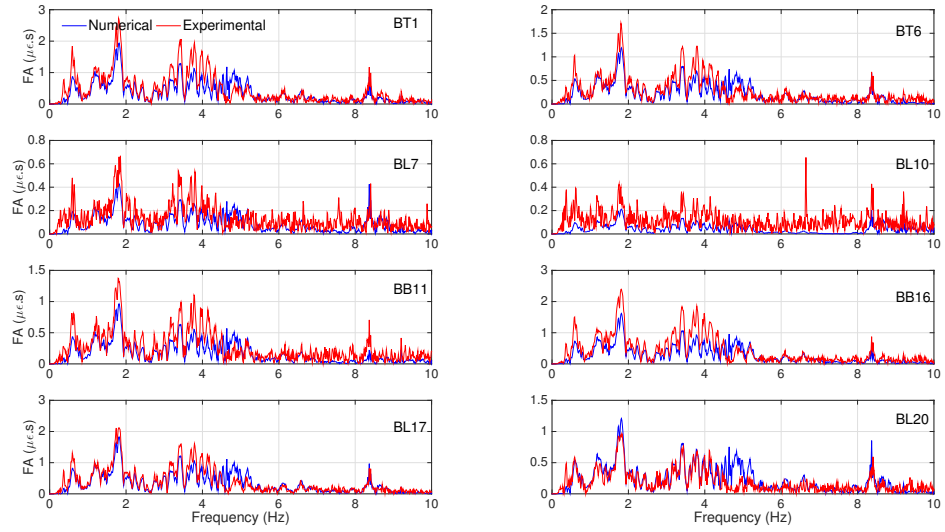

Figure 4.59: Comparison of the Fourier amplitude spectra of the rectangular structure for motion #03.

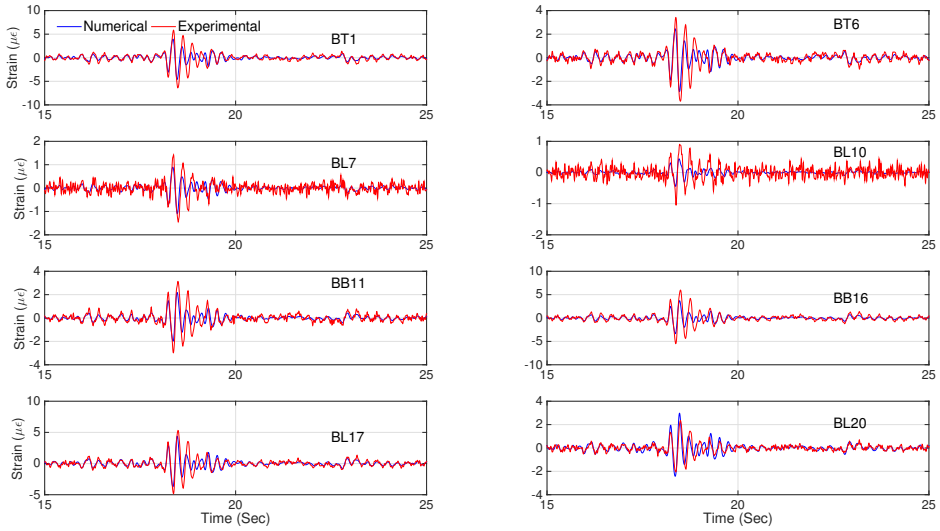

Figure 4.60: Comparison of the time series of the dynamic bending strains of the rectangular structure for motion #04.

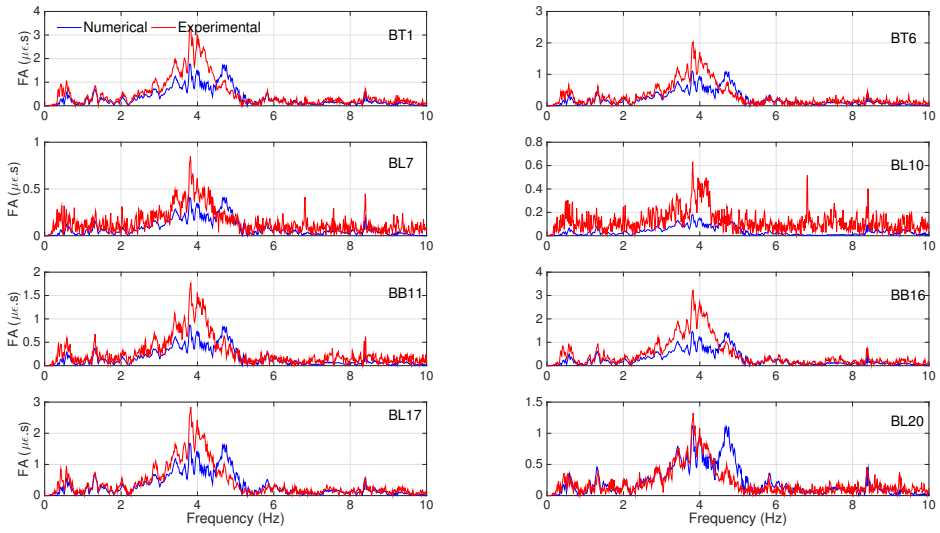

Figure 4.61: Comparison of the Fourier amplitude spectra of the rectangular structure for motion #04.

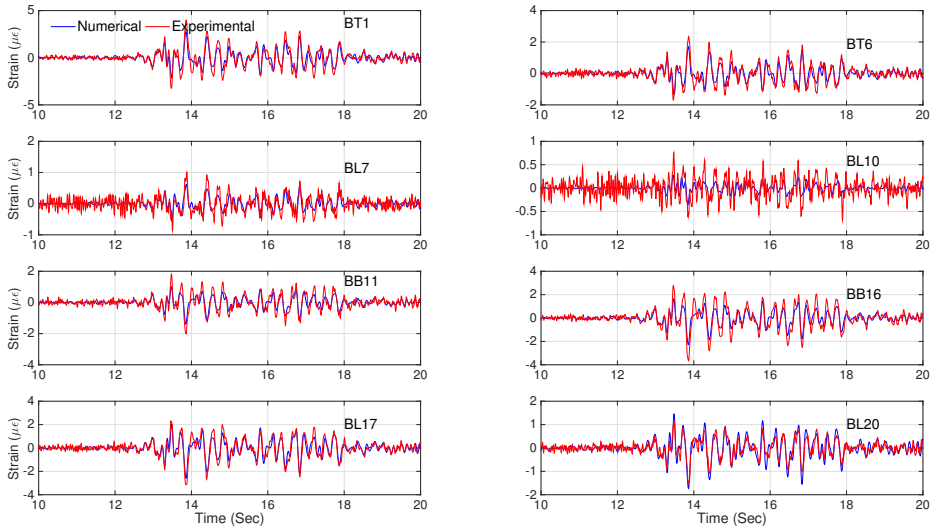

Figure 4.62: Comparison of the time series of the dynamic bending strains of the rectangular structure for motion #05.

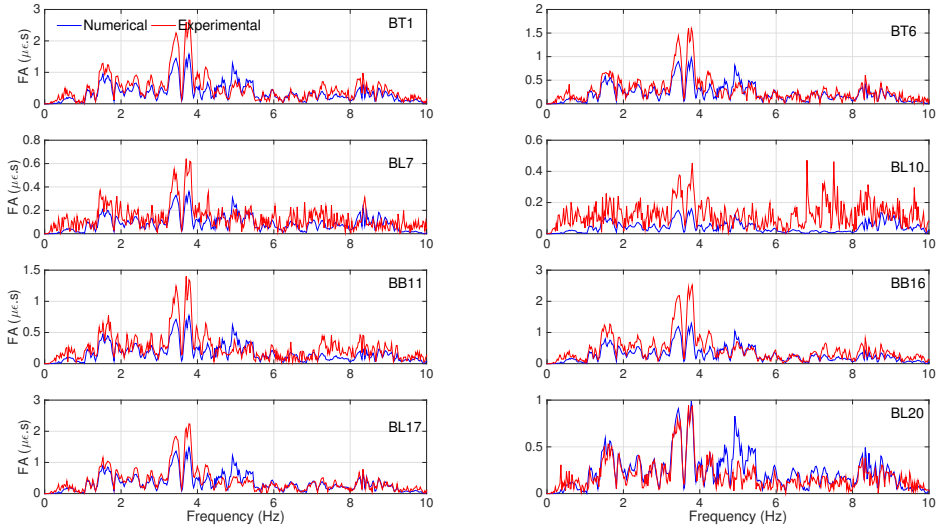

Figure 4.63: Comparison of the Fourier amplitude spectra of the rectangular structure for motion #05.

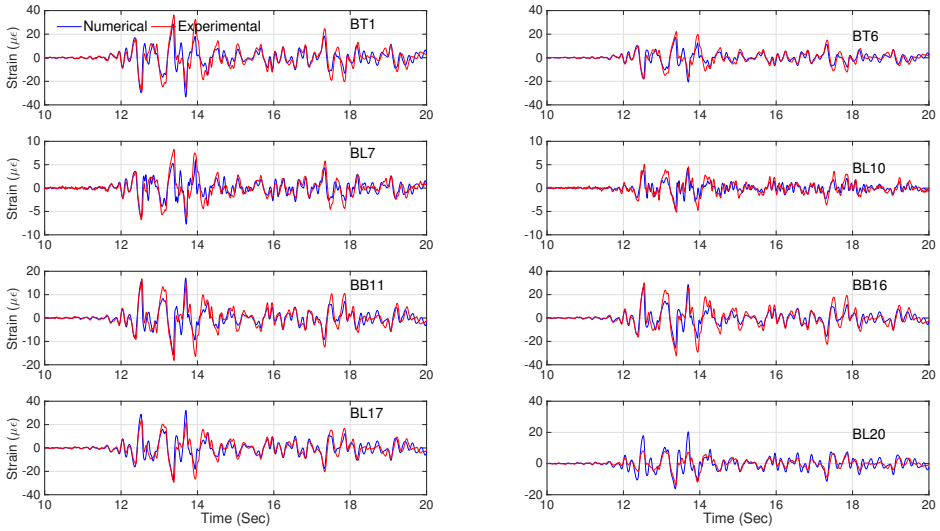

Figure 4.64: Comparison of the time series of the dynamic bending strains of the rectangular structure for motion #06.

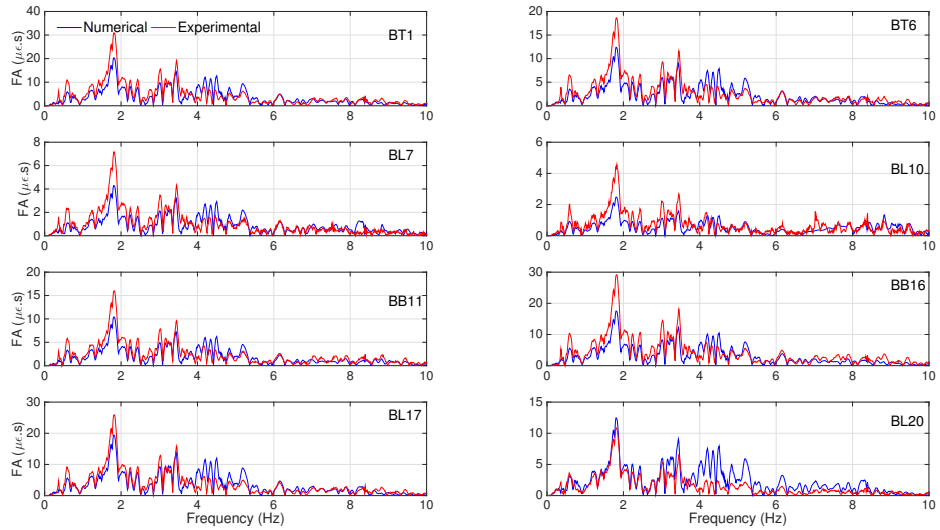

Figure 4.65: Comparison of the Fourier amplitude spectra of the rectangular structure for motion #06.

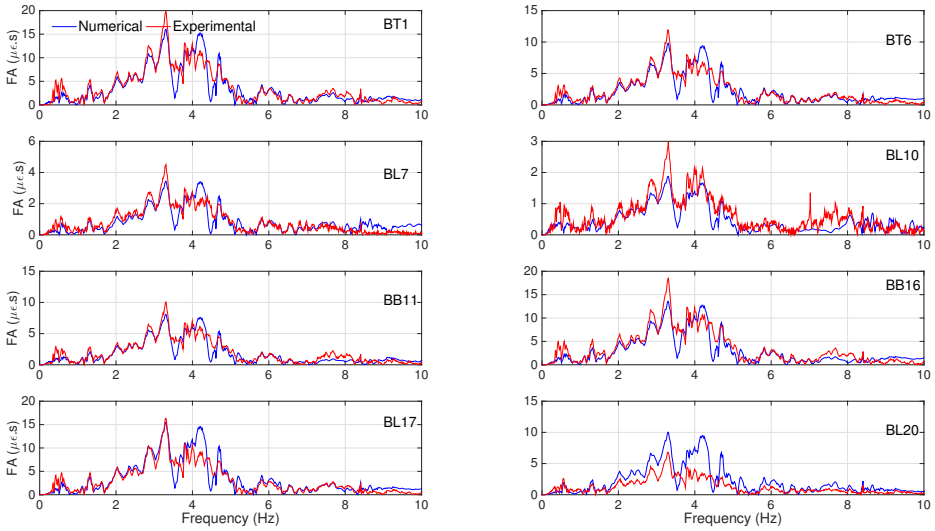

Figure 4.67: Comparison of the Fourier amplitude spectra of the rectangular structure for motion #07.

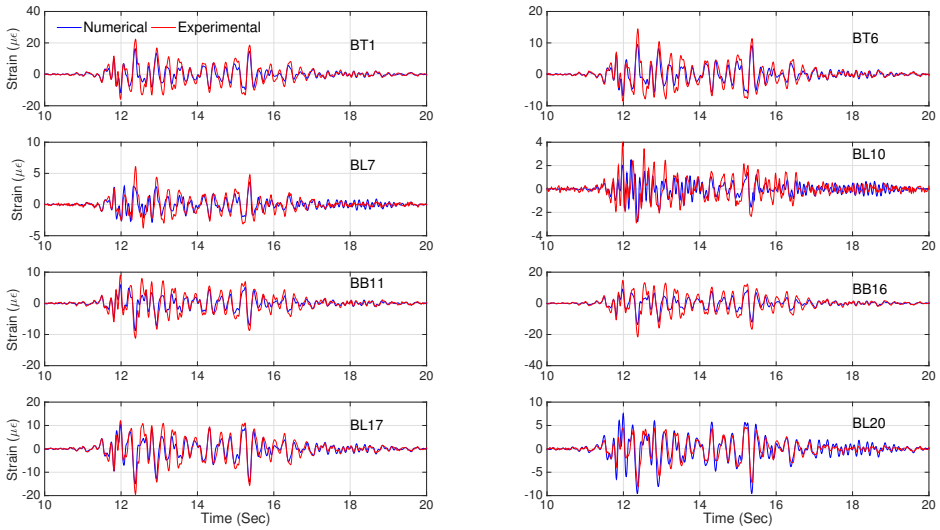

Figure 4.68: Comparison of the time series of the dynamic bending strains of the rectangular structure for motion #08.

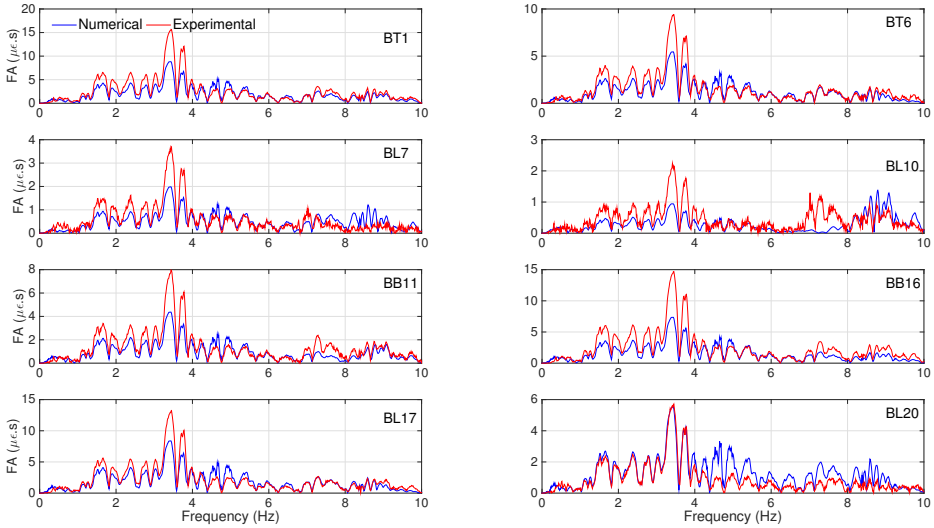

Figure 4.69: Comparison of the Fourier amplitude spectra of the rectangular structure for motion #08.

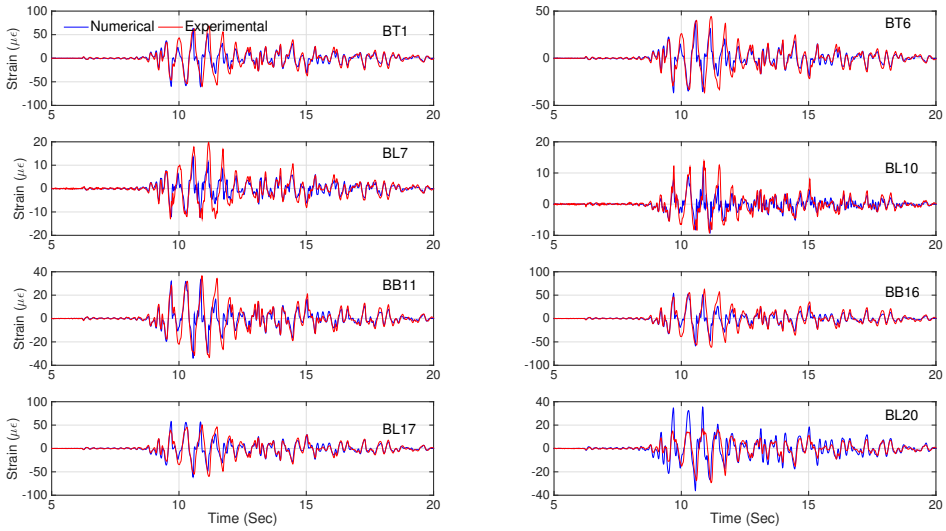

Figure 4.70: Comparison of the time series of the dynamic bending strains of the rectangular structure for motion #09.

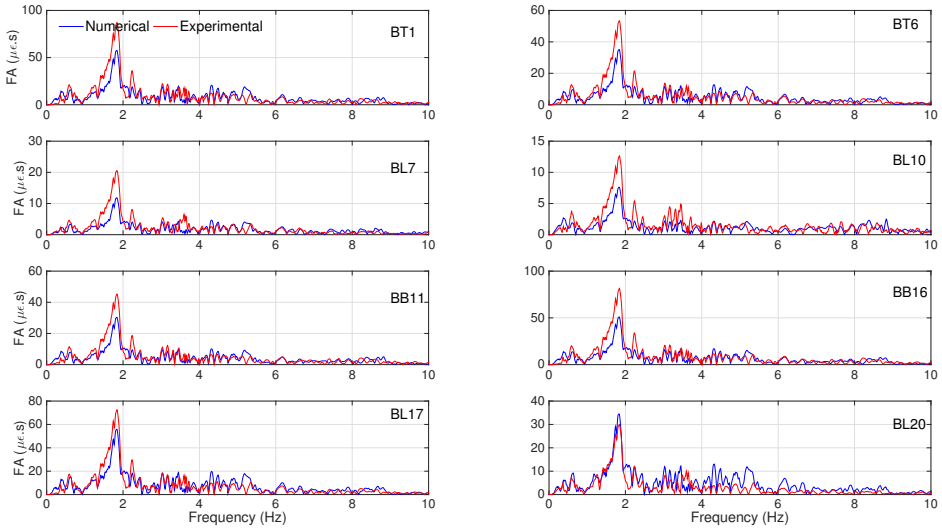

Figure 4.71: Comparison of the Fourier amplitude spectra of the rectangular structure for motion #09.

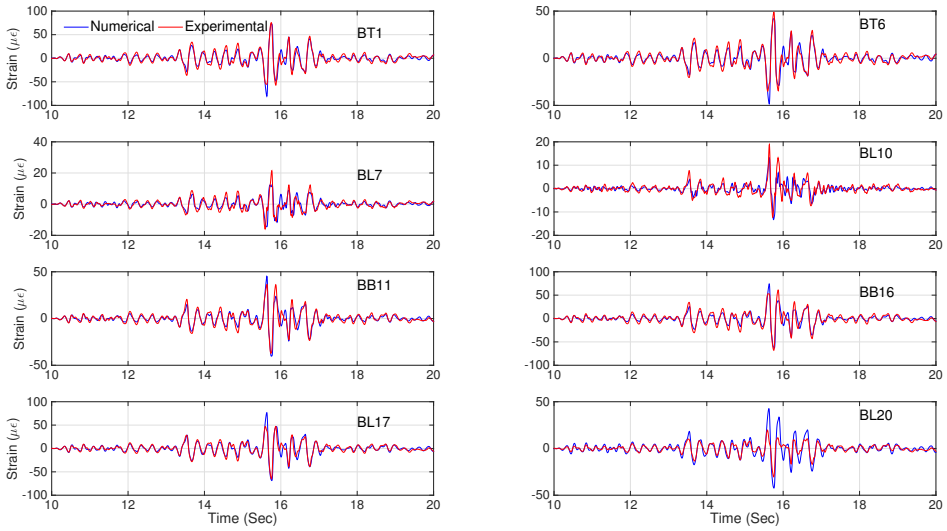

Figure 4.72: Comparison of the time series of the dynamic bending strains of the rectangular structure for motion #10.

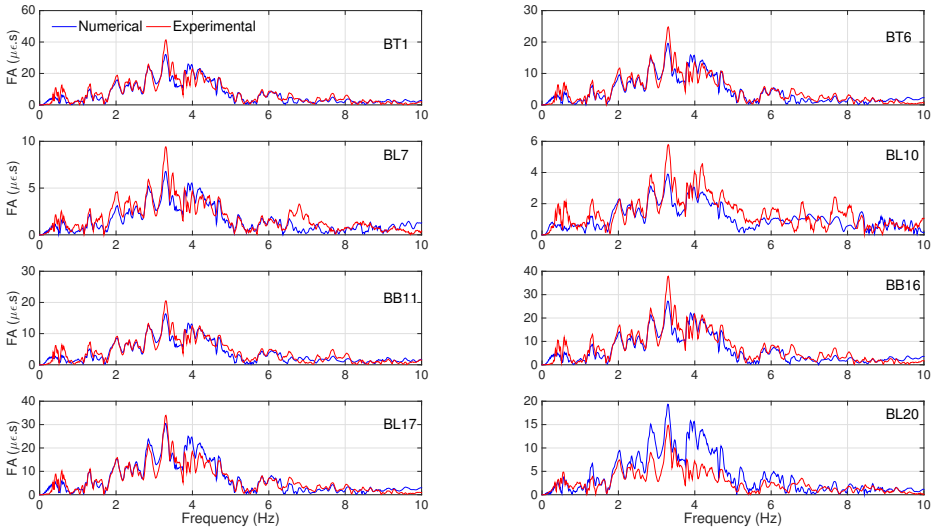

Figure 4.73: Comparison of the Fourier amplitude spectra of the rectangular structure for motion #10.

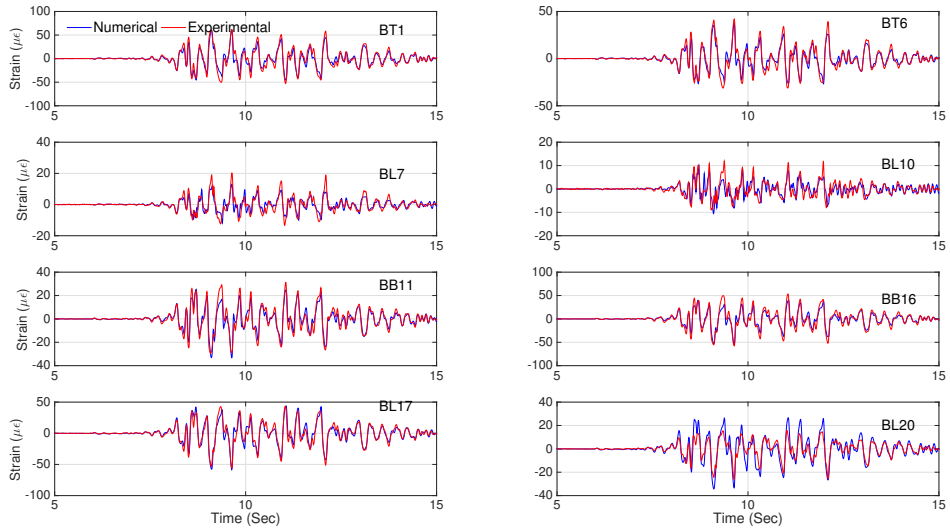

Figure 4.74: Comparison of the time series of the dynamic bending strains of the rectangular structure for motion #11.

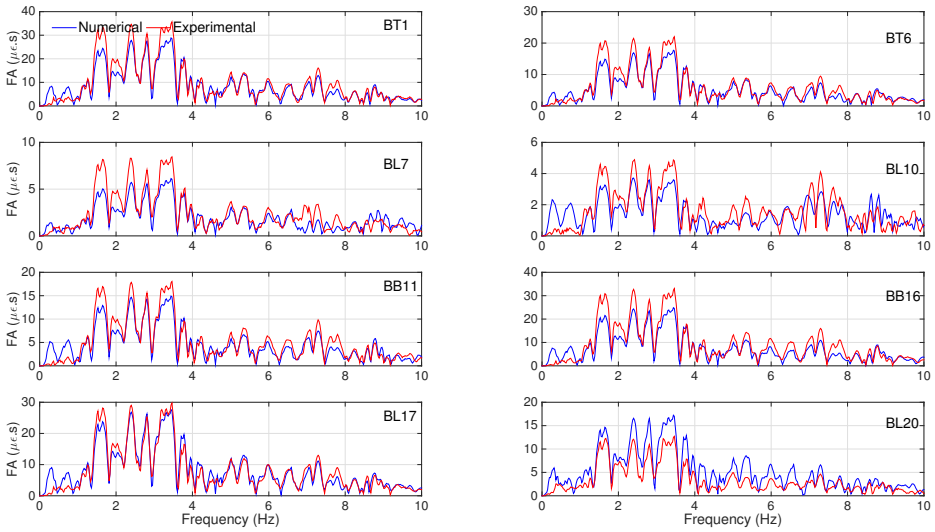

Figure 4.75: Comparison of the Fourier amplitude spectra of the rectangular structure for motion #11.

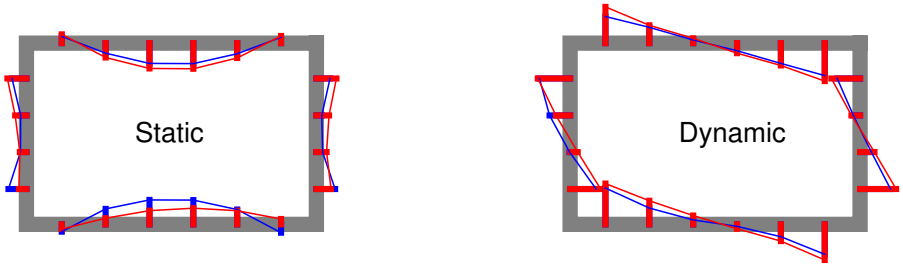

Figure 4.76: Comparison of the maximum static and dynamic bending strain profiles of the rectangular structure for motion #03.

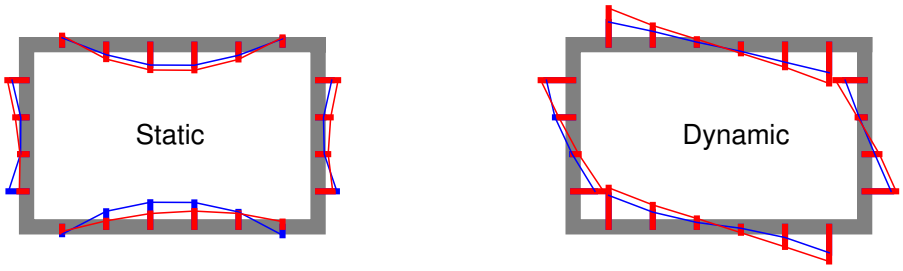

Figure 4.77: Comparison of the maximum static and dynamic bending strain profiles of the rectangular structure for motion #04.

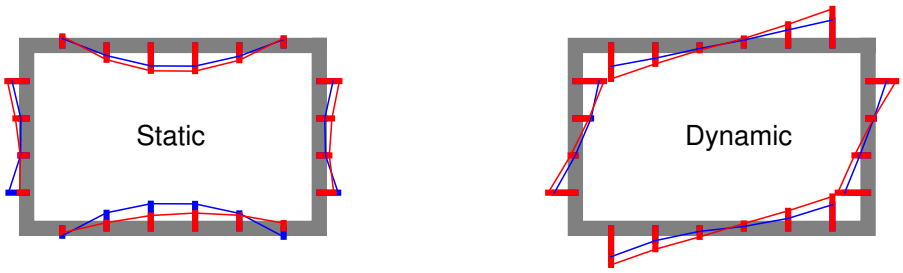

Figure 4.78: Comparison of the maximum static and dynamic bending strain profiles of the rectangular structure for motion #05.

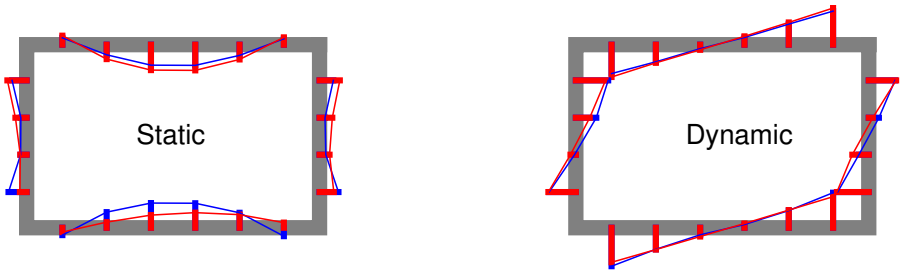

Figure 4.79: Comparison of the maximum static and dynamic bending strain profiles of the rectangular structure for motion #06.

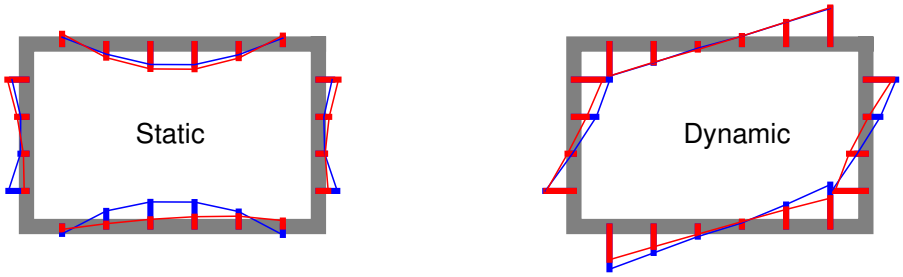

Figure 4.80: Comparison of the maximum static and dynamic bending strain profiles of the rectangular structure for motion #07.

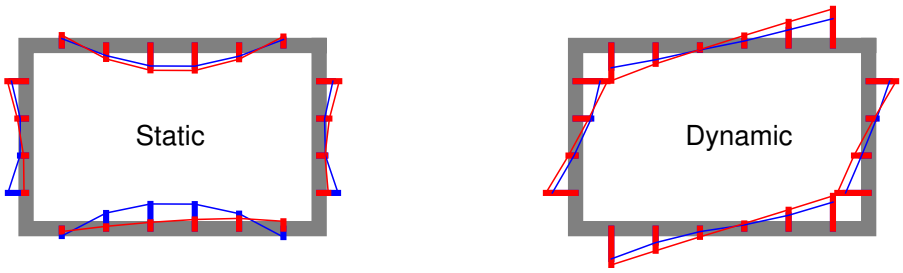

Figure 4.81: Comparison of the maximum static and dynamic bending strain profiles of the rectangular structure for motion #08.

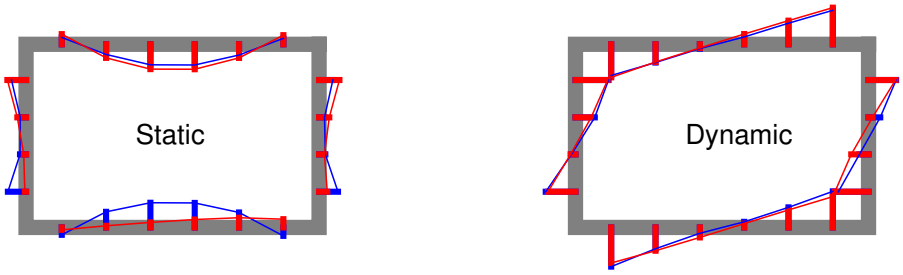

Figure 4.82: Comparison of the maximum static and dynamic bending strain profiles of the rectangular structure for motion #09.

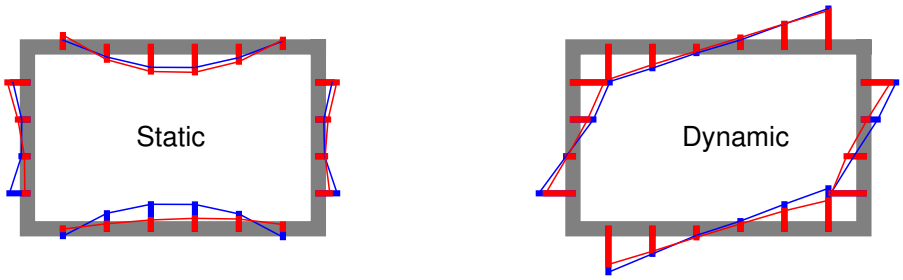

Figure 4.83: Comparison of the maximum static and dynamic bending strain profiles of the rectangular structure for motion #10.

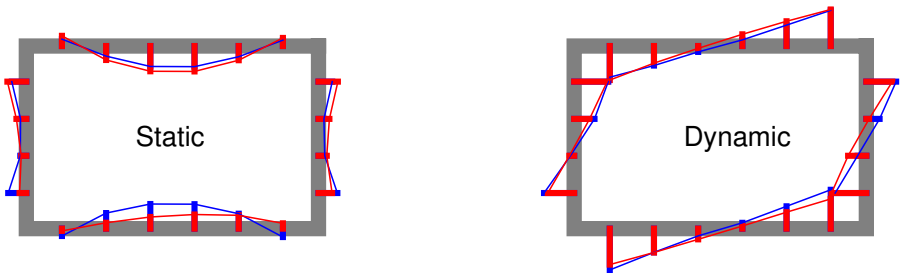

Figure 4.84: Comparison of the maximum static and dynamic bending strain profiles of the rectangular structure for motion #11.

4.4.3.4 Comparison of in-plane bending strains for circular culvert

Similarly, Figures 4.85-4.102 display the comparisons for the time series and Fourier amplitude spectra of the dynamic bending strains for the circular culvert, and Figures 4.103-4.111 display the comparisons for both static and dynamic bending strain profiles. As shown, the numerical model approach is again successful in general to capture bending strain time series. However, agreements are not perfect at all locations. Moreover, although the numerical model is successful in capturing the dynamic strain profile, it was unable to do so for the static case. This can be partially attributed to the fact that we are not modeling the soil densification in our numerical simulations and the initial condition is the same for all experiments. This is while in the actual centrifuge experiment we possibly had some soil densification around the circular structure as it was difficult to pluviate soil uniformly, and we had to use a hand vibrator to increase soil densification around it prior to the test. It is likely that this effort was not entirely successful. That said, the static strains are much smaller than the dynamic strains, and are incidentally more difficult to measure.

4.4.3.5 Comparison of hoop strains for circular culvert

Figures 4.112-4.129 display the comparisons for the time series and Fourier amplitude spectra of hoop strains for the circular culvert, and Figures 4.130-4.138 show comparisons for both the static and dynamic hoop strain profiles. In general, the range of hoop strains are smaller

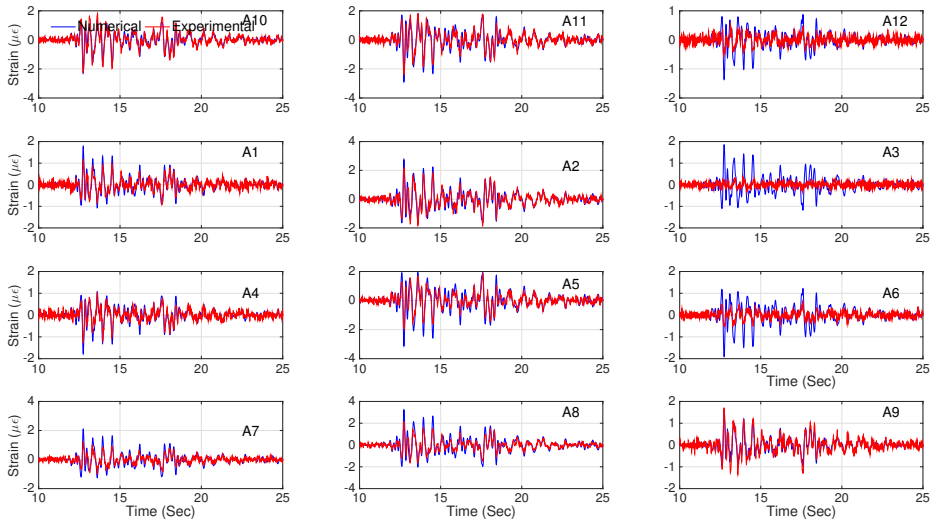

Figure 4.85: Comparison of the time series of the dynamic bending strains of the circular structure for motion #03.

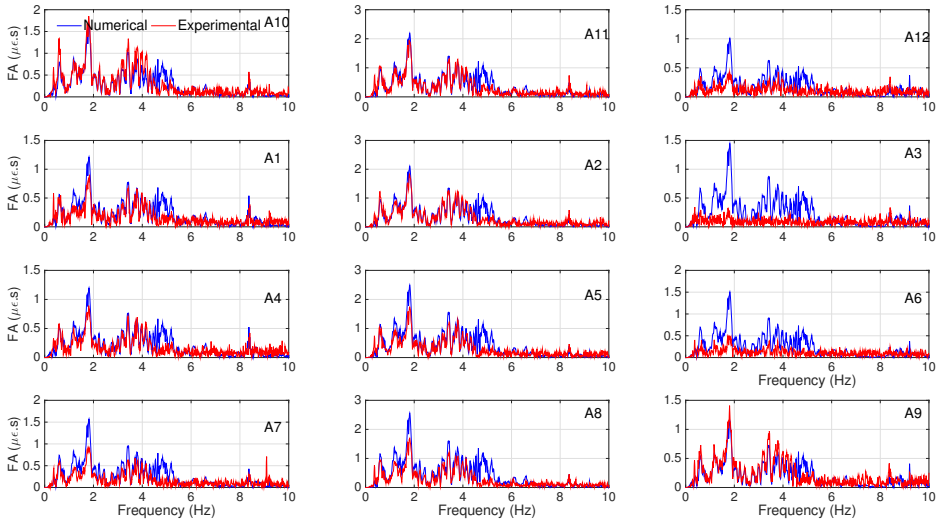

Figure 4.86: Comparison of Fourier amplitude spectra of the circular structure for motion #03.

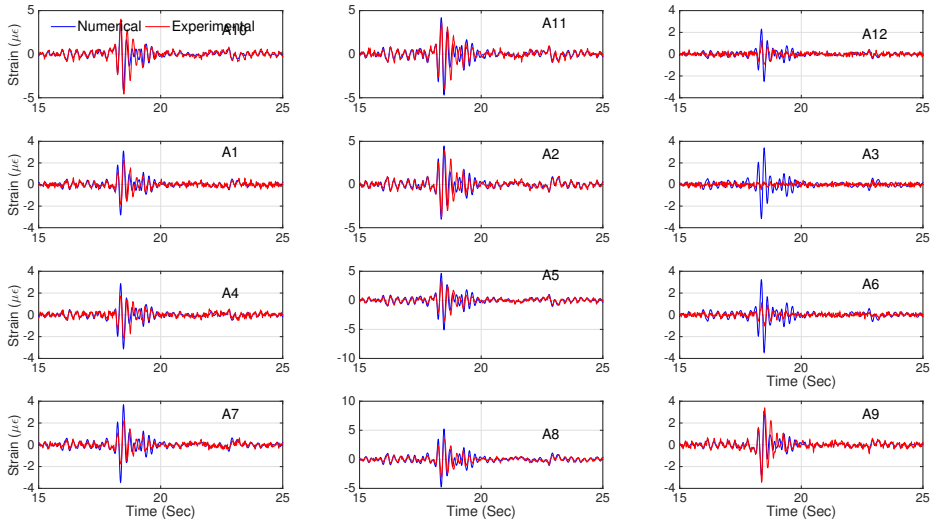

Figure 4.87: Comparison of the time series of the dynamic bending strains of the circular structure for motion #04.

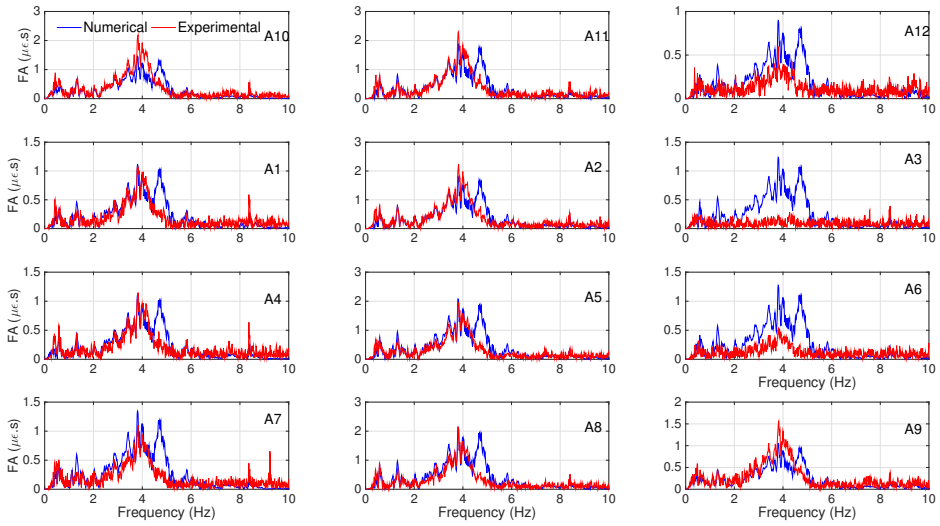

Figure 4.88: Comparison of the Fourier amplitude spectra of the circular structure for motion #04.

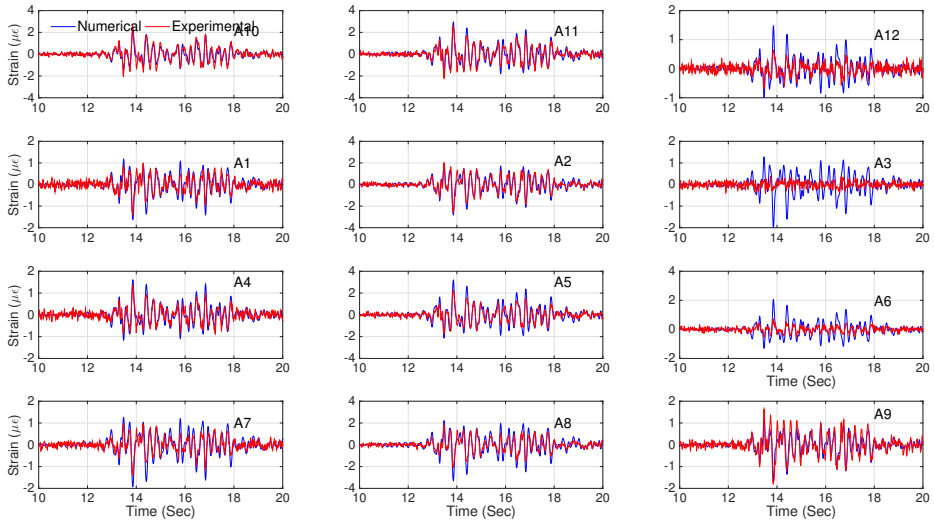

Figure 4.89: Comparison of the time series of the dynamic bending strains of the circular structure for motion #05.

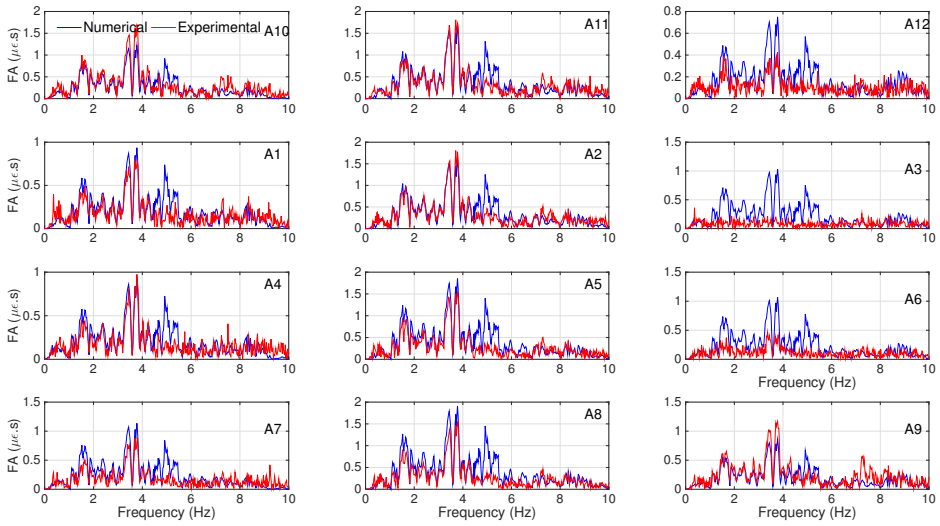

Figure 4.90: Comparison of the Fourier amplitude spectra of the circular structure for motion #05.

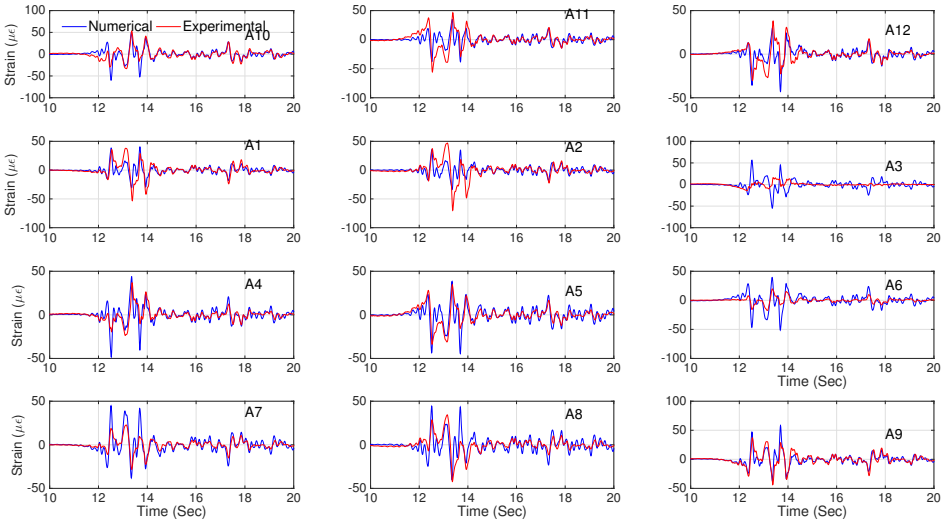

Figure 4.91: Comparison of the time series of the dynamic bending strains of the circular structure for motion #06.

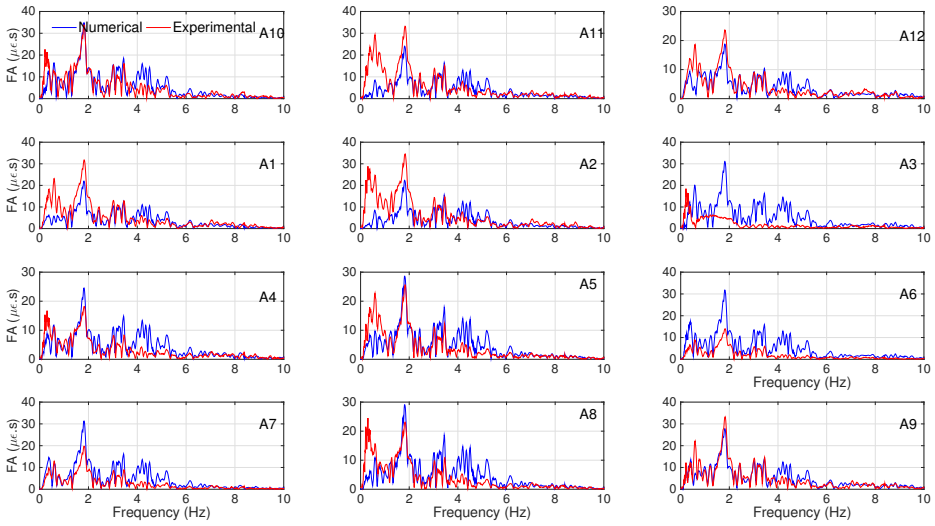

Figure 4.92: Comparison of the Fourier amplitude spectra of the circular structure for motion #06.

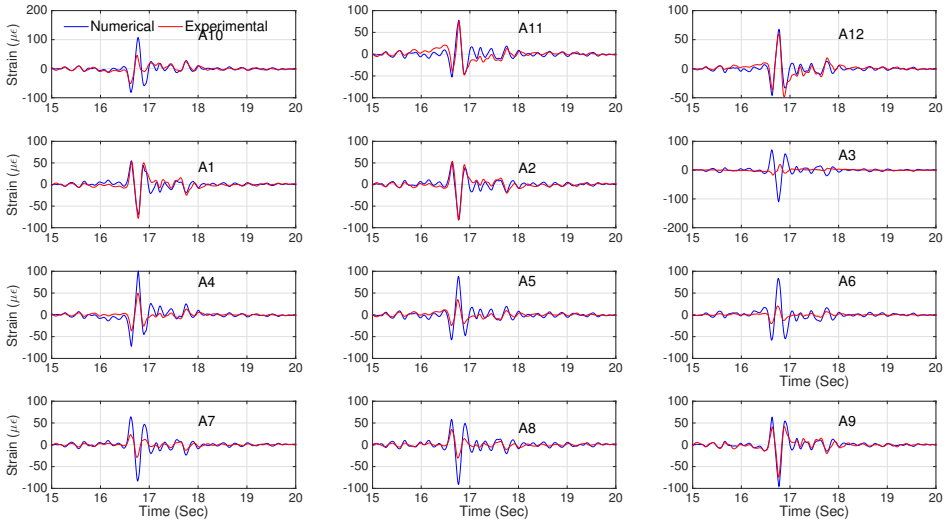

Figure 4.93: Comparison of the time series of the dynamic bending strains of the circular structure for motion #07.

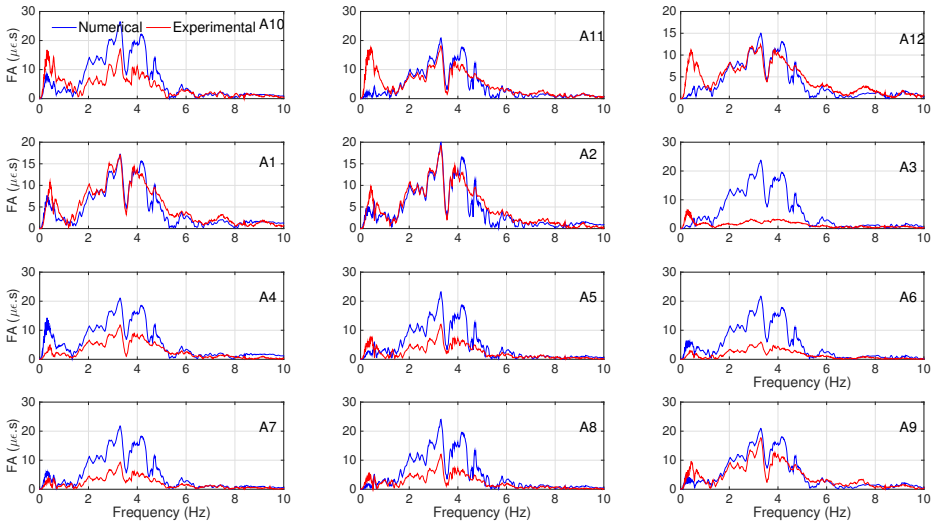

Figure 4.94: Comparison of the Fourier amplitude spectra of the circular structure for motion #07.

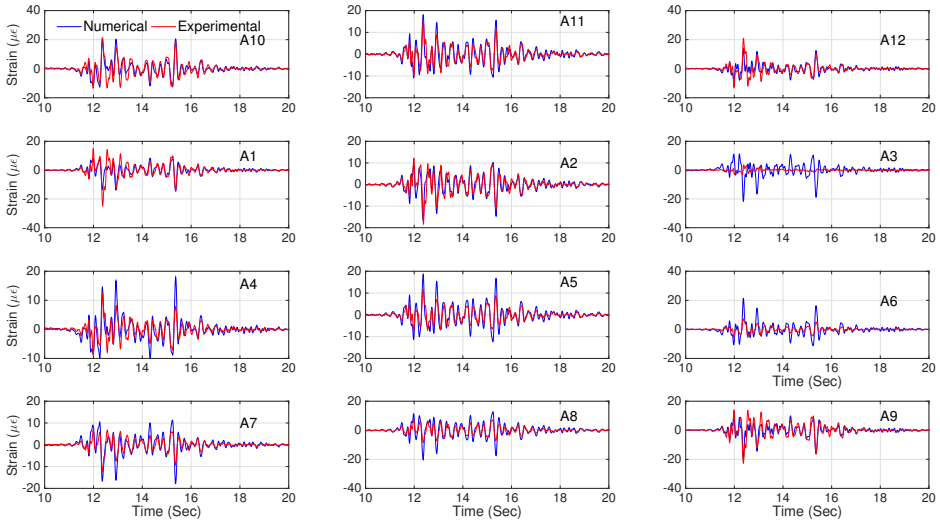

Figure 4.95: Comparison of the time series of the dynamic bending strains of the circular structure for motion #08.

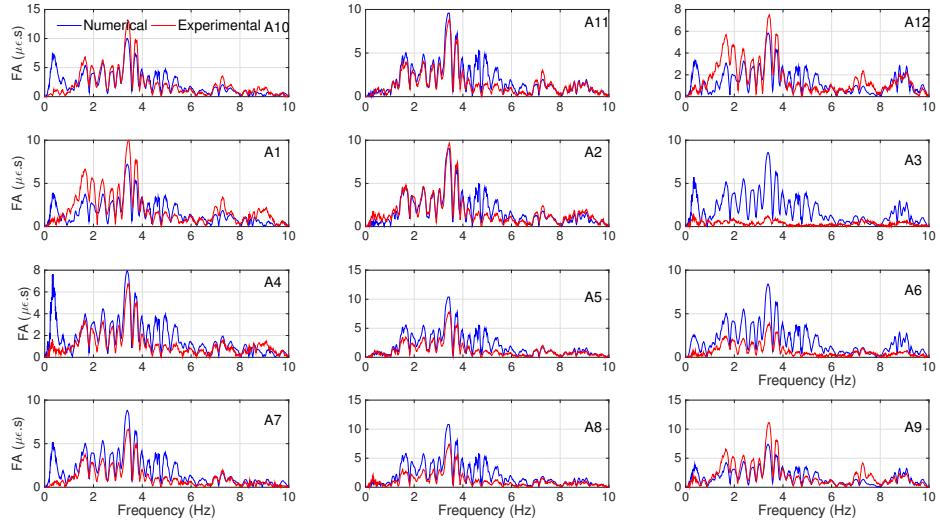

Figure 4.96: Comparison of the corresponding Fourier amplitude spectra of the circular structure for motion #08.

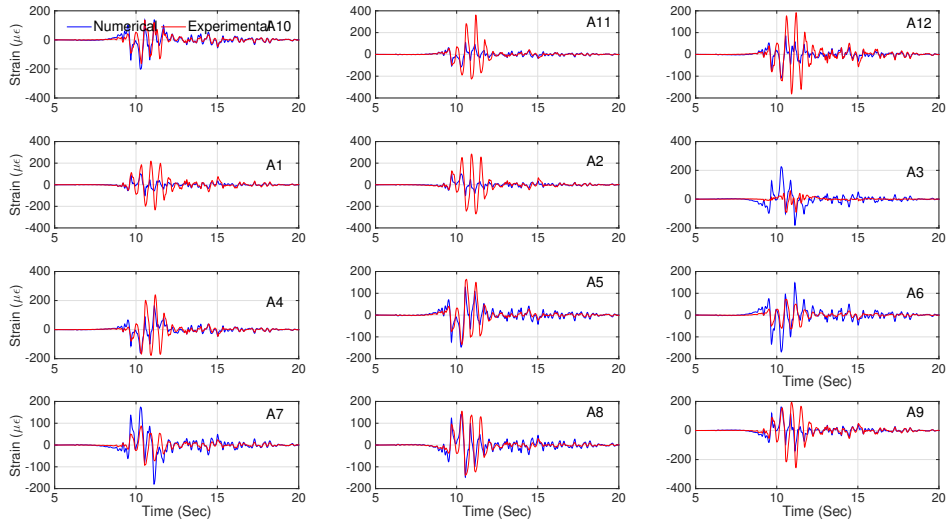

Figure 4.97: Comparison of the time series of the dynamic bending strains of the circular structure for motion #09.

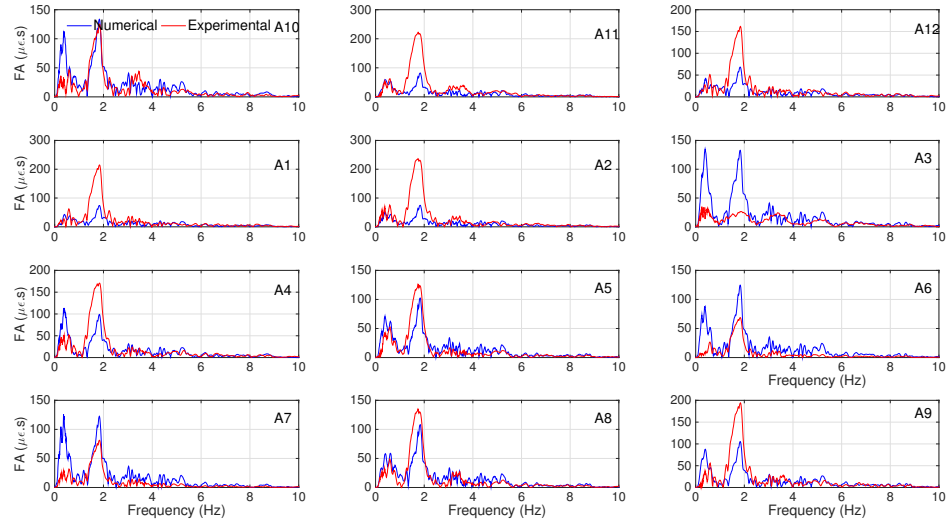

Figure 4.98: Comparison of the Fourier amplitude spectra of the circular structure for motion #09.

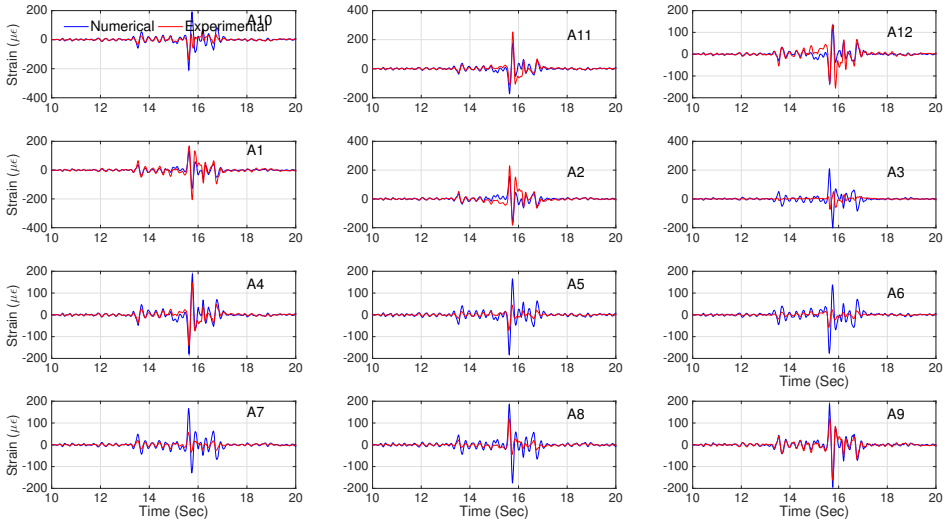

Figure 4.99: Comparison of the time series of the dynamic bending strains of the circular structure for motion #10.

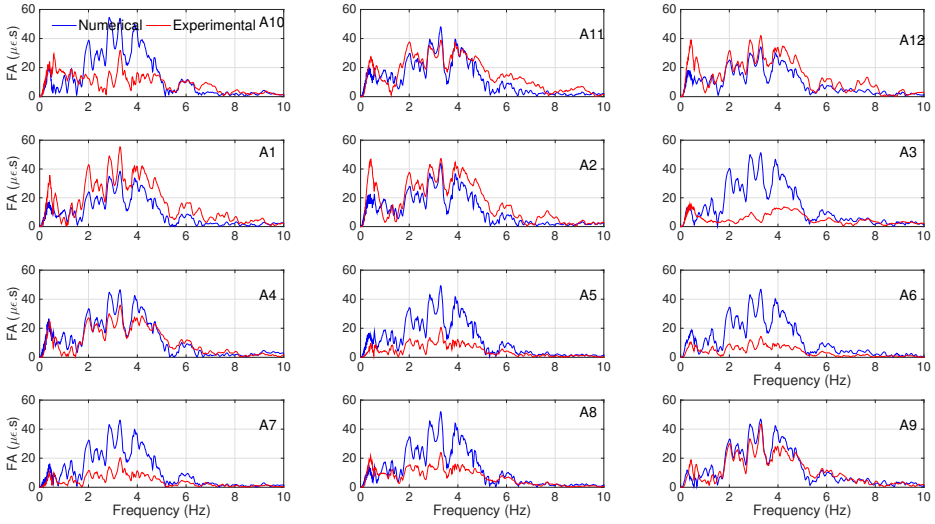

Figure 4.100: Comparison of the Fourier amplitude spectra of the circular structure for motion #10.

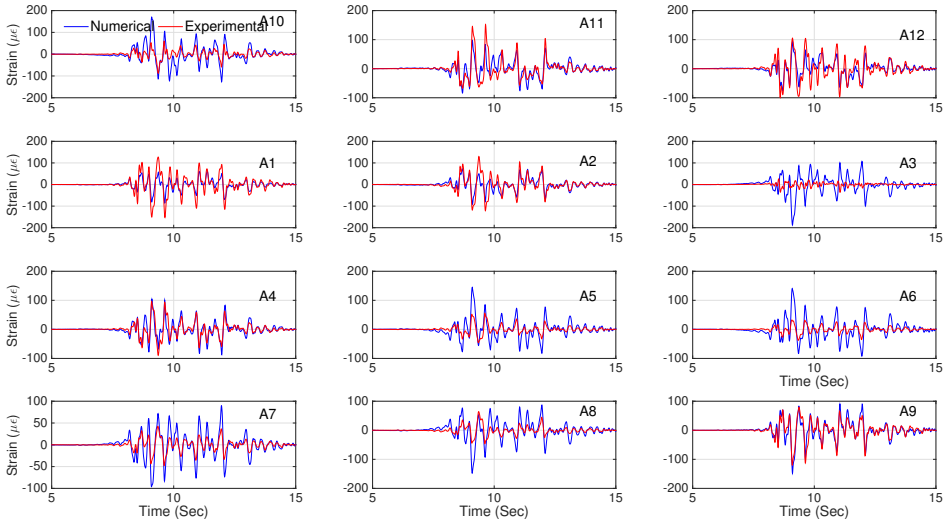

Figure 4.101: Comparison of the time series of the dynamic bending strains of the circular structure for motion #11.

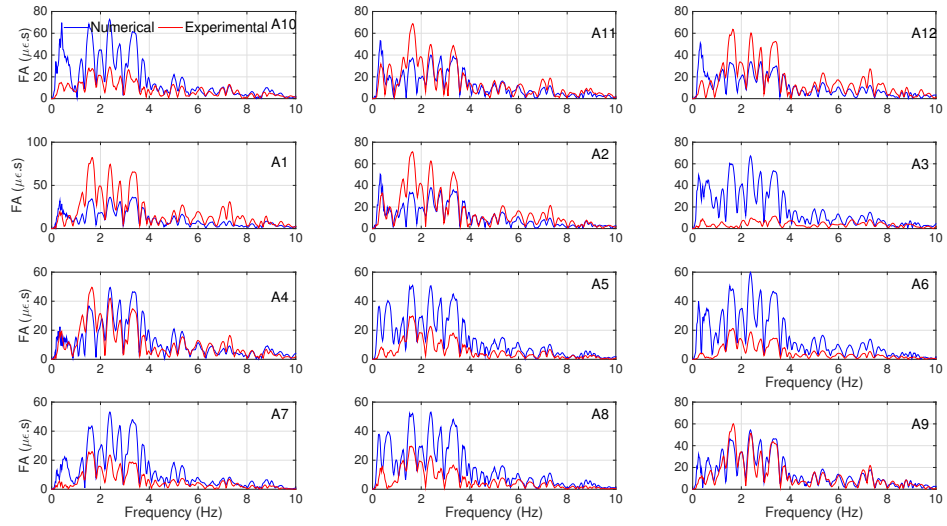

Figure 4.102: Comparison of the Fourier amplitude spectra of the circular structure for motion #11.

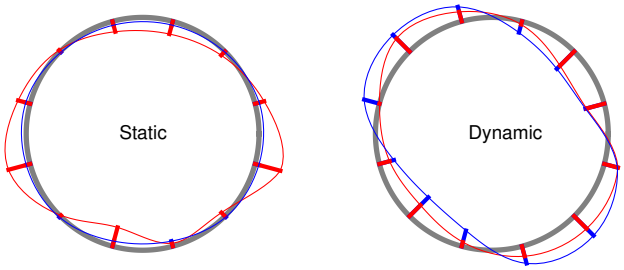

Figure 4.103: Comparison of the maximum static and dynamic bending strain profiles of the circular structure for motion #03.

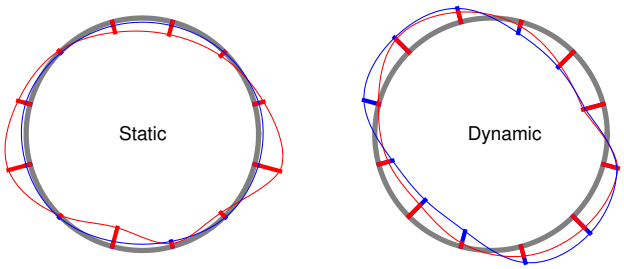

Figure 4.104: Comparison of the maximum static and dynamic bending strain profiles of the circular structure for motion #04.

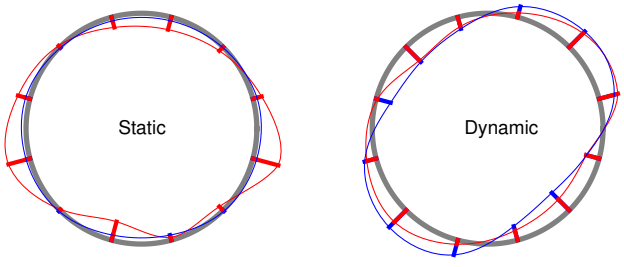

Figure 4.105: Comparison of the maximum static and dynamic bending strain profiles of the circular structure for motion #05.

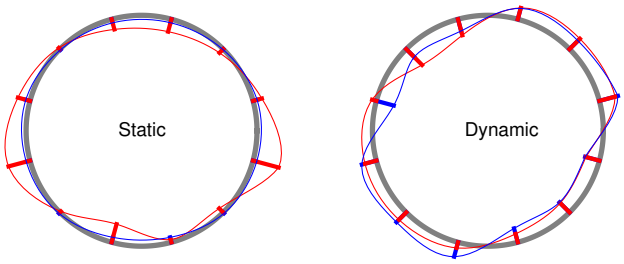

Figure 4.106: Comparison of the maximum static and dynamic bending strain profiles of the circular structure for motion #06.

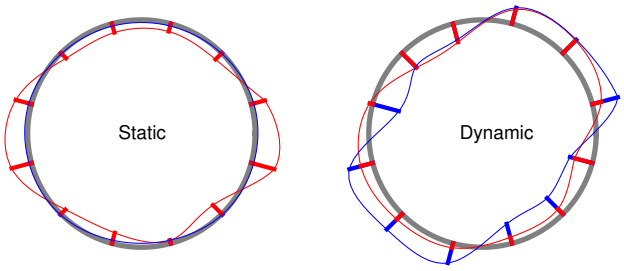

Figure 4.107: Comparison of the maximum static and dynamic bending strain profiles of the circular structure for motion #07.

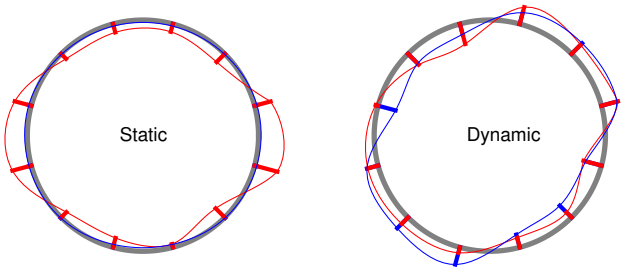

Figure 4.108: Comparison of the maximum static and dynamic bending strain profiles of the circular structure for motion #08.

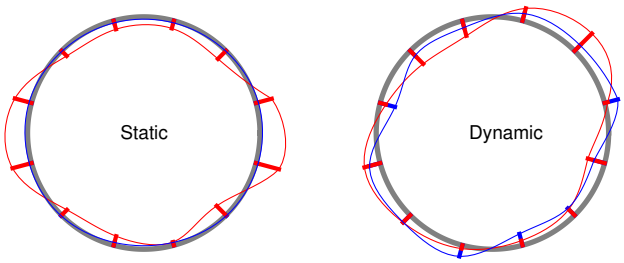

Figure 4.109: Comparison of the maximum static and dynamic bending strain profiles of the circular structure for motion #09.

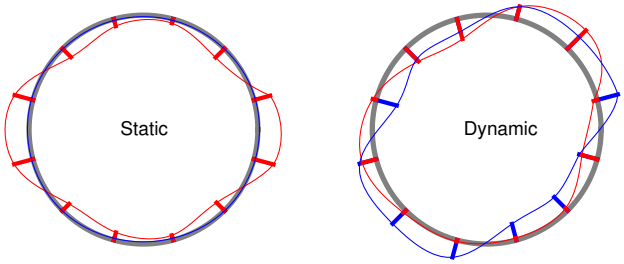

Figure 4.110: Comparison of the maximum static and dynamic bending strain profiles of the circular structure for motion #10.

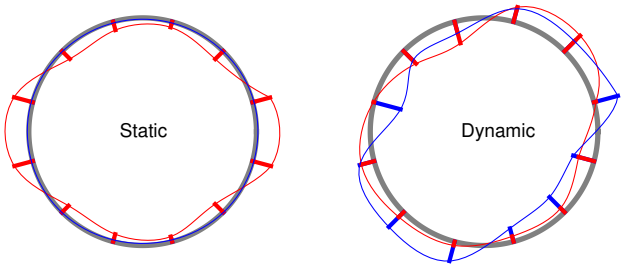

Figure 4.111: Comparison of the maximum static and dynamic bending strain profiles of the circular structure for motion #11.

than the bending strains, and as such, they inherently have inherently lower signal-to-noise ratios. Not surprisingly, therefore, we could achieve better agreements between experimental hoop strain data and FE results for higher amplitude motions. Although the agreement is not uniformly good at all locations, the numerical model could capture very similar static and dynamic hoop strain profiles in general; and interestingly, the static profile agreement is much better than what was observed for the static in-plane bending strains shown previously.

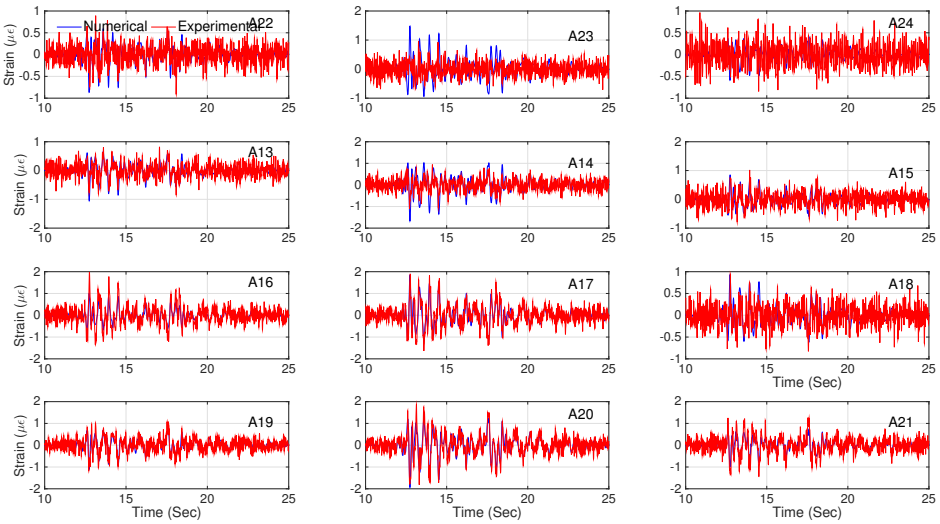

Figure 4.112: Comparison of the time series of the dynamic hoop strains of the circular structure for motion #03.

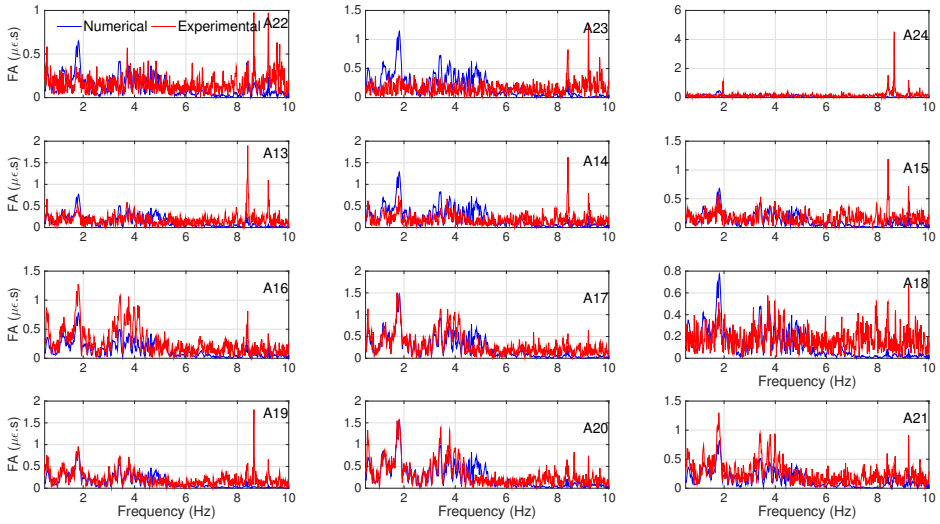

Figure 4.113: Comparison of the Fourier amplitude spectra of the circular structure for motion #03.

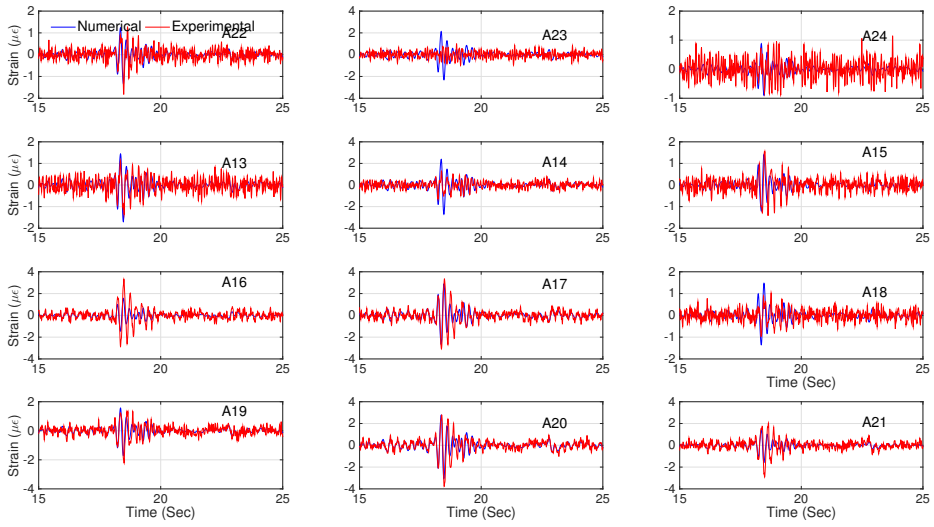

Figure 4.114: Comparison of the time series of the dynamic hoop strains of the circular structure for motion #04.

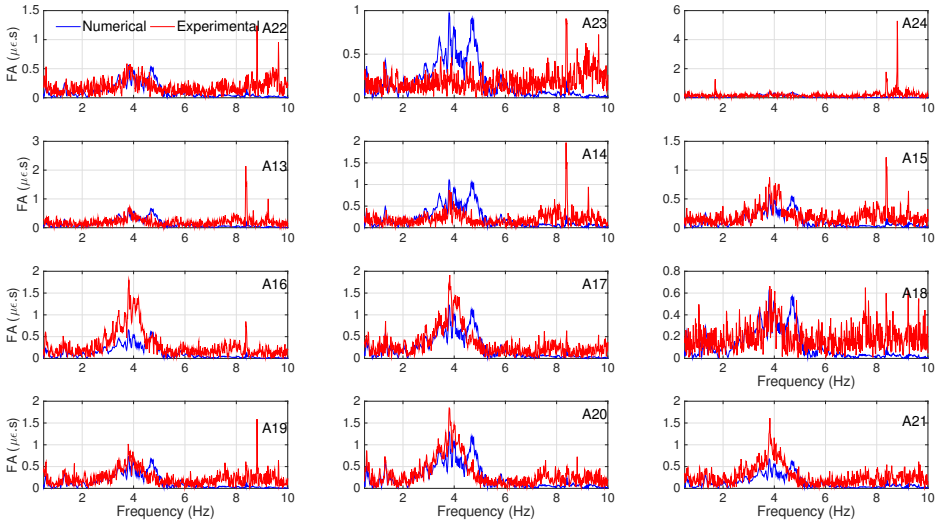

Figure 4.115: Comparison of the Fourier amplitude spectra of the circular structure for motion #04.

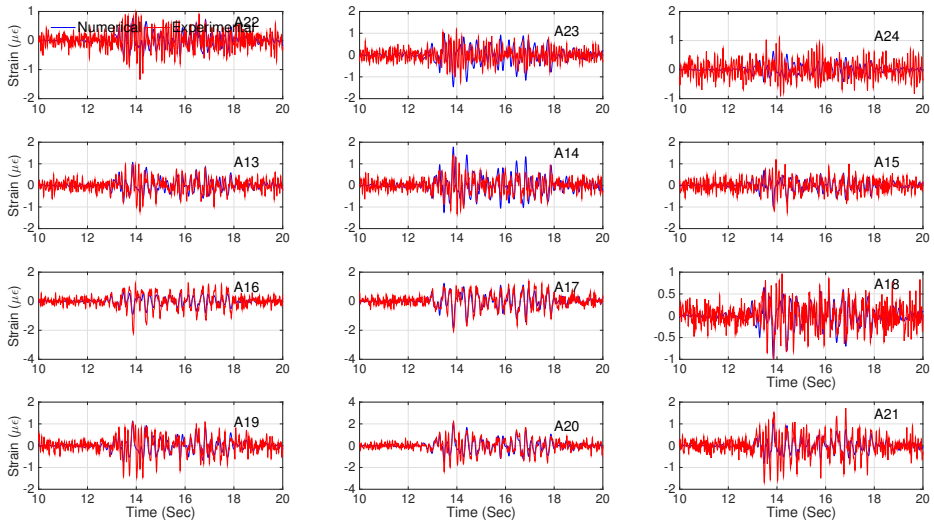

Figure 4.116: Comparison of the time series of the dynamic hoop strains of the circular structure for motion #05.

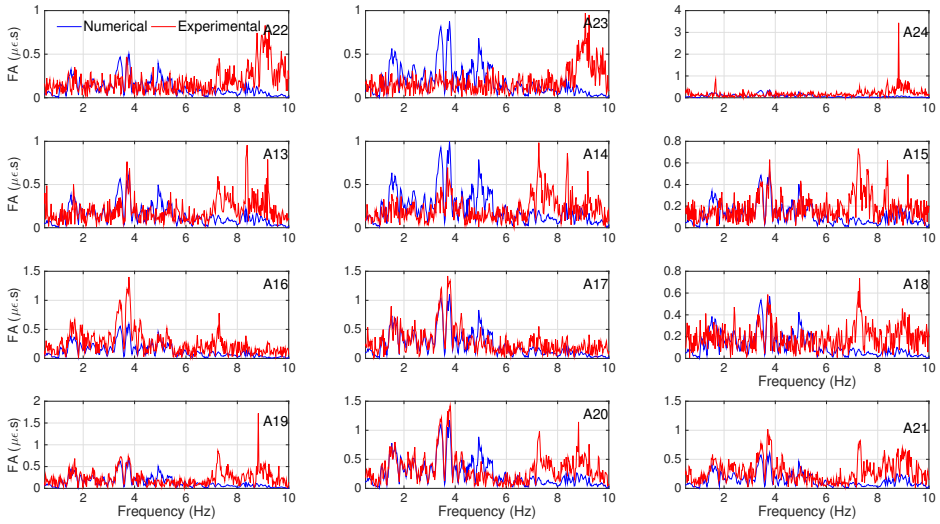

Figure 4.117: Comparison of the Fourier amplitude spectra of the circular structure for motion #05.

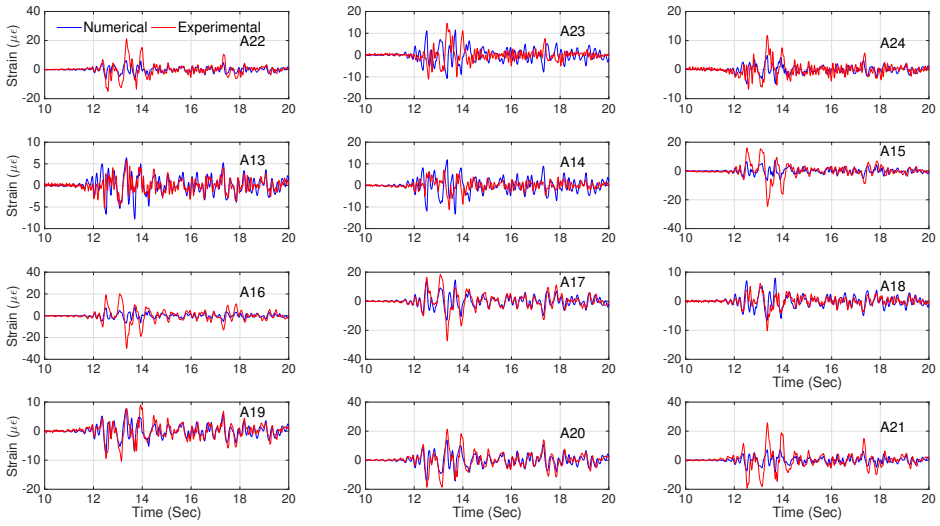

Figure 4.118: Comparison of the time series of the dynamic hoop strains of the circular structure for motion #06.

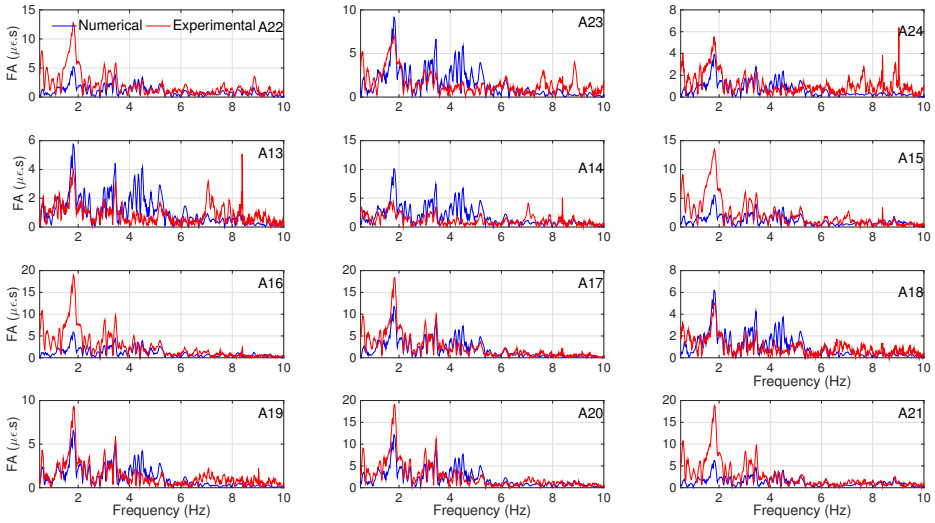

Figure 4.119: Comparison of the Fourier amplitude spectra of the circular structure for motion #06.

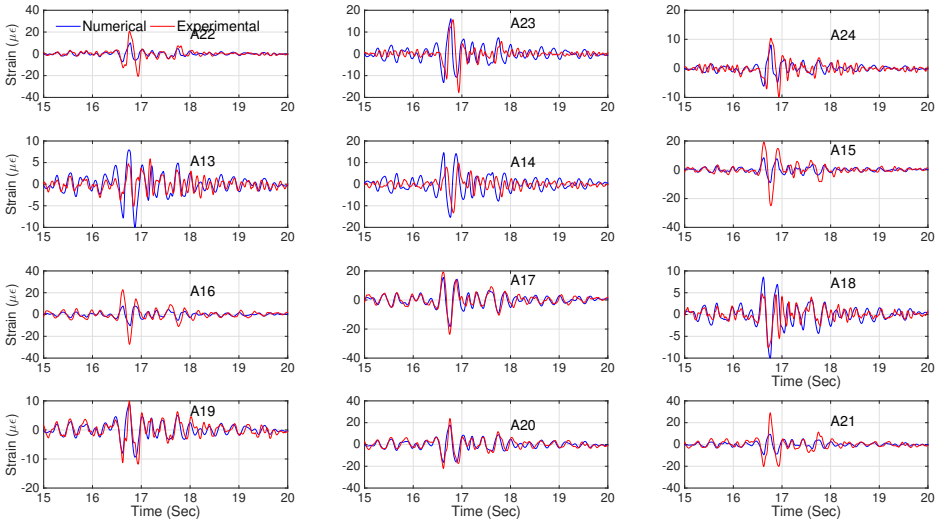

Figure 4.120: Comparison of the time series of the dynamic hoop strains of the circular structure for motion #07.

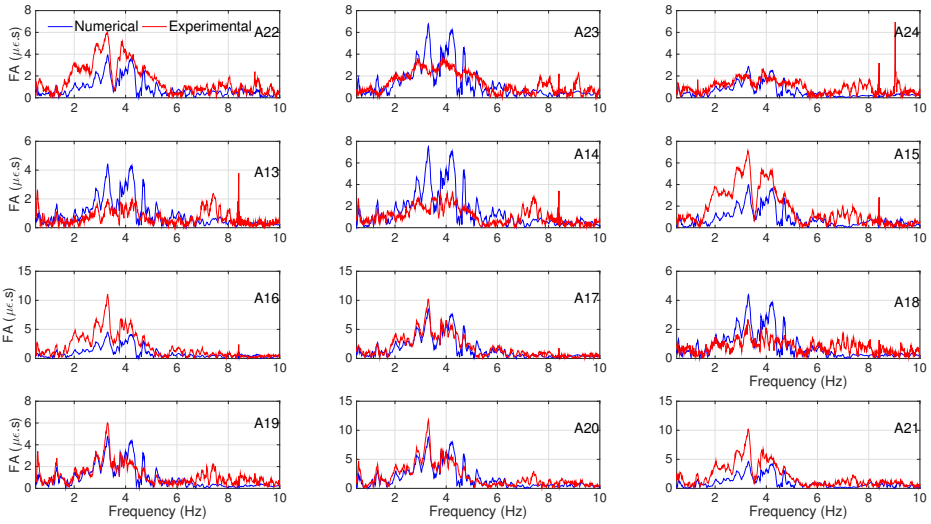

Figure 4.121: Comparison of the Fourier amplitude spectra of the circular structure for motion #07.

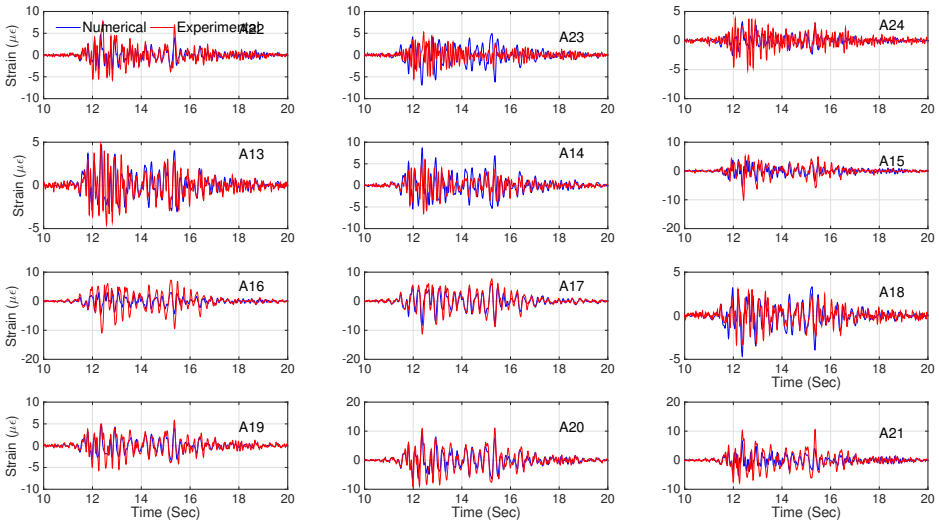

Figure 4.122: Comparison of the time series of the dynamic hoop strains of the circular structure for motion #08.

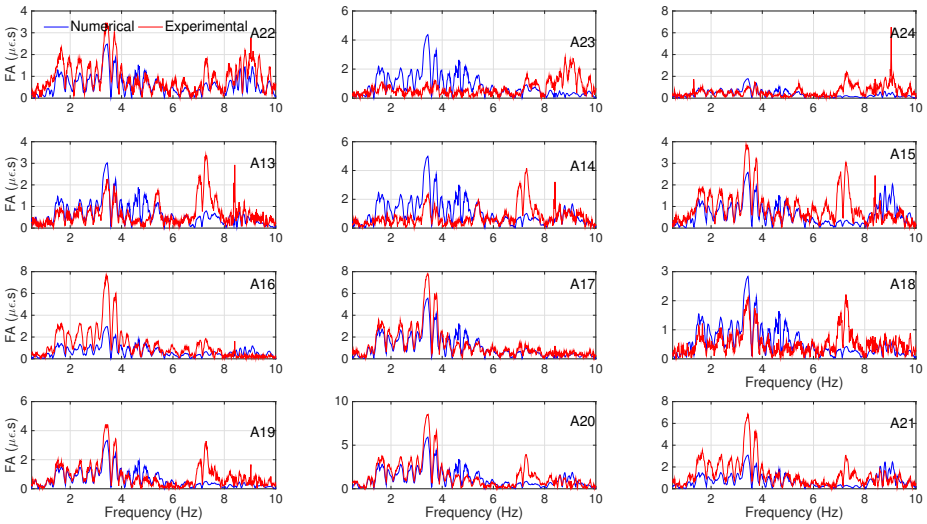

Figure 4.123: Comparison of the Fourier amplitude spectra of the circular structure for motion #08.

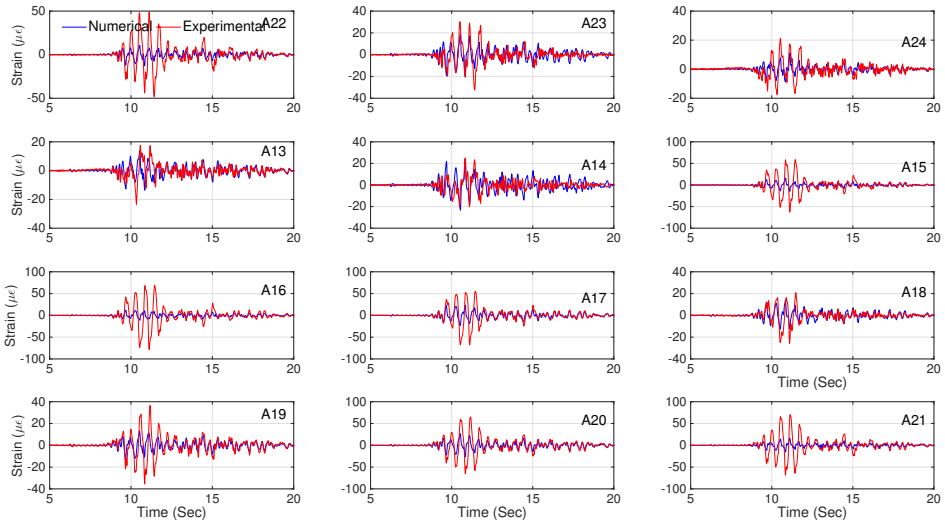

Figure 4.124: Comparison of the time series of the dynamic hoop strains of the circular structure for motion #09.

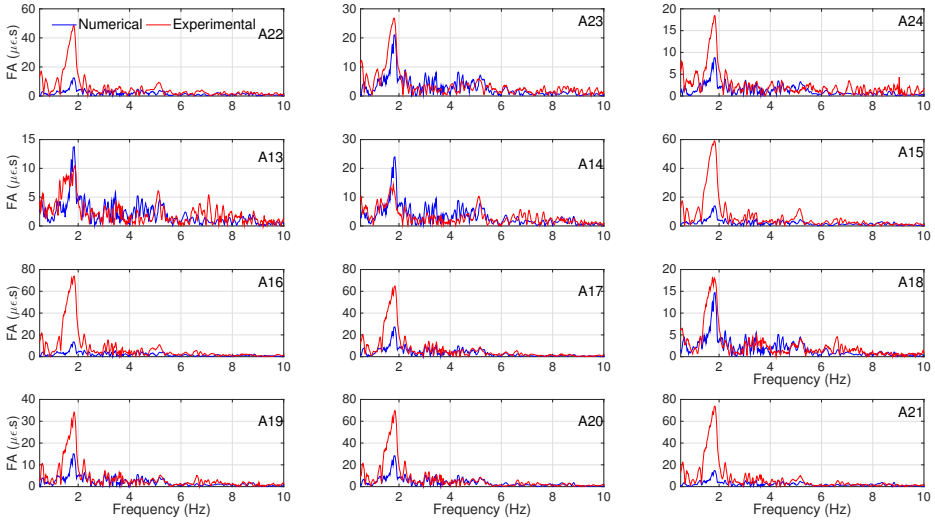

Figure 4.125: Comparison of the Fourier amplitude spectra of the circular structure for motion #09.

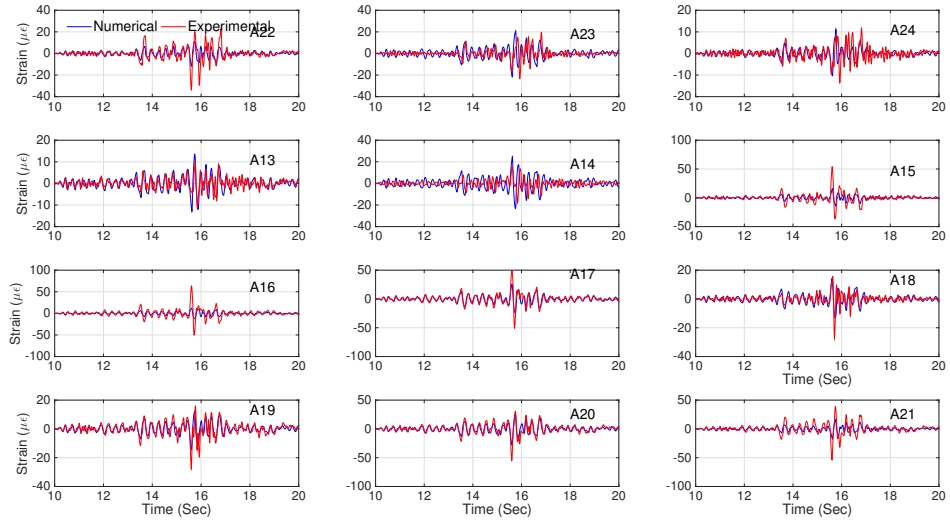

Figure 4.126: Comparison of the time series of the dynamic hoop strains of the circular structure for motion #10.

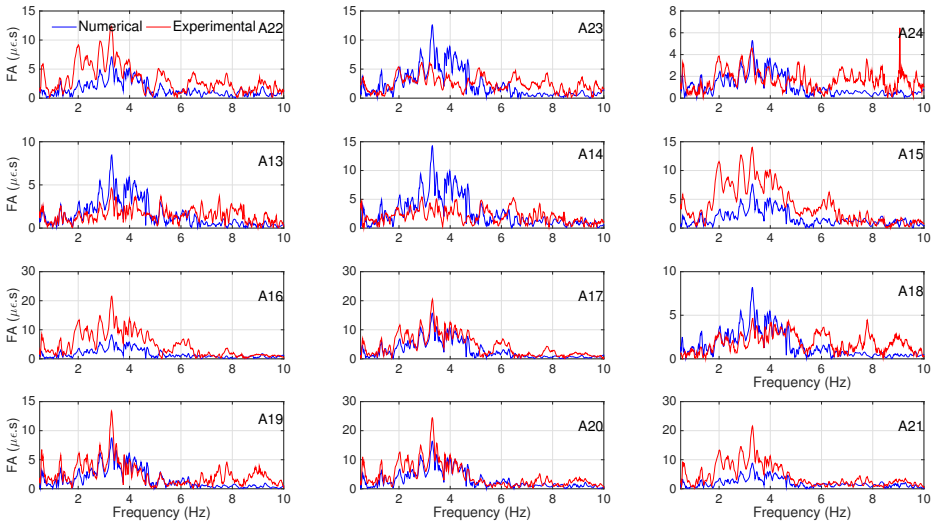

Figure 4.127: Comparison of the Fourier amplitude spectra of the circular structure for motion #10.

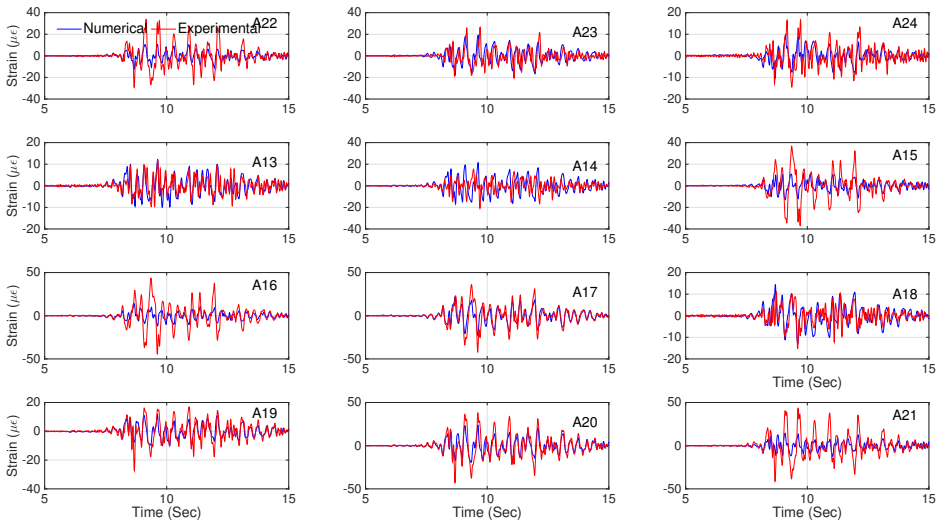

Figure 4.128: Comparison of the time series of the dynamic hoop strains of the circular structure for motion #11.

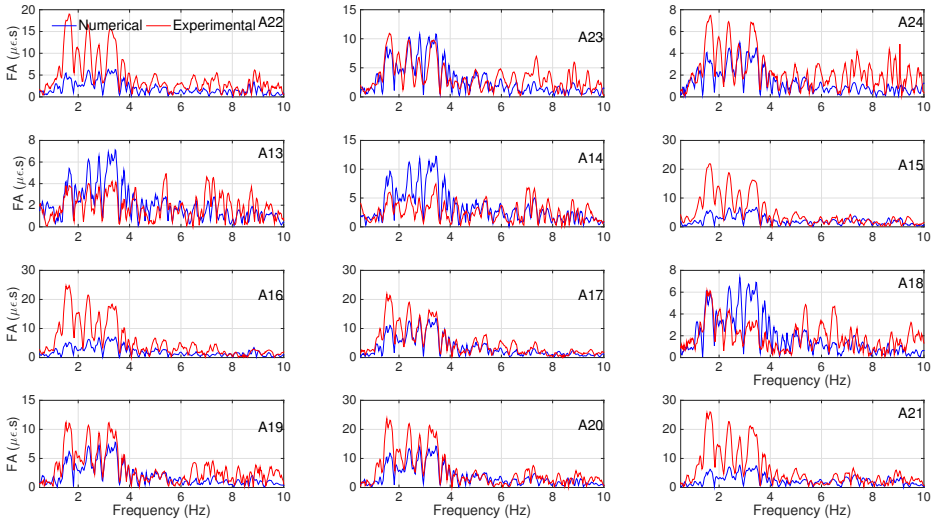

Figure 4.129: Comparison of the Fourier amplitude spectra of the circular structure for motion #11.

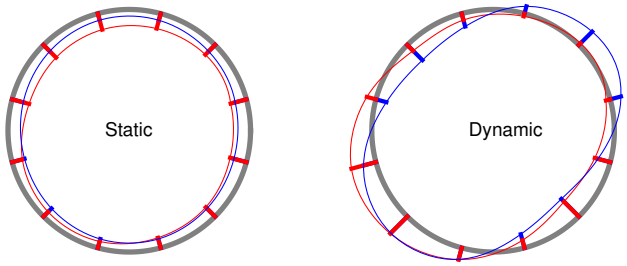

Figure 4.130: Comparison of the maximum static and dynamic hoop strain profiles of the circular structure for motion #03.

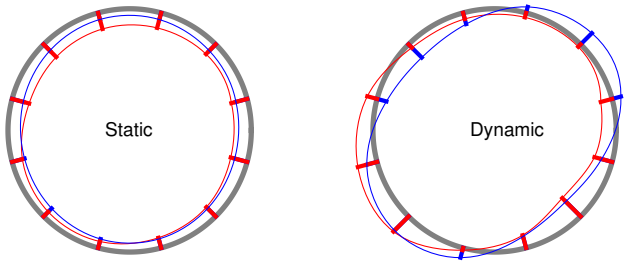

Figure 4.131: Comparison of the maximum static and dynamic hoop strain profiles of the circular structure for motion #04.

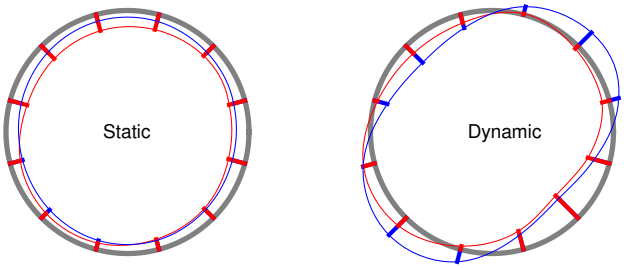

Figure 4.132: Comparison of the maximum static and dynamic hoop strain profiles of the circular structure for motion #05.

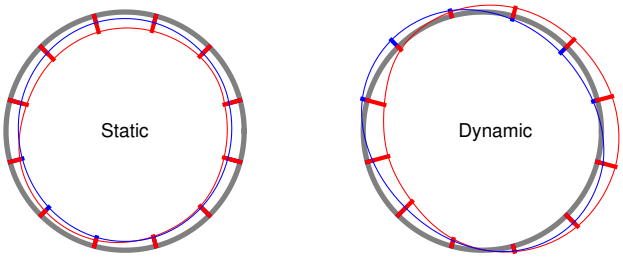

Figure 4.133: Comparison of the maximum static and dynamic hoop strain profiles of the circular structure for motion #06.

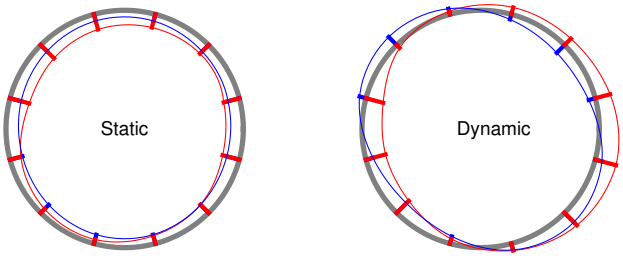

Figure 4.134: Comparison of the maximum static and dynamic hoop strain profiles of the circular structure for motion #07.

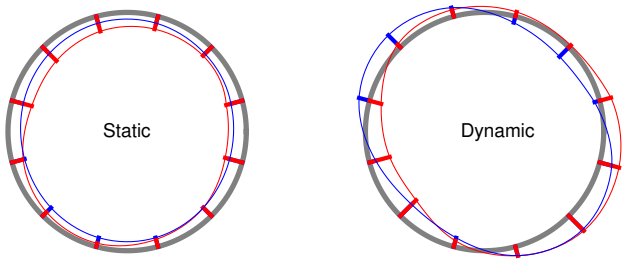

Figure 4.135: Comparison of the maximum static and dynamic hoop strain profiles of the circular structure for motion #08.

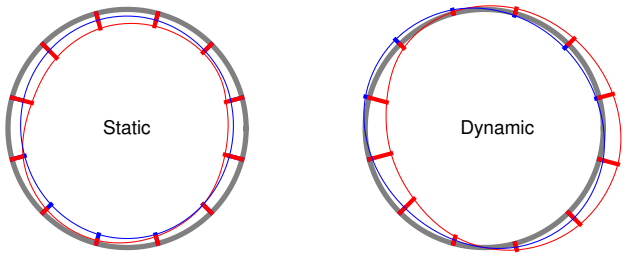

Figure 4.136: Comparison of the maximum static and dynamic hoop strain profiles of the circular structure for motion #09.

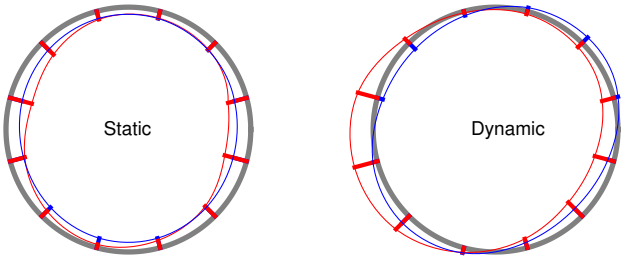

Figure 4.137: Comparison of the maximum static and dynamic hoop strain profiles of the circular structure for motion #10.

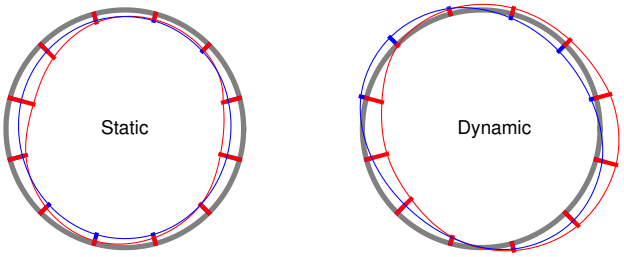

Figure 4.138: Comparison of the maximum static and dynamic hoop strain profiles of the circular structure for motion #11.

4.4.3.6 Maximum dynamic deformation profiles of culvert specimens

In order to investigate the dominant mode of deformation in both structures when the bending strain is maximum, we read the dynamic displacements of different nodes along the edge of the structure at the same time that we obtained the bending strain profiles. Figures 4.139 and 4.140 display the maximum deformation profiles for both the rectangular and the circular structure under all 9 motions. It should be noted that in both figures the resulting deformations are magnified 100 times.

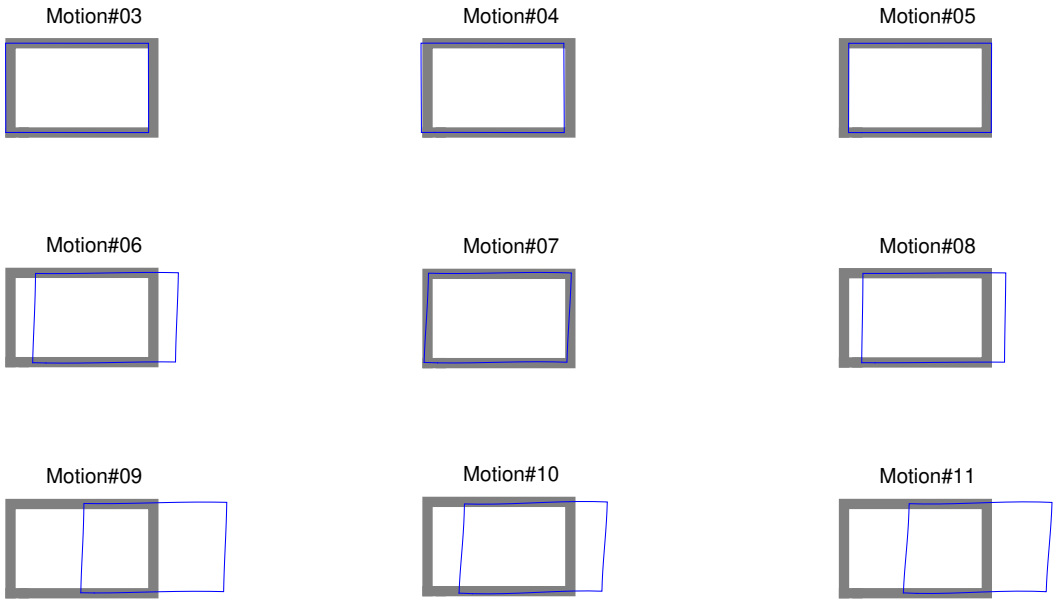

Figure 4.139: Maximum deformation plot for rectangular structure.

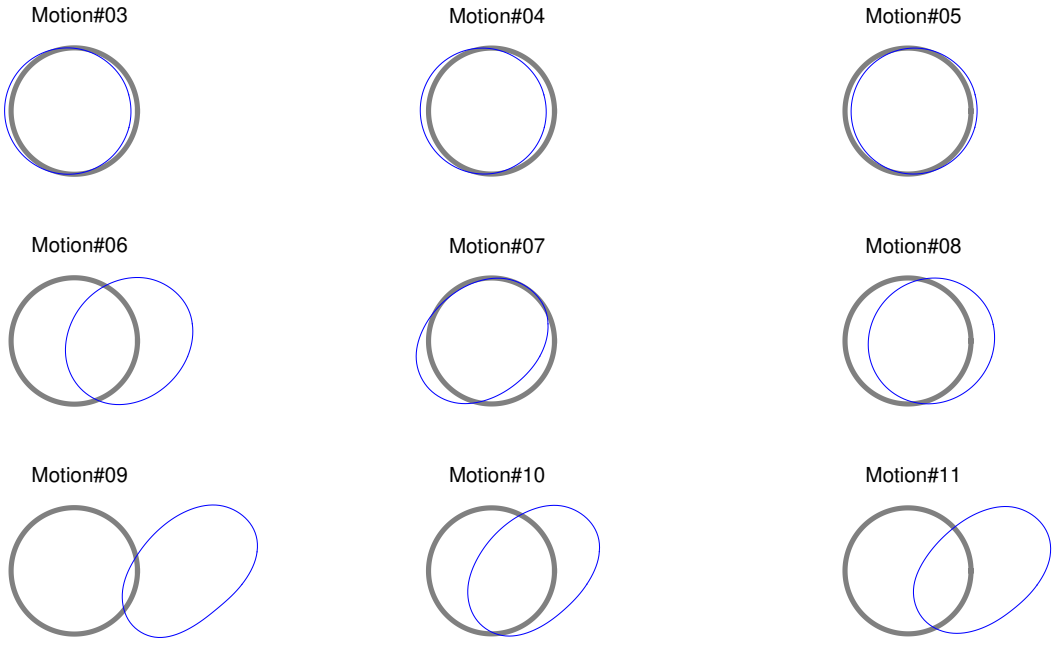

Figure 4.140: Maximum deformation plot for circular structure.

4.4.3.7 Error analysis

In order to summarize the capability of the calibrated numerical model in predicting different response parameters studied in this report, we compute the relative root-mean-square error (RMSE) for each response parameter as follows:

$$\text{Relative RMSE} = \frac{\sqrt{\left[\frac{1}{n}\sum_{k=1}^{n}\left(\mathrm{r}_k^{\mathrm{exp}} - \mathrm{r}_k^{\mathrm{num}}\right)^2\right]}}{\sqrt{\left[\frac{1}{n}\sum_{k=1}^{n}\left(\mathrm{r}_k^{\mathrm{exp}}\right)^2\right]}} \times 100\% \tag{4.35}$$

where n is the total number of time steps considered in the response time-series; and $\mathbf{r}^{\mathrm{exp}}$ and $\mathbf{r}^{\mathrm{num}}$ are the experimental and numerical response time-series, respectively. Considering each data point in the response time-series as different predictions in the dataset, the relative RMSE can be interpreted as the coefficient of variation, i.e. $\sigma/|\mu|$, where σ is the standard deviation and $|\mu|$ is the absolute mean value.

Figures 4.141 and 4.149 display the relative RMSE for all base shakings used in this report. We recall that AA1, AD18, AF28, AC16, AE26, and AFH30 are the ICPs measuring horizontal accelerations at the left and middle arrays in the soil; 7 and 1 are the ICPs at the bottom and top of the left wall of the rectangular structure; BT1, BL7, BB16, and BL17 are the bending strain bridges at corners of the rectangular culvert; 16 and 14 are the ICPs measuring the horizontal accelerations at θ=180 and 270 degrees, respectively, of the circular culvert; A11, A2, A5, and A8 are the bending strain bridges at θ=45, 135, 225, 315 degrees; and A23, A14, A17, and A20 are the hoop strain bridges at θ=45, 135, 225, 315 degrees. As shown, RMSE is less for higher amplitude motions in general, which is due to inherently higher signal-to-noise ratios in those experiments.

Finally, Table 4.12 summarizes the resulting maximum bending strain ratios for the rectangular culvert, maximum bending and hoop strain ratios for the circular culvert, and von Mises stress for both culverts, compared to those we obtained using the finite element model (FEM).

Table 4.12: Maximum bending and hoop strain ratios, and von Mises stress ratios between experiment and FE model predictions.

Motion	$e_b^{\square}$	$e_b^{\bigcirc}$	$e_h^{\bigcirc}$	$\sigma_{vm}^{\square}$	$\sigma_{vm}^{\bigcirc}$
3	0.89	1.37	0.98	0.89	1.29
4	0.81	1.14	0.81	0.81	1.17
5	0.77	1.26	0.87	0.77	1.26
6	1.05	0.86	0.49	1.05	0.89
7	1.17	1.33	0.63	1.17	1.15
8	0.83	0.87	0.88	0.83	0.91
$9^{(a)}$	1.07	0.63	0.34	1.07	0.59
10	1.19	0.83	0.45	1.19	0.85
11	1.13	1.23	0.53	1.13	1.22

$^{(a)}$ Only motion 9 is used for calibrating parameters of the noninear soil model for all analyses.

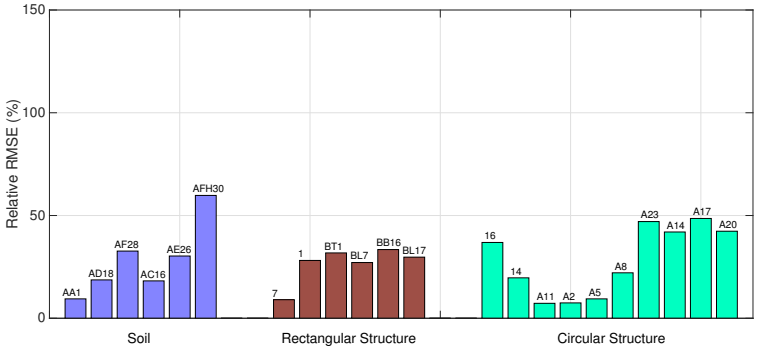

Figure 4.141: Relative RMSE for motion #03.

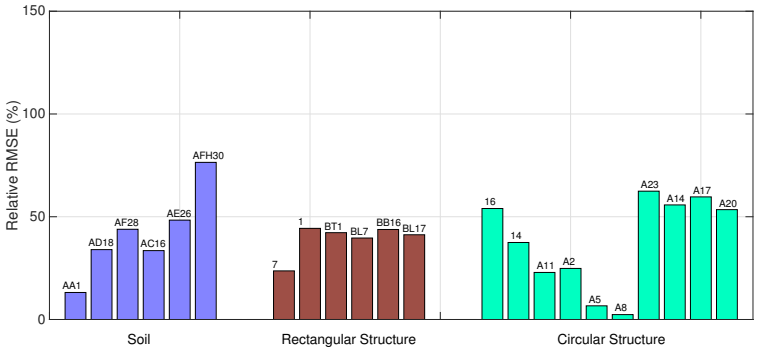

Figure 4.142: Relative RMSE for motion #04.

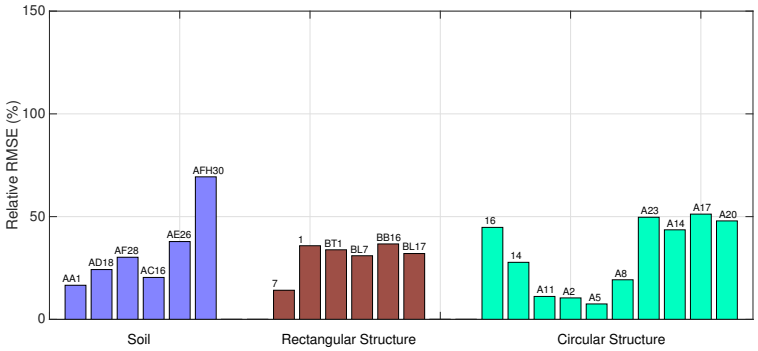

Figure 4.143: Relative RMSE for motion #05.

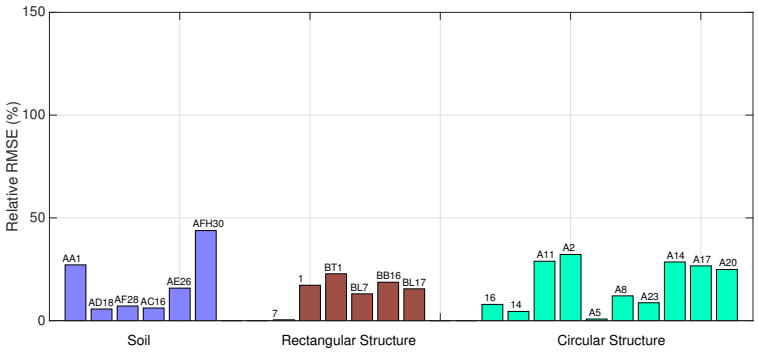

Figure 4.144: Relative RMSE for motion #06.

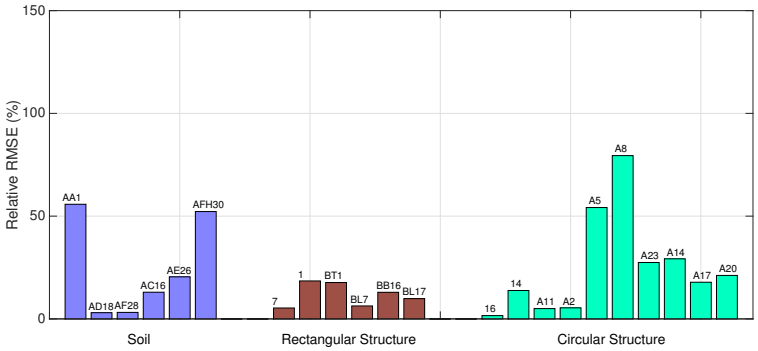

Figure 4.145: Relative RMSE for motion #07.

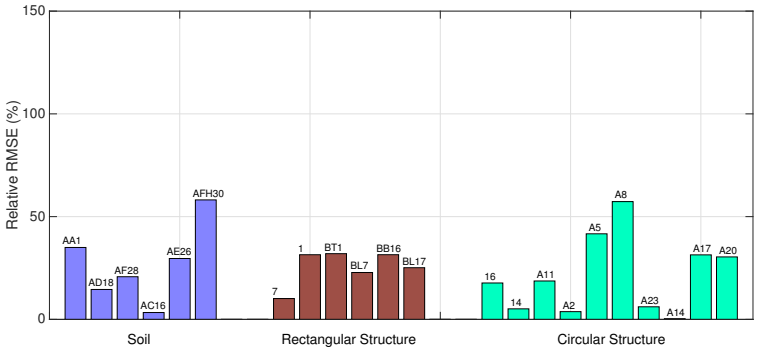

Figure 4.146: Relative RMSE for motion #08.

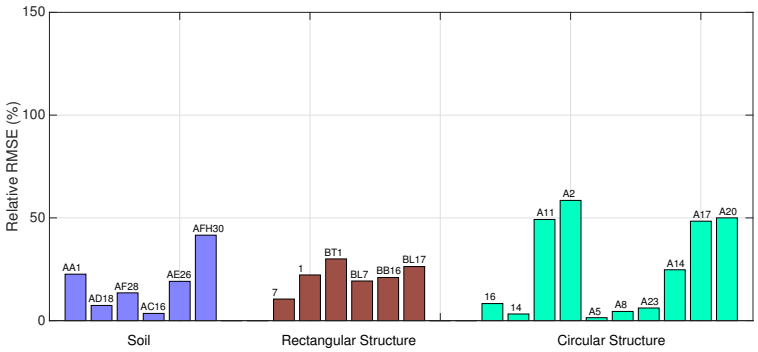

Figure 4.147: Relative RMSE for motion #09.

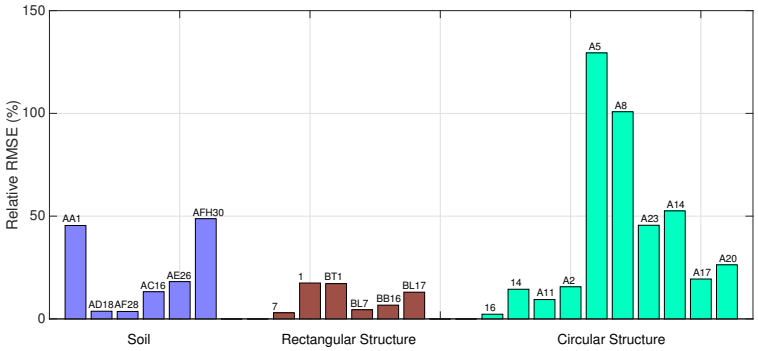

Figure 4.148: Relative RMSE for motion #10.

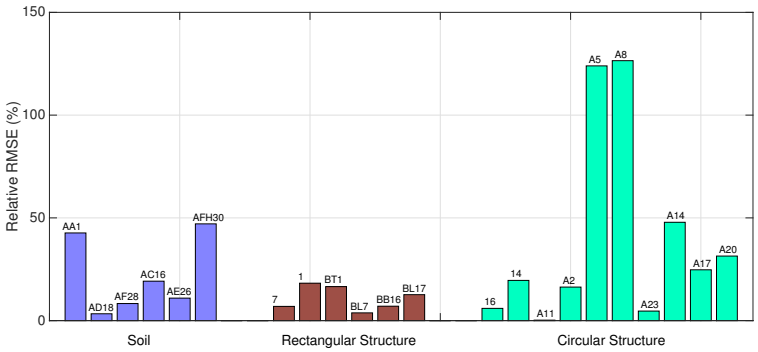

Figure 4.149: Relative RMSE for motion #11.

CHAPTER 5

A quantitative assessment of the NCHRP 611 method for soil-structure interaction analysis of buried circular structures and a proposed improvement

As mentioned in chapter 4, current seismic design practices—which are comprehensively articulated in the NCHRP Report 611 [18]—are primarily based on the procedures proposed by Wang [19] and Penzien [42] for circular and rectangular buried structures, respectively. Due to its computational simplicity, it has been widely adopted as a reference in the design of buried structures. More recently, a number of experimental (e.g., [132, 134, 135]), numerical (e.g., [140, 135, 152, 153, 154, 155, 156]), and analytical (e.g., [144, 145]) studies have been conducted to explore the accuracy of the aforementioned procedures. These studies have revealed that depending on the particular algorithmic branch of the NCHRP 611 methods adopted, some of the structural strains were over-predicted while others were under-predicted. Such inaccuracies should not necessarily lead to catastrophic results for culverts/tunnels, but they nonetheless reduce the margins of safety and economy in their designs.

The aforementioned past studies, however, evaluated and bracketed the performance of NCHRP 611 method only in a limited manner—in particular, the effects of flexibility ratio and the frequency content of the input excitations were not adequately explored, and typically fewer than 10 ground motions were considered. A more comprehensive study was recently conducted on buried rectangular structures [155], but it has also been identified that the responses of rectangular and circular structures are profoundly different, and that the SSI behavior of circular structures is more difficult to capture [135] compared to rectangular

one [71].

In this chapter, a quantitative assessment of the NCHRP 611 method is carried out to comprehensively evaluate the accuracy of the NCHRP 611 method for soil-structure analysis of buried circular structures. Parametric studies with 400 simulations using a broad range of ground motions, nonlinear soil properties, embedment depths and structural flexibility ratios, as well as no-slip and full-slip interface conditions are considered to bracket the acceptable ranges of applicability of the NCHRP 611 method. Please refer to [157] for more details about this work.

5.1 The NCHRP approach with nonlinear soil model

As seen in 4.2.1, in order to compute seismic demands using the NCHRP 611 methodology, we first need to estimate the maximum free-field strain $\gamma_{\max}$ in the soil deposit as well as the corresponding effective compatible shear modulus G_m. Then, the seismic demands can be computed following the steps outlined above. For shallow structures one may use Eq. 4.1 to estimate $\gamma_{\max}$. However, in order to use that equation, we need to know the strain-compatible shear modulus (G_m) of the ground surrounding the culvert or pipe, which itself is a function of $\gamma_{\max}$. For linear soil response one may simply use the elastic shear modulus $G_{\max}$ to represent G_m. For the nonlinear soil response, we can either perform a 1D site response analysis to compute G_m, or use an iterative procedure to obtain it, as described below:

1. To start the procedure (iteration $i = 0$), provide an initial guess for the maximum shear strain at the elevation of the bottom of the circular structure. This initial guess can be any reasonable value. Here, we simply use $\gamma_{\max,0} = 0.05\%$.

2. For iteration i, predict G_m for the circular structure, which can be achieved using $\gamma_{\max,i-1}$ and the $G/G_{\max}$ curve of the soil. Subsequently, correct the maximum shear strain $\gamma_{\max,i}$ using Eq. 4.1.

3. Repeat step 2 until $|\gamma_{\max,i} - \gamma_{\max,i-1}| <= \text{TOL}$ for the predefined tolerance TOL.

The NCHRP 611 report suggests using 1D site response analysis to compute the maximum shear strain as well; whereas the iterative procedure described above produces a self-consistent pair of ($\gamma_{\max}$, G_m).

Given all the different options above, it is best to delineate the NCHRP611 method into its two variants as shown in Table. 5.1. Of the two, the variant labeled "NCHRP611-NonLinIterative" has not been described in any prior publication, to the best of the authors' knowledge; however, it is probably a distinct variant that at least some practitioners must have used, and as such, it is essential to include it in the comparisons.

Table 5.1: Two variants of the NCHRP611 method.

Label	**NCHRP611-NonLinIterative**	**NCHRP611-NonLinRefined**
Procedure	(1) Set $\gamma_{\max,0} = 0.05\%$ and then use the iterative procedure to compute both $\gamma_{\max}$ and G_m; (2) Follow Eqs. 4.2–4.7 to compute R_d and then hoop thrust and bending moment.	(1) Perform nonlinear 1D site response analysis to compute $\gamma_{\max}$; (2) Use computed $\gamma_{\max}$ to interpolate the $G/G_{\max}$ curve (corresponding to layer of soil where $\gamma_{\max}$ occurs) to get the G_m; (3) Follow Eqs. 4.2–4.7 to compute R_d and then hoop thrust and bending moment.
Remarks	$\gamma_{\max}$ is computed using the $G/G_{\max}$ curves but not the damping curves, which can lead to inaccurate results, especially for high damping ratios of high strain values.	Bears the highest computational cost, but potentially the most accurate.

5.2 Numerical experiments

A circular culvert (Fig. 5.1) embedded in soil is modeled using the finite element (FE) method and analyzed under dynamic excitations in parametric studies to quantify the accuracy of the NCHRP 611 method. Dimensions of the exterior domain and the domain of interest in the constructed FE model(s) are 180m×45m and 120m×30m, respectively. The culvert diameter is 3m. The side and bottom boundaries of the computational domain are truncated using the Lysmer and Kuhlemeyer [20] absorbing boundary conditions (ABCs). The dashpot coefficients c are determined as,

$$\text{For the bottom boundary } \rightarrow \begin{cases} c_x = \rho \cdot V_s \cdot A_b \\ c_y = \rho \cdot V_p \cdot A_b \end{cases} \tag{5.1}$$

$$\text{For the side boundaries } \rightarrow \begin{cases} c_x = \rho \cdot V_p \cdot A_s \\ c_y = \rho \cdot V_s \cdot A_s \end{cases} \tag{5.2}$$

where ρ is the density of the soil; V_s and V_p are shear and compressional wave velocities, respectively; A_b and A_s are the areas of the bottom and side soil elements that correspond to the dashpots used. The validity of the numerical model has been verified by comparing with experimental data from the centrifuge tests [149].

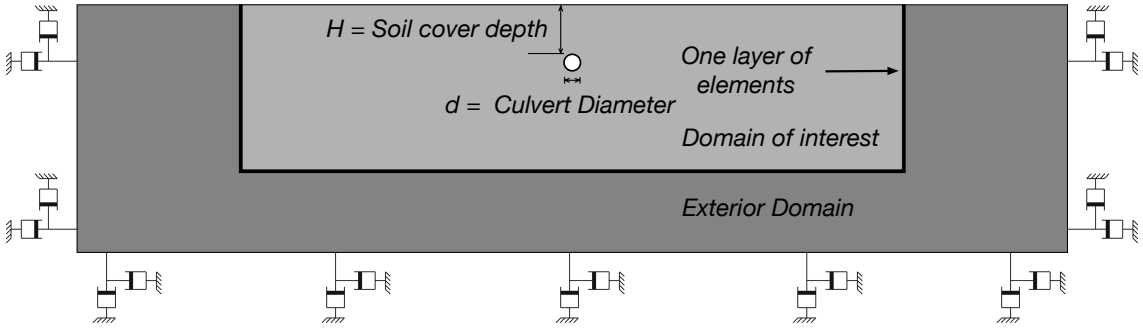

Figure 5.1: Side view of the numerical model.

In order to reduce the computational domain while modeling a semi-infinite domain under remote excitations, we use the domain reduction method (DRM). DRM is a two-step finite element procedure proposed by Bielak et al. [117] for modeling the seismic responses of heterogeneous subdomains. DRM enables the conversion of the half-space problem to an equivalent one in which the effects of incoming waves due to remote excitations are translated into equivalent nodal forces that are applied inside a domain that is truncated by ABCs.

In DRM, the equivalent nodal force vector is computed using Eq. (5.3) per [117] and applied to the nodes located at a single layer of elements that form the interface between the exterior and the near-field domains as shown in Fig. 5.1.

$$\mathbf{P}^{eff} = \begin{bmatrix} \mathbf{P}_i^{eff} \\ \mathbf{P}_b^{eff} \\ \mathbf{P}_e^{eff} \end{bmatrix} = \begin{bmatrix} \mathbf{0} \\ -\mathbf{M}_{be}^{\Omega+}\ddot{\mathbf{u}}_e^0 - \mathbf{C}_{be}^{\Omega+}\dot{\mathbf{u}}_e^0 - \mathbf{K}_{be}^{\Omega+}\mathbf{u}_e^0 \\ +\mathbf{M}_{eb}^{\Omega+}\ddot{\mathbf{u}}_b^0 + \mathbf{C}_{eb}^{\Omega+}\dot{\mathbf{u}}_b^0 + \mathbf{K}_{eb}^{\Omega+}\mathbf{u}_b^0 \end{bmatrix} \tag{5.3}$$

where the subscripts $_b$ and $_e$ refer to the nodes along the inside and outside inteface of the one layer of elements, respectively. The terms $\mathbf{u}^0$ and $\mathbf{P}^{eff}$ respectively denote the free-field displacements and forces for the nodes on the one layer of elements, which can be obtained by performing 1D site response analysis for a given ground motion time-history. $\mathbf{M}^{\Omega+}$, $\mathbf{C}^{\Omega+}$ and $\mathbf{K}^{\Omega+}$ are the mass, damping and stiffness matrices assembled for only the above mentioned single layer of elements.

In the present study, the DRM method is implemented in ABAQUS [114], and the accuracy of this implementation is verified by comparing the numerical results obtained from DRM and single-soil-column simulations [118].

5.2.1 Material Models & Soil-Structure Interface Conditions

In the numerical simulations, the soil is modeled with 4-node quadrilateral plane strain elements, each of which has a near-uniform size of 0.5m × 0.5m. The circular culvert lining is modeled with 100 equal-sized beam elements, because NCHRP equations are derived based on the assumptions of beam elements. The element size is chosen such that approximately 12 discretized nodes exist within the minimum wavelength [158], which, for the present simulations is $\lambda_{\min}/12 = V_s/f_{\max} = 200\text{m/s}/10\text{Hz}/12 \approx 1.67\text{m}$. Table 5.2 summarizes the mechanical properties of the culvert lining adopted in this study.

For the surrounding soil, nonlinear material behavior is considered. The elastic material properties of the soft and stiff soils are provided in Table 5.3. In the nonlinear analyses, the soil deposits are modeled using a bounding surface plasticity model, which was originally developed by Borja et al. [63, 69]. This nonlinear soil model has been thoroughly calibrated and validated using data from multiple centrifuge tests by Zhang et al. [71]. Here, we choose the material parameters of this nonlinear soil model as $h = 0.3\ G_{\max},\ m = 1.2,\ R = 0.006\ G_{\max},\ H_0 = 0.01\ G_{\max}$, which are calibrated based on the Ottawa sand properties [2]. The parameters h, m and H_0 are three parameters, which control the intensity, rate, and final state of hardening. R is the radius of the bounding surface. The selected hysteresis and stiffness degradation and damping curves are shown in Figs. 5.2 (a) and (b), respectively.

In order to examine the accuracy of the NCHRP 611 method for domains involving soil layers, a two-layer soil deposit is considered in addition to the uniform soil. The shear wave velocity curves for homogeneous and two layered half-space cases are shown in Fig. 5.2 (c). In addition to these considerations, the modeling variations of the soil-structure interface are examined by using full-slip contact, wherein the ABAQUS [114] built-in node-to-node hard-contact formulation with finite sliding was used, as well as no-slip (perfectly bonded) interface conditions, wherein the liner elements were tied to the adjacent soil nodes and the interface could sustain tension. As reported in [159], the soil-lining interface properties can significantly affect the internal forces developed in the lining of a circular tunnel.

Table 5.2: Mechanical properties of the culvert lining.

Material	Diameter (m)	Young's Modulus (GPa)	Poisson's Ratio	Density (kg/m^3)
Properties	3	68.9	0.3	2700

Table 5.3: Mechanical properties of the soil deposits.

	Shear Modulus (MPa)	Poisson's Ratio	Density (kg/m^3)
Soft soil	80	0.3	1900
Stiff soil	320	0.3	2000

5.2.2 Effects of Embedment Depth

Upon creating the model matrix with different material properties and soil-structure interface conditions, we explore the effects of embedment depths by varying the embedment depth ratio—defined as H/d (see Fig. 5.1)—from 0.5 to 5 in increments of 0.5. The incident wave is defined based on Eq. 5.4 with $a_{\max} = 0.1g$ and $T = 0.5$ sec.

$$\ddot{u}(t) = \frac{a_{\max}}{2} \sin(2\pi t/T)\big[1 - \cos(2\pi t/10T)\big] \tag{5.4}$$

Fig. 5.3 displays the variations of maximum bending strain, hoop strain, and diameter change ratios (of NCHRP611 methods to the finite element method) with respect to embedment depth ratio. The figure presents the results for homogeneous and two layered half-space cases.

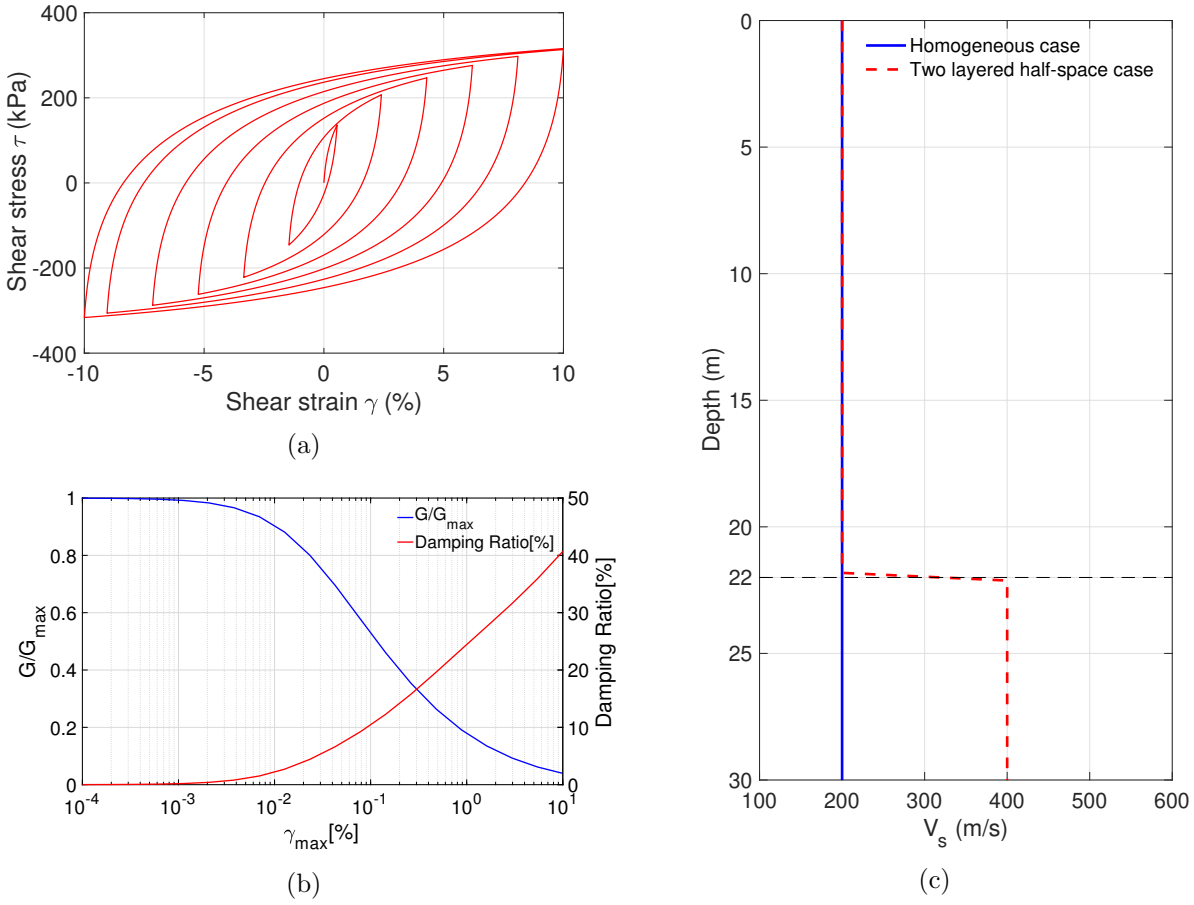

Figure 5.2: (a) Hysteresis curve of the adopted nonlinear soil model, (b) stiffness degradation and damping curves, and (c) shear wave velocity profiles.

Strain variations along the circumference of the structure are also examined by computing contour plots for hoop and bending strain profiles shown in Fig. 5.4 and Fig. 5.5. The following can be observed from these figures:

- Generally, the full-slip interface produces higher ratios than the no-slip case (i.e., it is more conservative)—while noting that the interface modeling assumption can also lead to a completely different profile (shape) for the maximum hoop strain. Given this observation, it appears reasonable that the NCHRP611 report recommends the use of a full-slip interface condition for the bending strain and diameter change, and a no-slip interface condition for the hoop strain.

- In the no-slip case, the NCHRP611-NonLinIterative method can both over- or underestimate the maximum hoop strain by up to a factor of 2.0 and 0.9, respectively.

- In the full-slip case, the NCHRP611-NonLinIterative method always overestimates the maximum bending strain and diameter change by up to 5.1 and 14.3, respectively.

- In all cases, the refined NCHRP method—namely, NCHRP611-NonLinRefined—exhibits better performance compared to the NCHRP611-NonLinIterative.

- Overall, the refined NCHRP method (i.e., NCHRP611-NonLinRefined) shows acceptable profile shapes for both hoop and bending strains.

5.2.3 Effects of Excitation Frequencies

As mentioned above, the NCHRP 611 method is based on pseudo-static considerations described in [19], the validity of which is related—among other things—to the frequency content of the considered ground motions. In principle, the broadband frequency content of seismic input excitations (i.e., seismic wavelengths) affect the seismic earth pressures [44], and thus the shear strain. Herein, we study the effects of excitation frequencies by using the function defined in Eq. 5.4 and by varying the input frequencies from 0.5 Hz to 10 Hz with 20 logarithmically even-spaced frequencies. Fig. 5.6 displays the maximum bending strain, hoop

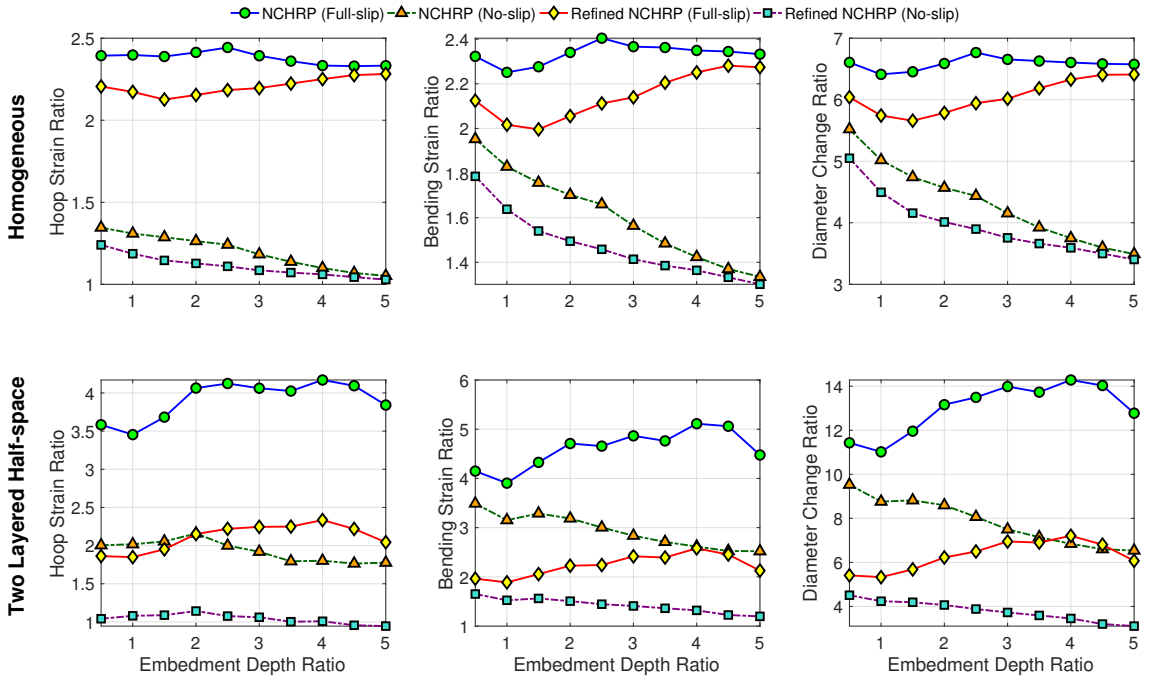

Figure 5.3: Ratios of maximum bending strain, hoop strain, and diameter change for (a) homogeneous and (b) two layered half-space cases versus embedment depth ratio.

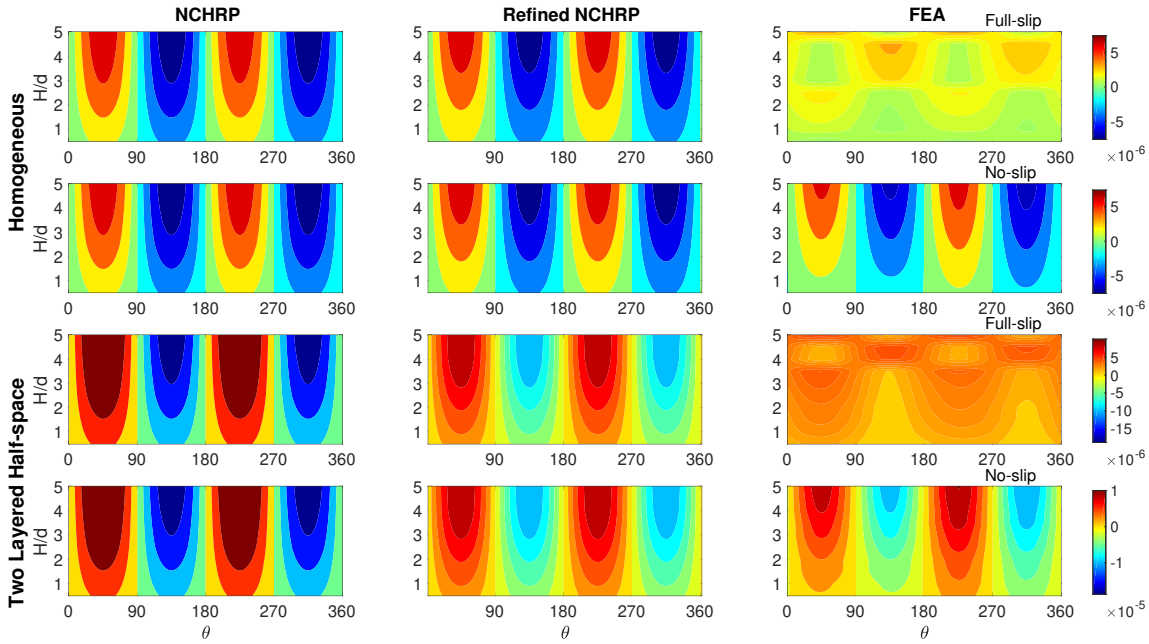

Figure 5.4: Maximum hoop strain profiles obtained using the NCHRP611-NonLinIterative, NCHRP611-NonLinRefined, and FEA approaches for (a) homogeneous and (b) two layered half-space cases versus embedment depth ratio.

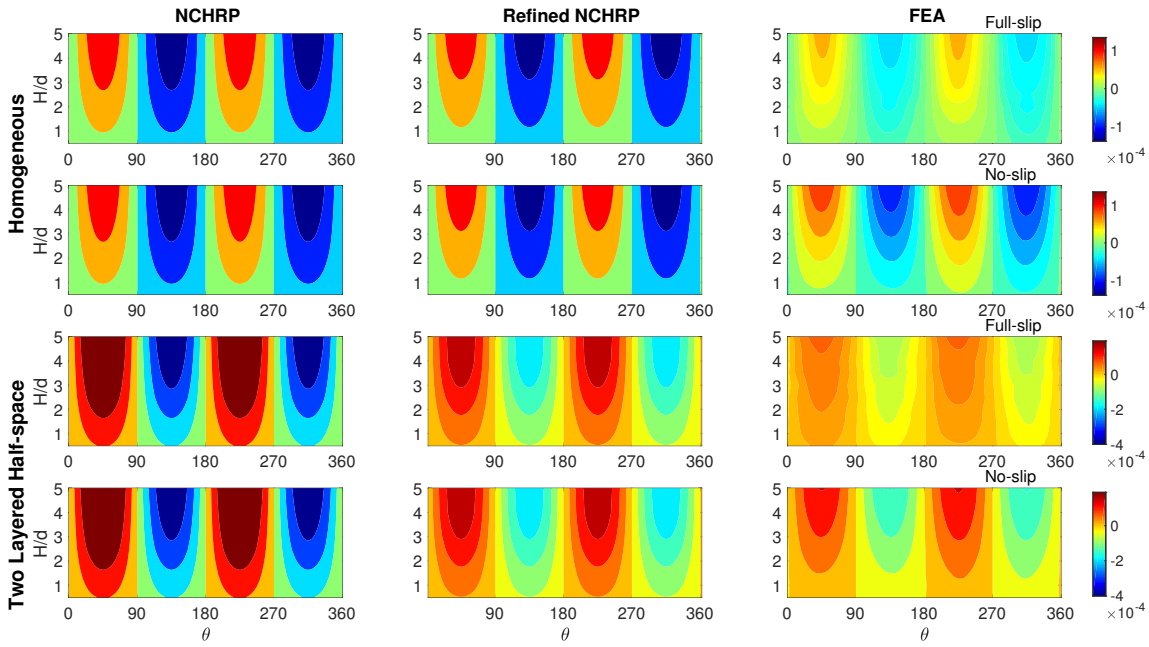

Figure 5.5: Maximum bending strain profiles obtained using the NCHRP611-NonLinIterative, NCHRP611-NonLinRefined, and FEA approaches for (a) homogeneous and (b) two layered half-space cases versus embedment depth ratio.

strain, and diameter change ratio versus the dimensionless term λ/d. The contour plots for hoop and bending strain profiles are shown in Fig. 5.7 and Fig. 5.8, respectively. Also, in order to understand the differences in the locations and amplitudes of γ_{max} between results obtained from 1D site response analyses and the empirical Eq. 4.1, surface plots (see Fig. 5.9) are generated that show the effects of excitation frequency on γ_{max}. An inspection of these figures/results reveals that:

- The NCHRP611-NonLinIterative method overestimates the maximum hoop and bending strains as well as the diameter change values for the lower λ/d ratios. The corresponding ratios can climb up to 5.4, 6.5 and 18.8, respectively. The main reason behind this mishap is that the NCHRP611-NonLinIterative approach estimates the key parameter γ_{max} at much higher values than the refined ones for the lower λ/d values.

- The refined NCHRP method (i.e., NCHRP611-NonLinRefined) significantly improves the overestimations and can reduce those ratios to 1.6, 3.4 and 7.3, respectively.

- In all cases, the refined NCHRP method produces more accurate results compared to the NCHRP611-NonLinIterative method.

- Not only the amplitude, but also the location where $\gamma_{\max}$ occurs vary. The empirical equation (i.e., Eq. 4.1) always assumes that $\gamma_{\max}$ occurs at the bottom of the culvert/tunnel, which is not necessarily true. As shown in Fig. 5.9, the maximum shear strain may occur at the top elevation of the culvert when λ/d is small.

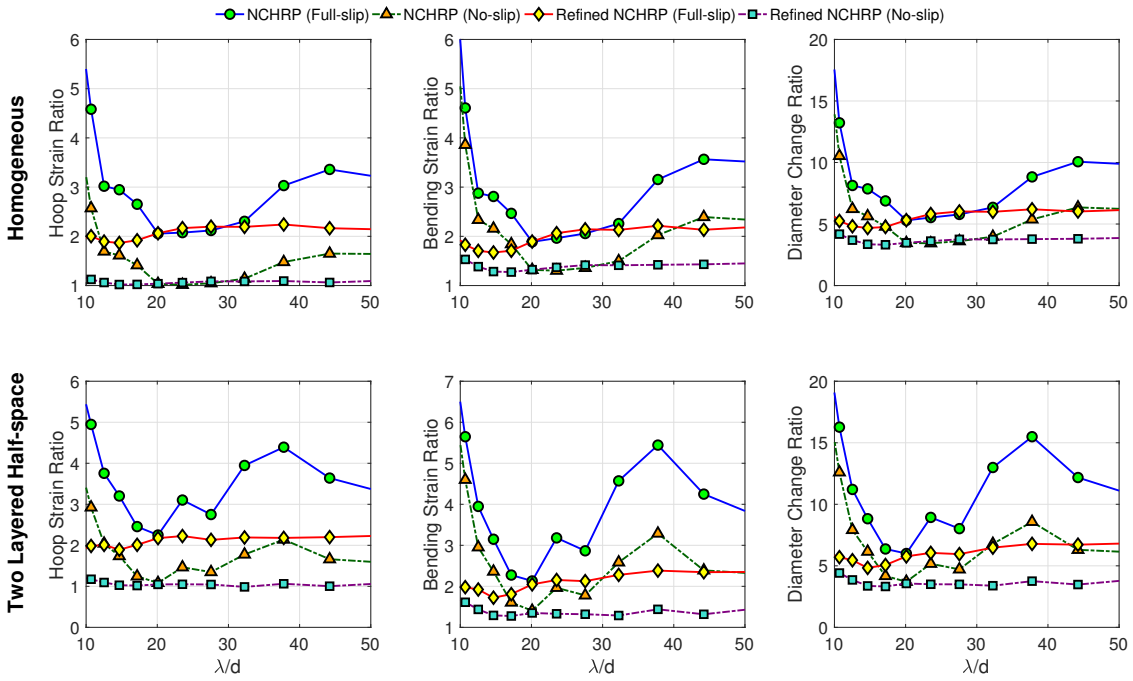

Figure 5.6: Ratios of maximum bending strain, hoop strain, and diameter change for (a) homogeneous and (b) two layered half-space cases versus λ/d.

5.2.4 Effects of Excitation Amplitude

Considering the potentially nonlinear behavior of surrounding soil under strong input motions, which can have considerable impacts on both G_m and $\gamma_{\max}$ in Eq. 4.1, it is critical to examine the effects of excitation amplitude. As in the previous parametric study, we also use Eq. 5.4 here as the input motion, but vary the amplitude, $a_{\max}$, from $0.01g$ to $1g$ with 10 logarithmically evenly spaced increments. Fig. 5.10 displays the maximum bending strain,

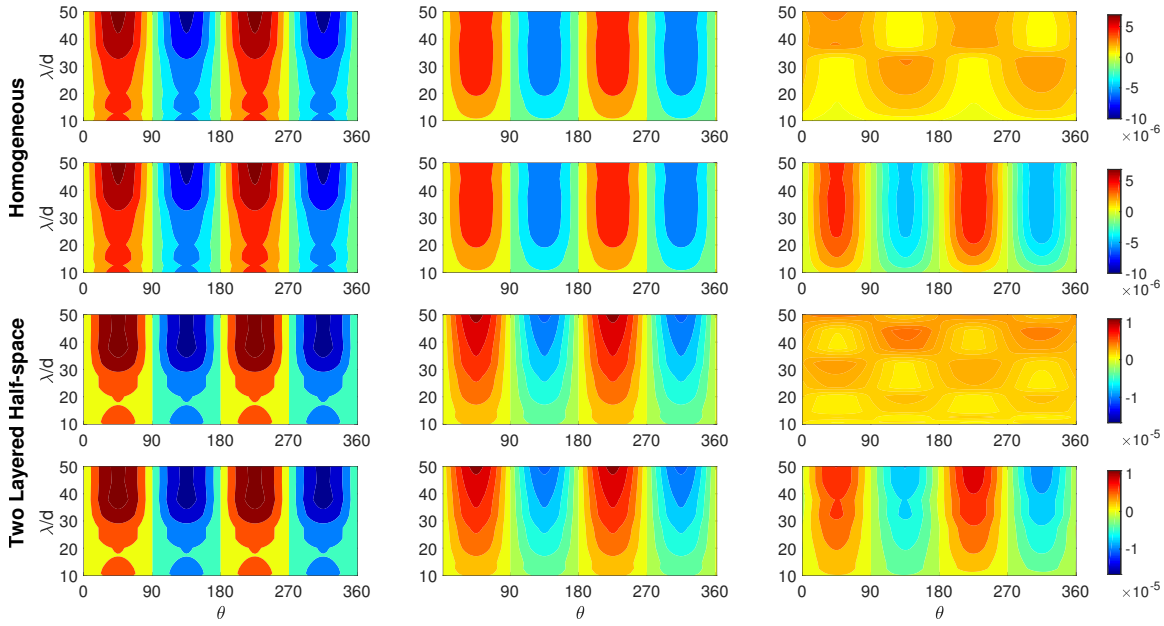

Figure 5.7: Maximum hoop strain profiles obtained using the NCHRP611-NonLinIterative, NCHRP611-NonLinRefined, and FEA approaches for (a) homogeneous and (b) two layered half-space cases versus λ/d.

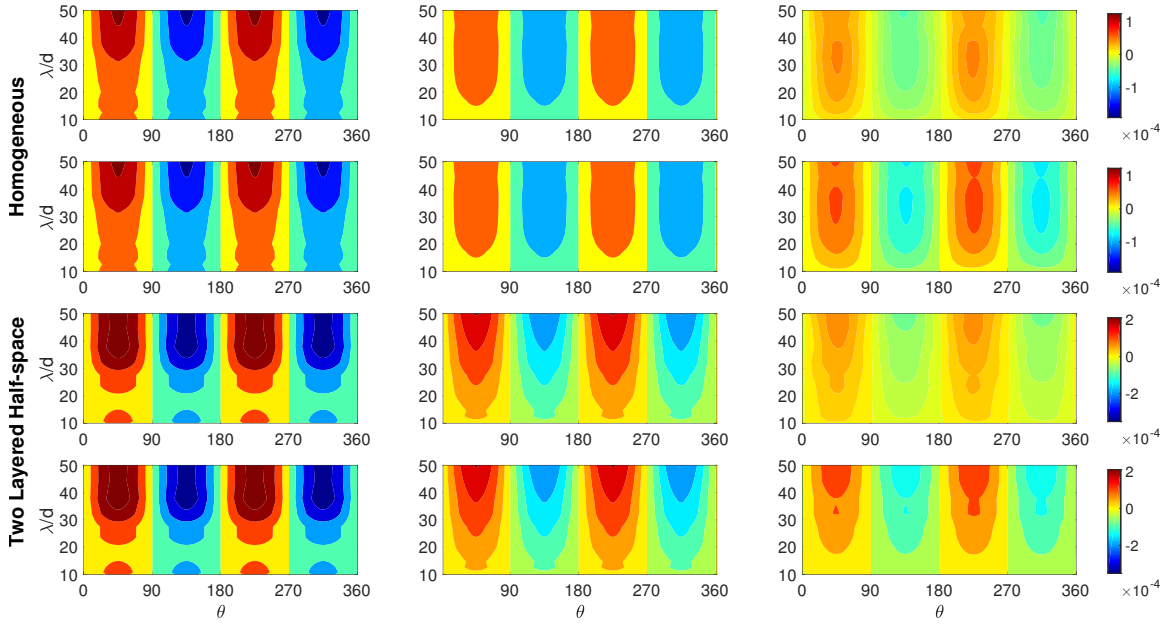

Figure 5.8: Maximum bending strain profiles obtained using the NCHRP611-NonLinIterative, NCHRP611-NonLinRefined, and FEA approaches for (a) homogeneous and (b) two layered half-space cases versus λ/d.

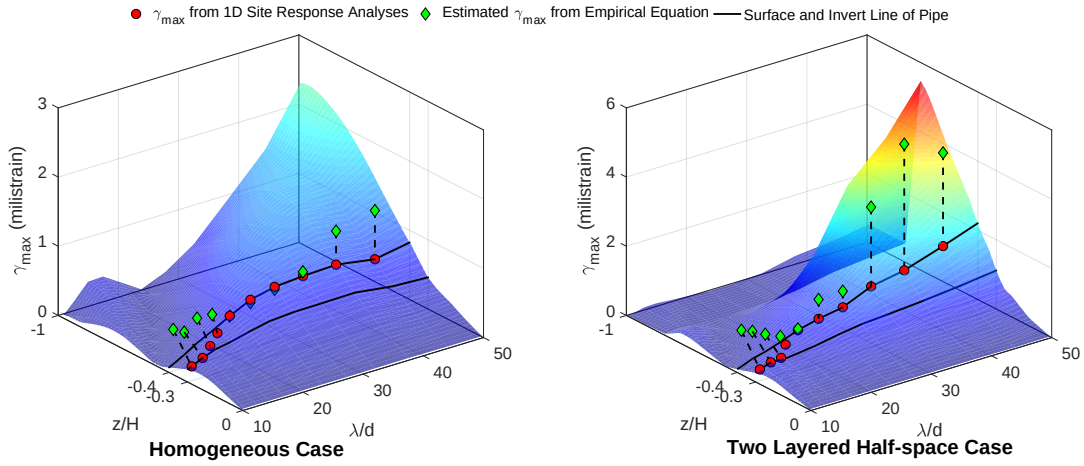

Figure 5.9: Surface plot for $\gamma_{\max}$ versus λ/d.

hoop strain, and diameter change ratios versus the Peak Ground Acceleration (PGA) obtained in the numerical experiments. The contour plots for hoop and bending strain profiles are shown in Fig. 5.11 and Fig. 5.12, respectively. Additionally, the extent of soil nonlinearity under different amplitudes of input motions are presented in Fig. 5.13. Findings from these figures can be summarized as follows:

- Both the soil stiffness and damping ratio varies dramatically as the PGA increases. This results in significant overestimations by the NCHRP611-NonLinIterative method, which predicts the ratios of the maximum hoop and bending strains and diameter change as 2.8, 8.8, and 26.0, respectively. However, the refined NCHRP method (i.e., NCHRP611-NonLinRefined) performs better again, and produce 0.9, 2.0 and 7.4 for the same response ratios, respectively.

- The NCHRP611-NonLinIterative method uses the previously mentioned iterative procedure to estimate both $\gamma_{\max}$ and G_m. This, however, only accounts for the stiffness reduction curve but not the damping ratio curve, which is also influential, especially under high-amplitude motions. Compared to the refined NCHRP method (i.e., NCHRP611-NonLinRefined), this omission leads to an underestimation of G_m, and subsequently the overestimation of all of the response ratios considered here.

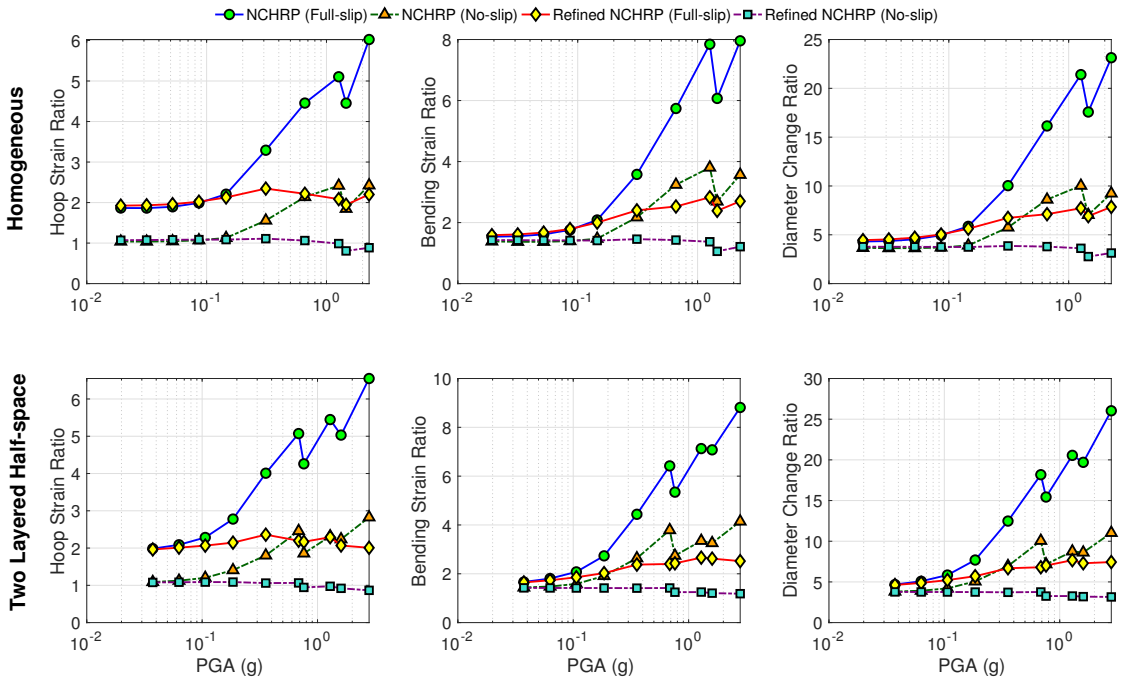

Figure 5.10: Ratios of maximum bending strain, hoop strain, and diameter change for (a) homogeneous and (b) two layered half-space cases versus PGA (g).

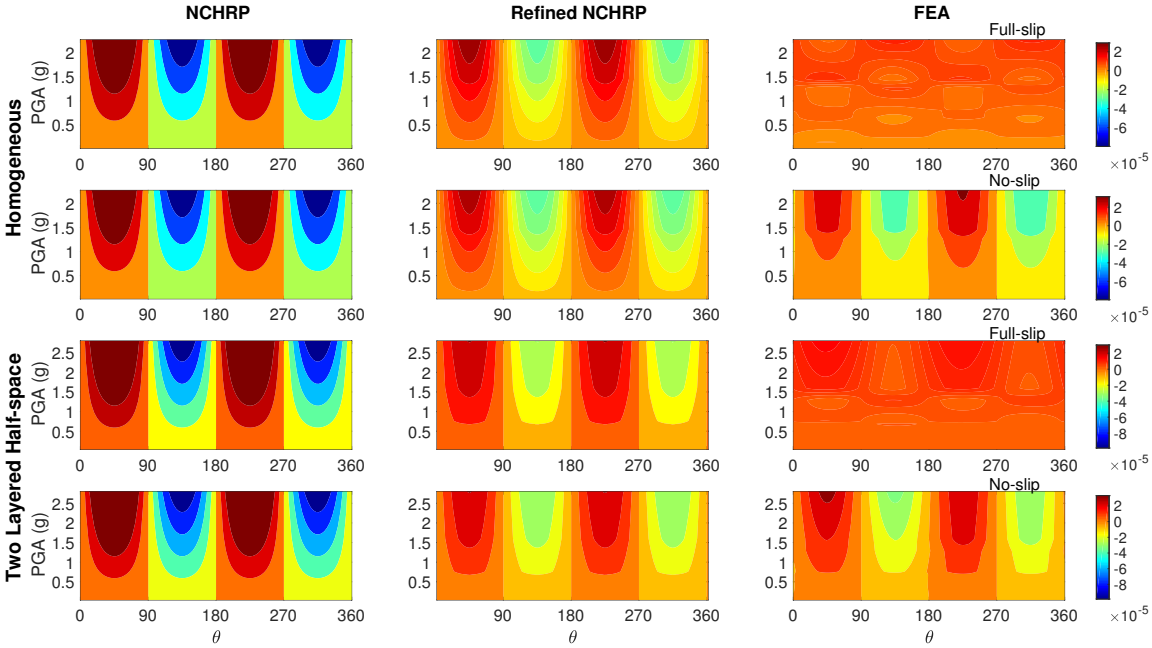

Figure 5.11: Maximum hoop strain profiles obtained using the NCHRP611-NonLinIterative, NCHRP611-NonLinRefined, and FEA approaches for (a) homogeneous and (b) two layered half-space cases versus PGA (g).

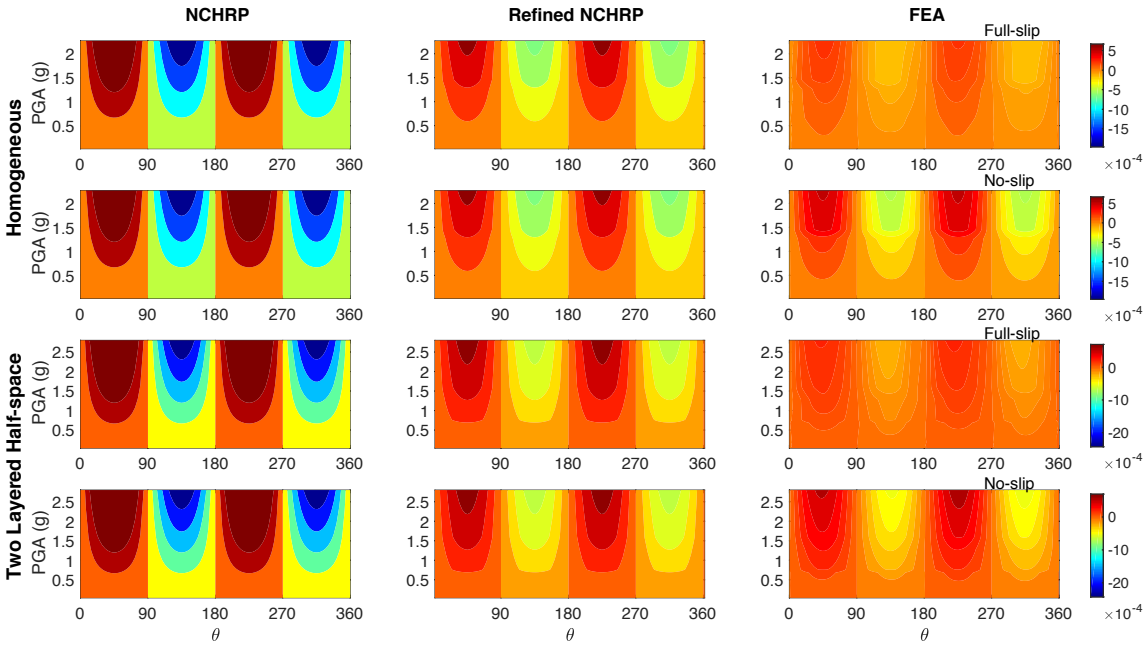

Figure 5.12: Maximum bending strain profiles obtained using the NCHRP611-NonLinIterative, NCHRP611-NonLinRefined, and FEA approaches for (a) homogeneous and (b) two layered half-space cases versus PGA (g).

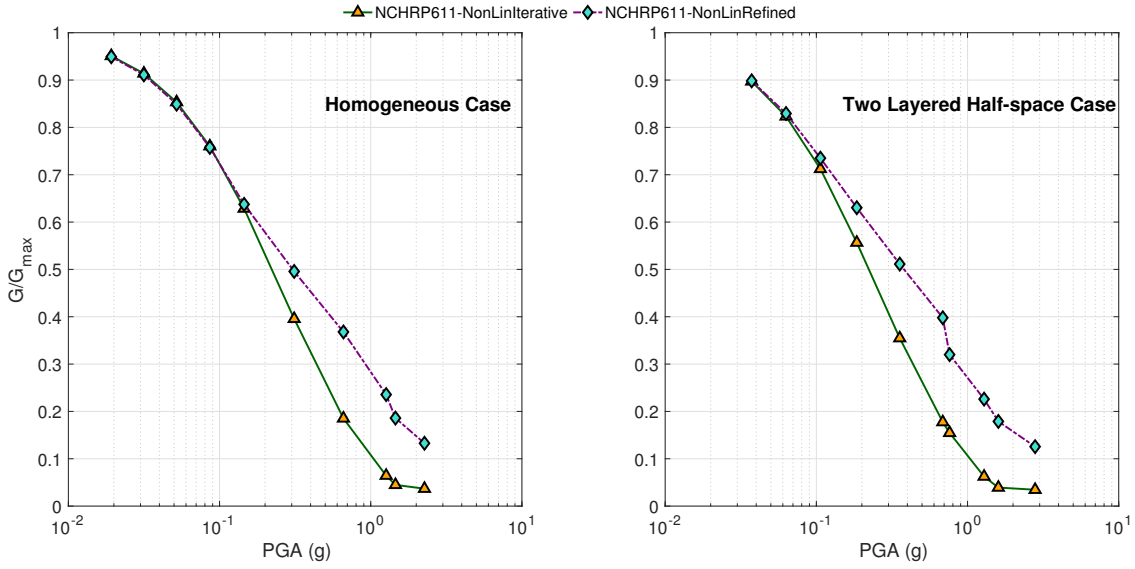

Figure 5.13: $G/G_{\max}$ versus PGA (g) curve.

5.2.5 Effects of Structural Stiffness

Next, the effects of culvert stiffness on the performance of the NCHRP method are examined. The thickness of the culvert is varied to scan through a wide range of stiffness values. As shown in Fig. 5.14, we summarize the ranges of F and C from all types of materials that are used for culverts (i.e., concrete, corrugated steel, corrugated aluminum and thermoplastic). And our performed analyses cover the entire range of F. Again, the incident wave is defined through Eq. 5.4 with $a_{\max} = 0.1$ g and $T = 0.5$ sec. Table. 5.4 summarizes the resulting flexibility and compressibility ratios of the culverts with different thickness. Fig. 5.15 shows the maximum bending and hoop strain ratio and diameter change ratio of NCHRP methods to numerical results versus flexibility ratios. Moreover, the contour plots for hoop and bending strain profiles are shown in Fig. 5.16 and Fig. 5.17. As seen, all of the computed ratios tend to increase, leading to relatively worse overestimations as the flexibility ratio increases. The refined NCHRP method (i.e., NCHRP611-NonLinRefined) exhibits, again, better performance compared to the NCHRP611-NonLinIterative in all cases.

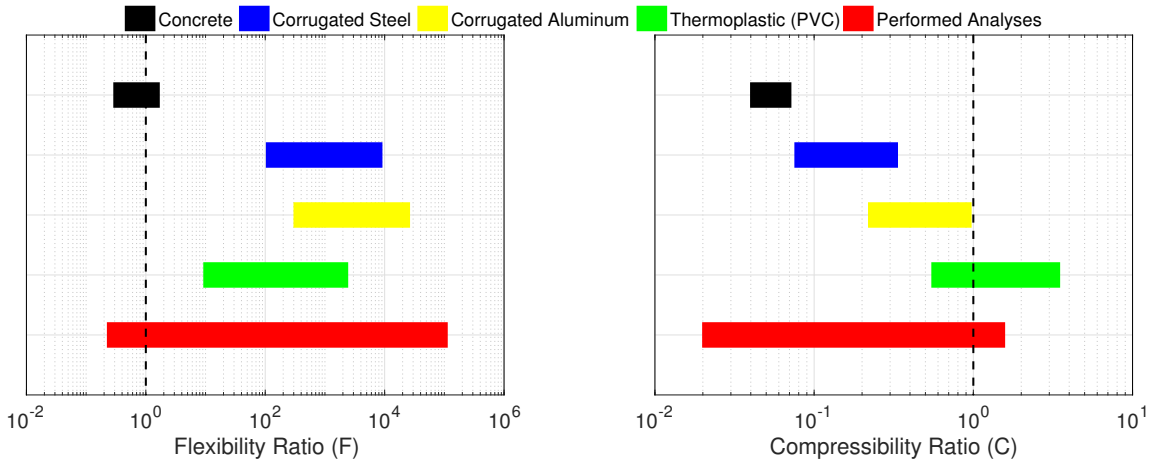

Figure 5.14: Flexibility ratio (F) and compressibility ratio (C) from different materials and performed analyses.

Table 5.4: Flexibility and compressibility ratios of the culvert.

Thickness (m)	Flexibility Ratio (F)		Compressibility Ratio (C)	
	Homogeneous	Two layered	Homogeneous	Two layered
0.005	62138.68	32399.29	0.86	0.45
0.010	7767.33	4049.91	0.43	0.22
0.020	970.92	506.24	0.22	0.11
0.030	287.68	150.00	0.14	0.07
0.040	121.36	63.28	0.11	0.06
0.050	62.14	32.40	0.09	0.04
0.060	35.96	18.75	0.07	0.04
0.070	22.65	11.81	0.06	0.03
0.080	15.17	7.91	0.05	0.03
0.090	10.65	5.56	0.05	0.02
0.100	7.77	4.05	0.04	0.02
0.200	0.97	0.51	0.02	0.01
0.242	0.55	0.29	0.02	0.01
0.300	0.29	0.15	0.01	0.01
0.400	0.12	0.06	0.01	0.01

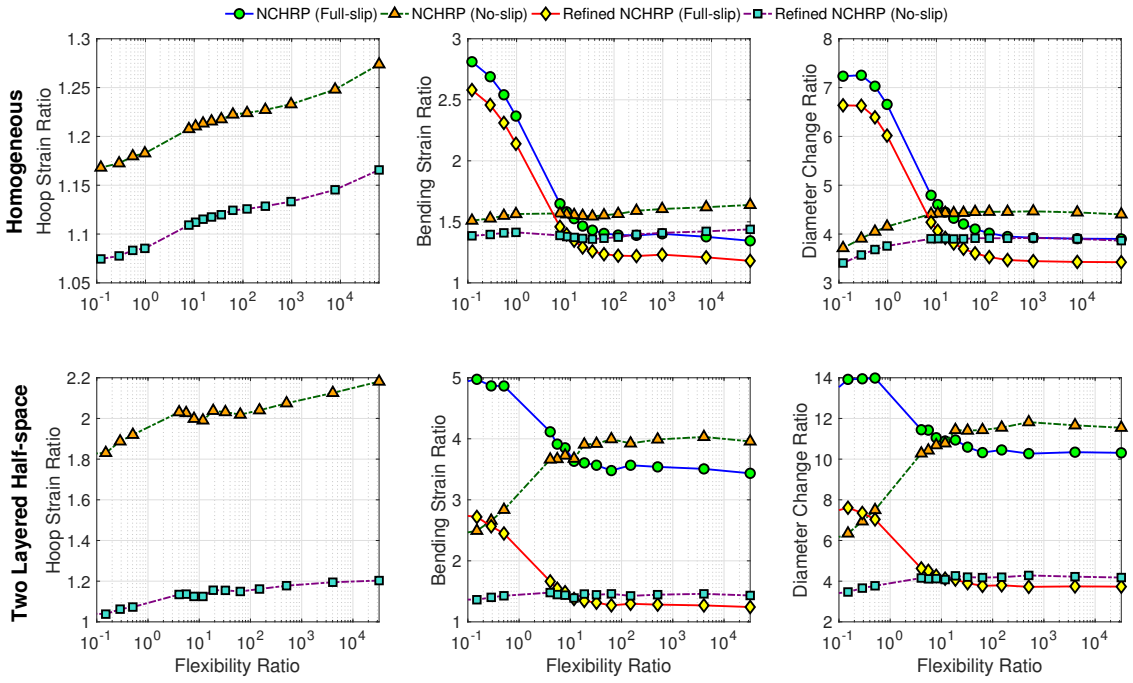

Figure 5.15: Ratios of maximum bending strain, hoop strain, and diameter change for (a) homogeneous and (b) two layered half-space cases versus flexibility ratio.

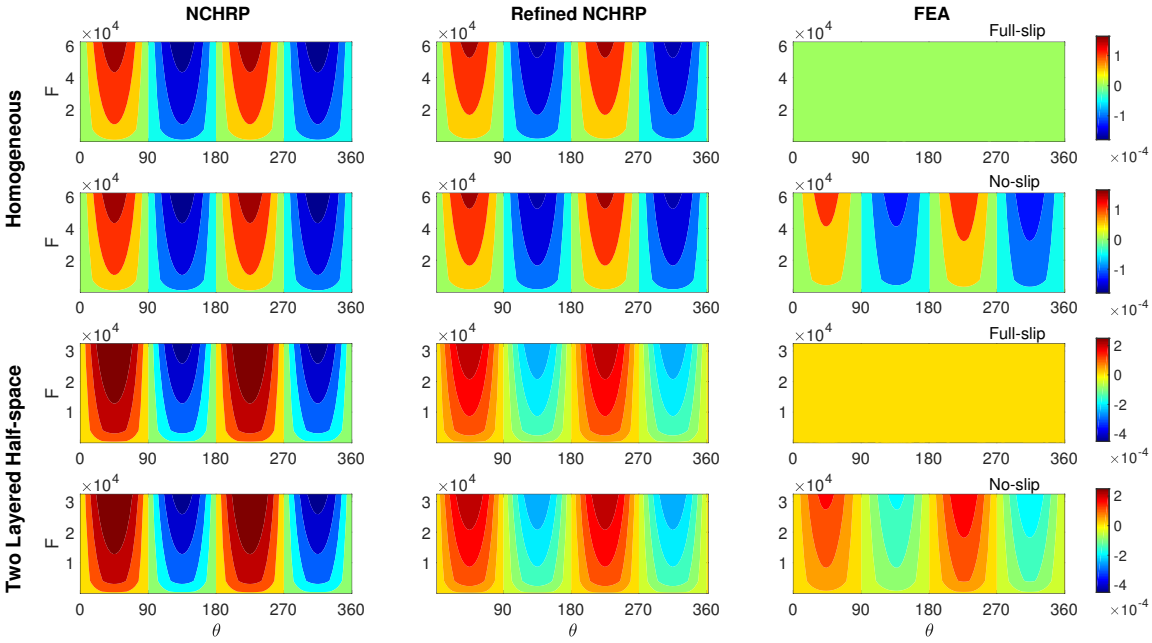

Figure 5.16: Maximum hoop strain profiles obtained using the NCHRP611-NonLinIterative, NCHRP611-NonLinRefined, and FEA approaches for (a) homogeneous and (b) two layered half-space cases versus flexibility ratio.

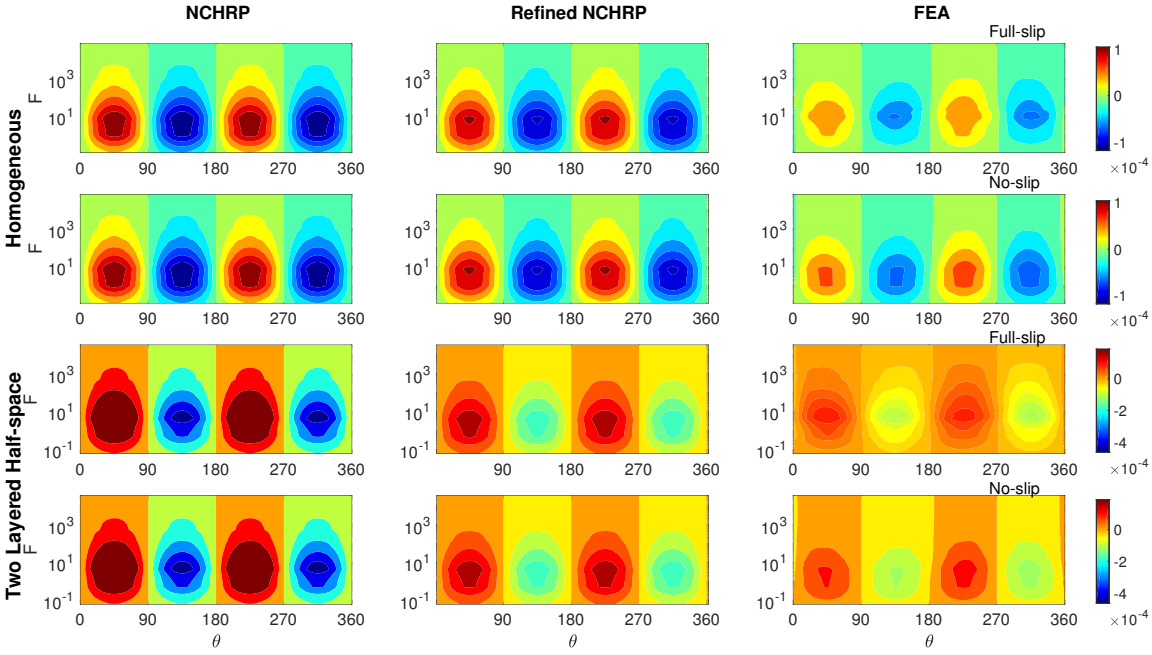

Figure 5.17: Maximum bending strain profiles obtained using the NCHRP611-NonLinIterative, NCHRP611-NonLinRefined, and FEA approaches for (a) homogeneous and (b) two layered half-space cases versus flexibility ratio.

5.2.6 Mode Shape Analyses

In order to have a closer look at the spatial distribution and temporal variation of deformation profile of the circular culvert, we use the method of principal component analysis [160]. For this, we (i) create the data matrix: $\mathbf{X} = \begin{bmatrix}\mathbf{e}_1 & \mathbf{e}_2 & ... & \mathbf{e}_n\end{bmatrix}^T$, where $\mathbf{e}_i$ for $i = 1, 2, ..., n$ is a displacement time-series at location i; (ii) compute the correlation matrix: $\mathbf{R} = \mathbf{X}\mathbf{X}^T/N$, where N is the total number of data points of the time-series; (iii) obtain the Eigen decomposition of the matrix $\mathbf{R}$, which is $\mathbf{R} = \mathbf{\Phi}\mathbf{\Lambda}^2\mathbf{\Phi}^T$, $\mathbf{\Phi} = [\phi_1 \ ... \ \phi_n]$ contains the so-called mode shape vectors ϕ_i and $\mathbf{\Lambda}$ is a diagonal matrix with entries λ_i to be the i-th singular value of the matrix $\mathbf{X}$; and (iv) compute the so-called modal contribution coefficients, which is $\mathbf{Q} = [q_1 \ ... \ q_n]^T = \mathbf{\Phi}^T\mathbf{X}$.

Figs. 5.18(a) and (b) display the first 6 proper orthogonal modes of the numerical results for the full-slip and no-slip cases, respectively. As seen, the first mode shape of both the full-slip and no-slip cases is a near perfect oval. For higher modes this resemblance of the mode shapes disappears (or at least their orders of appearance are different). This discrepancy results in the differences in the hoop strain profiles for the two cases. The higher the modes are, the more flexible the mode shape deformations appear, as expected. However, the full-slip case clearly exhibits more of this effect than the no-slip case. The participation factors of the principal components shown in Fig. 5.18 can be computed using the eigenvalues of the correlation matrix as in

$$E_{\lambda_i} = \frac{\lambda_i^2}{\sum_{i=1}^{i=n} \lambda_i^2} \quad \text{for} \quad i = 1, \ ..., \ n. \tag{5.5}$$

The values of these participation factors for the first and second modes for all of the considered cases are tabulated in the Appendix B.

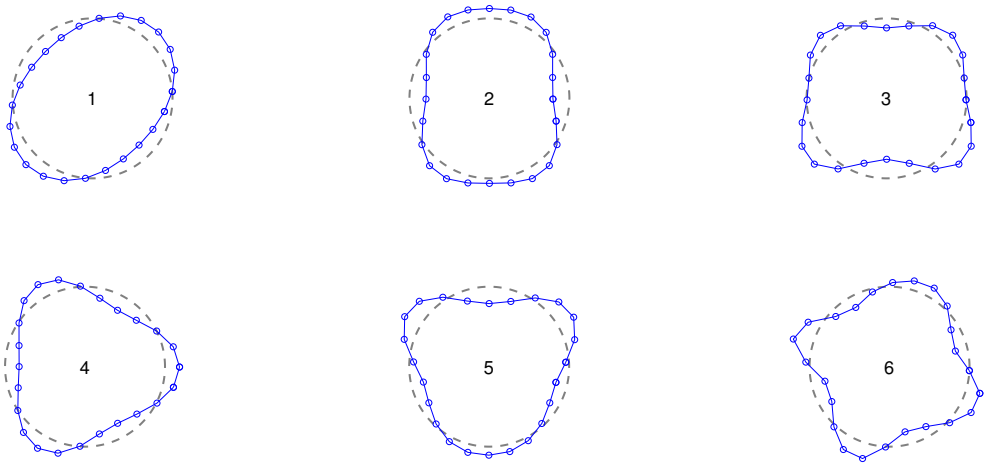

(a)

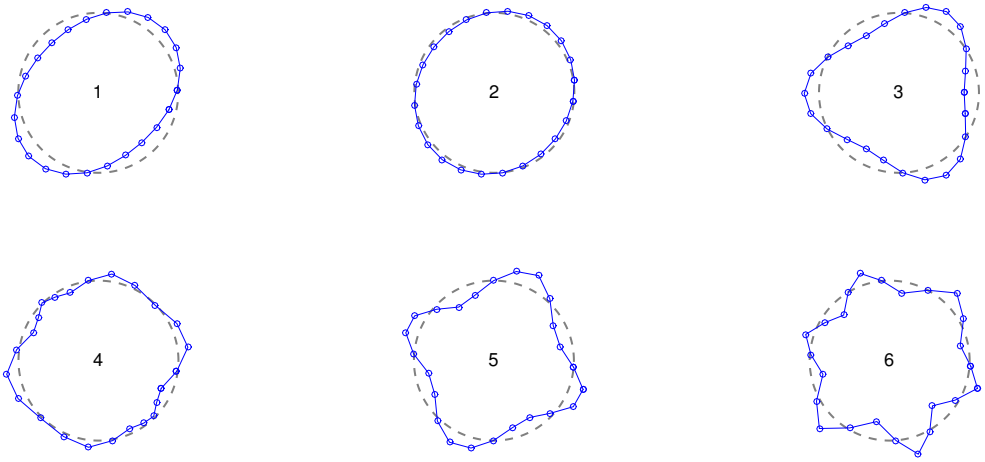

(b)

Figure 5.18: First 6 proper orthogonal modes of the numerical results for (a) full-slip and (b) no-slip case.

CHAPTER 6

Fragility-based seismic performance assessment of buried circular structures

Due to its capability of accounting for epistemic and aleatoric uncertainties that exist in predictive response models, material properties, and ground motions, performance-based seismic assessment (PBSA) methodologies are becoming widely adopted [161, 162, 163]. However, there are no analysis guidelines or performance criteria for PBSA of underground structures, even though such structures are typically very critical and some have experienced significant damages in large earthquakes [13, 164]. At present, seismic assessment of underground structures is mainly based on expert judgment [165] or empirical fragility curves derived from damage data in past earthquakes [166, 167, 168].

The past decade has brought not only significant recent advances in computational capabilities, but also broad improvements in ground motion characterization, soil-structure interaction analysis, and inelastic modeling of structural and geotechnical systems. When combined, these ingredients have made it possible to devise site- and structure-specific application of PBSA methodologies to large fully or partially embedded structures, such as tunnels [169, 170, 153, 171, 172, 173], dams [174], subway stations [175, 176].

Specifically, [169] developed the fragility curves of shallow tunnels in alluvial deposits by conducting equivalent linear quasi-static analysis. And later [170, 153] extended to nonlinear dynamic analysis and considered the soil-structure interaction (SSI) and aging effects due to corrosion in the tunnel lining. [172, 173] proposed the fragility curves for a group of rock mountain tunnels with different diameters, embedment depths, and lining thicknesses by performing nonlinear time history analysis, and utilized the machine learning tools to predict

the fragility curves. [175] performed the fragility analysis of a subway station box structure by incremental dynamic analysis. [176] developed the fragility curves for rectangular cut-and-cover tunnels from nonlinear quasi-static frame analyses, and investigated the performance of various intensity measures of the ground motions.

Due to the constraint of the computational cost and the complexities in modeling the buried structures—i.e., constitutive models for soil and structural components, absorbing boundary conditions (ABCs), appropriate input motions, soil-structure interface contact behavior, etc—aforementioned studies simply performed either quasi-static or incremental dynamic analysis with limited ground motions (less than 20), adopted the Mohr-Coulomb and elastic perfectly plastic models for the soil and structures, respectively when conducting nonlinear analysis, and applied the Lysmer [20] dashpots as the ABCs. As known, however, buried structures are significantly sensitive to the frequency contents of the ground motions [157]. Therefore, extensive input ground motions are preferred to bracket the site uncertainties and hence produce more accurate fragility curves.

In this study, a fragility-based seismic assessment methodology for a buried circular culvert is presented. The perfectly matched layer (PML) and domain reduction method (DRM) implemented by [118] are used for absorbing the scattered outgoing waves, and prescribing the input motions, respectively. This combined tool can dramatically reduce the size of the computational domain and generate consistent input motions. 100 input motions are generated based on the average spectral acceleration (SAT) for a region in Los Angeles. Three shear wave velocity profiles are used to investigate the effects of soil heterogeneity. The soil domain and the structure are modeled using a multi-dimensional plasticity model with a vanished elastic region [63, 71] and an elastic-plastic model with isotropic hardening calibrated through the experimental stress-strain curve obtained from coupon test, respectively. Two-dimensional nonlinear finite element models are then used in Probabilistic Seismic Demand Analysis (PSDA) procedure [177], and along with a total of 300 nonlinear time history analyses, are carried to analyze the fragility of the buried circular culvert.

6.1 Numerical Modeling

6.1.1 Problem definition

A large buried circular culvert (see Fig. 6.1) is modeled and analyzed using the finite element method. The dimensions of the exterior domain, domain of interest are 90m×30m, 78m×24m, respectively. The culvert diameter is 3m, and its embedment depth (i.e., from the ground surface to the crown) is 9m.

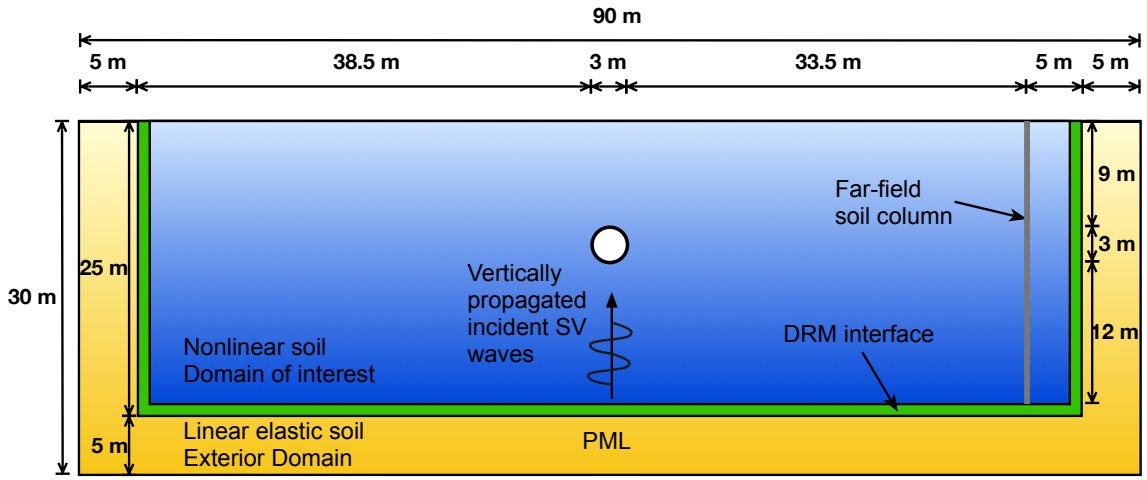

Figure 6.1: Side view of the numerical model.

In order to reduce the computational domain while modeling a semi-infinite domain under remote excitations, we use the domain reduction method (DRM) [117] truncated by the perfectly matched layer (PML) [106]. DRM is a two-step finite element procedure for modeling the seismic responses of heterogeneous subdomains. DRM enables the conversion of the half-space problem to an equivalent one in which the effects of incoming waves due to remote excitations are translated into equivalent nodal forces that are applied inside a domain that is truncated by PML. As a powerful wave absorbing boundary, the PML can eliminate reflections at the truncated near-field boundary for all non-zero-frequency impinging waves, irrespective of their angles of incidence. In the present study, both the DRM and PML are implemented in ABAQUS [114] by Zhang et al. [118].

6.1.2 Material Models & Soil-Structure Interface Conditions

In the numerical simulations, the soil is modeled with 4-node quadrilateral plane strain elements, each of which has a near-uniform size of 1.0m × 1.0m, considering the vertically propagated incident SV waves are applied and the computational cost. The circular culvert lining is modeled with 100 equal-sized beam elements, of which the accuracy is verified in the following section. The element size is chosen such that approximately 12 discretized nodes exist within the minimum wavelength [158], which, for the present simulations is $\lambda_{\min}/12 = V_s/f_{\max} = 200\text{m/s}/10\text{Hz}/12 \approx 1.67\text{m}$.

6.1.2.1 Soil model

For the surrounding soil, nonlinear material behavior is considered. Both linear and nonlinear soils have the same density $\rho = 2000\text{kg/m}^3$, and Poisson's ratio $\nu = 0.3$. As shown in Fig. 6.2 (c), three soil profiles are considered. In the nonlinear analyses, the soil deposits are modeled using a bounding surface plasticity model, which was originally developed by Borja et al. [63, 69]. This nonlinear soil model has been thoroughly calibrated and validated using data from multiple centrifuge tests by Zhang et al. [71]. Here, we choose the material parameters of this nonlinear soil model as $h = 0.3\ G_{\max},\ m = 1.2,\ R = 0.005\ G_{\max},\ H_0 = 0$, which are calibrated based on the Ottawa sand properties [2]. The parameters h, m and H_0 are three parameters, which control the intensity, rate, and final state of hardening. R is the radius of the bounding surface. The selected hysteresis and stiffness degradation and damping curves are shown in Figs. 6.2 (a) and (b), respectively.

6.1.2.2 Culvert model

For the buried structure, we analyze a corrugated steel pipe culvert, using a built-in elastic-plastic model with isotropic hardening in ABAQUS [114]. The elastic properties of the culvert lining are included in Table 6.1. And as shown in Fig. 6.3, the plastic properties are calibrated based on the stress-strain curves of the A36 steel obtained from the coupon test

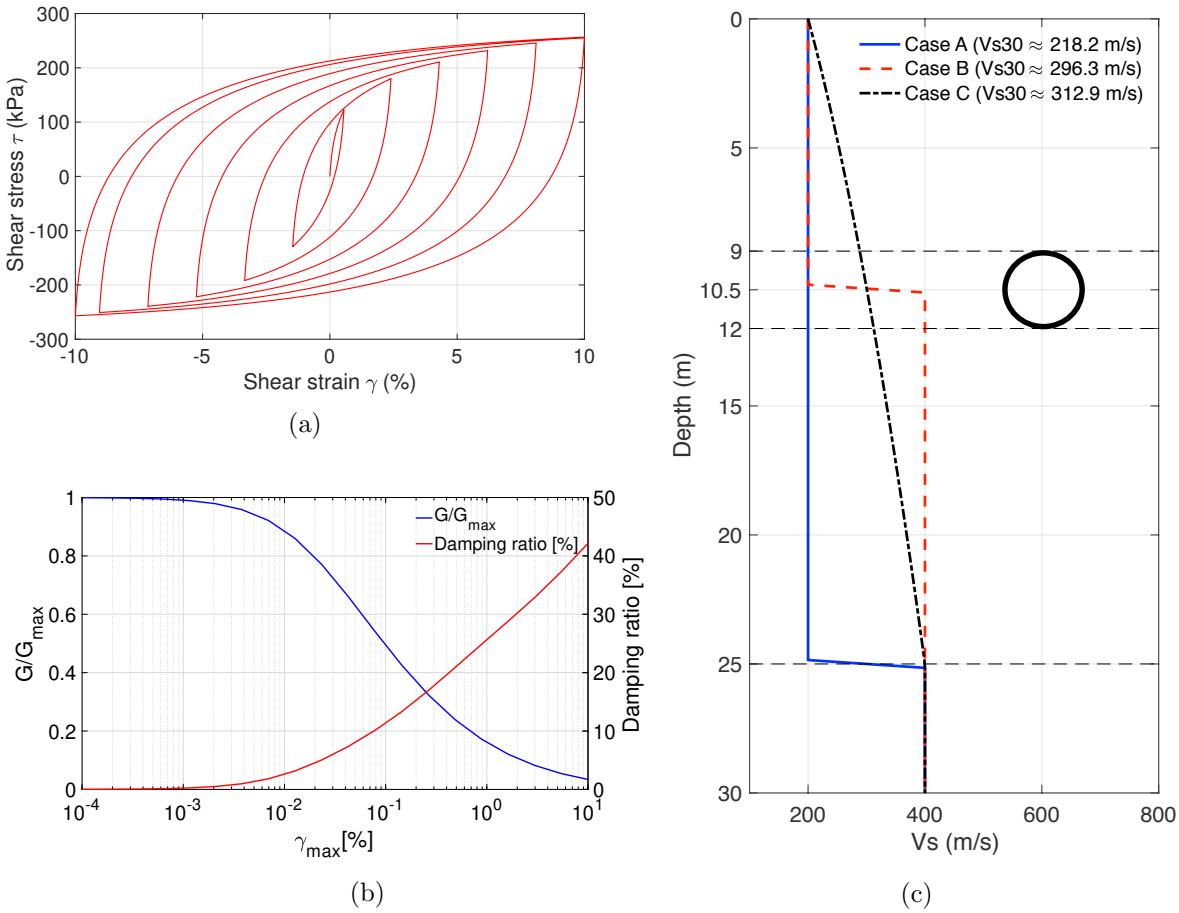

Figure 6.2: (a) Hysteresis curve of the adopted nonlinear soil model, (b) stiffness degradation and damping curves, and (c) shear wave velocity profiles.

[178], resulting the yield stress and ultimate strength as $\sigma_y = 250$MPa and $\sigma_u = 415$MPa, respectively. The sectional configuration of the corrugated steel pipe adopted in this study is shown in Fig. 6.4, and other required parameters are summarized in Table 6.2, which are selected based on the standard ASTM A796 [179].

Table 6.1: Elastic properties of the culvert lining.

Steel grade	Young's modulus (GPa)	Poisson's ratio	Density (kg/m^3)
A36	200	0.26	7850

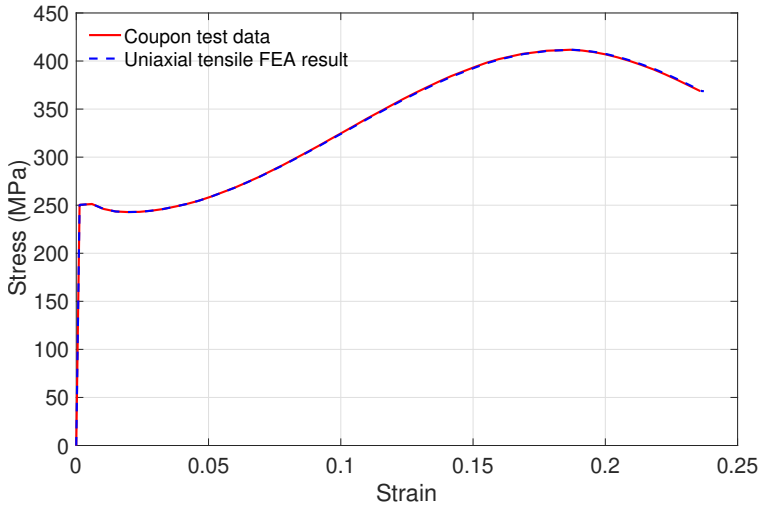

Figure 6.3: Stress-strain curve of the A36 steel.

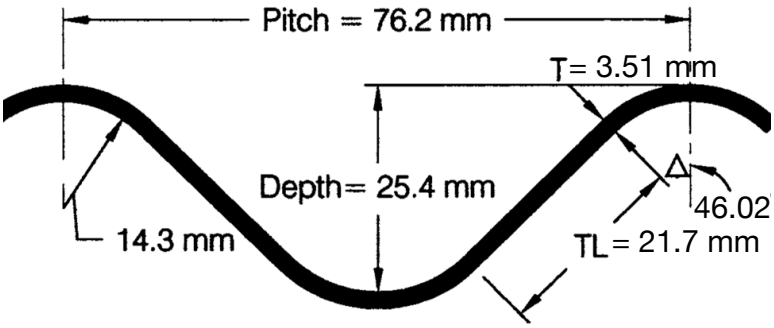

Figure 6.4: Sectional configuration of corrugated steel sheets for corrugation of 75 by 25mm.

Since the beam elements are used to model the culvert lining with corrugation, verification studies are necessary to be carried out to demonstrate its validity and accuracy. To this end, we 1) construct a sophisticated 3.66m-long 3D corrugated steel culvert model using the

Table 6.2: Sectional properties of the culvert lining.

Corrugation (mm)	Thickness (mm)	Area of section (mm^2/mm)	Moment of inertia (mm^3/mm)	h (mm)	t (mm)
75 by 25	3.51	4.250	330.61	19.79	2.092

aforementioned material and sectional properties (see Fig. 6.5 (a)), 2) perform parallel-plate test—i.e., vertical line-load applied on the upper surface of the culvert and the bottom surface is assumed to be simply supported—using 3D solid elements, 3D shell elements, and 2D beam elements with three different configurations, in which we simply use a rectangular section with unit width and change the height to match either area (A) or the moment of inertia (I) in Table 6.2, and we also use a box section with unit width and change the height and thickness to match both A and I (see Fig. 6.5 (b)), 3) compare the force-vertical and -horizontal displacement curves for the crown and rightmost point of the culvert, respectively, obtained by using the 2D beam models and the 3D models using solid and shell elements. As shown in Fig. 6.6, only the beam model that has the equivalent A and I produces satisfied agreement when compared with detailed 3D models.

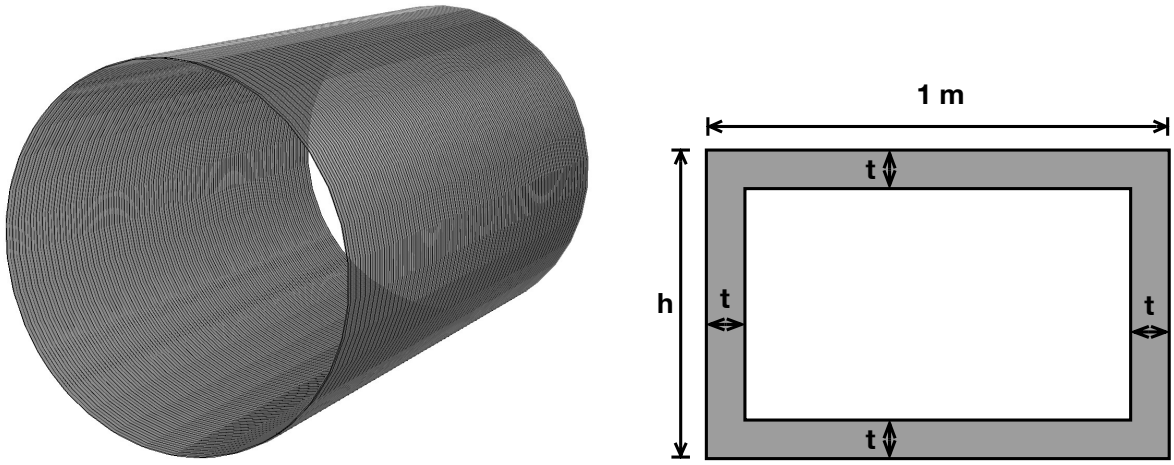

(a) (b)

Figure 6.5: (a) Detailed 3D model with corrugation and (b) box section of the beam model with equivalent A and I.

To further validate our proposed beam model, we conduct another parallel-plate test and compare the numerical results obtained by using the beam model that has the equivalent A and I with experimental data, provided by [180]. The mechanical properties of this test are

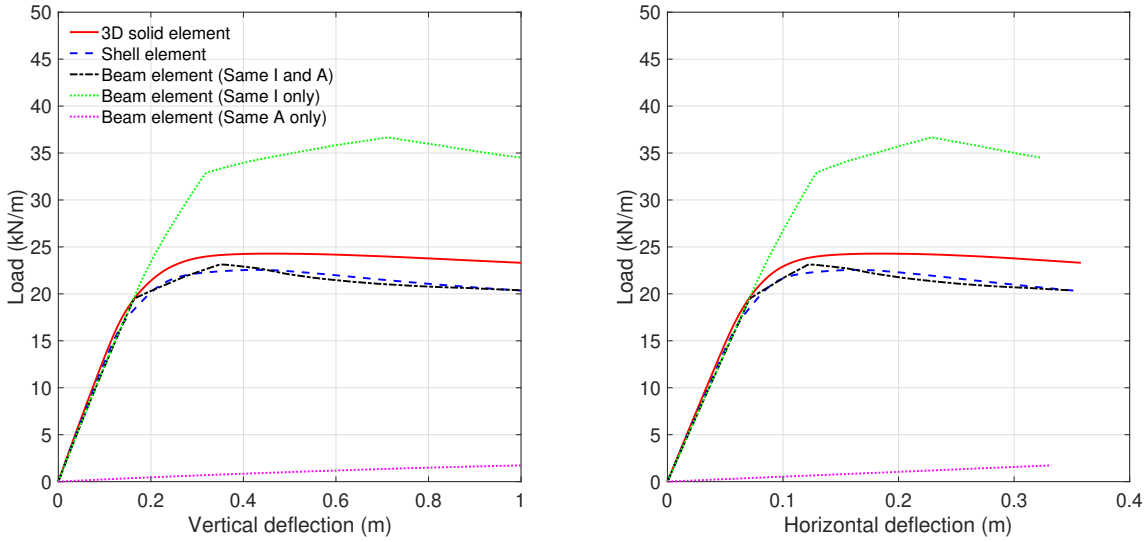

Figure 6.6: Force-displacement curves of the parallel-plate test using beam and 3D models.

summarized in Table 6.3. As seen in Fig. 6.7. Again, the proposed beam model shows an acceptable accuracy.

Table 6.3: Mechanical properties of the culvert lining for validation test.

Material	Young's modulus (GPa)	Poisson's ratio	Density (kg/m^3)
	180	0.26	7850
Sectional	Thickness (mm)	Area of section (mm^2/mm)	Moment of inertia (mm^3/mm)
	2.01	1.507	60.65

6.1.2.3 Soil-structure interface conditions

In terms of modeling the soil-structure interface conditions, the ABAQUS [114] built-in node-to-node hard-contact formulation with finite sliding is used, as well as the recommended friction angle (see Eq. 6.1) for a cohesionless soil–smooth steel interface according to ASCE-ALA [181] guidelines. As reported in [159], the soil-lining interface properties can significantly affect the internal forces developed in the lining of a circular tunnel.

$$\tan\left(\phi_{\text{interface}}\right) = \tan\left(0.7\phi_{\text{soil}} = 32^o\right) \approx 0.41 \tag{6.1}$$

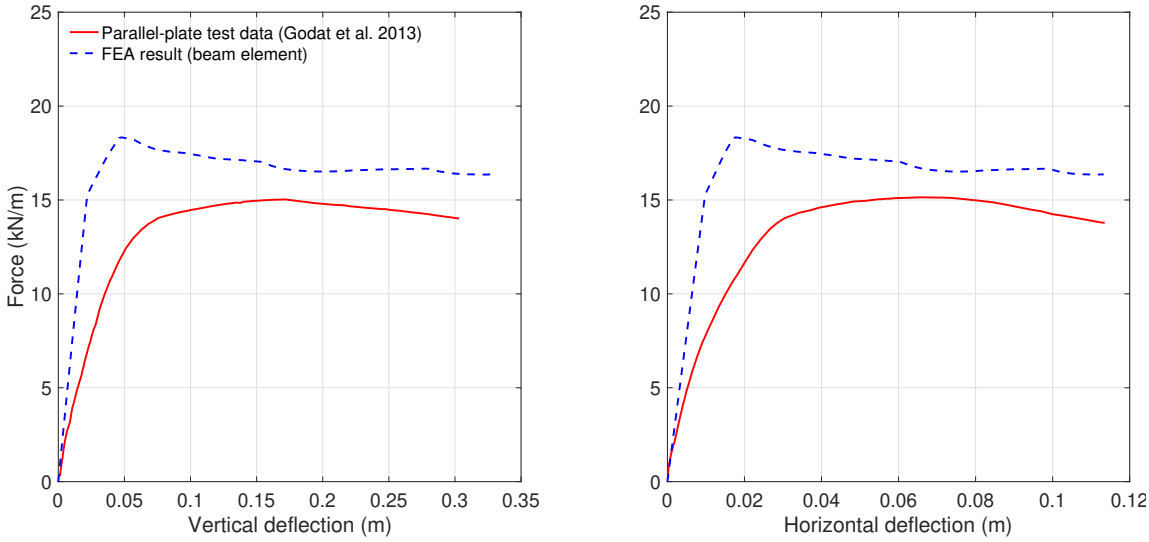

Figure 6.7: Comparison of the force-displacement curves of the parallel-plate test using proposed beam model and the experimental data.

6.1.3 Input motions

In this study, we select Los Angeles as a representative city and then use USGS web services (https://earthquake.usgs.gov/hazards/designmaps/usdesign.php) to retrieve the seismic design data—e.g., S_{DS} and S_{D1}, the 5% damped design spectral response acceleration parameters at short periods and 1 second, respectively. Upon these, a suite of 100 ground motions (GMs) is selected conditioned on the average spectral acceleration (SAT) from a large database of GMs (NGA WEST2) developed by PEER [182]. The acceleration response spectra of the selected records is shown in Fig. 6.8.

Given each GM, the procedure to generate input motion for the numerical model shown in Fig. 6.1 is described below,

1. Perform the 1D linear site response analysis for each soil profile shown in Fig. 6.2 (c) and each GM.

2. Scale the responses of all the nodes on the 1D soil model in step 1 using the same factor, so that the peak ground acceleration (PGA) of the 1D model matches the PGA of each GM.

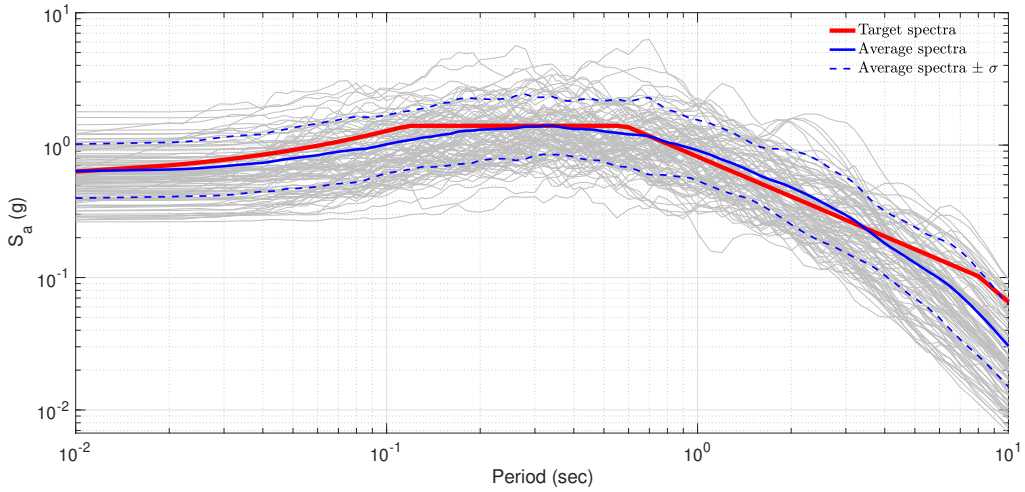

Figure 6.8: 5% damped acceleration response spectra of the selected records.

3. Use the scaled responses to compute and prescribe the equivalent nodal forces for all the nodes along the DRM interface, and conduct nonlinear time history analysis. Please refer to [118] for more details about this step.

6.2 NCHRP 611 approach for the calculation of the internal forces in a circular culvert

Current seismic design practices—which are comprehensively articulated in the NCHRP Report 611 [18]—are primarily based on the procedures proposed by Wang [19] and Penzien [42] for circular and rectangular buried structures, respectively. Due to its computational simplicity, it has been widely adopted as a reference in the design of buried structures. An engineer needs to execute the following steps to determine the seismic demands due to ovaling of a circular embedded structure:

1. *Estimate the free-field ground strains* ($\gamma_{\max}$) *at the bottom elevation of the embedded structure*: For highway structures with burial depths less than 50 ft, $\gamma_{\max}$ may be

estimated using PGA,

$$\gamma_{\max} = \frac{\tau_{\max}}{G_m}, \quad \tau_{\max} = (\text{PGA}/g)\sigma_v R_d \tag{6.2}$$

Or PGV for deep buried structures,

$$\gamma_{\max} = \frac{V_{s_{\max}}^{\text{culvert}}}{C_{se}^{\text{culvert}}}, \quad V_{s_{\max}}^{\text{culvert}} = (\text{PGV})R_d, \quad C_{se}^{\text{culvert}} = \sqrt{\frac{G_m}{\rho}} \tag{6.3}$$

where G_m is the effective-strain-compatible shear modulus of the surrounding soil, PGA is the peak ground acceleration, σ_v is the overburden pressure at the depth corresponding to the invert of the culvert/tunnel, and R_d is a depth-dependent stress reduction factor given by

$$R_d = \begin{cases} 1 - 0.00233z & z < 30\text{ft} \\ 1.174 - 0.00814z & 30\text{ft} \leq z \leq 75\text{ft} \end{cases} \tag{6.4}$$

with z denoting the depth to the midpoint of the culvert. $V_{s_{\max}}^{\text{culvert}}$ and ρ are the shear wave peak particle velocity and density of soil at the culvert elevation, respectively, and C_{se}^{culvert} is the effective shear wave velocity of the medium surrounding the culvert. One may also estimate $\gamma_{\max}$ by performing a 1D site response analysis [157].

2. *Calculate the flexibility and compressibility ratios*: Compressibility (C) and flexibility (F) ratios are used for determining the relative stiffness of the lining with respect to the surrounding ground [150], and can be computed as:

$$F = \frac{E_m(1-\nu_1^2)R^3}{6E_1I_1(1+\nu_m)} \tag{6.5}$$

$$C = \frac{E_m(1-\nu_1^2)R}{E_1A_1(1+\nu_m)(1-2\nu_m)} \tag{6.6}$$

where E_m is the strain-compatible elastic modulus, and ν_m is the Poisson's ratio of the surrounding soil. The terms R, E_1, ν_1, A_1, t and I_1 respectively denote nominal

radius, elastic modulus, Poisson's ratio, cross-sectional area, thickness, and moment of inertia of the culvert lining. For $F < 1$, the lining is considered to be stiffer than the surrounding soil while for $F > 1$, it is expected that the lining can deform more than the free-field.

3. *Estimate the lining deformation and seismic demands*: For estimation of the resulting moment (M), it is recommended to consider a full-slip interface assumption, which allows normal stresses without normal separation and tangential forces. On the other hand, for estimation of the resulting thrust (T), a no-slip interface assumption is recommended. Therefore,

$$M = -\frac{1}{6} k_1 \frac{E_m}{1+\nu_m} R^2 \gamma_{\max} \cos 2(\theta + \frac{\pi}{4}) \quad \text{(full-slip)} \tag{6.7}$$

$$T = -k_2 \frac{E_m}{2(1+\nu_m)} R \gamma_{\max} \cos 2(\theta + \frac{\pi}{4}) \quad \text{(no-slip)} \tag{6.8}$$

$$T = M/R \quad \text{(full-slip)} \tag{6.9}$$

where θ is the angle counterclockwise measured from the right point on the center plane of the culvert.

$$k_1 = 12 \frac{1-\nu_m}{2F + 5 - 6\nu_m}\,, \tag{6.10}$$

$$k_2 = 1 + \frac{F(1-2\nu_m)(1-C) - 0.5(1-2\nu_m)^2 C + 2}{F[(3-2\nu_m) + (1-2\nu_m)C] + C[2.5 - 8\nu_m + 6\nu_m^2] + 6 - 8\nu_m}\,. \tag{6.11}$$

As seen, in order to compute seismic demands using the NCHRP 611 methodology, we first need to estimate the maximum free-field strain $\gamma_{\max}$ in the soil deposit as well as the corresponding effective compatible shear modulus G_m. Then, the seismic demands can be computed following the steps outlined above. For shallow structures one may use Eqs. 6.2 or 6.3 to estimate $\gamma_{\max}$. However, in order to use that equation, we need to know the strain-compatible shear modulus (G_m) of the ground surrounding the culvert or pipe, which itself is a function of $\gamma_{\max}$. If not considering the soil nonlinearity one may simply use the elastic shear modulus $G_{\max}$ to represent G_m and $\sqrt{G_{\max}/\rho}$ to obtain C_{se}^{culvert}. If do consider the soil

nonlinearity, we can either perform a 1D site response analysis to compute G_m, or use an iterative procedure to obtain it, as described below:

1. To start the procedure (iteration $i = 0$), provide an initial guess for the maximum shear strain at the elevation of the bottom of the circular structure. This initial guess can be any reasonable value. Here, we simply use $\gamma_{\max,0} = 0.05\%$.

2. For iteration i, predict G_m for the circular structure, which can be achieved using $\gamma_{\max,i-1}$ and the $G/G_{\max}$ curve of the soil. Subsequently, correct the maximum shear strain $\gamma_{\max,i}$ using Eqs. 6.2 or 6.3.

3. Repeat step 2 until $|\gamma_{\max,i} - \gamma_{\max,i-1}| <= \text{TOL}$ for the predefined tolerance TOL.

The NCHRP 611 report suggests using free-field site response analysis to compute the maximum shear strain as well; whereas the iterative procedure described above produces a self-consistent pair of ($\gamma_{\max}$, G_m). Please refer to [157] for more details about this procedure.

6.2.1 Verification of the numerical model

To verify the numerical model, we compare the numerically obtained results (i.e., bending moment and hoop thrust) from FEA, with the analytical solution explained in Eqs. 6.2-6.11. As known, the analytical solution is derived based on quasi-static condition in a full-space homogeneous media. The effects of embedment depth are considered via the depth-dependent factor R_d. However, it is not sensitive to the inherently broadband frequency content of seismic input excitations. In this following verification study, using the same model shown in Fig. 6.1, but with a homogeneous and linear elastic soil layer with parameters as, shear wave velocity $V_s = 200\text{m/s}$, density $\rho = 2000\text{kg/m}^3$, and Poisson's ratio $\nu = 0.3$, is adopted. Two analyses with no-slip and full-slip interface conditions are used. The incident wave is defined based on Eq. 6.12 with $a_{\max} = 1.0$ g and $T = 10.0$ sec. Its acceleration time

history and Fourier amplitude are shown in Fig. 6.9.

$$\ddot{u}(t) = \frac{a_{\max}}{2} \sin(2\pi t/T)\big[1 - \cos(2\pi t/10T)\big] \tag{6.12}$$

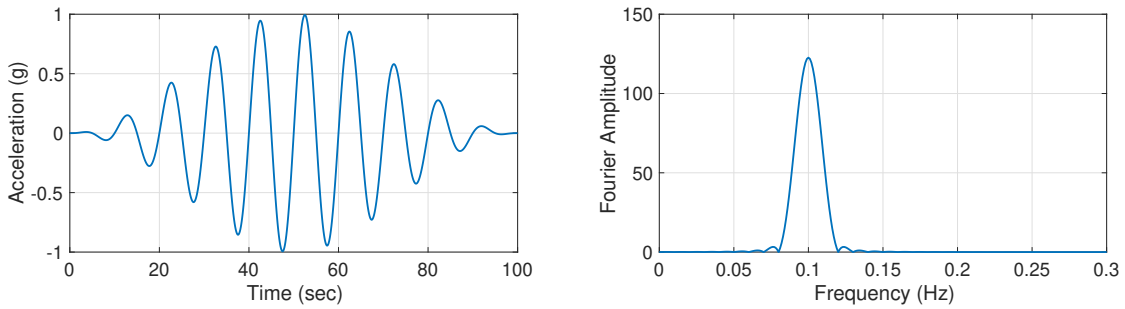

Figure 6.9: Acceleration and Fourier amplitude plots for the applied input motion.

The resulting hoop thrust, bending moment and the $\gamma_{\max}$ profiles are shown in Fig. 6.10. As seen, the FEA results are in good agreement with analytical solutions (i.e., NCHRP approach). And by using the $\gamma_{\max}$ obtained from the 1D site response analysis (1D SRA), the differences are reduced, especially for the hoop thrust.

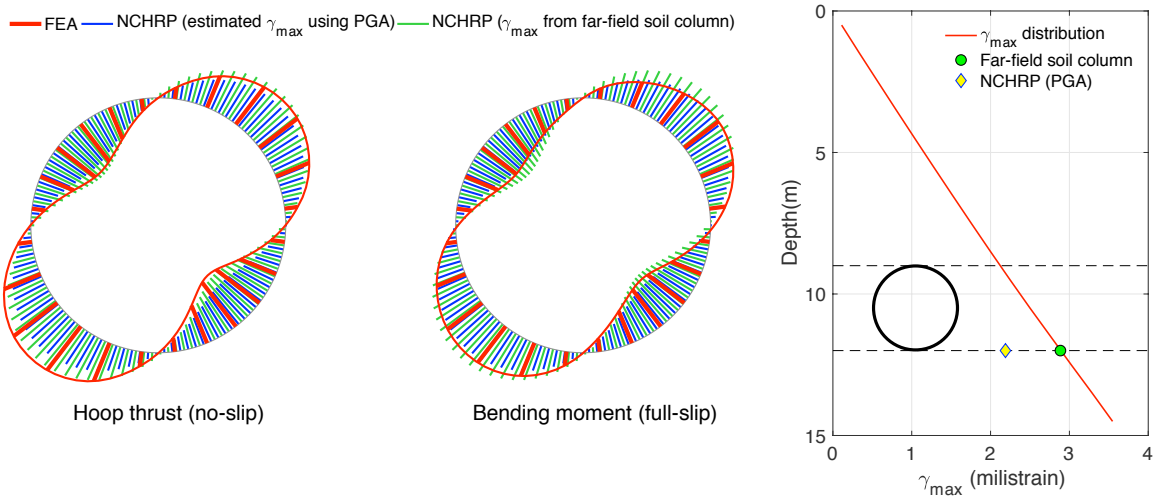

Figure 6.10: Comparisons of the hoop thrust, bending moment and the $\gamma_{\max}$ profiles.

6.3 Results

In this section, the responses of the buried circular culvert—i.e., hoop thrust and bending moment—for each soil profile and GM, obtained from FEA, are presented and compared with the NCHRP 611 approach. Besides, the maximum shear strain ($\gamma_{\max}$) is computed by performing 1D site response analysis, using the peak ground acceleration (PGA), peak ground velocity (PGV), and peak velocity at the elevation of culvert are extracted from the far-field soil column of the numerical model. The $\gamma_{\max}$ and PGV are also compared with the estimated method described in NCHRP report (see Eq. 6.13), to further investigate its accuracy.

6.3.1 Peak velocity

As mentioned in NCHRP 611 report, for a culvert or pipe structure constructed at a significant depth below the ground surface, the most appropriate design ground motion parameter to characterize the ground motion effects is not PGA. Instead, PGV is a better indicator for ground deformations ($\gamma_{\max}$) induced during ground shaking. The NCHRP uses a simple equation (see Eq. 6.13) to estimate the PGV from S_{a1}, and Eq. 6.3 to get the peak velocity at the elevation of culvert.

$$\text{PGV (in/sec)} = 55 S_{a1} \text{ (g)} \tag{6.13}$$

where S_{a1} is the spectral acceleration of the ground surface at 1s.

Fig. 6.11 shows the estimated and real peak velocities at the ground surface and the elevation of culvert for different soil profiles, obtained from Eq. 6.13 and the far-field soil column, respectively. As seen, the simple equation (i.e., Eq. 6.13) generally over-predicts the peak velocities, especially for the soft soil (i.e., case A). And later we will use both PGVs to compute the seismic demands—hoop thrust and bending moment.

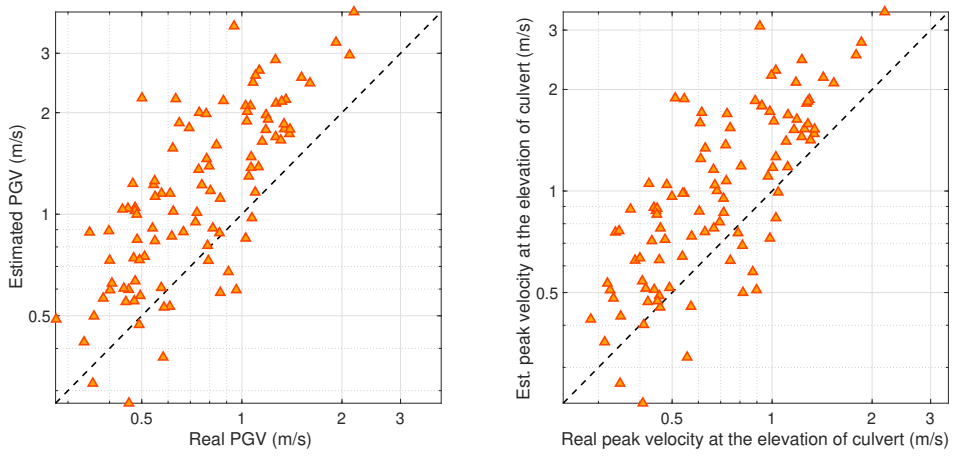

(a)

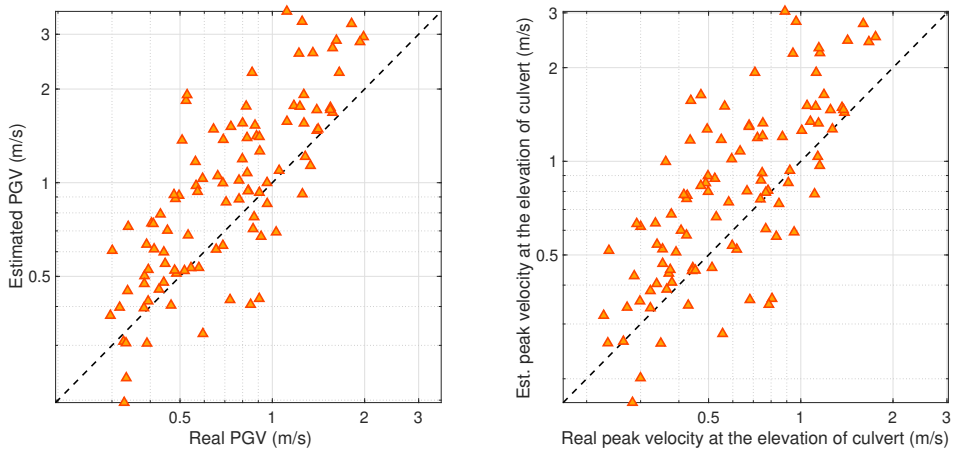

(b)

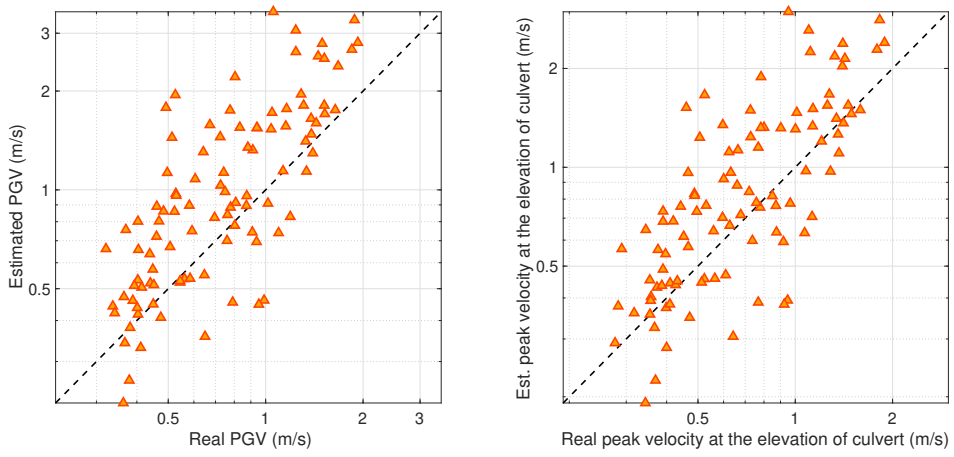

(c)

Figure 6.11: The estimated and real peak velocities obtained from the far-field soil column at ground surface and the elevation of culvert for different soil profiles (a) case A (b) case B and (c) case C.

6.3.2 Maximum free-field shear strain ($\gamma_{\max}$)

The maximum free-field shear strain ($\gamma_{\max}$) is the key parameter for later predicting the response of the structure. In this section, we compare the $\gamma_{\max}$ obtained from the 1D site response analysis, with ones from the NCHRP approach by using both PGA and PGV, with and without considering the soil nonlinearity, for all three soil profiles. To include the soil nonlinearity, the iterative procedure illustrated earlier is used to obtain the self-consistent pair of ($\gamma_{\max},\ G_m$). Otherwise $G_{\max}$ is simply used to represent G_m.

Fig. 6.12 shows the $\gamma_{\max}$ at the elevation of culvert for different soil profiles, obtained from the NCHRP approach by using PGA and PGV, and the 1D site response analysis, with and without considering the soil nonlinearity. As seen, the behavior of using PGA and PGV changes over different soil profiles. But it can be deduced that by using PGA, $\gamma_{\max}$ is significantly under-predicted for the profile of which the shear wave velocity notably changes near the elevation of the culvert (i.e., case B). And the prediction is much improved after considering the soil nonlinearity, especially for those using PGA.

6.3.3 Hoop thrust

Fig. 6.13 shows the comparison of the maximum dynamic hoop thrust ($T_{\max}$) computed based on the $\gamma_{\max}$ from the NCHRP approach by using PGA, PGV, and the 1D site response analysis at the elevation of culvert with FEA results, for different soil profiles, with and without considering the soil nonlinearity. "NS" and "FS" refer to no-slip and full-slip interface conditions, respectively. It can be seen that no-slip interface remarkably over-predicts the response. However, on the contrary, full-slip case mostly under-predicts the response, which is indeed within expectation, because an in-between interface condition—i.e., a frictional interface with coefficient of 0.41, see Eq. 6.1—is adopted in FEA. That's also the reason why NCHRP recommends to use no-slip interface condition for the calculation of hoop thrust. Again, the predictions are improved after considering the soil nonlinearity.

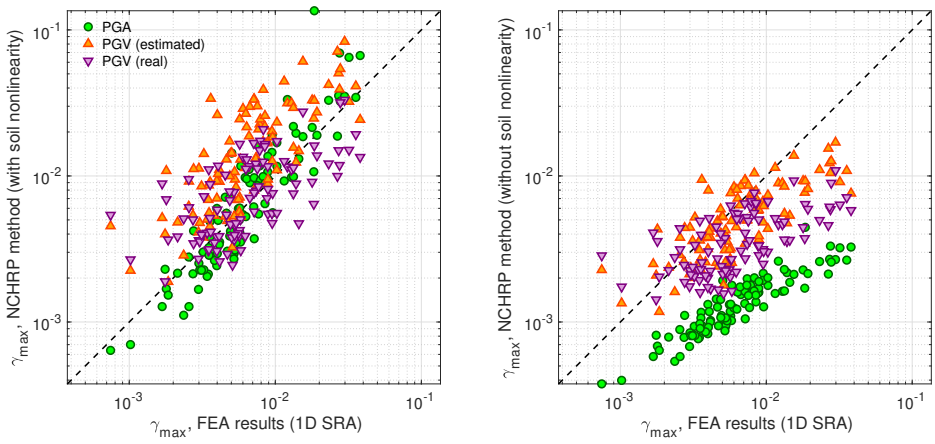

(a)

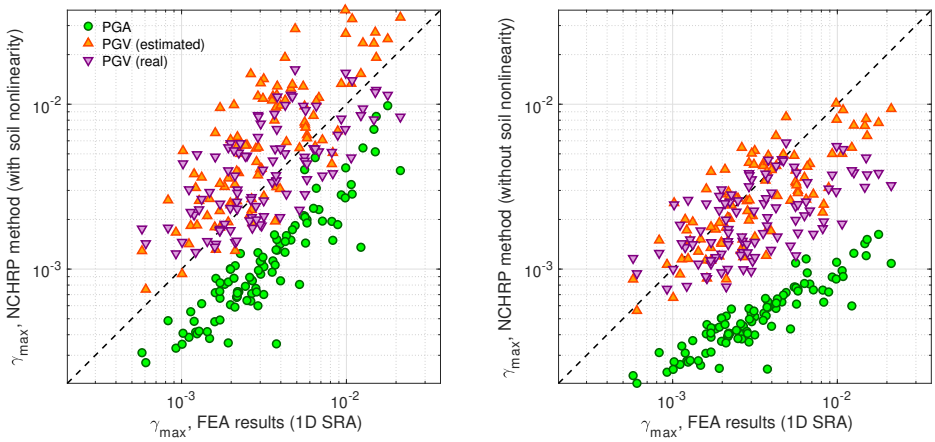

(b)

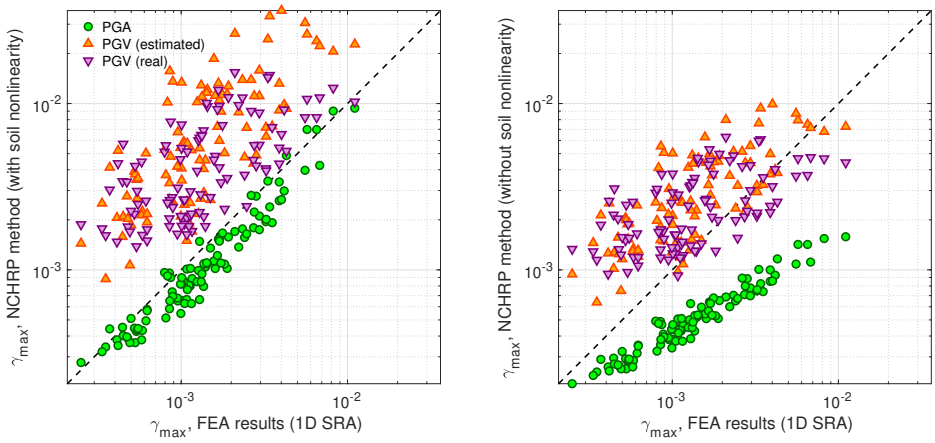

(c)

Figure 6.12: γ_{max} at the elevation of culvert, obtained from the NCHRP approach by using PGA and PGV, and the 1D site response analysis for different soil profiles (a) case A (b) case B and (c) case C.

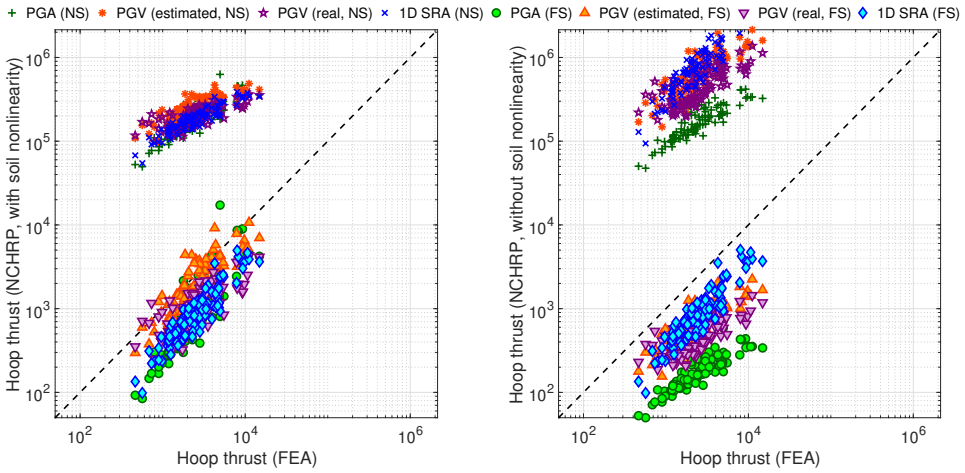

(a)

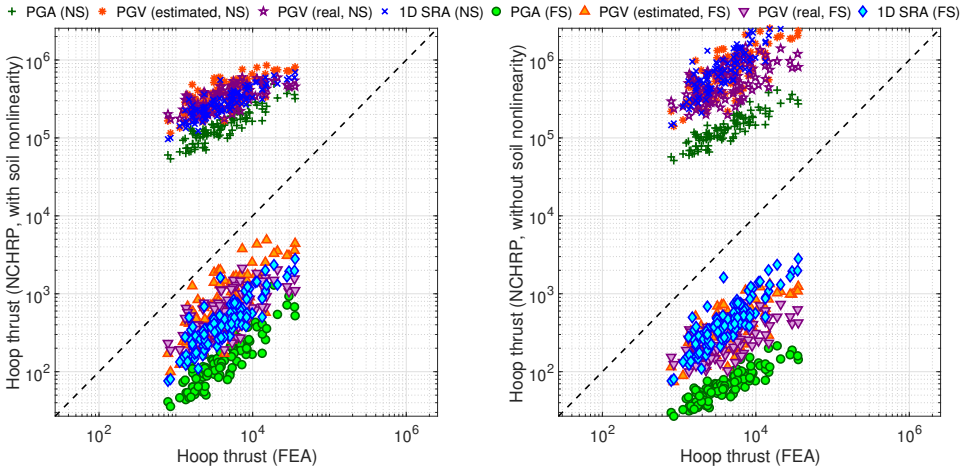

(b)

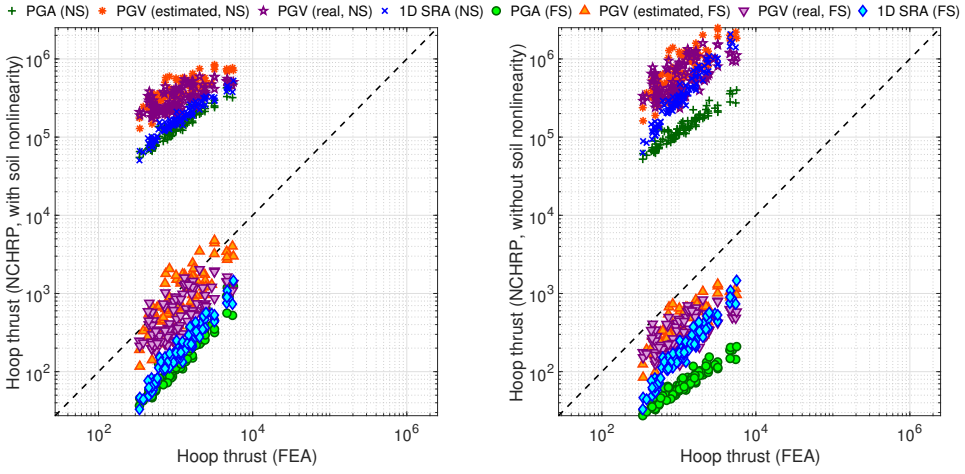

(c)

Figure 6.13: Maximum dynamic hoop thrust ($T_{\max}$) obtained from the NCHRP approach by using PGA, PGV, the 1D site response analysis, and FEA for different soil profiles (a) case A (b) case B and (c) case C.

6.3.4 Bending moment

Fig. 6.14 shows the comparison of the maximum dynamic bending moment ($M_{\max}$) computed based on the $\gamma_{\max}$ from the NCHRP approach by using PGA, PGV, and the 1D site response analysis at the elevation of culvert with FEA results, for different soil profiles, with and without considering the soil nonlinearity. For bending moment, the NCHRP approach only provides the solution for full-slip interface condition. And the FEA still uses the frictional interface with coefficient of 0.41. As seen, using the $\gamma_{\max}$ from 1D site response analysis gives the most accurate predictions for all the cases, compared with those using PGA and PGV. It should be noted that for case B, in which the shear wave velocity notably changes near the elevation of the culvert, PGV, compared with PGA, is a better parameter for predicting the bending moment. Finally, it's important to take soil nonlinearity into account.

6.4 Fragility-based analysis

6.4.1 Damage states (DS)

Comprehensive studies have been conducted for the performance-based seismic design of superstructures (i.e., above-ground buildings), and guidelines, such as FEMA-445 [183], summarizes the standard engineering demand parameters (EDPs) and their damage states, such as peak interstory drift and peak floor accelerations, which are for structural and nonstructural systems. However, there are no analysis guidelines or performance criteria for PBSA of underground structures. In [184, 185], the number of plastic hinges activated at the tunnel lining is used as EDP and three damage levels are defined. Besides, the ratio of the maximum bending moment on the lining to its capacity has been widely used to define the damage states [169, 172, 176]. In this study, we follow the criteria described in [13], adopt the maximum total stress ($\sigma_{\max}^{\text{total}} = T_{\max}^{\text{total}}/A + M_{\max}^{\text{total}}h/(2I)$) of the lining due to static and dynamic hoop thrust and bending moment as the EDP, and define three limit damage states based on that (see Table 6.4).

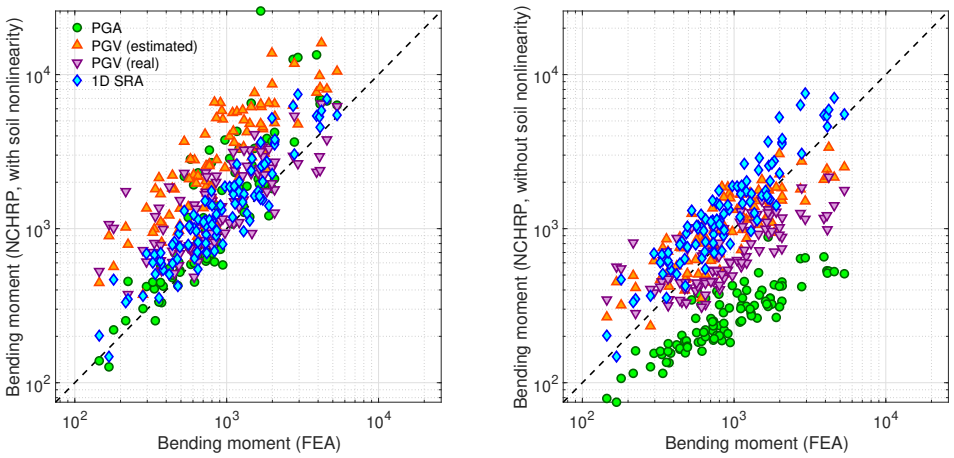

(a)

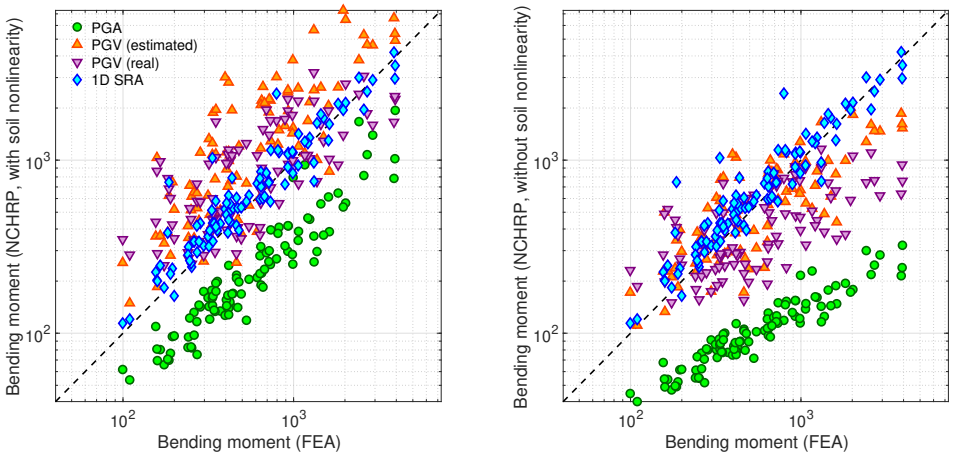

(b)

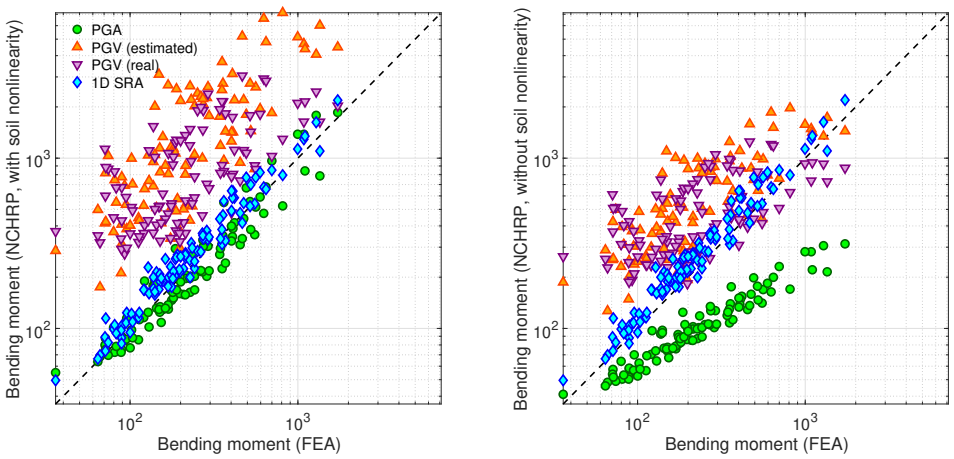

(c)

Figure 6.14: Maximum dynamic bending moment ($M_{\max}$) obtained from the NCHRP approach by using PGA, PGV, the 1D site response analysis, and FEA for different soil profiles (a) case A (b) case B and (c) case C.

Table 6.4: Definition of damage states for tunnel lining.

Damage state (DS_i)	Range of damage index (DI)
DS0	$\sigma_{\max}^{\text{total}} \leq \sigma_y \approx 0.6\sigma_u$
DS1	$\sigma_y \leq \sigma_{\max}^{\text{total}} \leq 0.75\sigma_u$
DS2	$0.75\sigma_u \leq \sigma_{\max}^{\text{total}} \leq 0.9\sigma_u$
DS3	$\sigma_{\max}^{\text{total}} > 0.9\sigma_u$

where σ_y and σ_u are the yield stress and ultimate strength of the adopted steel, which are equal to 250MPa and 415MPa, respectively. And such thresholds are defined based on the typical design criterion of steel structures. Here the categories of those damage states (e.g., minor, moderate, major, etc.) are not specified, because the requirement of the maximum internal stress is different for culverts with different purposes (e.g., gas, oil, water, etc.).

6.4.2 Intensity measure (IM)

Intensity measure (IM) is another key ingredient for generating the fragility curves. Especially for underground structures, because both amplitude and frequency contents of ground motions, as well as the soil profiles, can deeply affect the response of structures [186]. Therefore, in this study, a variety of IMs are utilized, such as PGA, SaT1, PGV and PGV/Vs30, to investigate their behavior. SaT1 is the 5% damped spectral acceleration at T1, the fundamental period of vibration, which is determined based on [85], $T_1 = 4H/\overline{Vs} = 0.5$, 0.355 and 0.334 sec, for cases A, B and C, respectively. In order to develop the fragility curves, first the EDP versus IM plots are generated and the median, and standard deviation of the best-fitting regression line are computed. Figs. 6.15-6.17 display these plots, and Table. 6.5 shows the associated properties of the fitting lines to be used in the subsequent fragility analyses. The probabilistic seismic demand models (PDMs) in which the demands are plotted versus the IMs are generated first by computing the median line and the standard dispersions as

follows:

$$S_d = me^{k\cdot \mathrm{IM}} \tag{6.14}$$

$$\beta_D = \sqrt{\sum_{i=1}^{n} \frac{[\ln d_i - \ln(S_{d_i})]^2}{n-1}} \tag{6.15}$$

$$\beta = \sqrt{\beta_C^2 + \beta_{DS}^2 + \beta_D^2} \tag{6.16}$$

where m and k are the regression coefficients, S_d is the median value of seismic demand; and β_D is the logarithmic dispersion of the demand conditioned on IM. According to [169], the total variability (β) should be modeled by the combination of the three contributors: (1) the capacity of the tunnel ($\beta_C = 0.3$ [187]), (2) the damage states definition ($\beta_{DS} = 0.4$ [168]), and (3) the ground motion demand (β_D). As shown in Figs. 6.15-6.17 and Table 6.5, PGA produces the least scattered plot for all the cases.

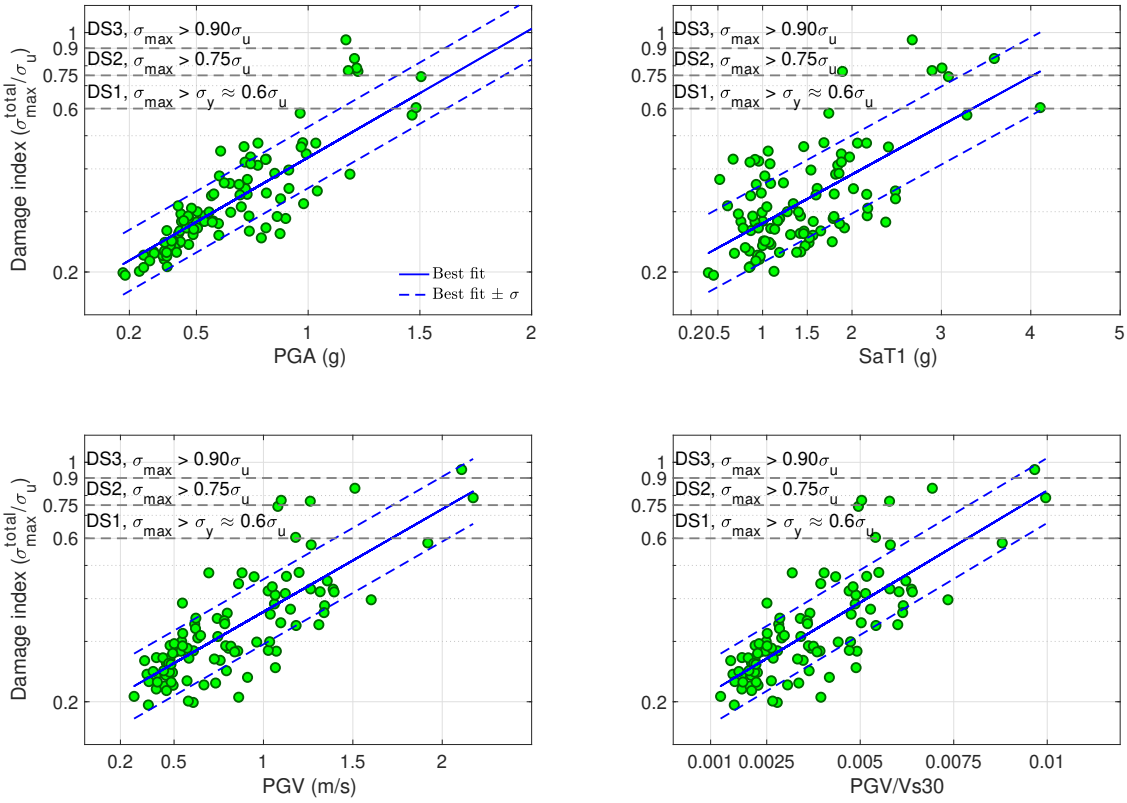

Figure 6.15: DI versus various IMs for case A.

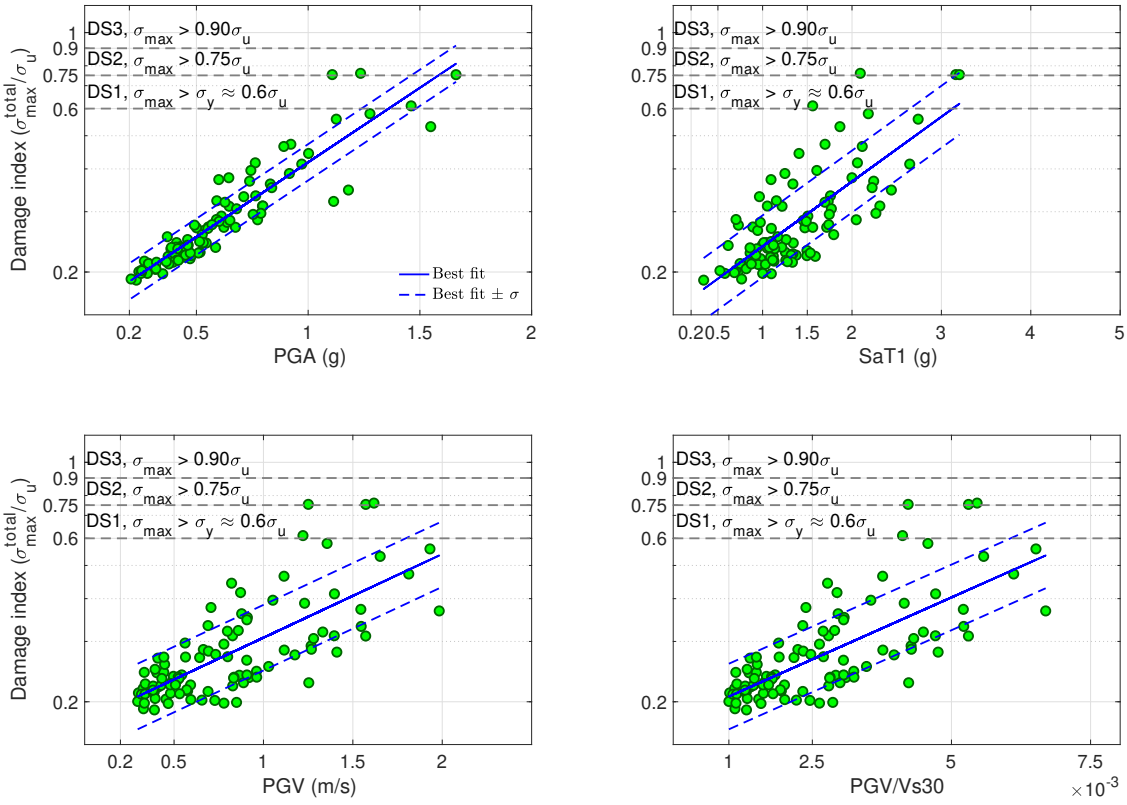

Figure 6.16: DI versus various IMs for case B.

Table 6.5: Statistical properties of the PDMs for four different IMs and cases.

Parameters/IMs		PGA	SaT1	PGV	PGV/Vs30
Case A	m	0.1929	0.2109	0.1946	0.1946
	k	0.8361	0.3186	0.6677	145.6881
	β_D	0.1996	0.2537	0.2113	0.2113
	β	0.5384	0.5607	0.5428	0.5428
Case B	m	0.5384	0.5607	0.5428	0.5428
	k	0.9646	0.4192	0.5407	160.2195
	β_D	0.1178	0.2007	0.2128	0.2128
	β	0.5137	0.5388	0.5434	0.5434
Case C	m	0.1707	0.1769	0.1870	0.1870
	k	0.5136	0.1945	0.2458	76.9259
	β_D	0.0487	0.1026	0.1233	0.1233
	β	0.5024	0.5104	0.5150	0.5150

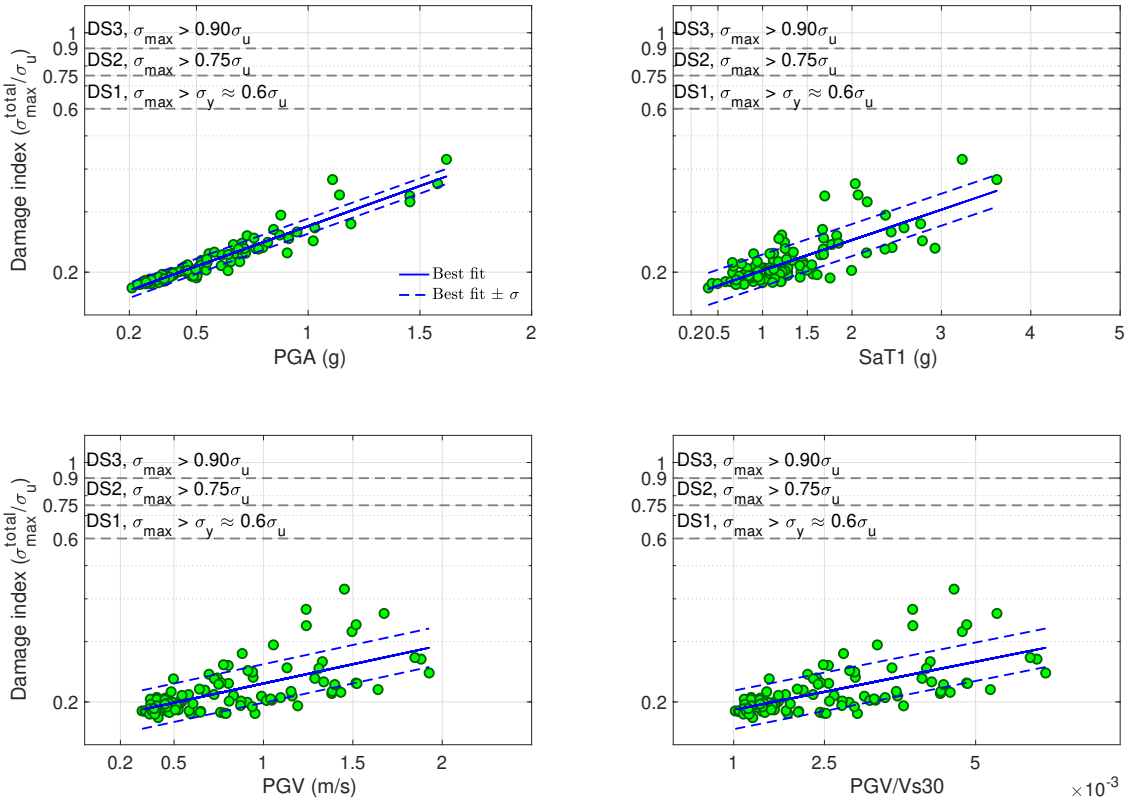

Figure 6.17: DI versus various IMs for case C.

6.4.3 Fragility curves

The seismic fragility curve represents the conditional probability of exceeding a predefined damage state as a function of a given intensity measured of ground motion. After defining the damage states and computing the median and standard deviation of the best-fitting regression line, the fragility curves are described by the lognormal probability distribution function as,

$$P(DS \geq DS_i | IM = X) = \Phi\left(\frac{\ln S_d(X) - \ln DS_i}{\beta}\right) \tag{6.17}$$

where $P(DS|IM)$ is the probability of being at or exceeding a particular damage state at a given intensity measure, and $\Phi(\cdot)$ is the standard normal cumulative distribution function.

As a result, Figs. 6.18-6.20 show the fragility curves for different damage states, intensity measures and cases. The IM PGV/Vs30 shows the best performance, in terms of the variations of the fragility curve for different cases. Because unlike the other three IMs, it explicitly considers the soil stiffness. Another thing needs attention is that, even though the culvert performed well in stiffer soil (i.e., case C), there still is some risk, because the damage probability values for most of the IMs are non-zero.

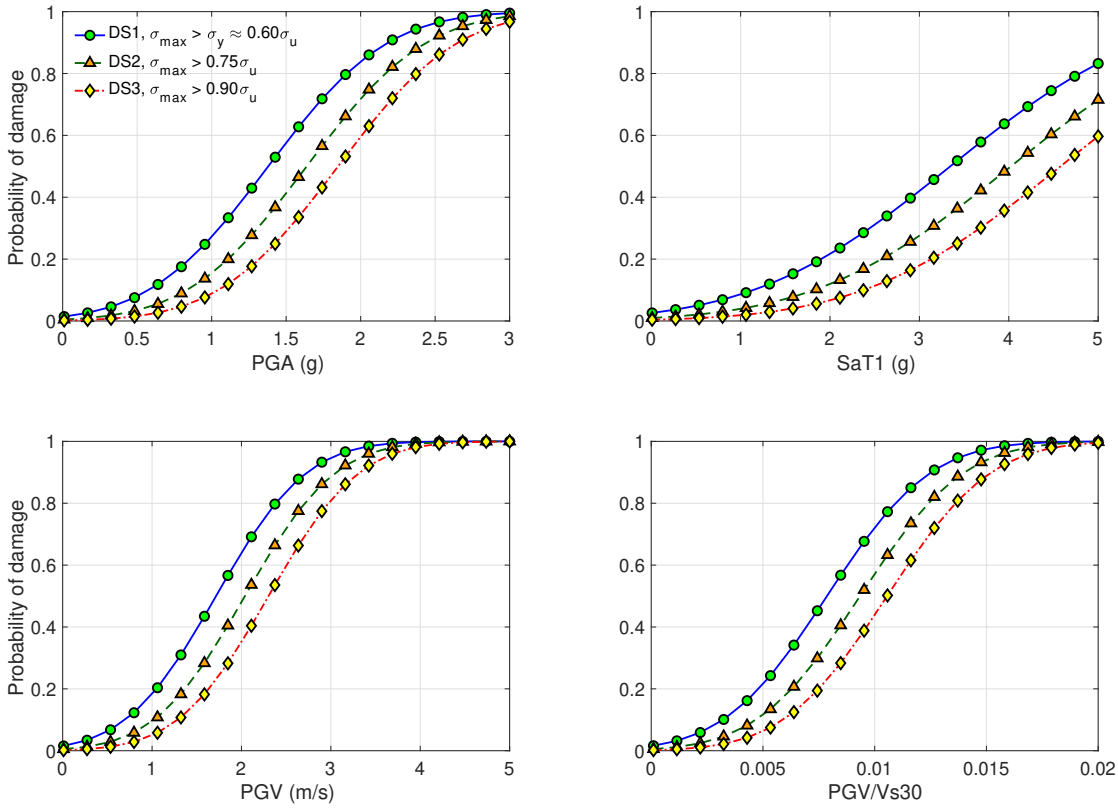

Figure 6.18: Fragility curves for different DSs and IMs for case A.

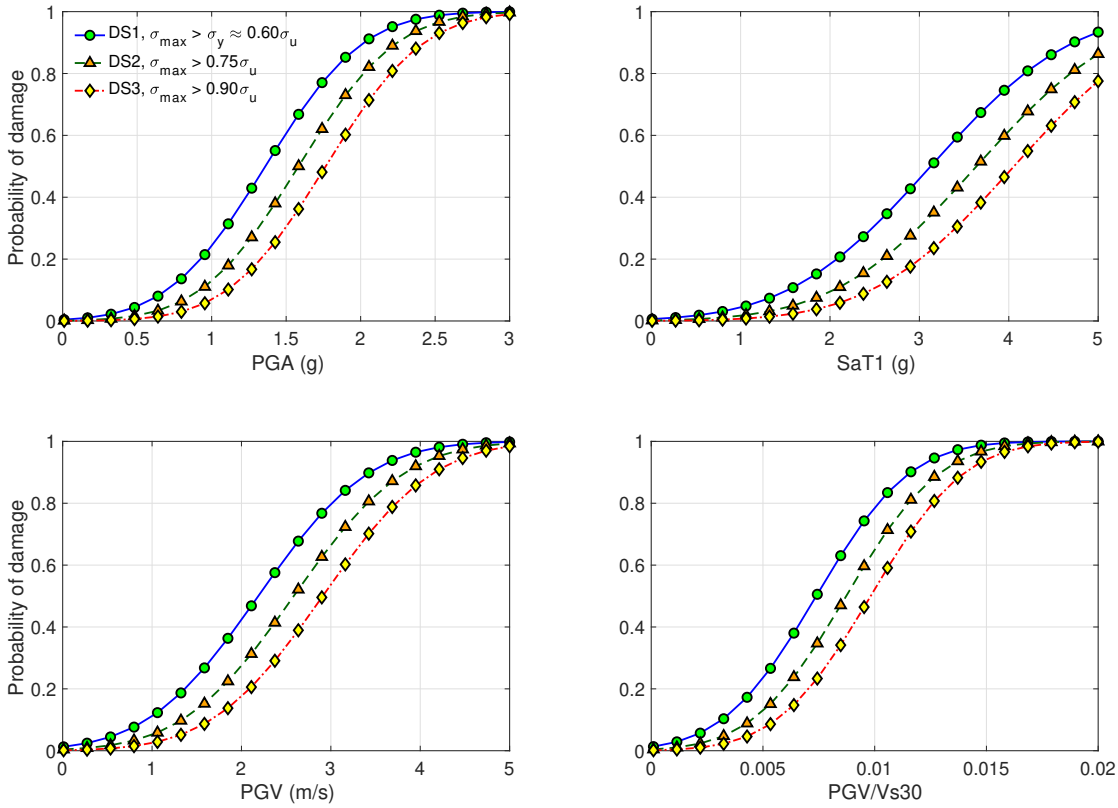

Figure 6.19: Fragility curves for different DSs and IMs for case B.

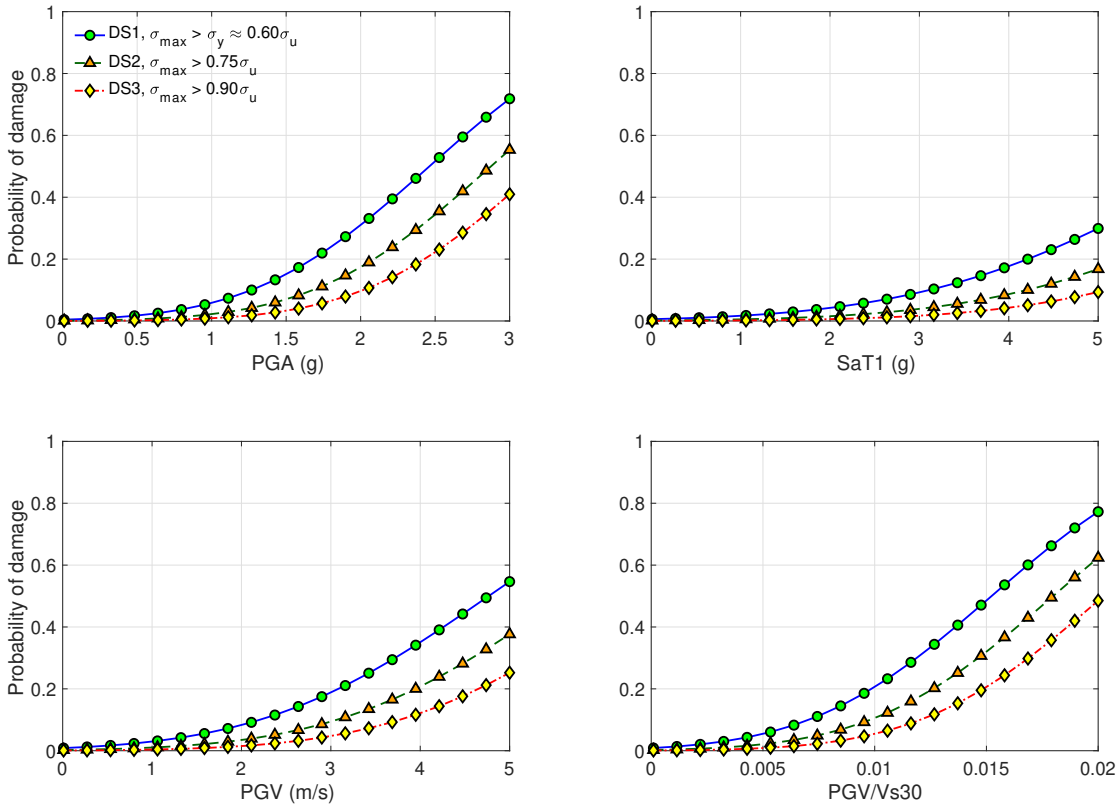

Figure 6.20: Fragility curves for different DSs and IMs for case C.

CHAPTER 7

Summary and conclusions

7.1 Chapter 2: validation of a three-dimensional constitutive model for nonlinear site response and soil-structure interaction analyses using centrifuge test data

In this chapter, we implemented a multi-axial soil constitutive model originally developed by Borja [63, 72] in ABAQUS. The expression of its consistent tangent stiffness moduli, when a viscous damping is applied to the soil model, is derived and tested during simple shear tests with strain-controlled harmonic loading. Furthermore, 1D site response analyses are conducted, the model is verified by comparing the results with the well-known site-response analysis tool DEEPSOIL. Validation is achieved by calibrating the material parameters using a theoretical material response curve, and by making blind comparisons with measurements made in several centrifuge tests on embedded structures, including structural strains and deformations, lateral earth pressures, accelerations, and surface settlements. These results indicated that the model can accurately predict inelastic soil responses in a plane-strain setting. Comparisons made with results obtained from equivalent linear models and a pressure-dependent multi-yield surface model suggested that the implemented model is generally superior to them in predicting responses over a broad range of inpute frequencies.

7.2 Chapter 3: reduced order modeling tools for SSI problems

In this chapter, we presented procedures for implementation of DRM and PML in ABAQUS for 2D and 3D problems, including a new version of DRM for inclined incident SV waves. We then carried out a comprehensive set of verification studies through problems involving vertical and inclined incident SV waves, 2D and 3D domains, homogeneous and heterogeneous soil layers, and concentrated and distributed loads. Finally, we presented practical application examples on the computation of impedance functions, and investigations of the angle of incidence of seismic waves on response of buried structures. The presented coupled DRM-PML technique is a key analysis tool for soil-structure interaction problems; and the presented ABAQUS implementation, will be disseminated for broader use, should enable researchers and practicing engineers to carry out state-of-the-art nonlinear seismic analyses of soil-structure systems in truncated domains.

7.3 Chapter 4: development of validated methods for soil-structure analysis of buried structures

NCHRP 611 Method: In this method, choosing a proper value for the maximum shear strain, which controls the seismic demand, plays the most critical role in the prediction of critical structural responses.

When we used the iterative procedure described in section 4.3 to estimate the maximum shear strain, the bending strains in both the rectangular and circular culverts were over-predicted (see, Table 4.11). The predicted values for the rectangular box ranged from being 2.17 times (for a low amplitude motion) to 4.50 times (for a high amplitude motion) the measured value. The situation was better for the circular culvert, with predicted values being 1.29 times (for a medium amplitude motion) to 2.85 times (for a high amplitude motion) the measured values. These appeared to be severe inaccuracies for the NCHRP 611 method in predicting the bending strains.

The hoop strains in the circular culvert computed using the same method were generally under-predicted[1], which was the case even when the NCHRP 611-recommended no-slip condition was used for computing the soil thrust—an option that provides higher values than the full-slip condition. The predicted hoop strains were as low as 0.48 times (for a high amplitude motion) and as high as 1.11 times (for a medium amplitude motion) the measured values.

The NCHRP 611 report recommends the use of more refined approaches—namely, one-dimensional site response analyses—to obtain better estimates of the maximum shear strain at the elevation of the culvert structures. As seen in Table 4.11, the use of this more refined approach resulted in improvement of the bending strain estimates for both structures, but further deterioration of the hoop strains for the circular culvert. The bending strains for the rectangular culvert were generally underestimated for the low and medium amplitude motions, and were generally overestimated for the high amplitude motions. That said, the NCHRP 611 method produced its best results for the latter (i.e., high amplitude motion) case, for which the bending strains were 1.15, 1.03, and 0.99 times the measured values for the three high amplitude base excitations. Unfortunately, while the bending strain estimate improved for the circular culvert, the hoop strains have deteriorated, which had considerable magnitudes.

Given these results, it can be concluded that using one-dimensional site response analysis in predicting the maximum shear strain should be preferred over obtaining this value (iteratively) from the modulus reduction curves, when using the NCHRP 611 methods.

Between the two structures, it was observed that the NCHRP 611 methods were more successful in capturing the relatively stiff structure's (i.e., the rectangular culvert's) responses than the flexible (circular) one. That said, it was observed that the NCHRP 611 method generally under-predicted the bending strains (especially for low and medium amplitude motions). For the circular structure, both the bending and hoop strains were under-predicted in general for all base excitations; and the worst cases of these inaccuracies were encountered

[1]The analogous (hoop) strains for the rectangular culvert were negligible in all experiments.

for the high-amplitude base excitations.

Another important response measure considered was the von Mises stresses, which is a typical quantity used in strength-based design. The von Mises stresses (see Table 4.10) exhibited trends that were similar to the strains. Namely, (*i*) they were more accurate when obtained using the one-dimensional site response analyses; (*ii*) they were more accurate for the stiff (i.e., rectangular) structure than they were for the flexible (circular) one. It appeared that for most cases, the von Mises stresses obtained using the refined NCHRP approach provided adequate estimates, as the NCHRP-to-experiment ratios von Mises stresses ranged between 0.7 to 1.2. This implies that a strength-based design would require a safety factor of at least $1/0.7 \approx 1.43$ just to handle uncertainties in input motions *and* the model features related to ground motions—henceforth collectively referred to as epistemic uncertainties. On the other hand, the same ratios were bracketed from 0.4 to 1.5 for the circular culvert, implying an factor of safety of 2.5, which is quite large.

Given these observations, it appears that the use of NCHRP 611 methods of analysis on flexible structures may not produce adequately safe designs. It is likely that the situation will be worse for structures with higher relative flexibility and for higher amplitude motions.

On the other hand, predictions obtained using the refined NCHRP approach for rigid culverts appear acceptable. It should be noted here that the use of the refined NCHRP approach requires one-dimensional site response analyses for *every* ground motion considered.

Finite Element (FE) Approach: Comparison of the numerical and experimental results showed that by using only a few sets of recorded free-field accelerations to calibrate the soil constitutive relationship, the finite element model was more systematically successful in predicting the key response parameters of both culvert specimens compared to the NCHRP 611 methods (see, §4.4.1, for details). As shown in Table 4.12, for both the rectangular and circular structures, the bending strain ratios are closer to one compared to those computed using the NCHRP methods. For the hoop strain, on the other hand, using the finite element approach resulted in ratios that are closer to those obtained using the NCHRP iterative method for the low amplitude motions, and closer to those obtained using the NCHRP

refined approach for the moderate and high amplitude motions. As such, it is concluded that the finite element approach performed better in predicting bending strains regardless of the structure flexibility, while its accuracy in capturing the hoop strains decreased for cases in which the soil behaves more nonlinearly.

For the rigid (rectangular) culvert the ratio of predicted-to-experimental von Mises stresses ranged from 0.77 to 1.19, implying an epistemic factor of safety of $1/0.77 \approx 1.30$ (as compared to 1.43 for the refined NCHRP method). For the circular culvert, the same ratio ranged from 0.59 to 1.29, implying an epistemic factor of safety of $1/0.59 \approx 1.70$ (as compared to 2.5 for the refined NCHRP method). As such, it can be concluded that the FE method can handle rigid as well as flexible culverts equally well, and generally better than the NCHRP method.

It is also important to note that the soil model in the FE calculations was calibrated only once, using the centrifuge free-field array records during motion #9. It is, therefore, reasonable to expect that the FE model predictions could be made better overall, if its soil model was calibrated using free-field motions from multiple tests.

7.4 Chapter 5: parametric studies of the NCHRP 611 approach to investigate its accuracy and acceptable ranges of applicability for soil-structure analysis of circular culverts.

Parametric studies were performed using detailed finite element models to investigate the accuracy and acceptable ranges of applicability of the NCHRP 611 method for soil-structure analysis of circular culverts. These finite element models were variations of a model that was validated using centrifuge testing in a prior study. The effects of several relevant factors were explored—namely, the embedment depth ratio, the frequency content of the input motions, the amplitude of the input motions, and the relative stiffness of surrounding soil and buried structure. By assuming the results obtained from finite element simulations as the "true" responses, the following conclusions and recommendations regarding the NCHRP

611 method can be drawn:

- The NCHRP 611 method is generally very conservative. That is, it over-predicts the hoop strains for shallow embedment, and bending strains and diameter changes in all cases. The level of accuracy of NCHRP 611 predictions deteriorates going from hoop strain, to bending strain, to diameter change. Choosing a proper value for the maximum shear strain, which controls the seismic demand, plays the most critical role in the prediction of critical structural responses using the NCHRP 611 method. Given the results of the parametric studies, it is clear that the *refined* variants of the NCHRP 611 method—namely, the variants that utilize one-dimensional site response analyses—yield better estimates of the maximum shear strain at the elevation of the culvert structures.

- The hoop strains with deep embedment, computed using the NCHRP611-NonLinIterative method, are under-predicted, when the NCHRP 611-recommended no-slip condition is used for computing the soil thrust. The refined variants improve the accuracy of the predictions.

- The frequency content of input excitations can significantly affect the performance of the NCHRP 611 method. With lower λ/d values, not only the estimated maximum shear strain from Eq. 4.1 is overestimated by huge margins, but also the location where it occurs is incorrectly assumed. The NCHRP 611 method assumes that the maximum shear strain takes place at the elevation of the invert of the culvert. However, the elevation at the top of the culvert can also be possibly the place. Again, one-dimensional site response analyses are capable of finding the exact location where the maximum shear strain occurs, and the incorporation of this information yields better predictions.

- The performance of NCHRP611-NonLinIterative method under low amplitude input motions is acceptable, which is expected because the method is derived based on linear elasticity. However, for the nonlinear cases, as the amplitudes of input excitations

increase, the over-predictions from these methods appear to be unacceptably high, mainly because the effects of increasing damping ratios are overlooked. The refined approach (i.e., NCHRP611-NonLinRefined) can remarkably remedy this issue, because one-dimensional site response analyses automatically account for both stiffness reduction and damping effects.

- In this study we use two different soil profiles for every simulation. One is a homogeneous soil layer, and the other one has two layers with different material properties. By performing 1D site response analyses to find the PGA and the maximum shear strain ($\gamma_{\max}$), the impact of a hard layer at the base of the structure has been implicitly considered. And the results have demonstrated that the refined approach (i.e., NCHRP611-NonLinRefined) has better performance. In the future, more different soil profiles will be used to further study such impact on the response of buried structures.

7.5 Chapter 6: fragility-based seismic assessment of a large buried circular culvert.

A fragility-based seismic assessment of a large buried circular culvert is performed using an advanced finite element model of the structure and its surrounding (inelastic near-field and elastic far-field) soil media. In order to develop the fragility curves, a suite of 100 site-specific ground motions is selected based on a target conditioned on an average spectral acceleration. The suite is then utilized—using a consistent method (DRM) to inject them as far-field motions into the computational domain truncated by PML—to perform a set of nonlinear time-history analyses to extract various EDPs. Finally, by using the statistical properties of the PDM plots, and also by considering appropriate damage states for the culvert lining, fragility curves are generated for four different IMs, including PGA, SaT1, PGV and PGV/Vs30. It is observed that PGA produces the least scattered results for all the cases. However, PGV/Vs30 shows a more stable behavior, as it considers the stiffness of the soil layer and hence their fragility curves slightly diverge for different soil layers.

The proposed numerical model is validated with available analytical solutions and experimental data, and also reveals the shortcomings of the analytical methods when nonlinear seismic analyses are performed. The accuracy of using PGA and PGV to estimate the maximum far-field shear strain ($\gamma_{\max}$), adopting simplified equation to estimate PGV based on S_{a1}, and utilizing the iterative procedure to consider the soil nonlinearity, is examined. Finally, it is concluded that using the $\gamma_{\max}$ obtained from 1D site response has the best performance.

With such a comprehensively validated and both soil, structure and ground motions characteristics appropriately considered numerical model, more accurate fragility curves can easily be generated for many other underground structures, including pipes, tunnels, culverts, water reservoirs, dams, etc.

APPENDIX A

Formulations and matrices for PML

For 2D domain, the semi-discrete form is:

$$\mathbf{M}_{\text{PML}}\ddot{\mathbf{u}} + \mathbf{C}_{\text{PML}}\dot{\mathbf{u}} + \mathbf{K}_{\text{PML}}\mathbf{u} = \mathbf{F}_{\text{ext}} \tag{A.1}$$

where the element matrices $\mathbf{M}_{\text{PML}}$, $\mathbf{C}_{\text{PML}}$ and $\mathbf{K}_{\text{PML}}$ are defined as

$$\mathbf{M}_{\text{PML}} = \begin{bmatrix} \mathbf{M}_a & \mathbf{0} \\ \mathbf{0} & -\mathbf{N}_a \end{bmatrix},\ \mathbf{C}_{\text{PML}} = \begin{bmatrix} \mathbf{M}_b & \mathbf{A}_e \\ \mathbf{A}_e & -\mathbf{N}_b \end{bmatrix},\ \mathbf{K}_{\text{PML}} = \begin{bmatrix} \mathbf{M}_c & \mathbf{A}_p \\ \mathbf{A}_p & -\mathbf{N}_c \end{bmatrix} \tag{A.2a}$$

$$\mathbf{u} = [\mathbf{u}_x\ \mathbf{u}_y\ \boldsymbol{\sigma}_{xx}\ \boldsymbol{\sigma}_{yy}\ \boldsymbol{\sigma}_{xy}]^T,\ \mathbf{F}_{\text{ext}} = [\mathbf{F}_x\ \mathbf{F}_y\ \mathbf{0}\ \mathbf{0}\ \mathbf{0}]^T \tag{A.2b}$$

The submatrices in Eq. A.2(a) are defined as,

$$\mathbf{M}_i = \int_{\Omega^e} i\rho\ \text{diag}\big(\boldsymbol{\Phi}\boldsymbol{\Phi}^T,\ \boldsymbol{\Phi}\boldsymbol{\Phi}^T\big)\ d\Omega, \quad i = a,\ b,\ c \tag{A.3a}$$

$$\mathbf{N}_i = \int_{\Omega^e} i \begin{bmatrix} \frac{\lambda+2\mu}{4\mu(\lambda+\mu)}\boldsymbol{\Psi}\boldsymbol{\Psi}^T & \frac{-\lambda}{4\mu(\lambda+\mu)}\boldsymbol{\Psi}\boldsymbol{\Psi}^T & \\ \frac{-\lambda}{4\mu(\lambda+\mu)}\boldsymbol{\Psi}\boldsymbol{\Psi}^T & \frac{\lambda+2\mu}{4\mu(\lambda+\mu)}\boldsymbol{\Psi}\boldsymbol{\Psi}^T & \\ & & \frac{1}{\mu}\boldsymbol{\Psi}\boldsymbol{\Psi}^T \end{bmatrix} d\Omega, \quad i = a,\ b,\ c \tag{A.3b}$$

$$\mathbf{A}_i = \int_{\Omega^e} \begin{bmatrix} \boldsymbol{\Phi}_{,x}\boldsymbol{\Psi}^T\hat{\lambda}_y^i & & \boldsymbol{\Phi}_{,y}\boldsymbol{\Psi}^T\hat{\lambda}_x^i \\ & \boldsymbol{\Phi}_{,y}\boldsymbol{\Psi}^T\hat{\lambda}_x^i & \boldsymbol{\Phi}_{,x}\boldsymbol{\Psi}^T\hat{\lambda}_y^i \end{bmatrix} d\Omega,\ i = e,\ p,\ \hat{\lambda}_j^e = \alpha_j,\ \hat{\lambda}_j^p = \beta_j,\ j = x,\ y \tag{A.3c}$$

where $a = \alpha_x\alpha_y$, $b = \alpha_x\beta_y + \alpha_y\beta_x$, $c = \beta_x\beta_y$. $\boldsymbol{\Phi}$ and $\boldsymbol{\Psi}$ are the shape functions for the displacement and stress components. And here we use identical 4-node bilinear shape

functions for $\mathbf{\Phi}$ and $\mathbf{\Psi}$ in 2D domain.

For 3D domain, the semi-discrete form is:

$$\mathbf{M}_{\text{PML}}\ddot{\mathbf{u}} + \mathbf{C}_{\text{PML}}\dot{\mathbf{u}} + \mathbf{K}_{\text{PML}}\mathbf{u} + \mathbf{G}_{\text{PML}}\bar{\mathbf{u}} = \mathbf{F}_{\text{ext}} \tag{A.4a}$$

$$\bar{\mathbf{u}} = \int_0^t \mathbf{u}(\tau)\, d\tau \tag{A.4b}$$

where the element matrices $\mathbf{M}_{\text{PML}}$, $\mathbf{C}_{\text{PML}}$, $\mathbf{K}_{\text{PML}}$ and $\mathbf{G}_{\text{PML}}$ are defined as

$$\begin{aligned} \mathbf{M}_{\text{PML}} &= \begin{bmatrix} \mathbf{M}_a & \mathbf{0} \\ \mathbf{0} & -\mathbf{N}_a \end{bmatrix}, \quad \mathbf{C}_{\text{PML}} = \begin{bmatrix} \mathbf{M}_b & \mathbf{A}_e \\ \mathbf{A}_e & -\mathbf{N}_b \end{bmatrix}, \\ \mathbf{K}_{\text{PML}} &= \begin{bmatrix} \mathbf{M}_c & \mathbf{A}_p \\ \mathbf{A}_p & -\mathbf{N}_c \end{bmatrix}, \quad \mathbf{G}_{\text{PML}} = \begin{bmatrix} \mathbf{M}_d & \mathbf{A}_w \\ \mathbf{A}_w & -\mathbf{N}_d \end{bmatrix} \end{aligned} \tag{A.5a}$$

$$\mathbf{u} = [\mathbf{u}_x\ \mathbf{u}_y\ \mathbf{u}_z\ \boldsymbol{\sigma}_{xx}\ \boldsymbol{\sigma}_{yy}\ \boldsymbol{\sigma}_{zz}\ \boldsymbol{\sigma}_{xy}\ \boldsymbol{\sigma}_{xz}\ \boldsymbol{\sigma}_{yz}]^T,\ \mathbf{F}_{\text{ext}} = [\mathbf{F}_x\ \mathbf{F}_y\ \mathbf{F}_y\ \mathbf{0}\ \mathbf{0}\ \mathbf{0}\ \mathbf{0}\ \mathbf{0}\ \mathbf{0}]^T \tag{A.5b}$$

The submatrices in Eq. A.5(a) are defined as,

$$\mathbf{M}_i = \int_{\Omega^e} i\rho \, \mathrm{diag}\big(\mathbf{\Phi}\mathbf{\Phi}^T,\ \mathbf{\Phi}\mathbf{\Phi}^T,\ \mathbf{\Phi}\mathbf{\Phi}^T\big)\, d\Omega, \quad i = a,\ b,\ c,\ d \tag{A.6a}$$

$$\mathbf{N}_i = \int_{\Omega^e} i \begin{bmatrix} \frac{\lambda+\mu}{\mu(3\lambda+2\mu)}\mathbf{\Psi}\mathbf{\Psi}^T & \frac{-\lambda}{2\mu(3\lambda+2\mu)}\mathbf{\Psi}\mathbf{\Psi}^T & \frac{-\lambda}{2\mu(3\lambda+2\mu)}\mathbf{\Psi}\mathbf{\Psi}^T & & & \\ \frac{-\lambda}{2\mu(3\lambda+2\mu)}\mathbf{\Psi}\mathbf{\Psi}^T & \frac{\lambda+\mu}{\mu(3\lambda+2\mu)}\mathbf{\Psi}\mathbf{\Psi}^T & \frac{-\lambda}{2\mu(3\lambda+2\mu)}\mathbf{\Psi}\mathbf{\Psi}^T & & & \\ \frac{-\lambda}{2\mu(3\lambda+2\mu)}\mathbf{\Psi}\mathbf{\Psi}^T & \frac{-\lambda}{2\mu(3\lambda+2\mu)}\mathbf{\Psi}\mathbf{\Psi}^T & \frac{\lambda+\mu}{\mu(3\lambda+2\mu)}\mathbf{\Psi}\mathbf{\Psi}^T & & & \\ & & & \frac{1}{\mu}\mathbf{\Psi}\mathbf{\Psi}^T & & \\ & & & & \frac{1}{\mu}\mathbf{\Psi}\mathbf{\Psi}^T & \\ & & & & & \frac{1}{\mu}\mathbf{\Psi}\mathbf{\Psi}^T \end{bmatrix} d\Omega,$$

$$i = a,\ b,\ c,\ d \tag{A.6b}$$

$$\mathbf{A}_i = \int_{\Omega^e} \begin{bmatrix} \mathbf{\Phi}_{,x}\mathbf{\Psi}^T\hat{\lambda}^i_{yz} & & & \mathbf{\Phi}_{,y}\mathbf{\Psi}^T\hat{\lambda}^i_{xz} & \mathbf{\Phi}_{,z}\mathbf{\Psi}^T\hat{\lambda}^i_{xy} & \\ & \mathbf{\Phi}_{,y}\mathbf{\Psi}^T\hat{\lambda}^i_{xz} & & \mathbf{\Phi}_{,x}\mathbf{\Psi}^T\hat{\lambda}^i_{yz} & & \mathbf{\Phi}_{,z}\mathbf{\Psi}^T\hat{\lambda}^i_{xy} \\ & & \mathbf{\Phi}_{,z}\mathbf{\Psi}^T\hat{\lambda}^i_{xy} & & \mathbf{\Phi}_{,x}\mathbf{\Psi}^T\hat{\lambda}^i_{yz} & \mathbf{\Phi}_{,y}\mathbf{\Psi}^T\hat{\lambda}^i_{xz} \end{bmatrix} d\Omega,$$

$$i = e,\ p,\ w,\ \hat{\lambda}^e_{jk} = \alpha_j\alpha_k,\ \hat{\lambda}^p_{jk} = \alpha_j\beta_k + \alpha_k\beta_j,\ \hat{\lambda}^w_{jk} = \beta_j\beta_k,\ j,\ k = x,\ y,\ z \tag{A.6c}$$

where coefficients $a,\ b,\ c,\ d$ are defined as

$$a = \alpha_x\alpha_y\alpha_z \tag{A.7a}$$

$$b = \alpha_x\alpha_y\beta_z + \alpha_x\beta_y\alpha_z + \beta_x\alpha_y\alpha_z \tag{A.7b}$$

$$c = \alpha_x\beta_y\beta_z + \beta_x\beta_y\alpha_z + \beta_x\alpha_y\beta_z \tag{A.7c}$$

$$d = \beta_x\beta_y\beta_z \tag{A.7d}$$

APPENDIX B

Values of the participation factors for the first and second modes of the buried circular structures

Table B.1: First and second mode participation factors for circular culverts with varying embedment depth ratios.

H/d	Full-slip		No-slip	
	$E_{\lambda_1}(\%)$	$E_{\lambda_2}(\%)$	$E_{\lambda_1}(\%)$	$E_{\lambda_2}(\%)$
0.5	97.00	2.75	97.57	2.42
1.0	98.61	1.05	96.59	3.41
1.5	98.01	1.76	95.84	4.15
2.0	98.65	1.08	95.92	4.07
2.5	98.77	0.94	96.80	3.20
3.0	98.98	0.79	97.54	2.45
3.5	99.07	0.76	97.81	1.35
4.0	99.12	0.66	98.83	1.16
4.5	99.23	0.67	98.98	1.02
5.0	98.90	0.93	99.25	0.75

Table B.2: First and second mode participation factors for circular culverts under varying input excitation frequencies.

λ/d	Full-slip		No-slip	
	$E_{\lambda_1}(\%)$	$E_{\lambda_2}(\%)$	$E_{\lambda_1}(\%)$	$E_{\lambda_2}(\%)$
6.7	95.36	4.31	99.57	0.32
7.8	95.11	4.57	98.44	1.21
9.1	99.18	0.58	98.71	1.21
10.7	99.08	0.71	98.80	1.16
12.5	99.35	0.50	98.40	1.59
14.7	99.62	0.27	99.37	0.63
17.2	99.48	0.31	98.76	1.24
20.1	99.77	0.15	98.29	1.71
23.5	99.72	0.20	97.80	2.20
27.6	99.63	0.27	98.38	1.62
32.3	99.16	0.61	98.67	1.33
37.8	97.61	2.09	98.50	1.50
44.2	96.90	2.51	90.38	9.57
51.8	95.94	2.88	94.72	5.27
60.6	97.11	2.35	86.64	13.34
71.0	97.07	2.30	91.24	8.75
83.1	97.23	2.30	95.31	4.69
97.3	97.22	1.92	98.28	1.72
113.9	92.94	5.63	99.04	0.96
133.3	86.82	12.08	97.40	1.34

Table B.3: First and second mode participation factors for circular culverts under varying input excitation amplitudes.

$a_{\max}$ (g)	Full-slip		No-slip	
	$E_{\lambda_1}(\%)$	$E_{\lambda_2}(\%)$	$E_{\lambda_1}(\%)$	$E_{\lambda_2}(\%)$
0.01	98.95	0.85	99.88	0.12
0.02	99.34	0.51	99.71	0.29
0.03	99.30	0.53	99.32	0.68
0.05	99.24	0.53	98.62	1.38
0.08	99.02	0.73	98.78	1.22
0.13	98.61	1.19	98.18	1.81
0.22	98.79	1.03	98.07	1.93
0.36	97.65	2.09	98.76	1.24
0.60	96.59	2.89	96.92	3.08
1.00	95.69	3.96	93.62	5.82

Table B.4: First and second mode participation factors for circular culverts with different thicknesses.

Thickness (m)	Full-slip		No-slip	
	$E_{\lambda_1}(\%)$	$E_{\lambda_2}(\%)$	$E_{\lambda_1}(\%)$	$E_{\lambda_2}(\%)$
0.005	79.74	9.60	94.67	5.18
0.010	76.33	10.66	96.25	3.66
0.020	87.18	7.42	95.38	4.55
0.030	74.11	10.42	94.39	5.52
0.040	80.68	7.97	97.00	2.92
0.050	91.28	4.03	97.10	2.86
0.060	96.14	2.06	91.27	8.67
0.070	95.37	2.48	97.53	2.44
0.080	96.80	1.76	97.85	2.12
0.090	97.22	1.72	95.17	4.79
0.100	96.62	2.28	96.04	3.93
0.200	98.98	0.79	97.54	2.45
0.242	99.14	0.58	98.65	1.34
0.300	98.27	1.39	99.03	0.97
0.400	97.97	1.41	99.75	0.25

REFERENCES

[1] O. Abuhajar, H. E. Naggar, and T. Newson, "Centrifuge modeling of the static and seismic soil culvert interaction," tech. rep., University of Western Ontario, 2014.

[2] F. Y. Menq, *Dynamic properties of sandy and gravelly soils*. PhD thesis, University of Texas at Austin, 2003.

[3] E. Esmaeilzadeh Seylabi, H. Ebrahimian, W. Zhang, D. Asimaki, and E. Taciroglu, "Bayesian estimation of nonlinear soil model parameters using centrifuge experimental data," in *The Proceedings of Geotechnical Earthquake Engineering and Soil Dynamics V*, (Austin, TX), 2018.

[4] G. Madabhushi, *Centrifuge modeling for civil engineers*. Taylor & Francis Group, 2014.

[5] J. P. Wolf, *Dynamic soil-structure interaction*. Englewood Cliffs, N.J. 07632: Prentice-Hall, 1985.

[6] G. Mylonakis and G. Gazetas, "Seismic soil structure interaction: Beneficial or detrimental?," *Journal of Earthquake Engineering*, vol. 43, pp. 277–301, 2000.

[7] J. P. Stewart, R. B. Seed, and G. L. Fenves, *Empirical evaluation of inertial soil-structure interaction effects*. Pacific Earthquake Engineering Research Center Univ. of California, Berkeley, CA, 1998.

[8] J. Luco and H. Wong, "Response of a rigid foundation to a spatially random ground motion," *Earthquake Engineering & Structural Dynamics*, vol. 14, no. 6, pp. 891–908, 1986.

[9] H. B. Seed and J. Lysmer, *The seismic soil-structure interaction problem for nuclear facilities*. Lawrence Livermore Laboratory,, 1980.

[10] C. Chang, M. Power, I. Idriss, P. Somerville, W. Silva, and P. Chen, "Engineering characterization of ground motion. task ii. observational data on spatial variations of earthquake ground motion. volume 3," tech. rep., Woodward-Clyde Consultants, 1986.

[11] J. J. Johnson and A. P. Asfura, "Soil-structure interaction (ssi): Observations, data, and correlative analysis," in *Developments in dynamic soil-structure interaction*, pp. 219–258, Springer, 1993.

[12] G. Gazetas, "Analysis of machine foundation vibrations: state of the art," *International Journal of Soil Dynamics and Earthquake Engineering*, vol. 2, no. 1, pp. 2–42, 1983.

[13] Y. M. Hashash, J. J. Hook, B. Schmidt, I. John, and C. Yao, "Seismic design and analysis of underground structures," *Tunnelling and underground space technology*, vol. 16, no. 4, pp. 247–293, 2001.

[14] A. T. C. (ATC), *Tentative provisions for the development of seismic regulations for buildings*. Redwood City, CA: ATC 3-06, 1978.

[15] NEHRP Consultants Joint Venture: A Partnership of the Applied Technology Council (ATC) and the Consortium of Universities for Research in Eqarthquake Engineering, *Soil-Structure-Interaction for Building Structures (NIST GCR 12-917-21)*. National Institute of Standards and Technology, Gaithersburg, MD 20899, September 2012.

[16] American Society of Civil Engineers, *Minimum design loads for buildings and other structures*, vol. 7. American Society of Civil Engineers, 2010.

[17] W. D. L. Finn, B. H. Pandey, and C. E. Ventura, "Modeling soil-foundation-structure interaction," *The Structural Design of Tall and Special Buildings*, vol. 20, pp. S47–S62, 2011.

[18] D. G. Anderson, G. R. Martin, I. Lam, and J. N. Wang, *NCHRP Report 611: Seismic analysis and design of retaining walls, buried structures, slopes, and embankments*. Transportation Research Board, Washington, DC, 2008.

[19] J. Wang, "Seismic design of tunnels: A simple state-of-the-art design approach," tech. rep., Parsons, Brinckerhoff, Quade and Douglas Inc., 1993.

[20] J. Lysmer and R. L. Kuhlemeyer, "Finite dynamic model for infinite media," *Journal of the Engineering Mechanics Division*, vol. 95, no. EM4, pp. 859–876, 1969.

[21] A. S. Veletsos, A. M. Prasad, and W. H. Wu, "Transfer functions for rigid rectangular foundations," *Earthquake Engineering and Structural Dynamics*, vol. 26, no. 1, pp. 5–17, 1997.

[22] E. Kausel, "Early history of soil-structure interaction," *Soil Dynamics and Earthquake Engineering*, vol. 30, pp. 822–832, 2010.

[23] J. P. Wolf, "Consistent lumped-parameter models for unbounded soil: physical representation," *Earthquake Engineering and Structural Dynamics*, vol. 20, pp. 11–32, 1991.

[24] E. Safak, "Time-domain representation of frequency-dependent foundation impedance functions," *Soil Dynamics and Earthquake Engineering*, vol. 26, pp. 65–70, 2006.

[25] J. P. Wolf, *Foundation Vibration Analysis Using Simple Physical Models*. Upper Saddle River, NJ 07458: Prentice Hall, 1994.

[26] W. Wu and W. Lee, "Systematic lumped-parameter models for foundations based on polynomila-fraction expansion," *Earthquake Engineering and Structural Dynamics*, vol. 31, pp. 1383–1412, 2002.

[27] W. Wu and W. Lee, "Nested lumped-parameter models for foundation vibrations," *Earthquake Engineering and Structural Dynamics*, vol. 33, pp. 1051–1058, 2004.

[28] M. Saitoh, "Simple model of frequency-depenent impedance functions in soil-structure interaction using frequency-independent elements," *Journal of Engineering Mechanics ASCE*, pp. 1101–1113, October 2007.

[29] X. Du and M. Zhao, "A local time-domain transmitting boundary for simulating cylindrical elastic wave propagation in infinite media," *Soil Dynamics and Earthquake Engineering*, vol. 30, pp. 937–946, 2010.

[30] J. Bielak and P. Christiano, "On the effective seismic input for non-linear soil-structure interaction systems," *Earthquake Engineering and Structural Dynamics*, vol. 12, pp. 107–119, 1984.

[31] B. Jeremic, S. Kunnath, and F. Xiong, "Influence of soil-foundation-structure interaction on seismic response of the i-880 viaduct," *Engineering Structures*, vol. 26, pp. 391–402, 2004.

[32] Y. Zhang, J. P. Conte, Z. Yang, A. Elgamal, J. Bielak, and G. Acero, "Two-dimensional nonlinear earthquake response analysis of a bridge-foundation-ground system," *Earthquake Spectra*, vol. 24, pp. 343–386, 2008.

[33] S. Carbonari, F. Dezi, and G. Leoni, "Linear soil-structure interaction of coupled wall-frame structures on pile foundations," *Soil Dynamics and Earthquake Engineering*, vol. 31, pp. 1296–1309, 2011.

[34] J. M. Solberg, Q. Hossain, J. A. Blink, S. R. Bohlen, G. Mseis, and H. Greenberg, "Development of a generalized methodology for soil-structure interaction analysis using nonlinear time-domain techniques," Tech. Rep. LLNL-TR-635762, NEAMS Program, DOE Office of Nuclear Energy (NE-41), April 2013.

[35] M. Iguchi and J. E. Luco, "Dynamic response of flexible rectangular foundations on an elastic half-space," *Earthquake Engineering and Structural Dynamics*, vol. 9, pp. 239–249, 1981.

[36] N. Gucunski and R. Peek, "Vertical vibration of circular flexible foundations on layered media," *Earthquake Engineering and Structural Dynamics*, vol. 12, pp. 183–192, 1993.

[37] N. Gucunski, "Rocking response of flexible circular foundations on layered media," *Soil Dynamics and Earthquake Engineering*, vol. 15, pp. 485–497, 1996.

[38] C. C. Spyrakos and C. Xu, "Dynamic analysis of flexible massive strip-foundations embedded in layered soils by hybrid bem-fem," *Computers and Structures*, vol. 82, pp. 2541–2550, 2004.

[39] S. Chen and J. Hou, "Modal analysis of circular flexible foundations under vertical vibration," *Soil Dynamics and Earthquake Engineering*, vol. 29, pp. 898–908, 2009.

[40] X. Du and M. Zhao, "Stability and indentification for rational approximation of frequency response function of unbounded soil," *Earthquake Engineering and Structural Dynamics*, vol. 39, pp. 165–186, 2010.

[41] N. Mononobe and M. Matsuo, "On the determination of earth pressures during earthquakes," in *Word Engineering Congress*, vol. 9, pp. 179–187, 1929.

[42] J. Penzien, "Seismically induced racking of tunnel linings," *International Journal of Earthquake Engineering and Structural Dynamics*, vol. 29, pp. 683–691, 2000.

[43] M. G. Katona, "Seismic Design and Analysis of Buried Structures with CANDE-2007," *Journal of Pipeline Systems Engineering and Practice*, vol. 1, no. 3, pp. 111–119, 2010.

[44] S. J. Brandenberg, G. Mylonakis, and J. P. Stewart, "Kinematic framework for evaluating seismic earth pressures on retaining walls," *Journal of Geotechnical and Geoenvironmental Engineering*, vol. 141, pp. 1–10, 2015.

[45] J. P. Stewart, K. Afshari, and Y. M. A. Hashash, "Guidelines for performing hazard-consistent one-dimensional ground response analysis for ground motion prediction," PEER Report No. 2014/16, Pacific Earthquake Engineering Research Center, UC Berkeley, CA, 2014.

[46] B. Jeremić, S. Kunnath, and F. Xiong, "Influence of soil–foundation–structure interaction on seismic response of the i-880 viaduct," *Engineering Structures*, vol. 26, no. 3, pp. 391–402, 2004.

[47] Y. Zhang, J. P. Conte, Z. Yang, A. Elgamal, J. Bielak, and G. Acero, "Two-dimensional nonlinear earthquake response analysis of a bridge-foundation-ground system," *Earthquake Spectra*, vol. 24, no. 2, pp. 343–386, 2008.

[48] S. Carbonari, F. Dezi, and G. Leoni, "Linear soil–structure interaction of coupled wall–frame structures on pile foundations," *Soil Dynamics and Earthquake Engineering*, vol. 31, no. 9, pp. 1296–1309, 2011.

[49] Seed and Idriss, "Influence of soil conditions on ground motions during earthquakes.," *ASCE J Soil Mech Found Div*, 1969.

[50] P. B. Schnabel, J. Lysmer, and H. B. Seed, "Shake: A computer program for earthquake response analyses of horizontally layered sites," Tech. Rep. UCB/EERC-72, University of California, Berkeley, 1972.

[51] Idriss and Sun, "Shake91: A computer program for conducting equivalent linear seismic response analyses of horizontally layered soil deposits," tech. rep., Department of Civil and Environmental Engineering, University of California Davis., 1992.

[52] G. Sugito and Masuda, "Frequency dependent equi-linearized technique for seismic response analysis of multi-layered ground.," *oboku Gakkai Rombun-Hokokushu/Proceedings of the Japan Society of Civil Engineers*, 1994.

[53] D. Assimaki, E. Kausel, and A. Whittle, "Model for dynamic shear modulus and damping for granular soils," *Journal of Geotechnical and Geoenvironmental Engineering*, vol. 126, no. 10, pp. 859–869, 2000.

[54] D. Park and Y. M. Hashash, "Soil damping formulation in nonlinear time domain site response analysis," *Journal of Earthquake Engineering*, vol. 8, no. 02, pp. 249–274, 2004.

[55] J.-H. Prévost, "Mathematical modelling of monotonic and cyclic undrained clay behaviour," *International Journal for Numerical and Analytical Methods in Geomechanics*, vol. 1, no. 2, pp. 195–216, 1977.

[56] N. GERom'mos and G. GAZETA, "Constitutive model for l—d cyclic soil behaviour applied to seismic analysis of layered deposits," *Soils and Foundations*, vol. 45, no. 3, pp. 147–159, 2005.

[57] S. Yniesta, S. Brandenberg, and A. Shafiee, "Arcs: A one dimensional nonlinear soil model for ground response analysis," *Soil Dynamics and Earthquake Engineering*, vol. 102, pp. 75–85, 2017.

[58] N. Matasovic and M. Vucetic, "Cyclic characterization of liquefiable sands," *Journal of Geotechnical Engineering*, vol. 119, no. 11, pp. 1805–1822, 1993.

[59] M. B. Darendeli, *Development of a new family of normalized modulus reduction and material damping curves*. University of Texas, Austin, 2001.

[60] C. Phillips and Y. M. Hashash, "Damping formulation for nonlinear 1d site response analyses," *Soil Dynamics and Earthquake Engineering*, vol. 29, no. 7, pp. 1143–1158, 2009.

[61] J. H. Prevost, "A simple plasticity theory for frictional cohesionless soils," *International Journal of Soil Dynamics and Earthquake Engineering*, vol. 4, no. 1, pp. 9–17, 1985.

[62] Z.-L. Wang, Y. F. Dafalias, and C.-K. Shen, "Bounding surface hypoplasticity model for sand," *Journal of engineering mechanics*, vol. 116, no. 5, pp. 983–1001, 1990.

[63] R. I. Borja and A. P. Amies, "Multiaxial cyclic plasticity model for clays," *Journal of geotechnical engineering*, vol. 120, no. 6, pp. 1051–1070, 1994.

[64] M. T. Manzari and Y. F. Dafalias, "A critical state two-surface plasticity model for sands," *Geotechnique*, vol. 47, no. 2, pp. 255–272, 1997.

[65] A. Elgamal, Z. Yang, E. Parra, and A. Ragheb, "Modeling of cyclic mobility in saturated cohesionless soils," *International Journal of Plasticity*, vol. 19, no. 6, pp. 883–905, 2003.

[66] Z. Yang, A. Elgamal, and E. Parra, "Computational model for cyclic mobility and associated shear deformation," *Journal of Geotechnical and Geoenvironmental Engineering*, vol. 129, no. 12, pp. 1119–1127, 2003.

[67] Z. Karimi and S. Dashti, "Numerical and centrifuge modeling of seismic soil-foundation-structure interaction on liquefiable ground," *Journal of Geotechnical and Geoenvironmental Engineering*, vol. 142, no. 1, pp. 04015061–1–14, 2016.

[68] H.-Y. Chao and R. I. Borja, "Nonlinear dynamic soil-structure interaction analysis and application to Lotung problem," Tech. Rep. J. A. Blume Earthquake Engrg. Ctr. Tech. Rep. 129, Stanford University, Stanford, CA, 1998.

[69] R. I. Borja, H.-Y. Chao, F. J. Montáns, and C.-H. Lin, "Nonlinear ground response at Lotung LSST site," *Journal of Geotechnical and Geoenvironmental Engineering*, vol. 125, no. 3, pp. 187–197, 1999.

[70] M. Vucetic and R. Dobry, "Effect of soil plasticity on cyclic response," *Journal of Geotechnical Engineering*, vol. 117, no. 1, pp. 89–107, 1991.

[71] W. Zhang, E. Esmaeilzadeh Seylabi, and E. Taciroglu, "Validation of a three-dimensional constitutive model for nonlinear site response and soil-structure interaction analyses using centrifuge test data," *International Journal for Numerical and Analytical Methods in Geomechanics*, vol. 41, no. 18, pp. 1828–1847, 2017.

[72] R. I. Borja, C.-H. Lin, K. M. Sama, and G. M. Masada, "Modeling nonlinear ground response of non-liquifiable soils," *Earthquake Engineering and Structural Dynamics*, vol. 29, pp. 63–83, 2000.

[73] A. Hushmand, S. Dashti, C. Davis, B. Hushmand, M. Zhang, M. Ghayoomi, J. McCartney, Y. Lee, and J. Hu, "Seismic performance of underground reservoir structures: insight from centrifuge modeling on the influence of structure stiffness," *Journal of Geotechnical and Geoenvironmental Engineering*, p. 04016020, 2016.

[74] Hibbit, Karlsson, and Sorensen, *ABAQUS/Standard Analysis User's Manual*. USA: Hibbitt, Karlsson, Sorensen Inc., 2007.

[75] Y. M. A. Hashash, M. I. Musgrove, J. A. Harmon, D. Groholski, C. A. Phillips, and D. Park, "Deepsoil v6.1, user manual," tech. rep., University of Illinois at Urbana-Champaign, Urbana, IL, 2016.

[76] Y. Deng, S. Dashti, A. Hushmand, C. Davis, and B. Hushmand, "Seismic response of underground reservoir structures in sand: Evaluation of class-c and c1 numerical simulations using centrifuge experiments," *Soil Dynamics and Earthquake Engineering*, vol. 85, pp. 202–216, 2016.

[77] E. Esmaeilzadeh Seylabi, C. Jeong, S. Dashti, A. Hushmand, and E. Taciroglu, "Seismic response of buried reservoir structures: comparison of numerical simulations with centrifuge experiments," *Soil Dynamics and Earthquake Engineering (under review)*, 2016.

[78] Y. F. Dafalias and E. P. Popov, "Cyclic loading for materials with a vanishing elastic region," *Nuclear Engineering and Design*, vol. 41, no. 2, pp. 293 – 302, 1977.

[79] J. Simo and T. Hughes, *Computational Inelasticity*. Interdisciplinary Applied Mathematics, Springer New York, 2000.

[80] R. I. Borja and W.-H. Wu, "Vibration of foundations on incompressible soils with no elastic region," *Journal of Geotechnical Engineering*, vol. 120, no. 9, pp. 1570–1592, 1994.

[81] C. G. Broyden, "A class of methods for solving nonlinear simultaneous equations," *Mathematics of Computation*, vol. 19, no. 92, pp. 577–593, 1965.

[82] MATLAB, *version R2018a)*. Natick, Massachusetts: The MathWorks Inc., 2018.

[83] E. E. Seylabi, C. Jeong, and E. Taciroglu, "On numerical computation of impedance functions for rigid soil-structure interfaces embedded in heterogeneous half-spaces," *Computers and Geotechnics*, vol. 72, pp. 15–27, 2016.

[84] J. P. Bardet, Q. Huang, and S. Chi, "Numerical prediction for model no. 1," in *Proceedings of the international conference on the verification of numerical procedures for the analysis of soil liquefaction problems*, vol. 1, (Netherlands), pp. 67–86, A.A. Balkema, 1993.

[85] Y. M. Hashash, S. Dashti, M. I. Romero, M. Ghayoomi, and M. Musgrove, "Evaluation of 1-D seismic site response modeling of sand using centrifuge experiments," *Soil Dynamics and Earthquake Engineering*, vol. 78, pp. 19–31, 2015.

[86] M. T. Heath, *Scientific Computing: An Introductory Survey*. New York: McGraw-Hill, second ed., 2002.

[87] F. Auger and P. Flandrin, "Improving the Readability of Time-Frequency and Time-Scale Representations by the Reassignment Method," *IEEE Transaction of Signal Processing*, vol. 43, no. 5, pp. 1068–89, 1995.

[88] K. Gillis, S. Dashti, and Y. M. Hashash, "Dynamic calibration of tactile sensors for measurement of soil pressures in centrifuge," *ASTM Geotechnical Testing Journal*, vol. 38, pp. 261–274, 2015.

[89] U.S. Naval Facilities Engineering Command, *Foundations and Earth Structures: Design Manual 7.2 (NAVFAC DM-7.2)*. U.S. Navy, U.S. Government Printing Office, Washington, D.C. 20402, 1986.

[90] S. Kramer, *Geotechnical Earthquake Engineering*. Prentice Hall International Series in Civil Engineering And, Prentice Hall, 1996.

[91] E. Esmaeilzadeh Seylabi, *Reduced order modeling of soil structure interaction problems*. PhD thesis, UCLA, 2016.

[92] S. Marburg and B. Nolte, *Computational acoustics of noise propagation in fluids: finite and boundary element methods*, vol. 578. Springer, 2008.

[93] R. L. Higdon, "Radiation boundary conditions for the scalar wave equation," *SIAM Journal on Numerical Analysis*, vol. 27, no. 4, pp. 831–870, 1990.

[94] D. Givoli, "High-order local non-reflecting boundary conditions: a review," *Wave Motion*, vol. 39, pp. 319–326, 2004.

[95] P. Joly and C. Tsogka, "Higher order absorbing boundary conditions for elastodynamics," in *Proc. of the 4th European Conference on Computational Mechanics (ECCM-2010)*, (Paris), May 2010.

[96] D. Rabinovich, D. Givoli, J. Bielak, and T. Hagstrom, "A finite element scheme with a high order absorbing boundary condition for elastodynamics," *Computer Methods in Applied Mechanics and Engineering*, vol. 200, no. 23-24, pp. 2048–2066, 2011.

[97] D. Baffet, J. Bielak, D. Givoli, T. Hagstrom, and D. Rabinovich, "Long-time stable high-order absorbing boundary conditions for elastodynamics," *Computational Methods in Applied Mechanics and Engineering*, vol. 241, no. 244, pp. 20–37, 2012.

[98] J. F. Claerbout, "Coarse grid calculations of waves in inhomogeneous media with application to delineation of complicated seismic structure," *Geophysics*, vol. 35, no. 3, pp. 407–418, 1970.

[99] J. F. Claerbout and A. G. Johnson, "Extrapolation of time-dependent waveforms along their path of propagation," *Geophysical Journal International*, vol. 26, no. 1-4, pp. 285–293, 1971.

[100] R. Clayton and B. Engquist, "Absorbing boundary conditions for acoustic and elastic wave equations," *Bulletin of the seismological society of America*, vol. 67, no. 6, pp. 1529–1540, 1977.

[101] T. Akiyoshi, K. Fuchida, and H. Fang, "Absorbing boundary conditions for dynamic analysis of fluid-saturated porous media," *Soil Dynamics and Earthquake Engineering*, vol. 13, no. 6, pp. 387–397, 1994.

[102] H. S. Kim, "Finite element analysis with paraxial & viscous boundary conditions for elastic wave propagation," *Engineering*, vol. 4, no. 12, p. 843, 2012.

[103] J. P. Berenger, "A perfectly matched layer for the absorption of electromagnetic waves," *Journal of Computational Physics*, vol. 114, pp. 185–200, 1994.

[104] U. Basu and A. K. Chopra, "Perfectly matched layers for time-harmonic elastodynamics of unbounded domains: theory and finite-element implementation," *Computer Methods in Applied Mechanics and Engineering*, vol. 192, no. 11–12, pp. 1337 – 1375, 2003.

[105] U. Basu and A. K. Chopra, "Perfectly matched layers for transient elastodynamics of unbounded domains," *International Journal for Numerical Methods in Engineering*, vol. 59, no. 8, pp. 1039–1074, 2004.

[106] S. Kucukcoban and L. F. Kallivokas, "Mixed pefectly-matched-layers for direct transient analysis in 2d elastic heterogeneous media," *Computational Methods in Applied Mechanics and Engineering*, vol. 200, pp. 57–76, 2011.

[107] S. Kucukcoban and L. Kallivokas, "A symmetric hybrid formulation for transient wave simulations in pml-truncated heterogeneous media," *Wave Motion*, vol. 50, no. 1, pp. 57–79, 2013.

[108] A. Fathi, B. Poursartip, and L. F. Kallivokas, "Time-domain hybrid formulations for wave simulations in three-dimensional pml-truncated heterogeneous media," *International Journal for Numerical Methods in Engineering*, vol. 101, no. 3, pp. 165–198, 2015.

[109] R. B. J. Brinkgreve, W. M. Swolfs, and E. Engin, *Plaxis Introductory: Student Pack and Tutorial Manual 2010*. Boca Raton, FL, USA: CRC Press, Inc., 2011.

[110] F. Itasca, "Fast lagrangian analysis of continua, ver. 8.0," *Itasca Consulting Group Inc., Minneapolis, Minn*, 2016.

[111] U. Basu, "Explicit finite element perfectly matched layer for transient three-dimensional elastic waves," *International Journal for Numerical Methods in Engineering*, vol. 77, no. 2, pp. 151–176, 2009.

[112] Livermore Software Technology Corporation, *LS-DYNA Keyword User's Manual*, 2017.

[113] M. K. Poul and A. Zerva, "Time-domain pml formulation for modeling viscoelastic waves with rayleigh-type damping in an unbounded domain: Theory and application in abaqus," *Finite Elements in Analysis and Design*, vol. 152, pp. 1–16, 2018.

[114] Hibbit, Karlsson, and Sorensen, *ABAQUS/Standard Analysis User's Manual*. USA: Hibbitt, Karlsson, Sorensen Inc., 2007.

[115] Y. Zheng and X. Huang, "Anisotropic perfectly matched layers for elastic waves in cartesian and curvilinear coordinates," tech. rep., Massachusetts Institute of Technology. Earth Resources Laboratory, 2002.

[116] H. M. Hilber, T. J. Hughes, and R. L. Taylor, "Improved numerical dissipation for time integration algorithms in structural dynamics," *Earthquake Engineering & Structural Dynamics*, vol. 5, no. 3, pp. 283–292, 1977.

[117] J. Bielak, K. Loukakis, Y. Hisada, and C. Yoshimura, "Domain reduction method for three-dimensional earthquake modeling in localized regions, part i: Theory," *Bulletin of the Seismological Society of America*, vol. 93, no. 2, pp. 817–824, 2003.

[118] W. Zhang, E. E. Seylabi, and E. Taciroglu, "An abaqus toolbox for soil-structure interaction analysis," *Computers and Geotechnics*, vol. 114, p. 103143, 2019.

[119] A. Fathi, *Full-waveform inversion in three-dimensional PML-truncated elastic media: theory, computations, and field experiments*. PhD thesis, University of Texas, Austin, 2015.

[120] E. Bécache, P. G. Petropoulos, and S. D. Gedney, "On the long-time behavior of unsplit perfectly matched layers," *IEEE Transactions on Antennas and Propagation*, vol. 52, no. 5, pp. 1335–1342, 2004.

[121] B. Poursartip, *Topographic amplification of seismic motion*. PhD thesis, University of Texas, Austin, 2017.

[122] J. P. Wolf, "Soil-structure-interaction analysis in time domain," *Nuclear engineering and design*, vol. 111, no. 3, pp. 381–393, 1989.

[123] G. Mylonakis, A. Nikolaou, and G. Gazetas, "Soil–pile–bridge seismic interaction: kinematic and inertial effects. part i: soft soil," *Earthquake Engineering & Structural Dynamics*, vol. 26, no. 3, pp. 337–359, 1997.

[124] J. Luco and R. Westmann, "Dynamic response of a rigid footing bonded to an elastic half space," *Journal of Applied Mechanics*, vol. 39, no. 2, pp. 527–534, 1972.

[125] Y. Wang and R. Rajapakse, "Dynamics of rigid strip foundations embedded in orthotropic elastic soils," *Earthquake engineering & structural dynamics*, vol. 20, no. 10, pp. 927–947, 1991.

[126] J. E. Luco and R. A. Westmann, "Dynamic response of circular footings," *Journal of Engineering Mechanics*, 1971.

[127] J. E. Luco, "Impedance functions for a rigid foundation on a layered medium," *Nuclear engineering and design*, vol. 31, no. 2, pp. 204–217, 1974.

[128] G. Lin, H. Zejun, and L. Jianbo, "An efficient approach for dynamic impedance of surface footing on layered half-space," *Soil Dynamics and Earthquake Engineering*, vol. 49, pp. 39–51, 2013.

[129] B. Poursartip, A. Fathi, and L. F. Kallivokas, "Seismic wave amplification by topographic features: A parametric study," *Soil Dynamics and Earthquake Engineering*, vol. 92, pp. 503–527, 2017.

[130] W. Zhang, E. E. Seylabi, and E. Taciroglu, "Effects of soil stratigraphy on dynamic soil- structure interaction behavior of large underground structures," in *Proc. of the 3rd Int. Conf. on Performance-based Design in Earthquake Geotechnical Engineering (PBD-III)*, (Vancouver, Canada), July 2017.

[131] C. Luo, M. Lou, G. Gui, and H. Wang, "A modified domain reduction method for numerical simulation of wave propagation in localized regions," *Earthquake Engineering and Engineering Vibration*, vol. 18, no. 1, pp. 35–52, 2019.

[132] U. Cilingir and S. P. G. Madabhushi, "A model study on the effects of input motion on the seismic behavior of tunnels," *Soil Dynamics and Earthquake Engineering*, vol. 31, pp. 452–462, 2011.

[133] U. Cilingir and S. P. G. Madabhushi, "Effect of depth on the seismic response of square tunnels," *Soils and Foundations*, vol. 51, no. 3, pp. 449–457, 2011.

[134] G. Lanzano, E. Billota, G. Usso, G. Silvestri, and S. P. G. Madabhushi, "Centrifuge modeling of seismic loading on tunnels in sand," *Geotechnical Testing Journal*, vol. 35, pp. 854–869, 2012.

[135] G. Lanzano, E. Billota, G. Russo, and F. Siverstri, "Experimental and numerical study on circular tunnels under seismic loading," *European Journal of Environmental and Civil Engineering*, vol. 19, pp. 539–563, 2015.

[136] G. Tsinidis, K. Pitilakis, G. Madabhushi, and C. Heron, "Dynamic response of flexible square tunnels: centrifuge testing and validation of existing design methodologies," *Géotechnique*, vol. 65, pp. 401–417, May 2015.

[137] D. Ulgen, S. Saglam, and M. Y. Ozkan, "Dynamic response of a flexible rectangular underground structure in sand: centrifuge modeling," *Bulletin of Earthquake Engineering*, vol. 13, pp. 2547–2566, 2015.

[138] O. Abuhajar, H. E. Naggar, and T. Newson, "Experimental and numerical investigations of the effect of buried box culverts on earthquake excitation," *Soil Dynamics and Earthquake Engineering*, vol. 79, pp. 130–148, 2015.

[139] M. A. Hashash, D. Park, and J. I.-C. Yao, "Ovaling deformations of circular tunnels under seismic loading, an update on seismic design and analysis of underground strucrures," *Tunneling and Underground Space Technology*, vol. 20, pp. 435–441, 2005.

[140] S. Kontoe, V. Avgerinos, and D. M. Potts, "Numerical validation of analytical solutions and their use for equivalent linear seismic analysis of circular tunnels," *Soil Dynamics and Earthquake Engineering*, vol. 66, pp. 206–219, 2014.

[141] G. Tsinidis, K. Pitilakis, and G. Madabhushi, "On the dynamic response of square tunnels in sand," *Engineering Structures*, vol. 125, pp. 419–437, 2016.

[142] G. Tsinidis, "Response characteristics of rectangular tunnels in soft soil subjected to transversal ground shaking," *Tunneling and Underground Space Technology*, vol. 62, pp. 1–22, 2017.

[143] A. Bobet, G. Fernande, H. Huo, and J. Ramirez, "A practical iterative procedure to estimate seismic-induced deformations of shallow rectangular structures," *Canadian Geotechnical Journal*, vol. 45, pp. 923–938, 2008.

[144] K. H. Park, K. Tantayopin, B. Tantavanich, and A. Owastsiriwong, "Analytical solution for seismic-induced ovaling of circular tunnel lining under no-slip interface conditions: a revisit," *Tunneling and Underground Space Technology*, vol. 24, pp. 231–235, 2009.

[145] A. Bobet, "Drained and undrained response of deep tunnels subjected to far-field shear loading," *Tunneling and Underground Space Technology*, vol. 25, pp. 21–31, 2010.

[146] B. L. Kutter, I. M. Idriss, T. Kohnke, J. Lakeland, X. S. Li, W. Sluis, X. Zeng, R. C. Tasuscher, Y. Goto, and I. Kubodera, "Design of a large earthquake simulator at uc davis," *In Centrifuge*, vol. 94, pp. 169–175, 1994.

[147] Department of Transportation State of California, "Standard plans (2015 edition)." http://www.dot.ca.gov/hq/esc/oe/project_plans/HTM/stdplns-US-customary-units-new15.htm, 2015.

[148] S. J. Brandenberg, S. Choi, B. L. Kutter, D. W. Wilson, and J. C. Santamarina, "A bender element system for measuring shear wave velocities in centrifuge models," in *6th International Conference on Physical Modeling in Geotechnics*, pp. 165–170, 2006.

[149] E. E. Seylabi, W. Zhang, E. Agapaki, D. Pitilakis, S. J. Brandenberg, J. Stewart, and E. Taciroglu, "Development of validated methods for soil-structure analysis of buried structures," tech. rep., University of California, Taciroglu, 2017.

[150] J. N. Wang, "Seismic design of tunnels: A simple state-of-the-art approach," tech. rep., Parsons, Brinckerhoff, Quade and Douglas Inc., 1993.

[151] J. Penzien, "Seismically induced racking of tunnel linings," *Earthquake Engineering and Structural Dynamics*, vol. 29, pp. 683–691, 2000.

[152] G. Tsinidis, K. Pitilakis, and C. Anagnostopoulos, "Circular tunnels in sand: dynamic response and efficiency of seismic analysis methods at extreme lining flexibilities," *Bulletin of Earthquake Engineering*, vol. 14, no. 10, pp. 2903–2929, 2016.

[153] S. Argyroudis, G. Tsinidis, F. Gatti, and K. Pitilakis, "Effects of ssi and lining corrosion on the seismic vulnerability of shallow circular tunnels," *Soil Dynamics and Earthquake Engineering*, vol. 98, pp. 244–256, 2017.

[154] G. Tsinidis, "Response of urban single and twin circular tunnels subjected to transversal ground seismic shaking," *Tunnelling and Underground Space Technology*, vol. 76, pp. 177–193, 2018.

[155] G. Tsinidis and K. Pitilakis, "Improved rf relations for the transversal seismic analysis of rectangular tunnels," *Soil Dynamics and Earthquake Engineering*, vol. 107, pp. 48–65, 2018.

[156] G. P. Kouretzis, K. I. Andrianopoulos, S. W. Sloan, and J. P. Carter, "Analysis of circular tunnels due to seismic p-wave propagation, with emphasis on unreinforced concrete liners," *Computers and Geotechnics*, vol. 55, pp. 187–194, 2014.

[157] W. Zhang, E. E. Seylabi, and E. Taciroglu, "A quantitative assessment of the nchrp 611 method for soil-structure interaction analysis of buried circular structures & a proposed improvement," *Computers and Geotechnics*, vol. 113, p. 103103, 2019.

[158] H. Bao, J. Bielak, O. Ghattas, L. F. Kallivokas, D. R. O'Hallaron, J. R. Shewchuk, and J. Xu, "Large-scale simulation of elastic wave propagation in heterogeneous media on parallel computers," *Computer methods in applied mechanics and engineering*, vol. 152, no. 1-2, pp. 85–102, 1998.

[159] G. P. Kouretzis, S. W. Sloan, and J. P. Carter, "Effect of interface friction on tunnel liner internal forces due to seismic s-and p-wave propagation," *Soil Dynamics and Earthquake Engineering*, vol. 46, pp. 41–51, 2013.

[160] I. T. Jolliffe, *Principal Component Analysis*. Springer Series in Statistics, Springer, 2nd ed., 2002.

[161] M. Shinozuka, S. E. Chang, R. T. Eguchi, D. P. Abrams, H. H. Hwang, and A. Rose, "Advances in earthquake loss estimation and application to memphis, tennessee," *Earthquake Spectra*, vol. 13, no. 4, pp. 739–758, 1997.

[162] D. Veneziano, J. Sussman, U. Gupta, and S. Kunnumkal, "Earthquake loss under limited transportation capacity: Assessment, sensitivity and remediation," in *The Seventh US National Conference on Earthquake Engineering 2002*, 2002.

[163] A. J. Kappos, G. Panagopoulos, C. Panagiotopoulos, and G. Penelis, "A hybrid method for the vulnerability assessment of r/c and urm buildings," *Bulletin of Earthquake Engineering*, vol. 4, no. 4, pp. 391–413, 2006.

[164] K. Pitilakis and G. Tsinidis, "Performance and seismic design of underground structures," in *Earthquake geotechnical engineering design*, pp. 279–340, Springer, 2014.

[165] C. Rojahn and R. L. Sharpe, *Earthquake damage evaluation data for California*. Applied technology council, 1985.

[166] S. Sharma and W. R. Judd, "Underground opening damage from earthquakes," *Engineering geology*, vol. 30, no. 3-4, pp. 263–276, 1991.

[167] A. L. Alliance, *Seismic Fragility Formulations for Water Systems: Guideline*. American Lifelines Alliance, 2001.

[168] F. F. E. M. Agency), *Multi-Hazard Loss Estimation Methodology?Earthquake Model: HAZUS MR4 Technical Manual*. US Department of Homeland Security, Federal Emergency Management Agency ?, 2004.

[169] S. Argyroudis and K. Pitilakis, "Seismic fragility curves of shallow tunnels in alluvial deposits," *Soil Dynamics and Earthquake Engineering*, vol. 35, pp. 1–12, 2012.

[170] S. Argyroudis, G. Tsinidis, F. Gatti, and K. Pitilakis, "Seismic fragility curves of shallow tunnels considering ssi and aging effects," in *2nd Eastern European Tunnelling Conference ?Tunnelling in a Challenging Environment*, pp. 1–10, 2014.

[171] T. S. Le, J. Huh, and J.-H. Park, "Earthquake fragility assessment of the underground tunnel using an efficient ssi analysis approach," *Journal of Applied Mathematics and Physics*, vol. 2, no. 12, p. 1073, 2014.

[172] G. Huang, W. Qiu, and J. Zhang, "Modelling seismic fragility of a rock mountain tunnel based on support vector machine," *Soil Dynamics and Earthquake Engineering*, vol. 102, pp. 160–171, 2017.

[173] W. Qiu, G. Huang, H. Zhou, and W. Xu, "Seismic vulnerability analysis of rock mountain tunnel," *International Journal of Geomechanics*, vol. 18, no. 3, p. 04018002, 2018.

[174] P. B. Tekie and B. R. Ellingwood, "Seismic fragility assessment of concrete gravity dams," *Earthquake engineering & structural dynamics*, vol. 32, no. 14, pp. 2221–2240, 2003.

[175] T. Liu, Z. Chen, Y. Yuan, and X. Shao, "Fragility analysis of a subway station structure by incremental dynamic analysis," *Advances in Structural Engineering*, vol. 20, no. 7, pp. 1111–1124, 2017.

[176] D.-D. Nguyen, D. Park, S. Shamsher, V.-Q. Nguyen, and T.-H. Lee, "Seismic vulnerability assessment of rectangular cut-and-cover subway tunnels," *Tunnelling and Underground Space Technology*, vol. 86, pp. 247–261, 2019.

[177] A. R. Ghotbi, "Performance-based seismic assessment of a large diameter extended pile shaft in a cohesionless soil," *Earthquake Engineering and Engineering Vibration*, vol. 14, no. 1, pp. 177–188, 2015.

[178] M. El-Reedy, *Onshore Structural Design Calculations: Power Plant and Energy Processing Facilities*. Butterworth-Heinemann, 2016.

[179] ASTM, "Structural design of corrugated steel pipe, pipe-arches, and arches for storm and sanitary sewers and other buried applications," 2015.

[180] O. Chaallal, M. Arockiasamy, and A. Godat, "Laboratory tests to evaluate mechanical properties and performance of various flexible pipes," *Journal of Performance of Constructed Facilities*, vol. 29, no. 5, p. 04014130, 2013.

[181] A. L. Alliance, "Guidelines for the design of buried steel pipe," in *American Society of Civil Engineers*, 2001.

[182] Peer, "Peer strong motion database," 2011.

[183] A. T. C. (ATC), "Next-generation performance-based seismic design guidelines: Program plan for new and existing buildings (fema-445)," 2006.

[184] G. Andreotti and C. Lai, "Seismic vulnerability of deep tunnels: numerical modeling for a fully nonlinear dynamic analysis," in *Proceedings of the 2nd European conference on earthquake engineering and seismology*, 2014.

[185] T.-H. Lee, D. Park, D. D. Nguyen, and J.-S. Park, "Damage analysis of cut-and-cover tunnel structures under seismic loading," *Bulletin of Earthquake Engineering*, vol. 14, no. 2, pp. 413–431, 2016.

[186] G. Tsinidis, L. Di Sarno, A. Sextos, and P. Furtner, "A critical review on the vulnerability assessment of natural gas pipelines subjected to seismic wave propagation. part 1: Fragility relations and implemented seismic intensity measures," *Tunnelling and Underground Space Technology*, vol. 86, pp. 279–296, 2019.

[187] M. Salmon, J. Wang, D. Jones, and C. Wu, "Fragility formulations for the bart system," in *Advancing Mitigation Technologies and Disaster Response for Lifeline Systems*, pp. 183–192, 2003.